

**OUT-OF-PLANE STABILITY OF REINFORCED MASONRY SHEAR WALLS  
UNDER SEISMIC LOADING: CYCLIC UNIAXIAL TESTS**

**by**

**Nazli Azimikor**

**B.Eng., The British Columbia Institute of Technology, 2009**

**A THESIS SUBMITTED IN PARTIAL FULFILLMENT OF  
THE REQUIREMENTS FOR THE DEGREE OF**

**MASTER OF APPLIED SCIENCE**

**in**

**THE FACULTY OF GRADUATE STUDIES**

**(Civil Engineering)**

**THE UNIVERSITY OF BRITISH COLUMBIA**

**(Vancouver)**

**April 2012**

**© Nazli Azimikor, 2012**

## **Abstract**

In recent years, widespread application of low-rise masonry construction, including post-disaster buildings like fire halls, has become limited in seismic regions of Canada. This is because the Canadian Masonry Design Standard (CSA S304.1-04) [Canadian Standard Association 2004] mandates stringent requirements on the design of ductile reinforced masonry (RM) shear walls, especially with regard to their height-to-thickness ( $h/t$ ) ratios, which were restricted to ensure against out-of-plane instability. This failure mechanism has been observed in the end zones of reinforced concrete shear walls loaded in-plane in experimental research and in past earthquakes. However, there is a lack of similar evidence for RM shear walls; this is a motivation for the research program described in this thesis.

The research consists of several major tasks. First, a review of the literature on previous experimental research studies on RM shear walls was conducted, followed by comprehensive investigation into the parameters affecting out-of-plane instability of RM shear walls. Based on the results of this literature review, the first phase of the experimental program was designed with a focus on modeling the RM wall end zone and understanding the mechanism of lateral instability. Five full-scale specimens representing the wall end zones were constructed and subjected to reversed cyclic axial tension and compression until failure. The effect of varying  $h/t$  ratios of the plastic hinge zone, as well as level of axial tensile strain on the out-of-plane instability was examined.

Based on the results of the experimental study, it was concluded that the level of applied tensile strain in the wall end zone is one of the critical factors governing its lateral instability. Therefore, the maximum tensile strain that may be imposed on a moderately ductile RM wall end-zone is determined based on a kinematic relationship between the axial strain and the out-of-plane displacement. A preliminary mechanic model has been proposed to predict the maximum tensile strain before instability takes place. The model can be incorporated into design provisions related to the thickness of shear walls of a given height. A comparison with the experimental results showed that the model offers conservative prediction of the maximum tensile strain.

## **Preface**

A version of Chapter 2 has been published. [Nazli Azimikor], Brzev, S., Elwood, K., and Anderson, D. (2011) Out-of-Plane Stability of Reinforced Masonry Shear Walls. 11th North American Masonry Conference, Minneapolis, MN. I conducted the review of all literature, analysis of database results and wrote most of the manuscript.

Section 3.1.3 on Material Properties is based on work conducted in the Structural Laboratory of British Columbia Institute of Technology (BCIT) by civil engineering students Porkeang Lim and Desmond Das under the supervision of Ken Zeleschuk, Assistant Instructor in the Civil Engineering Department. I was responsible for supervision of material sampling, molding of grout prisms, as well as post-processing of test data and reporting on testing procedure.

## Table of Contents

<b>Abstract</b> .....	<b>ii</b>
<b>Preface</b> .....	<b>iii</b>
<b>Table of Contents</b> .....	<b>iv</b>
<b>List of Tables</b> .....	<b>vi</b>
<b>List of Figures</b> .....	<b>vii</b>
<b>Acknowledgements</b> .....	<b>xi</b>
<b>Chapter 1: Introduction</b> .....	<b>1</b>
1.1 Objective and Scope.....	2
<b>Chapter 2: Literature Review</b> .....	<b>4</b>
2.1 Objective and Scope.....	4
2.2 Earthquake Evidence.....	4
2.3 Review of Code Provisions Related to Out-of-Plane Instability.....	5
2.4 Experimental Studies on RM Shear Walls.....	6
2.4.1 Experimental Studies on RM Shear Walls Which Encountered Out-of-plane Instability	9
2.4.2 Experimental Studies on Reinforced Concrete Shear Walls Encountering Out-of-Plane Instability .....	10
2.5 Database of Experimental Results related to RM Shear Walls.....	12
2.6 Analysis of Research Data.....	17
2.7 Summary and Conclusions .....	19
<b>Chapter 3: Experimental Program</b> .....	<b>20</b>
3.1 Background.....	20
3.2 Specimen Properties.....	21
3.2.1 Specimen Design.....	23
3.2.2 Specimen Construction.....	25
3.2.3 Material Properties .....	34
3.2.3.1 Masonry Units.....	34
3.2.3.2 Mortar .....	34
3.2.3.3 Grout.....	35
3.2.3.4 Masonry Prisms.....	38
3.2.3.5 Reinforcing Steel.....	39
3.3 Test Setup .....	42
3.3.1 Test Apparatus .....	42
3.3.2 Instrumentation .....	45
3.3.3 Data Acquisition System .....	47
3.4 Testing Procedure.....	47
3.4.1 Loading Protocols .....	48
3.4.1.1 Specimen C1 .....	48
3.4.1.2 Specimen C2 .....	49
3.4.1.3 Specimen C3 .....	49
3.4.1.4 Specimen C4 .....	50
3.4.1.5 Specimen C5 .....	51

3.5	Conclusions.....	52
<b>Chapter 4: Experimental Results .....</b>		<b>53</b>
4.1	Failure Mechanisms .....	53
4.2	Experimental Observations.....	54
4.2.1	Specimen C1 .....	54
4.2.2	Specimen C2.....	59
4.2.3	Specimen C3.....	69
4.2.4	Specimen C4.....	81
4.2.5	Specimen C5.....	94
4.3	Summary of Experimental Results.....	108
<b>Chapter 5: Characterization of Lateral Instability .....</b>		<b>109</b>
5.1	The General Behaviour of Reinforced Masonry Columns Subjected to Cyclic Axial Tension and Compression Loading.....	109
5.2	Strain-Based Design Criteria .....	113
5.3	Characterizing Out-of-plane Instability of Reinforced Masonry Columns.....	114
5.3.1	Determining Maximum Tensile Strain which Leads to Lateral Instability, $\epsilon_{sm}$ .....	115
5.3.1.1	Estimating residual strains based on an assumed bedjoint rotation distribution	119
5.3.1.2	Estimating residual strains based on an assumed curvature distribution .....	124
5.4	Determining the Inelastic Strain Demand, $\epsilon_{id}$ .....	132
5.5	Minimum Wall Thickness .....	134
<b>Chapter 6: Summary and Conclusions .....</b>		<b>136</b>
6.1	Failure Mechanisms of Axially Loaded Reinforced Masonry Columns .....	136
6.2	Analytical Approaches in Characterization of the Lateral Instability Phenomena.....	137
6.3	Recommendations for Future Research.....	140
<b>Bibliography .....</b>		<b>142</b>
<b>Appendix A Design of Specimen Cap Plates .....</b>		<b>145</b>
<b>Appendix B Development of the Reinforcement Weld Connection Detail.....</b>		<b>149</b>
<b>Appendix C Design of Specimen Retrofit with Glass Fiber Reinforced Polymer.....</b>		<b>154</b>
<b>Appendix D Design of the Test Apparatus .....</b>		<b>156</b>
D.1	Design Calculations.....	159
D.2	Design Drawings.....	177

## List of Tables

Table 2-1	Summary of experimental studies on flexural response of RM shear walls.....	14
Table 3-1	Specimen matrix .....	22
Table 3-2	Compressive strength of mortar cubes.....	35
Table 3-3	Compressive strength of grout prisms .....	37
Table 3-4	Compressive strength of grout cylinders .....	37
Table 3-5	Compressive strength of masonry prisms .....	39
Table 3-6	Properties of reinforcing steel.....	40
Table 4-1	Summary of specimen behaviour and failure modes.....	53
Table 4-2	Experimental observations for specimen C2 .....	63
Table 4-3	Experimental observations for specimen C3 .....	78
Table 4-4	Experimental observations for specimen C4 .....	90
Table 4-5	Experimental observations for specimen C5 .....	104
Table 5-1	Comparison between experimental total tensile strain leading to lateral instability and calculated maximum tensile strain based on crack rotations...	123
Table 5-2	Residual plastic strain based on different curvature models.....	125
Table 5-3	Comparison between experimental total tensile strain leading to lateral instability and calculated maximum tensile strain based on linear curvature distribution.....	126
Table B- 1	Weld sizes considered for connecting rebar to steel plates .....	150
Table B- 2	Weld size results.....	150
Table B- 3	Results of welding capacity tests.....	153
Table B- 4	Results of welding capacity tests for connection of 10M bars with 2mm tip .	153

## List of Figures

Figure 1-1	Out-of-plane instability mechanism in a RM shear wall.....	2
Figure 2-1	Hysteretic force-deformation plot .....	13
Figure 2-2	Effect of key wall design parameters on the failure mechanism.....	17
Figure 3-1	End zone of shear walls subjected to axial loads during reversed lateral loading.....	20
Figure 3-2	Test specimens after the construction .....	23
Figure 3-3	Welding detail for connection of rebar to specimen plates.....	24
Figure 3-4	Layout of SikaWrap 100G GFRP to the top half of specimens C3, C4 and C5 . .....	25
Figure 3-5	Bottom base plates showing welded reinforcing bars extending over the specimen height.....	26
Figure 3-6	Typical 140 mm thick concrete masonry block units used in construction of specimens: a. double ender unit, b. stretcher unit, c. half block unit .....	27
Figure 3-7	Welding of reinforcing bars to the top specimen plate .....	28
Figure 3-8	Application of GFRP over the top half of specimens C3 through C5.....	31
Figure 3-9	Mechanism to connect threaded rods to bottom specimen plate.....	32
Figure 3-10	Prestressing and lifting of the specimen into the test rig.....	33
Figure 3-11	Pinwheel method of preparation of grout prisms .....	36
Figure 3-12	Construction of masonry prisms .....	38
Figure 3-13	Testing reinforcement bars in the Baldwin universal testing machine .....	39
Figure 3-14	Stress-strain relationship for reinforcing bars .....	41
Figure 3-15	Test apparatus.....	43
Figure 3-16	Two-dimensional pantograph acting as a motion guide by restricting translation along one axis while allowing translation in the other.....	44
Figure 3-17	Horizontal translation of the pantograph (showing a nonlinear increase at large deformations) .....	45
Figure 3-18	Instrumentation scheme.....	46
Figure 3-19	Loading protocol for specimen C2.....	49
Figure 3-20	Loading protocol for Specimen C3 after the retrofit.....	50
Figure 3-21	Loading protocol for specimen C4.....	51
Figure 3-22	Loading protocol for specimen C5.....	51
Figure 4-1	Crack pattern for Specimen C1 .....	55
Figure 4-2	Rebar location within the specimen core (specimen C1).....	56
Figure 4-3	Axial stress vs. axial compressive strain response for specimen C1 .....	57
Figure 4-4	Axial load versus lateral displacement at midheight for specimen C1 .....	57
Figure 4-5	Specimen C1 at failure: note a continuous vertical splitting crack along the end block core (left) and disintegration of masonry in the crushed portion of the specimen (right).....	58
Figure 4-6	Specimen C2 cross-section and reinforcement layout relative to top and bottom specimen plates .....	59
Figure 4-7	Plot of a. applied axial load vs. axial strain over the plastic hinge height and b. applied axial load vs. maximum normalized lateral deformation at midheight at $\epsilon_t=0.80\%$ .....	60

Figure 4-8	Uniformly distributed horizontal cracks developed in specimen C2 along mortar bed joints during a tension loading cycle .....	61
Figure 4-9	Crack patterns for specimen C2 at increasing levels of tension displacements . .....	64
Figure 4-10	Specimen C2 at failure .....	65
Figure 4-11	Specimen C2 at the end of the test, after experiencing out-of-plane instability . .....	66
Figure 4-12	Local crushing of the masonry face shell at the top of specimen C2 after experiencing out-of-plane instability .....	67
Figure 4-13	Buckled shape of specimen C2 during the cycle of $\epsilon_t=0.8\%$ .....	67
Figure 4-14	Axial load versus axial deformation response for specimen C2. ....	68
Figure 4-15	Axial load versus lateral deformation at mid-height of specimen C2.....	68
Figure 4-16	Specimen C3 cross-section and reinforcement layout relative to top and bottom specimen plates .....	69
Figure 4-17	The splitting cracks at the top three courses of specimen C3 before retrofitting .....	70
Figure 4-18	Plot of a. applied axial load vs. axial strain over the plastic hinge region and b. applied axial load vs. maximum normalized lateral deformation at midheight at $\epsilon_t=0.8\%$ .....	70
Figure 4-19	Horizontal cracks developed along all bed joints in the last tension cycle in specimen C3 .....	71
Figure 4-20	Open cracks underneath the GFRP overlay led to crushing of the overlay under compression loads (specimen C3).....	72
Figure 4-21	Rotation of the open cracks at bed joints at low compression loads during the compression half-cycle (specimen C3) .....	73
Figure 4-22	Specimen C3 at the end of the test, after experiencing out-of-plane instability . .....	74
Figure 4-23	Local crushing of specimen C3 at the compression face where crack closed after the specimen had become laterally unstable .....	75
Figure 4-24	Buckled shape of specimen C3, during load cycle $\epsilon_t=0.8\%$ .....	76
Figure 4-25	Axial load versus axial deformation for specimen C3 .....	76
Figure 4-26	Axial load versus lateral deformation at mid-height for specimen C3 .....	77
Figure 4-27	Axial load versus lateral deformation at $\frac{1}{4}$ from the bottom for specimen C3.....	77
Figure 4-28	Crack patterns at increasing tension displacements for specimen C3.....	80
Figure 4-29	Plot of a. applied axial load vs. axial strain over the plastic hinge region and b. applied axial load vs. maximum normalized lateral deformation at midheight at $\epsilon_t=0.7\%$ .....	81
Figure 4-30	Uniformly distributed horizontal cracks over as well as vertical splitting cracks at tensile strain level equal to 1.3% (specimen C4).....	82
Figure 4-31	Rotation at the location of open horizontal cracks when specimen C4 experienced lateral displacements (Loading cycle #5) .....	83
Figure 4-32	a. Specimen in tension, b. first mode of buckling, c. second mode of buckling. .....	84
Figure 4-33	Buckled shape of specimen C4 during the load cycle $\epsilon_t=1.7\%$ .....	84
Figure 4-34	Axial load versus overall axial deformation for specimen C4.....	85

Figure 4-35	Axial load versus lateral deformation at the lower quarter point for specimen C4 .....	86
Figure 4-36	Axial load versus lateral deformation at midheight for specimen C4.....	86
Figure 4-37	Sliding at the bed joint on the north face of specimen C4 at the ultimate stage . .....	87
Figure 4-38	Specimen C4 at the end of the test after experiencing lateral instability .....	88
Figure 4-39	Deformed shape of the bottom portion of specimen C4 after experiencing lateral instability .....	89
Figure 4-40	Crack patterns at increasing tensile displacement levels for specimen C4.....	93
Figure 4-41	Specimen C5: cross-section and reinforcement layout relative to top and bottom specimen plates .....	94
Figure 4-42	Plot of a. Applied axial load vs. axial strain over the plastic hinge region and b. Applied axial load vs. maximum lateral deformation at midheight normalized with respect to thickness for specimen C5, $\epsilon_t=0.73\%$ .....	95
Figure 4-43	Horizontal cracks at bed joints uniformly distributed over the bottom half of specimen C5 .....	96
Figure 4-44	Specimen C5 experienced eastward out-of-plane displacements after tensile half-cycle with the maximum axial displacement of $4.9\Delta_y$ .....	97
Figure 4-45	Large horizontal and vertical crack developed at the masonry course below the stiffened portion (above the 8th masonry course from base of the wall) of specimen C5 during load cycle #6 ( $\Delta= 4.3\Delta_Y$ ).....	98
Figure 4-46	Reinforcing bar protruding through the block face shell during the compression half-cycle after the tensile axial displacement of $5.9\Delta_y$ .....	99
Figure 4-47	Localized buckling of the reinforcing bar, caused spalling of block face-shells and crumbling of the grout. ....	99
Figure 4-48	Specimen C5 after experienced the failure characterized by localized buckling of the reinforcement and crushing of the masonry.....	100
Figure 4-49	Continuous vertical splitting crack in specimen C5 at the end of the test ....	101
Figure 4-50	Buckled shape of specimen C5 during load cycle $\epsilon_t=1.6\%$ .....	102
Figure 4-51	Axial load vs. overall axial deformation for specimen C5.....	102
Figure 4-52	Axial load vs. lateral deformation at lower quarter point for specimen C5..	103
Figure 4-53	Axial load vs. lateral deformation at midheight for specimen C5 .....	103
Figure 4-54	Crack patterns at increasing tensile displacement levels for specimen C5 ...	107
Figure 5-1	Axial reversed cyclic response of a reinforced masonry column with point (e) only occurring during the loading cycle corresponding to lateral instability	110
Figure 5-2	Vertical forces across the wall thickness.....	111
Figure 5-3	Elastic buckling load of rebar for the different reinforcement schemes .....	113
Figure 5-4	The maximum tensile strain in terms of its constituents.....	115
Figure 5-5	The assumed deformed shape of the wall end zone under pinned-fixed and fixed-fixed boundary conditions .....	117
Figure 5-6	Rotation of bedjoints related to residual plastic strains.....	120
Figure 5-7	Variation of the residual plastic strain vs. assumed length of plastic hinge..	127
Figure 5-8	Deformed shape experimental and predicted for specimen C2.....	128
Figure 5-9	Deformed shape experimental and predicted for specimen C3.....	129
Figure 5-10	Deformed shape experimental and predicted for specimen C4.....	130
Figure 5-11	Deformed shape experimental and predicted for specimen C5.....	131

Figure 5-12	Displacement demand in a cantilever wall subjected to lateral loads .....	133
Figure 5-13	Strain profile across the length of a shear wall subjected to overturning moment.....	133
Figure 5-14	Variation of h/t ratio with increased tensile strain demand.....	135
Figure A- 1	Steel specimen plate .....	147
Figure A- 2	Shear and moment diagrams along the width of specimen plate .....	147
Figure A- 3	Shear and moment diagram along the specimen plate length .....	148
Figure B- 1	Loading of the weld connection sample in the Baldwin Machine .....	151
Figure B- 2	a. Specimens after the testing, b. Typical failure, c. Typical weld detail, d. Necking of the rebar .....	152
Figure D- 1	Specimen cross section.....	157
Figure D- 2	Top floating beam shear and moment diagram .....	161
Figure D- 3	Free body diagram of top floating beam .....	164
Figure D- 4	Cross section of top floating beam .....	164
Figure D- 5	Welded connections to the top floating beam .....	166
Figure D- 6	Moment and shear diagram for plates .....	169
Figure D- 7	Shear and moment diagram for bottom plate .....	173
Figure D- 8	Shear and moment diagram for specimen plates.....	175
Figure D- 9	Plan view of test apparatus.....	177
Figure D- 10	Profile view of test apparatus .....	178
Figure D- 11	Elevation view of test apparatus and pantograph detail .....	179
Figure D- 12	Floating beam detail .....	180
Figure D- 13	Column detail .....	181
Figure D- 14	Column supporting actuator detail .....	182
Figure D- 15	Plates detail .....	183
Figure D- 16	Specimen plates detail .....	184

## **Acknowledgements**

I would like to thank my research advisors, Drs. Ken Elwood and Svetlana Brzev for their valuable support and guidance that has both inspired me and kept me motivated. Special thanks to Dr. Don Anderson whose insight was of great assistance to all throughout this research. I would also like to offer many thanks to BCIT research assistant students Porkeang Lim, Desmond Das and Paul Lam for their assistance in material testing and help in the laboratory. Special thanks to Porkeang Lim and my fellow UBC researcher, Brook Robazza whose ideas and support helped expedite the experimental study.

I also offer my enduring gratitude to UBC laboratory staff Blair Patterson and Scott Jackson as well as Ken Zeleschuk, Assistant Instructor, BCIT Department of Civil Engineering, whose thorough work and expert knowledge made the experimental portion of this study possible.

Many thanks to Mr. Jim Bromely from Harris Rebar for donating reinforcing bars to our research effort and Mr. Jim Fullerton from CRSI Northwest Consultants for supporting communication. Special thanks are due to the crew from Retro Group and Grant Raeburn who performed the retrofit of specimens at a discounted rate.

The study presented here was financially supported by the Natural Sciences and Research Council of Canada through a NSERC Collaborative Research Grant for the project " Stability of Reinforced Masonry Shear Walls Under Seismic Loading" in partnership with industry sponsors, the Canadian Concrete Masonry Producers Association and the Masonry Institute of BC. I also received a financial support in the form of a NSERC Industrial Postgraduate Scholarship. Special thanks are due to Bill McEwen from the Masonry Institute of BC whose contribution and presence both made this project possible and fun.

Loving thanks to my family and friends, for their understanding and support during my studies.

To my loving parents.

## Chapter 1: Introduction

In earthquake prone regions of Canada, the construction economy of many structures depends on their seismic performance. For low-rise buildings, reinforced masonry (RM) shear walls constructed using hollow concrete blocks reinforced with vertical and horizontal bars offer effective and economical solutions to seismic design of structures.

In Canada, RM buildings are designed for seismic safety such that the lateral load capacity of the RM shear walls, determined according to the Masonry Design Standard (CSA S304.1-04), exceeds the expected lateral loads of a design earthquake as prescribed by the National Building Code of Canada 2010 (NBCC 2010). CSA S304.1 and NBCC 2010 classify RM walls based on their ability to dissipate energy during earthquake shaking as either “Conventional Masonry Shear Walls” (with ductility factor,  $R_d=1.5$ ) or “Moderately Ductile Masonry Shear Walls” ( $R_d=2.0$ ). NBCC 2010 requires that an  $R_d$  factor of at least 2.0 is provided for post-disaster buildings (e.g. fire halls and police stations), which mandates the use of “Moderately Ductile Shear Walls” for masonry design applications.

In recent years, despite the widespread practice of low-rise masonry construction in Canada, the use of typical RM shear walls to provide seismic protection to high-importance buildings has become limited. This is because the Canadian Masonry Design Standard (CSA S304.1-04) [Canadian Standard Association 2004] mandates stringent requirements on the design of ductile RM shear walls, especially with regard to their height-to-thickness ( $h/t$ ) ratios. CSA S304.1-04 prescribes a maximum  $h/t$  limit of 18 and 14 for RM walls with limited ductility and moderately ductile RM shear walls respectively. The  $h/t$  limit for moderately ductile squat walls is 20. This means that for moderately ductile walls built with the 200 mm standard block size, the height of the wall cannot be taller than 2.8 m. Such stringent limits diminish the construction economy and practicality of RM shear walls for common masonry design applications, even those at locations with relatively low-seismicity such as Toronto, Ontario.

The CSA S304.1-04 limits on the  $h/t$  ratios of RM walls are to ensure their lateral stability under the combined effects of axial loads and in-plane bending moments, as explained by Anderson and Brzev (2009). However, there is no previous experimental evidence supporting the specified  $h/t$  ratio limits in CSA S304.1-04. Moreover, a review of international seismic design provisions of masonry design standards reveals that no other standard places such stringent restrictions on the  $h/t$  ratio of RM shear walls.

Out-of-plane instability of shear walls, illustrated in Figure 1-1-a, is associated with their flexural response to in-plane seismic loads. A rational explanation for lateral instability of reinforced masonry shear walls was initially presented by Paulay (1986) and Paulay and Priestley (1993). When the wall experiences large curvature ductility, the vertical bars at one end of the wall experience large inelastic tensile strains. As a result, uniformly spaced horizontal cracks of considerable width develop over the plastic hinge length as illustrated in Figure 1-1-b.

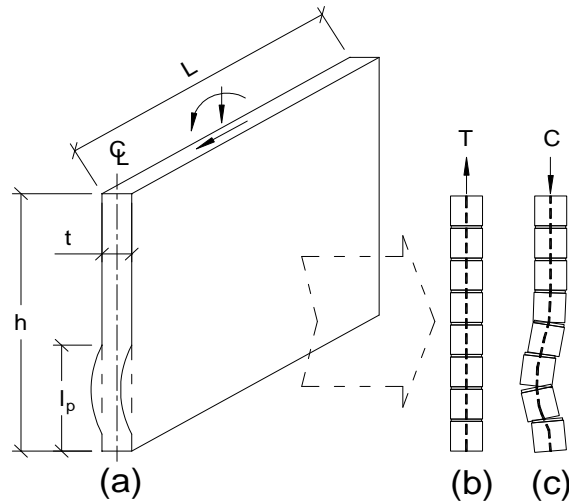


**Figure 1-1 Out-of-plane instability mechanism in a RM shear wall:**

a) buckled zone within plastic hinge region under axial and in-plane lateral loads, b) residual tensile cracks form following the application of tensile stress, and c) out-of-plane buckling of wall in compression.

Upon reversal of the loading direction, the tensile stresses in these bars will first drop to zero and then turn into compression stresses. At this stage, unless the cracks close, all compression stresses imposed on the wall section must be resisted by the vertical reinforcement, which offers very small stiffness against lateral deformation. This increases the likelihood of rapid out-of-plane displacements leading to out-of-plane instability as shown in Figure 1-1-c.

However, if the cracks close before the portion of the wall previously subjected to tension becomes subjected to compression, masonry compressive stresses will develop in the section. This provides additional stiffness against lateral deformation and an out-of-plane instability may be avoided.

The absence of experimental evidence related to out-of-plane instability of RM shear walls justifies the need for a comprehensive experimental and analytical study to evaluate that current CSA S304.1 height-to-thickness ratio restrictions.

### 1.1 Objective and Scope

The general objective of this project is to establish rational criteria for the out-of-plane instability of RM shear walls and ensure safe and economical seismic design of RM shear wall structures in Canada.

The specific objectives are to:

- i. Develop a rational analysis procedure and criteria for out-of-plane instability of RM shear walls, and

- ii. Establish safe height-to-thickness ratio limits for the design of RM walls at ductility levels prescribed by the seismic design provisions of Canadian codes and standards.

The test results will contribute to better understanding on how to relate the slenderness to ductility capacity of RM shear walls.

This research is the first phase of a two-phase effort investigating the factors contributing to the out-of-plane instability phenomena in reinforced masonry shear walls. While the first phase focuses in understanding the out-of-plane instability failure mechanism by studying isolated wall end zones, phase II will involve testing of full-length walls. The specimens and analytical model used in the second phase will be designed according to the results of the first phase and will later be verified by the results of the second phase.

It is expected that the results of this project will contribute to the CSA S304.1 standard for design of masonry structures in Canada which is currently in the review stage and the next edition is scheduled for 2014. The results of this project have the potential of making a significant impact to seismic design of RM shear walls in Canada.

## **Chapter 2: Literature Review**

As the initial phase of a comprehensive investigation into the parameters affecting out-of-plane instability of reinforced masonry shear walls, a review of the literature on previous experimental research on reinforced masonry shear walls was conducted.

Yancey et al. (1991) conducted a review of research studies on masonry shear walls which included both experimental and analytical data. A more recent review of research on RM walls was done by the Federal Emergency Management Agency (FEMA 307) in 1999. This chapter presents a review of experimental research studies on the seismic performance of RM shear walls with focus on walls that exhibited a flexural response.

### **2.1 Objective and Scope**

The literature review presented in this chapter was carried out with the following objectives:

- To evaluate the range and depth of existing knowledge on the behaviour of RM shear walls under earthquake loads based on experimental results
- To determine key parameters affecting out-of-plane instability of RM shear walls
- To identify areas where further research is required

The technical information is presented in a condensed format from the most relevant experimental research publications in Section 2.3. Results are tabulated for ease of use and reference in Section 2.5. The experimental data from previous research studies together with the outcome of the proposed research will help identify key parameters influencing the out-of-plane buckling of compression zone in reinforced masonry shear walls. A preliminary analysis of research data is presented in Section 2.6 in order to aid the development of the test matrix for this project.

### **2.2 Earthquake Evidence**

It is noteworthy that out-of-plane instability as a failure mechanism has not been observed in reinforced masonry shear wall buildings in past earthquakes. However, out-of-plane buckling of reinforced concrete shear walls was observed in the buildings affected by the February 27, 2010 Chile earthquake. In reinforced concrete wall structures, a majority of damage was reported in transverse walls in the first storey of multi-storey structures. Buckling of the longitudinal reinforcement and lateral buckling of web were reported in thin walls with widely spaced transverse reinforcement (EERI, 2010). It should also be noted that out-of-plane buckling of reinforced concrete shear walls occurred in experimental specimens in several research studies (initial studies on this subject date back to 1970s). Provisions for preventing out-of-plane buckling of reinforced concrete shear walls have been included in the design standard for reinforced concrete structures in Canada [CSA A23.3-04].

### **2.3 Review of Code Provisions Related to Out-of-Plane Instability**

A review of seismic design provisions contained in international masonry design standards shows that similar provisions are either non-existent or are less stringent. U.S. Building Code Requirements and Specification for Masonry Structures (TMS 402-08/ACI 530-08/ASCE 5-08) do not contain any height/thickness restrictions for RM shear walls. Note that the latter document contains a requirement for boundary elements which need to be provided in case of walls with larger compression zones (C1.3.3.6.5.3a). However, boundary elements are not required for walls with low axial load level (less than 10% compressive capacity of masonry) characteristic of low-rise masonry buildings.

The New Zealand masonry design standard (NZS 4230:2004) includes provisions which restrict the thickness of ductile RM shear walls (displacement ductility ranges from 2.0 to 4.0); however these provisions are somewhat less stringent than the current Canadian provisions. For walls up to three stories high, the height/thickness ratio is limited to 20 (C1.7.3.3). The document defines the height as a clear vertical distance between lines of effective horizontal support, or a clear horizontal distance between lines of effective vertical support. When the distance between horizontal supports exceeds the code limits, this requirement can be met by providing vertical lines of support at prescribed spacing (e.g. pilasters or cross walls). The standard also prescribes a more stringent h/t limit of 13.3 for ductile walls more than three stories high. However, a larger h/t ratio is permitted for walls with a relatively small compression zone (the criteria for this condition are very similar to CSA A23.3-04).

In order to safeguard against possible instability in ductile reinforced concrete shear walls, CSA 23.3-04 places limitations on their thickness in terms of the wall length (which dictates the length of the compression zone) in plastic hinge zones. It also requires that the regions of the walls where yielding of the reinforcement and concrete compressive strains in excess of 0.0015 are expected be checked for stability. To ensure ductility in the plastic hinge region, the inelastic rotational capacity of the wall is also required to be greater than the inelastic rotational demand. The inelastic rotational demand is calculated based on specified ductility demands.

The New Zealand Concrete Code, NZS3101:2006 addresses the issue of premature failure in thin reinforced concrete walls due to out-of-plane buckling (SNZ, 2006) by placing minimum limits on the thickness of boundary elements. Premature out-of-plane buckling in flexural hinge regions of reinforced concrete shear walls is not addressed in existing NZSEE Guidelines (NZSEE, 2006) or ASCE 41-06 (ASCE, 2006).

The research undertaken by Paulay and Priestley (1993), which proposes a methodology to estimate the limiting plastic rotation associated with out-of-plane wall buckling, forms the basis for current NZS3101 code requirements for wall buckling.

## 2.4 Experimental Studies on RM Shear Walls

This section provides an overview of experimental studies on RM shear walls subjected to reversed cyclic lateral loading. All specimens experienced either flexural failure mechanisms or a combination of flexure and shear. There was no evidence of out-of-plane instability in any of the studies described in this section. However, the review of these studies will aid in bounding the design parameters that may influence out-of-plane instability.

Nolph (2010) conducted an experimental study on the in-plane shear performance of five partially grouted and one fully grouted reinforced masonry walls. All specimens had h/l aspect ratio of 0.92, h/t ratio of 14.7, were constructed using standard 200 mm blocks, and contained both horizontal and vertical reinforcement. The specimens were partially grouted, that is, only the cells with vertical reinforcement were grouted. Vertical reinforcement ratio, was approximately equal to 0.45% (the ratio of the area of all longitudinal bars and the wall cross-sectional area). Different distribution of vertical reinforcement along the length of the wall was used in the study. All specimens were loaded in-plane according to a cyclic loading protocol until the walls had lost 20% of their maximum lateral load capacity. All walls exhibited shear failure, characterized by diagonal step cracking and some vertical cracking.

Minaie et al. (2010) carried out an experimental study on four special reinforced masonry shear walls. The walls were constructed based on the provisions of the Masonry Standards Joint Committee (MSJC) code and were special in that they were partially grouted at grout spacing less than the current U.S. practice of 1,220 mm on centre. The test variables across the specimen matrix included the level of axial stress, boundary conditions, as well as mortar formulation. Two of the walls had h/l aspect ratio of 1.37, while the remaining two had aspect ratio of 0.67. All specimens had vertical reinforcement ratio of 0.15% and h/t ratio of 13.9. The two specimens which were subjected to axial compression of 0.7 MPa and had cantilever boundary conditions, exhibited toe crushing characteristic of flexural mechanism. The other two specimens which had fixed-fixed boundary condition and no applied axial compression failed in sliding shear. It appears that walls with applied axial stress dissipated more energy in their hysteretic response. (Minaie, et al., 2010)

Yoshida et al. (2007) performed tests on six fully grouted reinforced masonry wall specimens to investigate their sliding shear capacity. Two specimens had an aspect ratio of 0.90 while the rest had 0.75 ratio. All walls had h/t ratio of 9.0 and wall thickness of 133 mm. All specimens contained both horizontal and vertical reinforcement. Five specimens contained flexural reinforcement of approximately 0.56% and horizontal reinforcement of 0.72%, while one specimen was heavily reinforced with flexural reinforcement ratio close to 1.1% but contained lower amount of horizontal reinforcement at 0.20%. The aforementioned flexural reinforcement ratio was calculated based on the amount of reinforcement placed in outermost cells of the wall. However, vertical reinforcement ratio, as smeared across the cross-section varied from 0.38% to 0.54% among the specimens. Two specimens were subjected to axial compression of 0.78 MPa. Most walls encountered flexural yielding of reinforcement, followed by some form of shear failure. (Yoshida, et al., 2007)

Shedid et al. (2005) tested three fully-grouted<sup>1</sup> reinforced concrete masonry walls to examine the possibilities of achieving high levels of energy dissipation in this type of construction. All walls had h/l aspect ratio of 2 and h/t ratio of 19 and were constructed with standard 200 mm blocks. All walls contained both horizontal and vertical reinforcement. Vertical reinforcement ratio was 1.31% for two specimens, and 0.76% for the third specimen. There was no applied axial stress on the walls. The behaviour of all walls was dominated by flexural response, including toe crushing and the formation of horizontal cracks along the bed joints. Buckling of end reinforcing bars was reported and it was not related to the amount of reinforcement. The buckling occurred after substantial spalling of masonry face shells and toe crushing. (Shedid, et al., 2005)

Miller et al. (2005) conducted an experimental study on four reinforced concrete masonry walls to evaluate their shear capacity. All walls were fully grouted and constructed with standard 200 mm concrete masonry units. All walls had h/l aspect ratios of 1.0. Two specimens had a h/t ratio of 10.5 and the other two had h/t ratio of 15.8. All walls had a vertical reinforcement ratio of 0.79% while horizontal reinforcement ratio varied between 0.07% to 0.13% across the specimen matrix. Two specimens were subjected to an axial load level of 1.0 MPa. The failure mechanism was characterized by substantial diagonal cracking followed by flexural cracking along bed joints and toe-crushing. One of the walls was reportedly subjected to out-of-plane loading during a loading cycle, which forced the researchers to stop pushing the wall in that direction. However, buckling of reinforcement or out-of-plane instability were not reported. (Miller, et al., 2005)

Kikuchi et al. (2010) carried out tests on 10 reinforced concrete masonry walls to investigate the effect of aspect ratio on their seismic performance. The aspect ratio varied from 0.91 to 1.51. All specimens had a h/t ratio of 9.0 and were constructed with 133 mm thick concrete masonry units used in Japan. All specimens were reinforced in both the horizontal and the vertical directions. Six specimens had flexural reinforcement ratio of 0.56% while four contained nearly 1.1% of flexural reinforcement. Most specimens exhibited flexural response, including flexural yielding or buckling of reinforcement. However, the failure of only three specimens was identified as having been dominated by flexure and the remaining walls failed either in sliding shear or diagonal shear. There was no mention of out-of-plane instability. (Kikuchi, et al., 2003)

Manos et al. (2003) reported on the response of two RM walls constructed with ½ scale 154 mm Greek type masonry units and tested to investigate the behavior of masonry walls under combined effects of seismic and gravity loads. The level of axial stress was at 4% of the compressive capacity of the blocks. The walls had aspect ratio of 1.0 and h/t ratio of 8.6. Both walls had horizontal reinforcement ratio of 0.1% and flexural reinforcement of 0.23%. The behaviour of the walls was characterized by flexural yielding of reinforcement followed by shear failure. (Manos, et al., 2003)

As part of a research effort to evaluate the post-cracking stiffness of reinforced masonry walls with openings, Elshafie et al. (1999) tested eight specimens to monotonic lateral

---

<sup>1</sup> One wall was later found to have been accidentally partially grouted

loading. The walls were built with 1/3 scale replica of 150 mm hollow blocks (with a unit thickness of 48 mm). One wall had an aspect ratio of 1.0 with a h/t ratio of 26.7 while the rest had aspect ratios of 0.7 with h/t ratio of 19.3. Five of the walls, including the one with the higher aspect ratio, contained 0.34% of flexural reinforcement, while the rest had a flexural reinforcement ratio of 0.67%. All walls responded mainly in flexure by forming plastic hinges at member ends. There was no report on out-of-plane instability. (Elshafie, et al., 1999)

Ibrahim and Suter (1999) tested five reinforced concrete masonry walls under reversed cyclic in-plane loads to evaluate their ductility levels. The walls were constructed using 140 mm hollow blocks and were fully grouted. The aspect ratio varied from 0.47 to 1.0 while the h/t ratio was 10 for all walls. All walls were reinforced with horizontal and vertical reinforcement. The amount of vertical reinforcement was 0.4% for four walls while one wall contained 0.6% of vertical reinforcement. Four of the walls, including the wall with the higher vertical reinforcement ratio were subjected to 0.69 MPa of axial compressive stress, and one wall was subjected to 1.73 MPa of axial compression. All specimens with the exception of one failed in shear. Vertical reinforcement in the specimen which experienced flexural failure mechanism was extensively elongated beyond yield. This wall had the highest aspect ratio (of 1.0?), but its flexural reinforcement ratio and level of applied axial stress level were not higher than other walls. (Ibrahim, et al., 1999)

Kikuchi et al. (1999) conducted tests on four RM walls to assess the effect of hollow units on the seismic behaviour of fully grouted walls. Two specimens were constructed using 125 mm blocks, while the other two were built using 190 mm thick units. All walls had h/l aspect ratio of 1.5, with one wall with each type of block having h/t ratio of 6.3 and the other 9.6. The ratio of total vertical reinforcement to net area of the wall cross section varied between 0.67% to 1.74% across the specimens. However, all vertical reinforcement with the exception of one bar were placed at the end zones of the walls. The specimens also contained shear reinforcement. All specimens failed in shear with one specimen experiencing flexural yielding of vertical reinforcement prior to shear failure. (Kikuchi, et al., 1999)

Schultz (1996) reported the results of an experimental study of 6 partially grouted reinforced concrete masonry walls constructed with standard 200 mm masonry blocks. All walls had h/t ratio of 7.3 while the aspect ratio varied from 0.5 to 1.0. The amount of horizontal and vertical reinforcement also varied across the specimen matrix, but all walls contained the same amount of vertical reinforcement in the wall end zone. flexural reinforcement ratio was about 1.47%. The level of applied axial stress varied from 0.9 MPa to 1.1 MPa for different specimens. All specimens experienced some form of flexural response characterized by the formation of vertical cracks. A decrease in unloading stiffness at low lateral load levels and deterioration of post-peak strength was more pronounced in specimens with higher aspect ratios. (Schultz, 1996)

Innamorato (1994) tested two reinforced concrete masonry walls under both axial compressive loads and reversed cyclic in-plane loads to evaluate the effectiveness of a composite overlay repair method for reinforced concrete masonry construction. The two walls were first tested to failure and then repaired using the application of the composite

overlay and tested again. Both walls had aspect ratios of 1.0 and h/t ratios of 12 and were constructed with 152 mm thick concrete masonry units. The vertical reinforcement ratios of the walls were 0.38% and 0.54% respectively. Both walls also contained horizontal reinforcement. One wall was subjected to axial compressive stress of 0.8 MPa and the other one to 1.9 MPa. The specimen with a smaller amount of horizontal reinforcement experienced shear failure while the other specimen exhibited flexural failure. (Innamorato, 1994)

#### **2.4.1 Experimental Studies on RM Shear Walls Which Encountered Out-of-plane Instability**

Shedid et al. investigated the behaviour of seven half-scale RM shear walls under in-plane reversed cyclic loads. A series of two- and three-storey high RM shear walls, all with the same in-plane length, were tested to evaluate the effectiveness of boundary elements on enhancing the ductile response of these walls. The following parameters were varied: configuration of the wall end zone, aspect ratios, levels of axial compressive stress, and reinforcement ratios. The failure mechanism in all specimens was characterized by yielding of flexural reinforcement and crushing at the wall toes, which was preceded by the development of vertical splitting cracks in the end blocks. Buckling of the outermost vertical bars accompanied by widening of the vertical cracks and crumbling of the grout was observed in the final stage. In the two specimens with boundary elements, buckling of the vertical reinforcement caused the lateral displacement at the wall toe. In a specimens without boundary elements, displacement of the outermost bar normal to the plane of the wall led to out-of-plane displacement at the wall toe. As shown in Table 1, Wall 4 characterized by the highest flexural reinforcement ratio, was the only specimen that experienced out-of-plane instability. (Shedid, et al., 2009)

In another research study, Shedid et al. (2008) tested six full-scale RM shear walls to failure under reversed cyclic loading. The purpose of this study was to evaluate the effect of reinforcement ratio and the level of axial compressive stress on ductile behaviour of RM walls. All specimens had aspect ratio of 2.0 with only two of the walls subjected to axial compressive loads. All walls behaved in flexure; horizontal cracking formed along the bed joints over the lower courses. Face shell spalling, grout cracking, and fracture and buckling of compression reinforcement were observed at high displacements. One specimen experienced out-of-plane buckling of the web in its bottom five courses at the end of the test. This specimen, which had a height-to-thickness ratio of 18.9, was heavily reinforced but was not subjected to axial compressive loads. (Shedid et al., 2008)

He and Priestley (1992) conducted a study to investigate the seismic performance of flanged masonry walls. Four full-scale T-shaped masonry wall specimens were tested to examine the influence of longitudinal reinforcement ratio, flange width, and confinement on their seismic response. All walls had a horizontal reinforcement ratio of 0.44%. Two of the walls had a vertical reinforcement ratio of 0.23% while the other two had a vertical reinforcement ratio of 0.50%. All walls were subjected to both reversed cyclic lateral loads and a constant axial compressive stress. The level of axial stress on all of the walls was less than 10% of their compressive capacity. After yielding of the vertical reinforcement had occurred in the

direction of the web in compression, the walls generally failed due to buckling of the vertical reinforcement. One flanged wall with end-zone steel confinement experienced lateral buckling in the web following a load sequence where the web reinforcement had been subjected to high residual inelastic tensile strains. The specimen had the highest vertical reinforcement ratio and axial load while offering low masonry compressive strength, and underwent the largest displacement. The remaining three specimens also demonstrated high displacement ductility level, but none of them experienced out-of-plane web buckling. (He, et al., 1992)

#### **2.4.2 Experimental Studies on Reinforced Concrete Shear Walls Encountering Out-of-Plane Instability**

Although out-of-plane instability of reinforced masonry shear walls has rarely been encountered in experimental studies or in actual earthquake events, this mechanism was observed in experimental studies of reinforced concrete (RC) shear walls as early as the 1970's. To gain insight into the out-of-plane instability mechanism itself and help its future characterization in reinforced masonry shear walls, experimental studies investigating this phenomena in reinforced concrete were reviewed. The following synopses of previous research work is extended from the literature review carried out by Brzev (2011) on experiments encountering out-of-plane instability in RC walls subjected to cyclic lateral loads.

In 1974, the Portland Cement Association (PCA) started an extensive experimental and analytical research investigation of the seismic performance of RC shear walls. In total, 16 specimens representing approximately one-third scale models of full-size flexural shear walls with aspect ratio of 2.4, were tested under quasi-static cyclic loading (Oesterle, et al., 1976)(Oesterle, et al., 1976)(Corley, et al., 1981). Flanged, barbell and rectangular cross sections were investigated. The specimens which failed in the flexural mode initially experienced horizontal flexural cracking in the end zones, which later progressed into coarsely distributed inclined cracks in the web. Intersecting cracks from opposite loading directions segmented the hinging region into several horizontal layers. Due to horizontal cracks, it was not possible for the diagonal strut action to develop, and shear transfer in the post-yield phase occurred primarily by shear friction and dowel action.

Two rectangular-shaped specimens, R1 and R2, were tested in this study. The only difference between these specimens was that specimen R2 had a confined boundary element at the end, while specimen R1 did not. Specimen R1 failed in flexural mechanism, with buckling of the end reinforcement, while specimen R2 experienced out-of-plane instability in the wall compression zone (in the lower 1 m of the wall height). The specimen R2 failed at over 80% higher load than specimen R1. Bowing of the compression zone was observed at a 0.5% drift; the compression boundary element was 6.4 mm out of plane at approximately 1.1 m above the base. Although this bowing progressed further with each cycle, the load-carrying capacity of the specimen R2 remained stable until the 2.8% drift, when a significant out of plane displacement of the compression zone within the lower 1.5 m was observed. It was reported that vertical reinforcement was subjected to permanent inelastic tensile deformations which caused it to elongate. As a result, cracks remained open in the subsequent loading

cycle causing compression in the wall, and an effective wall cross-section was limited to that of steel area alone, and also the stability was reduced against out-of-plane displacements. Bar fracture followed with subsequent load reversals because of the previous kinking of the bars at the base. Although the load-carrying capacity of the specimen continued to decrease, the specimen sustained at least 80% of the maximum measured load through 14 complete inelastic cycles.

A comprehensive experimental study on seismic response of RC shear walls was performed at the University of California at Berkeley. Six approximately one-third scale wall specimens were tested, comprising of four barbell and two rectangular sections (Vallenas, et al., 1979). The three-storeyed wall specimens had aspect ratio of 1.3. The researchers identified the following three types of buckling failure:

- i. buckling of longitudinal reinforcement between ties in the wall end zones after the cover had spalled and ties have ruptured,
- ii. buckling of boundary elements after cover spall, characterized by asymmetric spalling of cover and associated eccentricity of axial load, thereby causing buckling of the compression zone over a height approximately equal to the thickness of boundary element; and
- iii. buckling of boundary element with residual open tensile cracks in the compression zone over the full first floor height.

The out-of-plane instability was observed in two out of six specimens. One of the specimens (No. 5) had rectangular cross section and  $h/t$  ratio of 10<sup>1</sup>. The authors concluded that lateral instability of rectangular sections may govern the structural response and appears to be affected by the clear height to web width in the lowest floor of the wall, width of tensile cracks, and strains in vertical reinforcement.

Goodsir (1985) performed an experimental study performed on four one-quarter scale two-storey wall specimens: three specimens had rectangular cross-section and one specimen had a T-shaped section. Two specimens, a rectangular-shaped (Wall 2) and a T-shaped (Wall 3) experienced out-of-plane instability, while the other two specimens experienced a material compression failure. Wall 2 experienced a significant loss of lateral load resistance at a displacement ductility of 6.0, when the compression end of the unit developed large out-of-plane displacement over the full first storey height. Dense near-horizontal cracks extended over the boundary region of the section. Concentrated reinforcement in the boundary region consisted of ten 12-mm deformed vertical bars, tied by 6-mm hoops at 72 mm spacing. The specimen had a  $h/t$  ratio of 10. The study showed that a potential for out-of-plane buckling of thin sections of ductile walls depends on the magnitude of inelastic tensile strains imposed on the end region of the wall, which is subjected to compression on subsequent load reversal. The study served as a basis for developing an analytical procedure for estimating critical wall thickness (Paulay, et al., 1993) which will be discussed later in Chapter 5:

Chai and Elayer (1999) conducted an experimental study to assess the lateral stability of the end zone of reinforced concrete walls subjected to cyclic axial tension and compression.

---

<sup>1</sup> The  $h/t$  ratio is calculated based on first storey height

Based on the results of their experimental study and the previous works done by Paulay and Priestley (1993), an equation for predicting the maximum tensile strain which leads to the onset of lateral instability in the wall end zone was proposed. Their work will be discussed later in Chapter 5:, where a similar approach is used to approximate critical tensile strains which would trigger lateral instability in reinforced masonry walls.

Zhang and Wang (2000) tested four slender reinforced concrete walls under reversed cyclic lateral loading. High axial load was used to simulate the response of RC shear walls in high-rise buildings (two specimens subjected to axial compressive stress corresponding to 24 and 35 % of the concrete compressive strength respectively). The concentrated reinforcement in the boundary zone consisted of 4-12 mm deformed vertical steel bars with 6 mm hoops at 50 mm spacing. The specimen SW8 experienced out-of-plane instability at a displacement ductility ratio of 4.3. Vertical cracks appeared in the compression zone shortly after the wall had yielded. The progression of out-of-plane displacements had caused an arch-like cracking pattern across the length of the wall. It should be noted that the two specimens subjected to higher axial load experienced out-of-plane buckling, while the other two specimens experienced material crushing of the boundary elements.

An experimental study on six quarter-scale reinforced concrete shear wall specimens subjected to cyclic loading was reported by Wallace (1998) and Thomsen and Wallace (2004). Out of the six specimens, three had rectangular cross-section (one with an opening), two were T-shaped, and one had a barbell-shaped cross-section with an opening. The two rectangular-shaped wall specimens without opening, RW1 and RW2, had the same geometry and material properties but had different detailing of boundary elements at wall end zones. In addition to 8 vertical bars and closed ties at a spacing of 76 mm, specimen RW1 had cross-ties. Specimen RW2 did not have cross-ties but it had more closely spaced ties at 51 mm on center. The performance of specimens RW1 and RW2 was similar in that the buckling of vertical reinforcement in the boundary region limited the flexural capacity of these specimens. At the drift of 2.5%, specimen RW1 experienced significant loss of lateral load capacity due to buckling of vertical reinforcement. Behaviour of specimen RW2 was very similar to RW1, except that lateral load capacity was maintained even after two complete cycles at 2.5% lateral drift. The improved behaviour is attributed to the closer spacing of the hoops at the wall boundaries, which delayed the onset of buckling of the vertical reinforcement.

## **2.5 Database of Experimental Results related to RM Shear Walls**

Table 2-1 presents a database of the pertinent experimental information contained in the various studies reviewed (Azimikor et al., 2011). Following is an explanation of the information presented in the table.

Since out-of-plane instability is a phenomenon related to the flexural failure mechanism in RM shear walls, only the studies which demonstrated flexural response were considered for this database. Also, only the specimens subjected to reversed cyclic lateral loading are included. Table 1 contains a summary of the most pertinent experimental research

publications reviewed. The information presented relates to specimens' design parameters, relevant response parameters, and their failure mechanisms.

To determine the specimen's aspect ratio (height-to-length ratio,  $h/l_w$ ), the height of the wall at which the lateral load was applied was used, denoted as  $h$ . Note that the height-to-thickness ratio ( $h_u/t$ ), was calculated using the laterally unsupported height of the first storey,  $h_u$ . The flexural reinforcement ratio,  $\rho_f$ , is indicative of the vertical reinforcement placed in the wall end zones. Note that vertical and flexural reinforcement ratio are identical for specimens with uniformly distributed vertical reinforcement,. The wall net area,  $A_n$ , was used to determine the applied compressive stress (Anderson and Brzev 2009). Shear area,  $A_v$ , was taken as 80 percent of the gross cross sectional area of the wall.

The response of the specimens to cyclic in-plane loads were interpreted from hysteretic curves for applied lateral load versus horizontal displacement. To ensure consistency throughout the database, the relevant wall response parameters are shown in Figure 2-1.

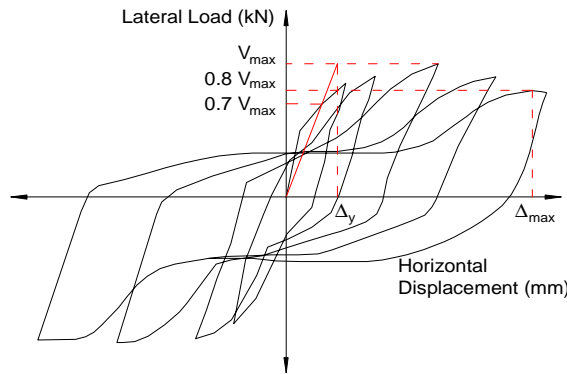


**Figure 2-1 Hysteretic force-deformation plot**

Note that the wall strength,  $V_{max}$ , is taken as the maximum lateral load-carrying capacity. Yield displacement,  $\Delta_y$ , was obtained by extending a line from the origin to a horizontal tangent extending from  $V_{max}$ , through the point on the hysteresis curve corresponding to  $0.7V_{max}$ . The ultimate displacement,  $\Delta_{max}$ , corresponds to  $0.8V_{max}$ . From these properties, parameters such as drift ratio at yield,  $\delta_y$ , ultimate drift capacity,  $\delta_u$ , and effective stiffness,  $K_{eff}$ , were calculated as follows:

$$\delta_y = \frac{\Delta_y}{h} \tag{2-1}$$

$$\delta_u = \frac{\Delta_{max}}{h} \tag{2-2}$$

$$K_{eff} = \frac{V_{max}}{\Delta_y} \tag{2-3}$$

**Table 2-1 Summary of experimental studies on flexural response of RM shear walls<sup>3</sup>**

Reference	Specimen	h (mm)	h <sub>u</sub> (mm)	$\frac{h}{l_w}$	$\frac{h_u}{t}$	$\frac{A_n}{A_g}$	$\rho_r$ (%)	f' <sub>m</sub> (MPa)	$\frac{P}{A_n f'_m}$	K <sub>eff</sub> (kN/m <sup>2</sup> )	$\frac{V_{max}}{A_v \sqrt{f'_m}}$	$\delta_y$ (%)	$\delta_u$ (%)	Failure Mode
Minaie et al., 2009	PCL 1	2640	2640	0.7	13.9	0.62	0.15	13.8	0.032	86	0.12	0.14	0.60	f
	MC 1	2640	2640	0.7	13.9	0.62	0.15	12.6	0.032	24	0.07	0.30	0.75	f
	PCL 2 <sup>4</sup>	2640	2640	0.7	13.9	0.62	0.15	13.8	0.000	37	0.09	0.25	0.75	c
	MC 2 <sup>6</sup>	2640	2640	0.7	13.9	0.62	0.15	12.6	0.000	26	0.08	0.33	0.75	c
	F-PCL 1	2640	2640	0.7	13.9	1.0	0.15	13.8	0.014	68	0.18	0.27	0.46*	c→f
	F-MC 1	2640	2640	0.7	13.9		0.15	12.6	0.014	87	0.17	0.20	0.78*	c→f
	F-PCL 2 <sup>5</sup>	2640	2640	0.7	17.4		0.15	13.8	0.018	364	0.16	0.04	0.45	b
	F-MC 2 <sup>7</sup>	2640	2640	0.7	17.4		0.15	12.6	0.018	332	0.15	0.04	0.75*	b
Shedid et al., 2009	W1	3990	1230	2.2	13.7	1.0	0.60	16.4	0.07	12	0.34	0.39	1.11	g
	W2	3990	1230	2.2	13.7		0.60		0.05	15	0.29	0.26	1.56	g
	W3	3990	1230	2.2	13.7		0.60		0.05	12	0.29	0.33	2.34	g→f
	W4	2660	1230	1.5	13.7		1.17		0.06	45	0.51	0.23	1.07	d
	W5	2660	1230	1.5	13.7		0.55		0.05	49	0.47	0.19	1.47	g
	W6	2660	1230	1.5	13.7		0.55		0.05	54	0.46	0.17	1.81	g→f
	W7	2660	1230	1.5	13.7		0.55		0.05	60	0.46	0.15	2.07	g
Shedid et al., 2008	1	3600	3600	2	18.9	1.0	0.29	14.8	0.00	11	0.14	0.35	2.15	g
	2	3600	3600	2	18.9		0.78		0.00	41	0.25	0.18	1.80	g
	3	3600	3600	2	18.9		0.73		0.00	20	0.23	0.33	1.30	g <sup>6</sup>
	4	3600	3600	2	18.9		1.31		0.00	22	0.36	0.47	1.51	g→d
	5	3600	3600	2	18.9		1.31		0.05	20	0.39	0.56	1.31	g <sup>7</sup>
	6	3600	3600	2	18.9		1.31		0.10	31	0.53	0.50	1.73	g
Yoshida et al., 2007	FN-0.90L-0	1200	1200	0.90	9.0	1.0	0.56	24.1	0.00	208	0.36	0.10	0.4	c
	FN-0.90L-LC2	1200	1200	0.90	9.0		0.56	27.2	0.03	303	0.49	0.10	2.5	c
	FN-0.75L-0	1200	1200	0.75	9.0		0.56	29.2	0.00	268	0.35	0.10	0.5	c
	FN-0.75L-LC	1200	1200	0.75	9.0		0.56	25.8	0.03	402	0.56	0.10	1.5	c
	SN-0.75L-LC2	1200	1200	0.75	9.0		1.09	27.4	0.03	475	0.64	0.10	1.7	c
Shedid et al. 2005	Wall 1	3600	3600	2	18.9	1.0 <sup>8</sup>	1.31	15.2	0.00	22	0.27	0.36	0.6*	f
	Wall 2	3600	3600	2	18.9	1.0	1.31		0.00	21	0.36	0.50	1.3*	g
	Wall 3	3600	3600	2	18.9	1.0	0.73		0.00	22	0.23	0.31	1.8	g

<sup>3</sup> Note that this database includes RM shear wall specimens subjected to in-plane quasi-static lateral loading

<sup>4</sup> Lateral loads were applied at specimen midheight

<sup>5</sup> Specimens built using clay masonry units with nominal dimensions 150x100x400 mm

<sup>6</sup> The vertical reinforcement experienced fracture prior to buckling

<sup>7</sup> Out-of-plane displacements were induced due to problems with the test set-up

<sup>8</sup> There were major un-grouted areas detected in this wall after testing was completed

Reference	Specimen	h (mm)	h <sub>u</sub> (mm)	$\frac{h}{l_w}$	$\frac{h_u}{t}$	$\frac{A_n}{A_g}$	$\rho_r$ (%)	f' <sub>m</sub> (MPa)	$\frac{P}{A_n f'_m}$	K <sub>eff</sub> (kN/m m)	$\frac{V_{max}}{A_v \sqrt{f'_m}}$	$\delta_y$ (%)	$\delta_u$ (%)	Failure Mode
Miller et al., 2005	1	2000	2000	1	10.5	1.0	0.79	15.4	0.06	273	0.34	0.08	0.4	b
	2	2000	2000	1	10.5		0.79	12.7	0.00	91	0.42	0.25	0.6*	g
	3	3000	3000	1	15.8		0.79	15.4	0.06	129	0.43	0.20	0.7*	a
	4	3000	3000	1	15.8		0.79	12.7	0.00	85	0.35	0.22	0.6*	a
Kikuchi et al., 2003	F-1.5L	1200	1200	1.51	9.0	1.0	0.45	28.3	0.03	90	0.36	0.15	3	a
	F-1.5L-S	1200	1200	1.51	9.0		0.45	29.2	0.03	143	0.38	0.10	2	a
	F-1.1L	1200	1200	1.13	9.0		0.39	26.5	0.03	209	0.43	0.10	2	c
	F-1.1L-S	1200	1200	1.13	9.0		0.65	32.1	0.02	215	0.40	0.10	1	a
	F-0.9L	1200	1200	0.90	9.0		0.56	32.5	0.02	284	0.42	0.10	2	c
	F-0.9L-S	1200	1200	0.90	9.0		0.56	32.1	0.02	157	0.47	0.20	1	c
	S-1.5L	1200	1200	1.51	9.0		0.79	27.2	0.03	180	0.49	0.10	1	b
	S-0.9L	1200	1200	0.90	9.0		0.56	30.2	0.03	377	0.58	0.10	1	c
	S-0.9L-S	1200	1200	0.90	9.0		0.56	34.6	0.02	496	0.57	0.08	0.2	b
Manos et al., 2003	Wall 17	1330	1330	1	8.6	0.43	0.23	5.0	0.04	20	0.22	0.30	0.8	c
	Wall 18	1330	1330	1	8.6	1.0	0.23		0.04	19	0.26	0.38	1.2	b
Ibrahim & Suter, 1999	Wall 1	1400	1400	1.00	7.4	1.0	0.40	21.3	0.03	60	0.29	0.25	1.1	b
Kikuchi et al., 1999	B-GM	1200	1200	1.5	6.3	1.0	1.07	29.2	0.03	213	0.39	0.10	1.9	b
Elshafie et al., 1999	A1	925	925	0.7	19.3	1.0	0.11	25.2	0.00	19	0.29	0.40	0.98	a
	A2	925	925	0.7	19.3		0.11	22.8	0.00	8	0.15	0.46	1.32	a
	A3	925	925	0.7	19.3		0.11	25.2	0.00	13	0.20	0.43	1.22	a
	A4	925	925	0.7	19.3		0.11	28.3	0.00	10	0.14	0.40	1.08	a
	B1	1280	1280	1.0	26.7		0.11	24.0	0.00	7	0.18	0.47	0.80	a
	C1	925	925	0.7	19.3		0.21	28.3	0.00	6	0.13	0.60	2.10	a
	C2	925	925	0.7	19.3		0.21	25.5	0.00	3	0.08	0.67	2.55	a
	C3	925	925	0.7	19.3		0.21	22.8	0.00	5	0.12	0.63	2.00	a
Schultz, 1996	Wall 1	1422	1422	0.5	7.3	0.44	1.47	17.6	0.06	187	0.10	0.07	0.96	a
	Wall 3 <sup>9</sup>	1422	1422	0.7	7.3	0.48	1.47	17.6	0.06	153	0.18	0.11	0.35	a
	Wall 5 <sup>11</sup>	1422	1422	1.0	7.3	0.54	1.47	17.6	0.05	190	0.14	0.05	0.21	a
	Wall 7 <sup>11</sup>	1422	1422	0.5	7.3	0.44	1.47	17.6	0.06	400	0.13	0.04	0.42	a
	Wall 9 <sup>11</sup>	1422	1422	0.7	7.3	0.48	1.47	17.6	0.05	192	0.14	0.07	0.35	a
	Wall 11 <sup>11</sup>	1422	1422	1.0	7.3	0.54	1.47	17.6	0.05	154	0.17	0.07	0.49	a
Innamorato, 1994	Flexure-I	1828.8	1828.8	1.0	12.0	1.0	0.38	14.5	0.05	62	0.30	0.22	0.60*	c→f
	Flexure-II <sup>10</sup>	1828.8	1828.8	1.0	12.0		0.38		0.05	34	0.36	0.49	2.29*	f
	Shear-I	1828.8	1828.8	1.0	12.0		0.54		0.13	93	0.42	0.21	0.49*	b
	Shear-II <sup>12</sup>	1828.8	1828.8	1.0	12.0		0.54		0.13	66	0.45	0.32	2.07	f

<sup>9</sup> Wall with opening<sup>10</sup> Specimens were initially tested under in-plane cyclic lateral loads and then repaired using a composite overlay

Reference	Specimen	h (mm)	h <sub>u</sub> (mm)	$\frac{h}{l_w}$	$\frac{h_u}{t}$	$\frac{A_n}{A_g}$	$\rho_f$ (%)	f' <sub>m</sub> (MPa)	$\frac{P}{A_n f'_m}$	K <sub>eff</sub> (kN/m m)	$\frac{V_{max}}{A_v \sqrt{f'_m}}$	$\delta_y$ (%)	$\delta_u$ (%)	Failure Mode
Foltz and Yancey, 1993	R2	1420	1420	1.2	7.5	0.55	-	7.5 <sup>11</sup>	0.34	63	0.31	0.18	0.54*	b
	R4	1420	1420	1.2	7.5	0.55	-		0.28	48	0.29	0.21	0.64*	b
	R5	1420	1420	1.2	7.5	0.55	-		0.39	65	0.39	0.21	0.54*	b
	R6	1420	1420	1.2	7.5	0.55	-		0.29	49	0.29	0.21	0.49*	b
	R7	1420	1420	1.2	7.5	0.55	-		0.31	35	0.31	0.32	0.48*	b
	R8	1420	1420	1.2	7.5	0.55	-		0.18	39	0.23	0.21	0.64*	b
	R9	1420	1420	1.2	7.5	0.55	-		0.36	46	0.35	0.27	0.67*	b
	R10	1420	1420	1.2	7.5	0.55	-		0.42	26	0.40	0.54	0.54*	b
	R11	1420	1420	1.2	7.5	0.55	-	0.33	42	0.34	0.29	0.54*	b	
Igarashi et al., 1993	One wall	7925	2438	1.95	16.0	1.0	0.17	13.0	0.00	24	0.17	0.16	0.50	e
Priestley & He, 1992	F1 <sup>12</sup>	3657.6	3657.6	3.1	25.6	1.0	0.55	11.6	0.06	14	0.62	0.54	1.1	g
	F2 <sup>14</sup>	3657.6	3657.6	3.1	25.6		0.25	11.6	0.06	30	0.50	0.21	1.1*	g
	F3 <sup>14</sup>	3657.6	3657.6	3.1	25.6		0.25	8.0	0.09	21	0.83	0.42	1.3*	f
	F4 <sup>14</sup>	3657.6	3657.6	3.1	25.6		0.55	8.0	0.09	14	0.83	0.63	1.7*	g→d
Shing et al., 1991	HCBL 1	1828.8	1828.8	1.0	12.8	1.0	0.38	20.1	0.07	61	0.41	0.35	1.7	f
	HCBL 2	1828.8	1828.8	1.0	12.8		0.38	20.1	0.09	86	0.47	0.28	1.3*	f
	HCBL 6	1828.8	1828.8	1.0	12.8		0.38	18.2	0.00	83	0.26	0.15	1.7	c
	HCBL 8	1828.8	1828.8	1.0	12.8		0.38	22.4	0.00	58	0.23	0.21	1.6	c
	HCBL 10	1828.8	1828.8	1.0	12.8		0.38	22.3	0.03	110	0.31	0.15	1.5	b
	HCBL 12	1828.8	1828.8	1.0	12.8		0.38	22.3	0.03	78	0.32	0.22	1.5	f
	HCBL 15	1828.8	1828.8	1.0	12.8		0.54	23.0	0.03	82	0.42	0.28	1.7	b
	HCBR 1 <sup>13</sup>	1828.8	1828.8	1.0	13.4		0.40	26.1	0.07	120	0.45	0.21	1.3	f
	HCBR 2 <sup>14</sup>	1828.8	1828.8	1.0	13.4		0.40	26.1	0.07	132	0.43	0.18	1.3	f
	HCBR 3 <sup>14</sup>	1828.8	1828.8	1.0	13.4		0.40	26.1	0.07	172	0.47	0.15	1.7*	f
HCBR 4 <sup>14</sup>	1828.8	1828.8	1.0	13.4	0.40	26.1	0.07	102	0.48	0.26	1.6	f		
Priestley & Elder, 1982	Wall 1	5400	2000	2.25	14.3	1.0	0.72	26.9	0.07	12	0.23	1.63	0.9	e→f
	Wall 2	5400	2000	2.25	14.3		0.72		0.07	13	0.23	1.63	1.3	g→f
	Wall 3	5400	2000	2.25	14.3		0.72		0.03	11	0.19	1.56	1.6	f

Notes:

\* The ultimate displacement at 0.8V<sub>max</sub> was not available. The value provided is the next closest representative of ultimate displacement.

\*\* Information on exact mode of failure not available.

FAILURE MODES					
A	=	Ductile Flexural Response with minimal strength degradation	e	=	Flexure/Lap-splice slip
B	=	Flexure/Diagonal Shear	f	=	Flexure/Toe crushing
C	=	Flexure/Sliding Shear	g	=	Flexure/Buckling of Flexural Reinforcement
D	=	Flexure/Out-of-Plane Wall Buckling	→	=	Followed by

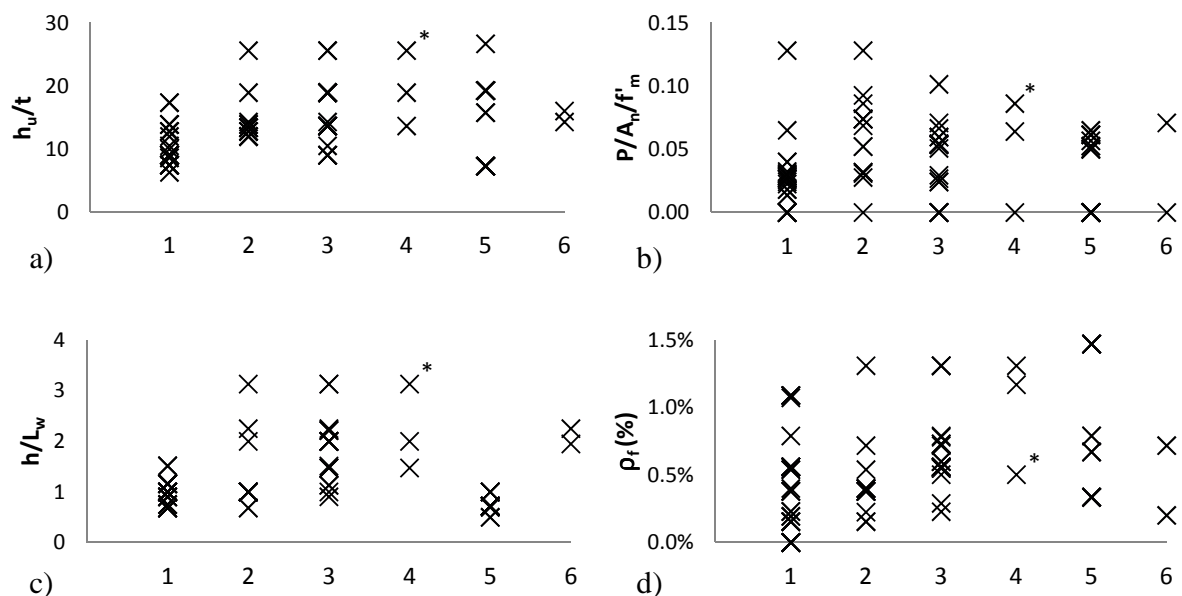
<sup>11</sup> Obtained from Table 4 of CSA S304.1-04 based on given masonry unit compressive strength of 13.1 MPa and type S mortar

<sup>12</sup> Flanged wall specimen

<sup>13</sup> Specimens built using hollow clay brick masonry units with nominal dimensions of 150x100x400 mm

## 2.6 Analysis of Research Data

Limited evidence of out-of-plane buckling in wall specimens tested to date prevents meaningful characterization of this mode of failure in RM shear walls. However, the tests, in which out-of-plane buckling did not occur, offer lower bound estimates on the critical height-to-thickness ratio while also helping to identify future research needs. The design parameters most likely related to the flexural response of walls leading to out-of-plane instability include the wall height/thickness ratio,  $h_u/t$ , aspect ratio,  $h/l_w$ , level of applied axial compressive stress,  $P/A_n/f'_m$ , and flexural reinforcement ratio,  $\rho_f$ . The range and variation of these parameters for each mode of failure are illustrated in Figure 2-2.



### FAILURE MODES

1	Combined flexure and shear	3	Buckling of vertical reinforcement	5	Unidentified flexural response
2	Toe crushing	4	Out-of-plane buckling	6	Lap-splice slip

**Figure 2-2 Effect of key wall design parameters on the failure mechanism**

a) height-to-thickness ratio, b) normalized applied axial compressive strength, c) height/length aspect ratio, and d) flexural reinforcement ratio

The most common failure mode encountered in these studies was that of combined flexure and shear. This failure mode is characterized by flexural yielding of vertical reinforcement followed by diagonal tension cracking or sliding along the bed joint. This is reflective of the focus of previous experimental studies which was to study the shear failure in reinforced masonry shear walls. In walls that failed in pure flexure, toe crushing is the most common failure mode, followed by buckling of the flexural reinforcement. Two of the flexural walls reported experienced lap-splice slip.

As shown in Table 2-1 and Figure 2-2, only three wall specimens experienced out-of-plane instability. The point distinguished in Figure 2-2 with an asterisk corresponds to the flanged wall tested by He and Priestley (1992). Although the wall had high aspect and  $h_u/t$  ratio, its flexural reinforcement ratio was relatively low. Due to the ambiguity in description of this specimen's response, this leaves room to believe that although the specimen may have experienced out-of-plane instability during the course of the experiment, this may not have been the mode of failure. The remaining two specimens failing in out-of-plane web buckling, (Shedid et al. 2008, 2009) had  $h_u/t$  ratios of 13.7 and 18.9 respectively and flexural reinforcement ratios greater than 1%. The details of the experimental studies on the above three specimens were discussed in Section 2.4.1.

As shown in Figure 2-2-a, the  $h_u/t$  ratios of the RM walls tested in previous studies that exhibited flexural response ranges between 6 and 27. However, only 4% of these walls had  $h_u/t$  ratios greater than 20, and 50% had  $h_u/t$  ratios greater than 13. All three walls that were reported as having experienced out-of-plane instability had  $h_u/t$  ratio between 13 and 27.

Nine wall specimens with applied axial compressive stress higher than  $0.13 f'_m$ , where  $f'_m$  is the masonry compressive strength, were tested by Foltz and Yancey (1993) to study the shear performance of masonry walls. These walls were reported as having experienced flexural "distress", however they didn't contain any flexural reinforcement, thus the flexural mechanism was assumed to have been limited to rocking and/or formation of horizontal cracks (this was confirmed by reviewing photos of damaged walls). Given the above, these nine specimens were left out of the plot in Figure 2-2-b. For the remainder of specimens, axial compressive stress ranged between zero and  $0.13 f'_m$ . One of the three walls that failed due to out-of-plane buckling of the wall end zone was not subjected to axial compressive stress.

All specimens failing in combined flexure and shear had aspect ratios ( $h/l_w$ ) between 0.5 and 1.5. More than half of the specimens that failed in pure flexure had aspect ratios greater than 1.0, and nearly 20% had aspect ratios greater than 2.0. Information on reinforced masonry shear walls with aspect ratios greater than 3.1 tested under reversed cyclic lateral loads was not readily available. This is to be expected since reinforced masonry walls are normally used in low-rise construction. Note that the three specimens which experienced out-of-plane instability had aspect ratios greater than 1.5.

Overall, the flexural reinforcement ratio ( $\rho_f$ ) did not exceed 1.5% of the wall gross area, with only 25% of walls containing more than 1.0% flexural reinforcement. Two of the three specimens that experienced out-of-plane instability had  $\rho_f$  greater than 1.0%.

All specimens with unspecified mode of failure had relatively low aspect ratios, levels of applied axial compressive stress, and reinforcement ratios. One of these walls had a high  $h_u/t$  ratio of 26.7, but a relatively low flexural reinforcement and aspect ratio (0.34% and 1.0 respectively). On the other hand, six of these flexural walls that had high reinforcement ratio (close to 1.5%) had a low  $h_u/t$  ratio of 7.3. Based on the available information, the likelihood of out-of-plane instability causing failure in these walls is considered to be low.

## **2.7 Summary and Conclusions**

Based on the literature review of experimental research on reinforced masonry and concrete shear walls, the wall physical parameters that seem to influence the flexural response of walls leading to their out-of-plane instability include  $h/t$  ratio,  $h/l_w$  aspect ratio, level of applied axial compressive stress, and the flexural reinforcement ratio. However, it is evident that curvature ductility demands and the level of applied tensile strain in vertical reinforcement at the wall end zone govern the onset of lateral instability. These parameters have an important role in determining the minimum wall thickness.

Based on the results of this literature review, the first phase of the experimental program was designed with a focus on isolating the reinforced masonry wall end zone and determining the effect of different  $h/t$  ratios, as well as levels of applied axial tensile strain on the out-of-plane instability of RM shear walls.

## Chapter 3: Experimental Program

### 3.1 Background

As previously discussed, the objective of this study is to identify the parameters influencing the out-of-plane instability of reinforced masonry shear walls under in-plane loads. Since no previous studies were carried out with the same objective, the database presented in the previous chapter only serves as the starting point for a comprehensive research study. To achieve the objectives of this study, a four-year research effort is underway, consisting of two phases of testing, first of which is presented here. This chapter describes the design, construction, and material properties of test specimens as well as the test setup and the testing procedure.

Figure 3-1 shows a reinforced masonry shear wall subjected to gravity loads and in-plane lateral loads due to earthquake motions. An overturning moment is developed along the base of the wall, thereby putting end regions of the wall into alternating cycles of axial tension and compression. Based on the review of previous research studies, it is expected that the reinforcement in the end region of the wall is going to experience large tensile strains causing uniformly spaced horizontal cracks to develop in the plastic hinge zone at the wall end regions. When the wall is subjected to subsequent compression load cycles, it may experience out-of-plane displacements and possible out-of-plane instability, as illustrated in the figure.

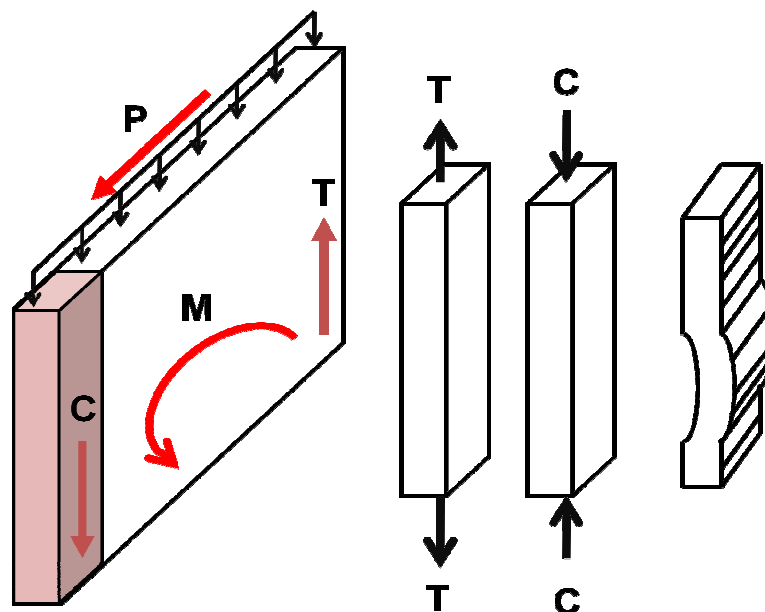


**Figure 3-1** End zone of shear walls subjected to axial loads during reversed lateral loading

The experimental study described in this thesis was focused on simulating the behaviour of such a wall's end zones while disregarding the influence of remaining portion of the wall. The objective was to understand the out-of-plane instability phenomenon and identify key

factors which influence the development of this failure mechanism. An additional reason for the decision to start the experimental research program in this manner was due to very limited previous experimental evidence on out-of-plane instability of RM shear walls. The absence of an analytical model which predicts the onset of out-of-plane instability in RM shear walls made it difficult to design wall specimens which would be fail by experiencing out-of-plane instability.

Therefore, the specimens tested in this experimental study look like columns intended to represent the wall end zone (see shaded region of the wall in Figure 3-1) and were subjected to reversed cyclic uniaxial loading. The actual boundary condition along the height of the wall end zone would be different than the boundary condition present along the height of the specimen. In reality, the end zone of a shear wall is constrained at one end by the remaining length of the wall. However, testing uniaxial specimens would assist in bounding the range over which design parameters influencing the out-of-plane instability vary and therefore, was deemed as a reasonable starting point in the investigation. The next phase of the experimental study consists of testing full-length walls carried out by another researcher in the same investigation team.

The objective of the loading protocol was to induce the tension and compression stresses and deformations which were expected to develop in the end zones of RM shear walls subjected to lateral in-plane seismic loads. The results of this study are expected to serve as the basis for the design of full-size wall specimens tested in the next phase of the research program.

### **3.2 Specimen Properties**

The results of previous studies as well as standard masonry construction practice were taken into consideration in the design of these specimens. From the results of previous studies on reinforced masonry walls, it is evident that several factors influence the development of out-of-plane instability of these walls, such as the  $h/t$  ratio of the wall panel, the amount of vertical reinforcement (reinforcement ratio), and the level of applied axial stress. Since the focus of this phase of the study was to investigate the parameters affecting the out-of-plane instability of the wall compression zone, reinforcement ratio and  $h/t$  ratio of the plastic hinge zone were the only parameters that varied across the set of specimens.

In a typical low-rise masonry building in Canada, reinforced masonry shear walls built with standard 200 mm concrete masonry units (190 x 190 x 400 mm) contain 15M bars in at least the outermost three cells in the wall end zones. This gives a flexural reinforcement ratio of 0.53%. However, the review of previous studies has shown that walls with flexural reinforcement ratio of 1.0% and higher were seemingly more prone to experience buckling of reinforcing steel and global out-of-plane instability under in-plane loads.

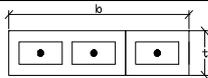
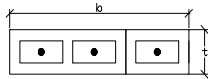
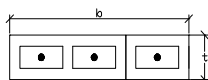
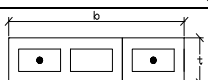
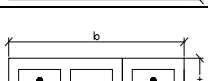
Keeping the above two reinforcement ratios in mind, the test matrix was designed to contain at least one specimen with flexural reinforcement ratio significantly lower than that used in standard practice, and at least one specimen with a reinforcement ratio on the high side (significantly higher than that used in practice). The remaining specimens were designed to

represent reinforcement ratios within the range set by these two extreme ends of the spectrum.

Since vertical reinforcement ratio was deemed to be the most important parameter influencing the out-of-plane instability, the five specimens were all constructed with 140 mm blocks, and a 3800 mm height (equivalent to 19 courses of masonry). This resulted in an average mortar bed-joint thickness of about 10 mm. The resulting h/t ratio for all specimens was originally 27. However, three of the specimens were later stiffened through the application of Glass Fiber Reinforced Polymer (GFRP) in the top portion of the panel. This limited the height over which tensile cracking was possible in these specimens, thereby effectively reducing the height of the plastic hinge zone (corresponding to an equivalent shear wall). Since h/t ratio is determined based on the height of the plastic hinge zone (for the purpose of out-of-plane instability), h/t ratio in retrofitted specimens was effectively reduced. Table 3-1 presents the specimen matrix and the key design parameters.

Four out of five specimens (C2 through C5) were tested under cyclic axial tension and compression loads as discussed later in section 4.2. Specimen C1 was tested under monotonic compression and served as a control specimen to evaluate load-resisting capacity and the failure mechanism for the specimen subjected to uniaxial monotonic loading.

**Table 3-1 Specimen matrix**

Specimen	Cross section	Reinforcement	h/t	Notes
C1		3-15M $\rho=0.71\%$	27	$\rho_f$ 34% higher than that used in standard practice **
C2		3-20M $\rho=1.07\%$	27	$\rho_f$ 100% higher than that used in standard practice (to provide upper bound for $\rho_f$ )
C3		3-15M $\rho=0.71\%$	22	$\rho_f$ 34% higher than that used in standard practice **** Stiffened with GFRP
C4		2-15M $\rho=0.48\%$	19	$\rho_f$ close to that used in standard practice Stiffened with GFRP
C5		2-10M $\rho=0.24\%$	16	$\rho_f$ is 45% lower than in standard practice and lower than the balanced case *** (to provide lower bound for $\rho_f$ ) Stiffened with GFRP over half the height

Notes:

- \* Height, h, is taken as the height of specimen over which tensile cracking is able to form. Note that effective h/t ratio in specimens C3 to C5 was reduced due to the GFRP retrofit
- \*\* Standard practice refers to 15M @ 200 oc. provided in at least the furthest three cells in the compression zone of a masonry wall built using standard 8" (190 x 190 x 400 mm) concrete masonry units. This is equivalent to  $\rho_f=0.53\%$ .
- \*\*\* Note that balanced  $\rho_f$  for masonry is 0.36%.
- \*\*\*\* Standard practice refers to 15M @ 200 oc. provided in at least the furthest three cells in the compression zone of a masonry wall built using standard 8" (190 x 190 x 400 mm) concrete masonry units. This is equivalent to  $\rho_f=0.53\%$ .

### 3.2.1 Specimen Design

Five reinforced masonry uniaxial (column) specimens with nominal dimensions of 140 mm x 600 mm x 3800 mm (length x thickness x height) were designed for this study. All specimens had steel plates welded to the reinforcement at top and bottom. Figure 3-2 shows specimens after the construction.



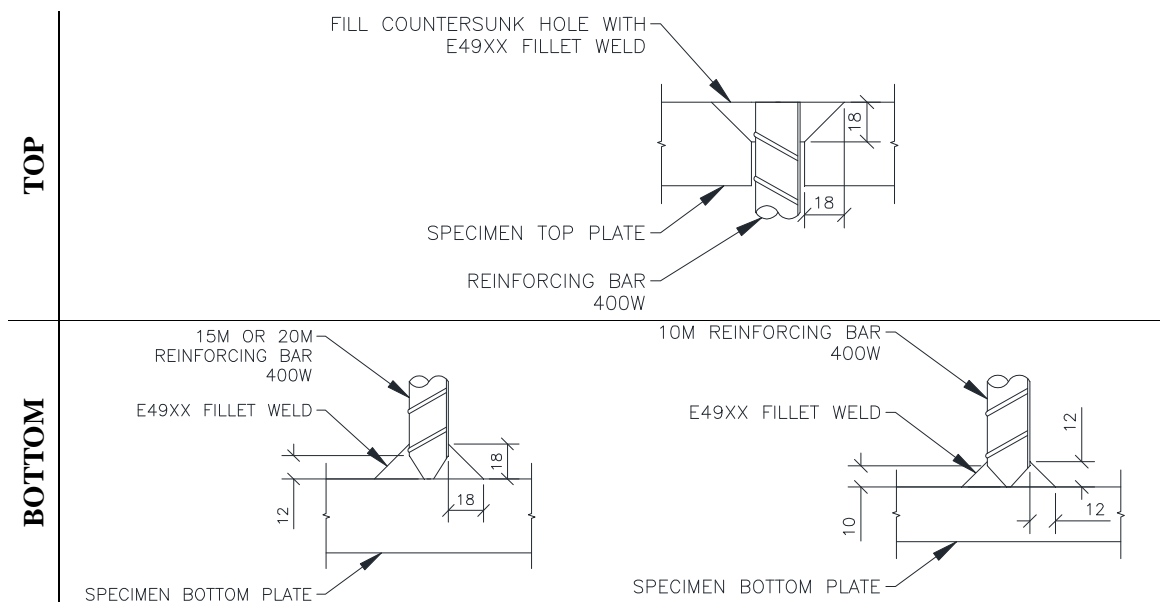
**Figure 3-2 Test specimens after the construction**

The top and bottom steel base plates attached to the specimens were used to allow for the construction of the specimens to a maximum height. Alternatively, concrete foundation and concrete cap could have been used, but the specimen height would need to be reduced as well; otherwise the specimens would be too tall to fit vertically in the test rig and/or be lifted into place using the crane available in the structure's lab. It was also decided that construction of the specimens in the horizontal position on the floor could compromise the integrity of the test results.

The top and bottom specimen plates for specimen C2, reinforced with 3-20M vertical bars, were 38 mm thick while the steel plates for other specimens were 25 mm thick. This was to ensure that there would be no bending in steel plates while the specimens were loaded in tension. Refer to Appendix A for the details of steel plate design.

The reinforcing bars had to be welded to the top and bottom specimen plates in order to ensure adequate anchorage of reinforcing bars and avoid bar fracture due to excessive tensile stresses. In other words, it was important to ensure that the yielding of the steel reinforcement occurs away from the welded connection to the steel plates and that the welded connection was stronger than the ultimate tensile capacity of reinforcing bars.

To this end, several welding details were designed and tested at BCIT (Lim, 2011). Figure 3-3 shows the welding details chosen as the most effective for the connection of reinforcement to the top and bottom specimen plates.



Note: the reinforcing bars were grinded to a pencil-tip shape at the bottom with a tip diameter of 5mm for 15M and 20M bars and 2 mm for 10M bars

**Figure 3-3 Welding detail for connection of rebar to specimen plates**

Refer to Appendix B for details of the welding proposed and the results of their testing.

As noted in Table 3-1, specimens C3, C4 and C5 were retrofitted with Glass Fiber Reinforced Polymer (GFRP) over the top half to limit their effective height over which tensile cracking occurs. For this purpose, SikaWrap 100G product was applied in horizontal and vertical direction, as shown in Figure 3-4.

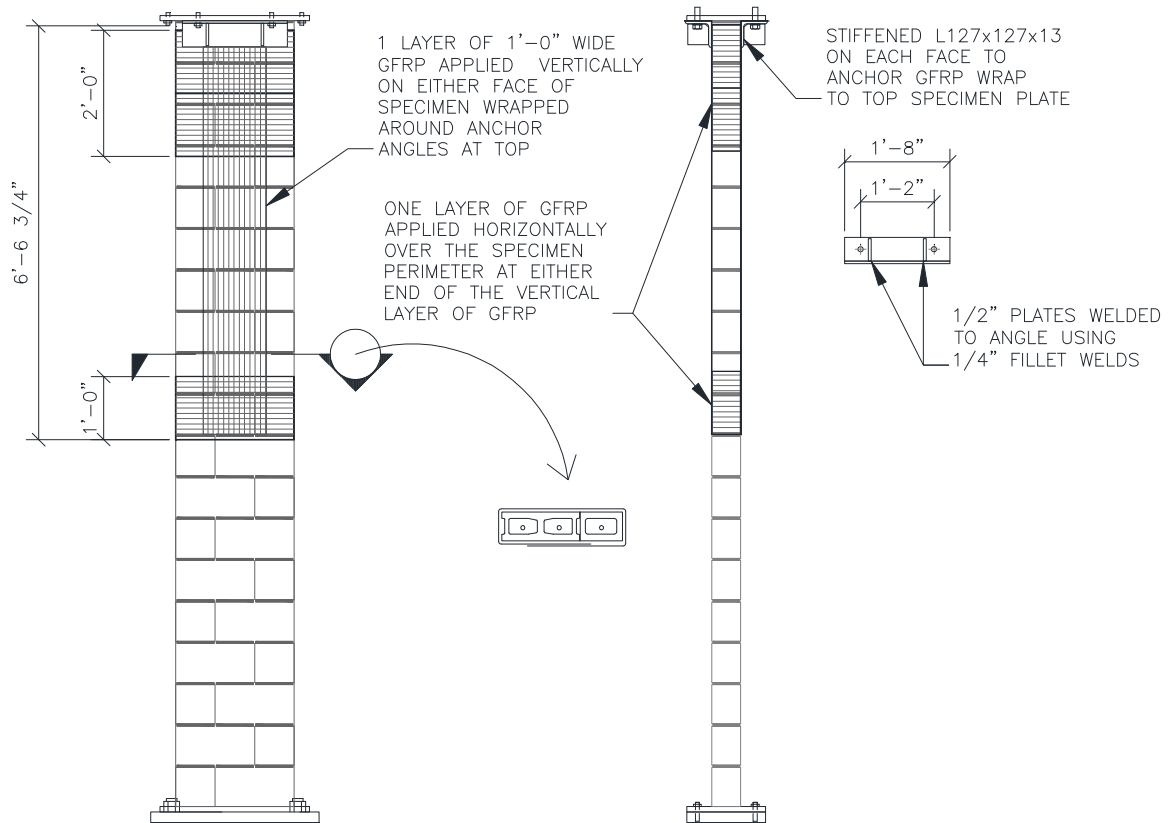


**Figure 3-4 Layout of SikaWrap 100G GFRP to the top half of specimens C3, C4 and C5**

As shown in Figure 3-4, two vertical GFRP strips were bonded to the specimen and wrapped beneath a stiffened angle at the top. The stiffened angle was in turn bolted tight to the test rig along with the specimen. These steel angles acted as anchors at the top, ensuring that the vertical GFRP strips share the tensile loads with the steel reinforcement. In effect, the vertical GFRP strips were able to contribute to the tensile strength of the specimen. The horizontal strips were wrapped around the vertical strip at top and bottom, in order to provide anchorage for the vertical strips and act as confinement, thereby increasing the specimen's compressive strength. Detailed design of the GFRP is included in Appendix C .

Note that the GFRP was applied on specimens C4 and C5 before any testing was done, but specimen C3 was tested and damaged before the retrofit was applied (as discussed later in section 4.2.3).

### 3.2.2 Specimen Construction

The construction of specimens took place in the Structure's Laboratory facility at the University of British Columbia on March 25, 2011.

The steel plates welded to bottom of the specimens were first drilled with threaded bolt holes around the edges as shown in Figure 3-5a. The function of these bolt holes on specimen bottom plates was to allow for bolted attachment of the specimen to another steel plate within the test apparatus that was anchored into the strong floor of the laboratory facility. The second purpose was to prestress specimens with full-height threaded rods and facilitate their safe lifting and transfer from their original location to the test rig.

At the time of construction, specimen steel plates were rested on the 2.5 foot thick, strong floor in the laboratory. Before the reinforcement was welded onto the base plates, it was ensured that surface of the strong floor on top of which they were placed, was perfectly level.

Continuous reinforcing bars were used in the construction to avoid possible effect of lap splices on the specimen behaviour. The reinforcing bars were grinded at one end to form a pencil-tip shape and were then welded to the specimen plates according the welding detail shown in Figure 3-3. Figure 3-5 shows photographs of the steel plates with welded reinforcing bars after construction.

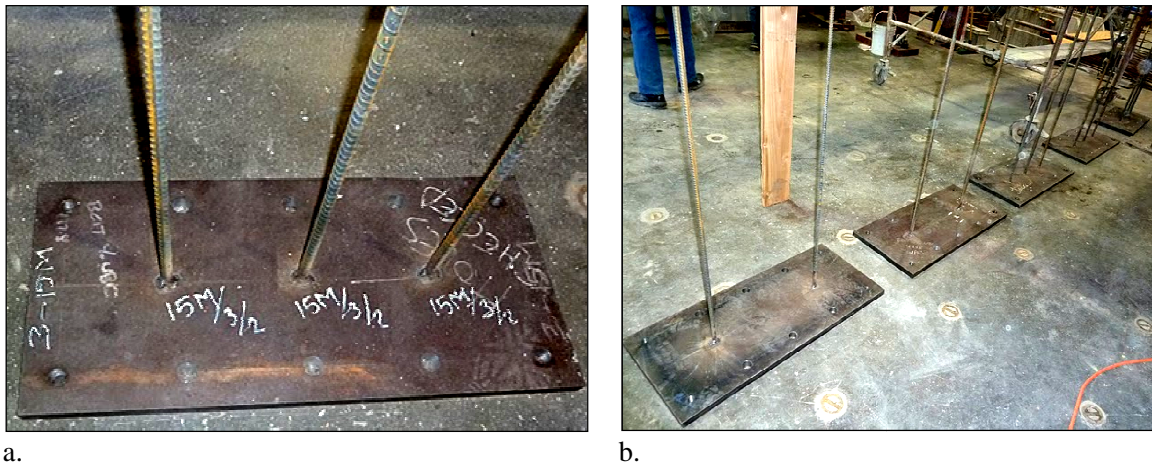


**Figure 3-5 Bottom base plates showing welded reinforcing bars extending over the specimen height**

A layer of mortar was placed between the steel base plates and the first course of masonry to ensure an even distribution of compressive stresses to the bottom of the test frame and subsequently to the strong floor of the lab during loading.

The specimens were single wythe,  $1\frac{1}{2}$  unit long, uniaxial elements constructed with concrete masonry units with nominal dimensions of 140 mm x 200 mm x 400 mm. As shown in Figure 3-6, regular and half-unit rectangular stretcher and plain-ended concrete masonry units were used to ensure a running bond pattern for the specimens, which is commonly used in block masonry wall construction in Canada.

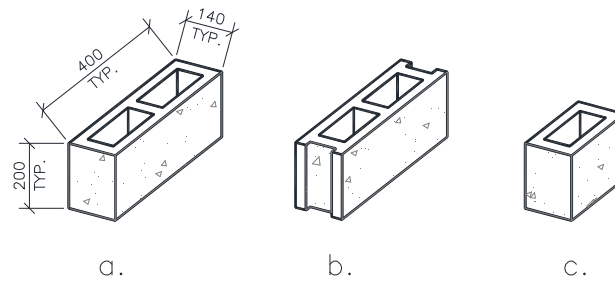


**Figure 3-6 Typical 140 mm thick concrete masonry block units used in construction of specimens: a. double ender unit, b. stretcher unit, c. half block unit**

All concrete masonry units were from the same batch. It was ensured that both types of two-cell units (i.e. stretcher and plain-ended) were used at random in the construction of wall elements so that they closely represented the end zone of walls constructed in standard practice.

All specimens were constructed simultaneously in one day by an experienced mason. The blocks were laid using a 10 mm mortar in running bond pattern. The mason took special care to ensure that specimens were built as close to perfectly straight as possible to minimize effects of eccentric loading on the behaviour of specimens during testing. To achieve this, he used a long level while laying each course of masonry, and was able to adjust the position and orientation of each unit accordingly. After the completion of each course, all excess mortar protruding from the joints was removed and the horizontal bed joints were finished with a curved steel jointing tool, forming a uniform concave bedjoint finish. The surface of the wall was then brushed clean.

During the specimen construction, two-block masonry prisms were also built by an experienced mason. The mortar samples for material testing were also taken at this time.

The specimens were laterally braced against two W310x158 steel columns and timber scaffolding at approximately 1.5 m and 3 m elevation above the lab floor level. This was to ensure wall stability while the masonry was curing and also during the pouring of grout.

The grout was poured three days after the wall construction to ensure that the mortar joints had gained enough strength not to burst under the hydrostatic pressure created by the grout. The grout mix was supplied by the same contractor who built the specimens according to standard practice. The grout was brought to the construction site in a mix-truck and was mixed prior to pouring. The grout was then poured into the wall cells using a grout pump by the masons.

A vibrator was not used to consolidate the grout due to concerns related to the slenderness and the reinforcement ratio of the specimens. However, the grout had clearly reached the bottom courses based on the moisture and seepage on the surface of the specimens. Grout samples were also taken at that time for material testing. For the details of material testing and the results refer to Section 3.2.3.

After the construction of the specimens was completed, reinforcing bars remained exposed above the top course of the walls, as shown in Figure 3-7a. Stiff cardboard templates identifying the exact location of reinforcing bars at the top of each specimen were prepared. Steel capping plates were then constructed according to these templates with countersunk holes to allow the passage of each steel reinforcing bar through the plate. Fast-setting concrete layer was placed between the top masonry course and the top specimen steel plates to ensure a perfectly flat interface between the specimen and the top loading beam, and also to provide even distribution of vertical compressive stresses. The rebar was then welded to the top specimen plate from above according to the top welding detail shown in Figure 3-3. The top surface of the specimen plate was then grinded smooth for a uniform contact to the top loading beam.

In a similar approach to the development process of the weld detail for the bottom steel plates, the weld detail for the steel cap plates was chosen from amongst a set of proposed weld details that were tested earlier to ensure that the steel would yield and fracture without damaging the weld connection. Figure 3-7 shows photographs of the welding of the top plate.



**Figure 3-7** Welding of reinforcing bars to the top specimen plate

Before the specimens were moved into the test rig, they were painted in white colour with a mixture of lime and water. Lime was used instead of paint because it does not add adhesion to the masonry and also sticks to the masonry surface fairly well. The purpose of covering the specimens with this white coat of lime was to facilitate the detection of cracks both while the specimen was being lifted and moved and during the experiment.

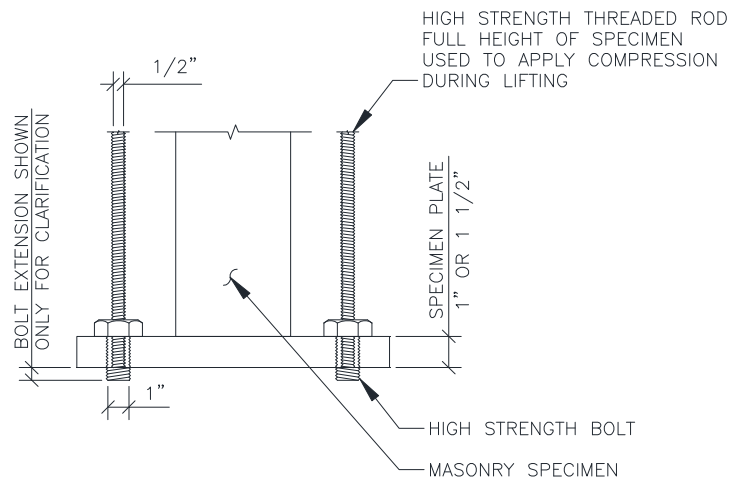
Specimens C3, C4 and C5 were reinforced with GFRP, as discussed in section 3.2.1. The surface over which the GFRP were to be applied was first cleaned and then grinded smooth. The SikaWrap-100G GFRP fabric was applied onto specimens using a two-part resin, Sikadur 300, as recommended by the manufacturer. Experienced contractors and authorized installers of Sika products carried out the surface preparation and installation of the GFRP. Figure 3-8 illustrates application of the GFRP.





Figure 3-8 Application of GFRP over the top half of specimens C3 through C5

Prestressing of the specimens during lifting was made possible by providing bolt holes in the top steel plates; the holes were drilled in line with those of the bottom plate. Four threaded rods extending the height of the specimens were used to prestress the specimen while it was being lifted and moved from the location of construction into the test rig. These rods were threaded into the bottom steel plate at each corner, via the connection detail shown in Figure 3-9.



**Figure 3-9 Mechanism to connect threaded rods to bottom specimen plate**

The threaded rods extended over the entire specimen height and through the bolt holes in the top steel plate. The rods were fastened by nuts from above of the top steel plate and torqued to ensure no cracking would occur during the transport of specimens. Figure 3-10 illustrates prestressing of the specimen and moving it into the test rig using the ceiling crane.

After each specimen was moved into place, it was carefully inspected to ensure that no cracks had formed. No evidence of cracking was found in the specimens after their placement into the test rig.



a.



b.



c.



d.

**Figure 3-10** Prestressing and lifting of the specimen into the test rig

### **3.2.3 Material Properties**

Samples of mortar, grout and masonry prisms as well as steel reinforcement were taken from the same batch of material used in the construction. Material testing was performed at the Structures Lab at the British Columbia Institute of Technology Department of Civil Engineering. The testing was performed according to pertinent CSA and ASTM standards. The key results of material testing are summarized in the following sections, and more details are provided in reports by Das (2011) and Lim (2011).

#### **3.2.3.1 Masonry Units**

The concrete masonry units used for the construction of specimens were manufactured by Tristar Brick and Block and conformed to the requirements of CSA A165 standard. All masonry units were from the same batch. Compressive strength was determined by testing the units in the Forney LT-704-3 Universal Testing Machine. One hollow concrete masonry unit and one half unit were tested to determine their compressive strengths. The tests to determine the compressive strength of the masonry units were carried out in accordance with CSA Standard A165. The blocks failed in a brittle manner with vertical cracks developing along the height, and propagating through the block thickness.

The compressive strength of the full-size masonry unit was 39.6 MPa, while that of the half unit was 38.3 MPa.

#### **3.2.3.2 Mortar**

The mortar mix used in the construction of specimens consisted of 1: ½ :4½ proportions of Portland Type I cement, Type S hydrated lime, and sand by volume to form a Type S mortar. The mortar mix was prepared in accordance with CSA Standard A179-04. The water content was monitored by the masons to ensure workability.

The mortar was mixed on site by the masons. Several batches of mortar were prepared during the course of the construction of the specimens. Samples were taken from each batch just after the mixing. Since each batch of mortar was used in less than two hours, the compressive strength of the mortar determined from the samples was deemed realistic.

The mortar flow was measured on-site just after mixing of each batch according to CSA Standard A179-04. The results of mortar flow tests indicate the workability of the mortar. For the construction of the specimens, mortar with high workability was required. Three sets of 50 mm cubes were prepared for material testing from the mortar mix used in the construction of each specimen. Mortar cubes were removed from plastic bags and placed in curing tub at room temperature of 20°C and 100% humidity as described in ASTM Standard C684, Procedure A. The preparation and storage of the mortar cubes conformed to the requirements of the CSA Standard A179-04.

The mortar cubes were tested using a standard Tinius Olsen Universal Testing machine at the British Columbia Institute of Technology according to the requirements of CSA Standard A179-04.

Table 3-2 summarizes the results of mortar flow tests and tests of compressive strength of mortar cubes. The average mortar flow was 175 mm which is higher than that specified by the CSA 179 standard (100-115 mm). The average compressive strength was 15.8 MPa which exceeds the minimum value of 12.5 MPa required for Type S mortar at 28 days.

**Table 3-2 Compressive strength of mortar cubes**

Cube	Mass (g)	Volume (cm <sup>3</sup> )	Density (g/cm <sup>3</sup> )	Area (mm <sup>2</sup> )	Applied Load (kN)	Compressive Strength (MPa)	Avg. Comp. Strength (MPa)	Flow (mm)
2-1	259.90	133.49	1.95	2612	47.5	18.2	19.8	155
2-2	261.30	134.43	1.94	2626	53.5	20.4		
2-3	259.10	134.11	1.93	2624	55.0	21.0		
3-1	253.30	133.58	1.90	2619	45.0	17.2	15.4	188
3-2	256.80	132.91	1.93	2611	40.0	15.3		
3-3	250.50	133.35	1.88	2617	36.0	13.8		
4-1	254.30	133.07	1.91	2602	34.5	13.3	13.9	181
4-2	247.70	131.20	1.89	2574	35.4	13.8		
4-3	253.30	132.34	1.91	2592	38.2	14.7		
5-1	258.40	135.59	1.91	2666	30.5	11.4	13.1	180
5-2	262.00	136.98	1.91	2682	38.1	14.2		
5-3	257.00	133.58	1.92	2621	35.7	13.6		
6-1	244.70	134.42	1.82	2645	38.3	14.5	16.6	170
6-2	251.00	134.03	1.87	2610	44.5	17.1		
6-3	260.00	133.43	1.95	2598	47.5	18.3		
Average =							15.8	175
Standard Deviation =							2.8	13
Coefficient of Variation =							17.5%	7.2%

### 3.2.3.3 Grout

The grout mix consisted of 1:3:2 proportion of Portland cement, sand, and aggregate by volume. Maximum aggregate size used in the grout mix was 10 mm. Grout was transported to the site of construction in a mix truck. The grout mix conformed to the requirements of CSA Standard A179-04.

Before the grout was poured, a standard slump test was carried out to determine the workability of grout. The grout fell approximately 320 mm from the top of the standard cone used for the slump test and spread horizontally to a maximum diameter of 533 mm and a minimum diameter of 419 mm.

To determine the average compressive strength of the grout, two different types of specimens were made from the grout mix according to CSA A179-04 standard as follows:

1. Grout cylinders, 100 mm in diameter and 200 mm in height
2. 75 mm x 75 mm x 190 mm grout prisms

Grout cylinders were constructed in standard 100 mm plastic moulds. These cylinders would represent ideal conditions in which there is no moisture absorption from the grout (referred to non-absorbent specimens).

Grout prisms were prepared using the pinwheel method. This is done by placing four concrete masonry units perpendicular to one another, such that a square cylindrical shaft is formed in the center, as shown in Figure 3-11.

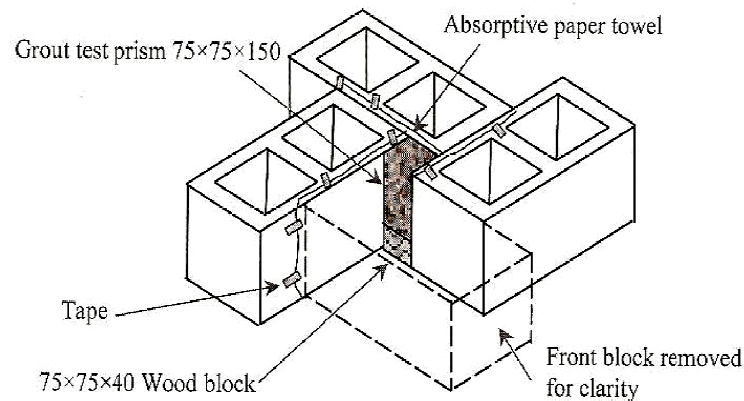


**Figure 3-11 Pinwheel method of preparation of grout prisms**

The pinwheel method ensures that the grout tested is as closely representative of the grout poured inside the masonry units as possible, because it allows the masonry units to absorb the grout moisture in the same fashion that this occurs during construction.

After three days, all grout specimens were removed from the moulds and placed in a curing tub at room temperature of 20°C and 100% humidity.

The compressive strength was determined in accordance to CSA Standard A179-04. The compression tests of the grout cylinders were done using the standard Forney Model LT-704-3 testing machine. Prior to testing, the end surfaces of the grout cylinders were grinded smooth to ensure even distribution of the compressive load. To the same end, two rubber

pads were placed at the top and bottom of the grout prisms inside the test rig. The results of all grout compressive strength tests are summarized in Table 3-3 and Table 3-4.

The grout prisms failed by forming a vertical crack splitting the specimens. Two out of ten grout cylinders failed by forming diagonal shear cracks, while the remaining specimens failed by forming a shear cone. Note that the prisms showed significant honeycombing. The average compressive strength of grout cylinders was 17.2 MPa which exceeds the minimum required compressive strength for masonry grout of 12.5 MPa at 28 days as per CSA A179-04 (for coarse grout).

**Table 3-3 Compressive strength of grout prisms**

Prism	Mass (g)	Volume (cm <sup>3</sup> )	Density (g/cm <sup>3</sup> )	Applied Load (kN)	Compression Strength (MPa)
B1	2316.1	1048.90	2.21	61.5	10.6
B2	2409.5	1107.09	2.18	53.3	8.8
B3	2474.2	1120.05	2.21	57.5	9.1
B4	2699.1	1222.49	2.21	67.3	9.9
Average =					9.6
Standard Deviation =					0.8
Coefficient of Variation =					8.5%

**Table 3-4 Compressive strength of grout cylinders**

Cylinder	Height (mm)	Mass (g)	Density (g/cm <sup>3</sup> )	Load (lb)	Load (N)	Compression Strength (MPa)
G1	194	3627.4	2.38	30084	133820	17.0
G2	191	3560.8	2.37	32166	143081	18.2
G3	195	3662.9	2.39	30671	136431	17.4
G4	189	3522.9	2.37	34542	153650	19.6
G5	188	3490.4	2.36	28569	127081	16.2
G6	189	3521.2	2.37	26853	119448	15.2
G7	197	3693.2	2.39	33782	150270	19.1
G8	191	3540.9	2.36	27359	121699	15.5
G9	195	3656.6	2.39	28735	127820	16.3
G10	195	3680.6	2.40	31770	141320	18.0
Average =						17.2
Standard Deviation =						1.5
Coefficient of Variation =						8.6%

### 3.2.3.4 Masonry Prisms

To determine the compressive strength of grouted and hollow masonry, ten two-course high, stack bond, masonry prisms were prepared by an experienced mason using concrete masonry units from the same batch that was used to build the specimens. The mortar used was also from one of the mortar batches used in the construction. To reflect the same environment as the specimens, the masonry prisms were built adjacent to the specimens, while construction of the specimens was taking place. Five of the masonry prisms were fully grouted three days later, at the same time that the specimens' grout was poured. The remaining five prisms remained ungrouted.



**Figure 3-12 Construction of masonry prisms**

The prisms were transported to the laboratory facility at the British Columbia Institute of Technology for testing, seven weeks after the initial construction. The prisms were carefully loaded onto a truck, were padded with several sheets of cardboard and strapped tight to a wooden skid secured to the bottom of the truck to make sure they do not get damaged during the transport. In all stages of loading and transporting the prisms, extreme caution was taken to ensure micro-cracking was minimized. In the event that micro-cracks may have formed during this process, their presence would not be expected to affect the compressive strength of the prisms.

Prior to the testing, the prisms were capped with fast-setting, high-strength gypsum cement, also referred to as hydro-stone. Compressive strength was determined by testing the prisms in the standard Forney Model LT-704-3 test machine in accordance with ASTM C140-99b Section 7. A pair of fiberboards were used to provide an even contact surface between the prisms and test rig's loading heads. Both hollow and grouted masonry prisms failed in a

brittle shear mode. The loading was timed as described in ASTM C140 Section 6.4.3. Table 3-5 summarizes the results.

**Table 3-5 Compressive strength of masonry prisms**

Prism	Area (mm <sup>2</sup> )	Max. Load (kN)	Compressive Strength, $f'_m$ (MPa)	Average Compressive Strength, $f'_m$ (MPa)	Standard Deviation (MPa)	C.O.V.
G1	54320	1322	24.3	23.2	1.5	6.3%
G2	54320	1170	21.5			
G3	54320	1284	23.6			
H1*	29252	659	22.5	26.7	3.7	14.0%
H2	29252	870	29.8			
H3	29252	816	27.9			

Notes:

\* Small crack was found along the mortar bed-joint prior to testing

G = Grouted Masonry Prism

H = Hollow Masonry Prism

### 3.2.3.5 Reinforcing Steel

All steel reinforcement used in the construction of specimens were obtained from the same manufacturer. Grade 400W deformed reinforcement bars were provided in 4500 mm lengths that were cut from the original length (18000 mm).

To determine properties of steel, five 900 mm long sample cuts were made at random from each size of reinforcement (10M, 15M and 20M). These samples were taken from the same batch of steel provided for the construction of all specimens.



**Figure 3-13 Testing reinforcement bars in the Baldwin universal testing machine**

Each steel rebar sample was prepared according to CSA-G30.18-M92 (R2002) and ASTM A370 standard, Section A9.3. The loading rate was applied according to the ASTM A370 standard, Section 7.4. Tensile strength of reinforcing bars was determined by testing bar specimens in a Baldwin Wiedemann BTE-120 universal testing machine at BCIT. A 200 mm manual dial gauge and Kyowa electronic strain gauge were used to measure strains during the test. The Kyowa electronic strain gauge was glued to the specimen and fed strain deformation data directly into the DAQ6 data acquisition program. The loading information was fed directly from the test machine. Table 3-6 summarizes the test results.

**Table 3-6 Properties of reinforcing steel**

Size of Bar	Area	Yield Load	Yield Stress	Yield Strain	Young Modulus	Ultimate Load	Ult. stress	Fail Load	Fail Stress	Onset of Strain Hardening	Elongation (%)
	(mm <sup>2</sup> )	(kN)	(MPa)		(GPa)	(kN)	(MPa)	(kN)	(MPa)		
10M-1	74.8	44.0	588.2	0.36%	163.4	62.7	838.1	51.5	688.4	N/A	21.5
10M-2	75.4	45.0	596.6	0.25%	238.6	63.17	837.5	53.8	713.2	N/A	22.5
10M-3	81.7	45.5	556.8	0.33%	168.7	64.6	790.6	52.3	640.1	1.3%	22
10M-4	77.0	45.5	591.1	0.38%	155.5	64.6	839.2	52.1	676.8	2.0%	19
10M-5	75.4	44.4	588.6	0.30%	196.2	65.4	867.0	55.4	734.5	1.6%	17.5
Average		44.9	584.3	0.32%	184.5	64.1	834.5	53.0	690.6	1.6%	20.5
Standard Deviation			15.7	0.0005	33.9		27.5		36.0	0.004	
Coefficient of Variation			0.03	0.16	0.18		0.0		0.05	0.22	
15M-1	176.7	91.4	517.2	0.26%	198.9	129	730.0	101	571.6	N/A	N/A
15M-2	179.1	89.5	499.7	0.29%	172.3	127.6	712.5	98.8	551.6	1.7%	20
15M-3	176.2	94.2	533.1	0.30%	177.7	133.8	757.2	104.8	593.1	1.5%	28.5
15M-4	171.8	94.6	550.6	0.31%	177.6	134.7	784.1	109.8	639.1	1.3%	24
15M-5	173.2	93.1	537.5	0.29%	185.4	133.1	768.5	102	588.9	1.4%	20
Average		92.6	527.6	0.29%	182.4	131.6	750.4	103.3	588.9	1.5%	23.1
Standard Deviation			19.6	0.0002	10.4		29.0		32.5	0.002	
Coefficient of Variation			0.04	0.06	0.06		0.04		0.06	0.12	
20M-1	313.9	141.2	449.5	0.35%	128.4	195.2	621.3	156	496.6	1.6%	17.5
20M-2	307.9	142.5	462.8	0.27%	171.4	198	643.1	158	513.2	1.5%	27.5
20M-3	304.8	142.2	466.5	0.29%	160.9	198.7	651.9	156	511.8	N/A	18.5
20M-4	306.3	142.3	464.6	0.28%	165.9	197.6	645.1	157	512.6	1.7%	17.5
20M-5	295.6	141.5	478.7	0.30%	159.6	197.6	668.5	159	537.9	1.4%	N/A
Average		141.9	464.4	0.30%	157.2	197.4	646.0	157.2	514.4	1.6%	20.3
Standard Deviation			10.4	0.0003	16.8		17.0		14.8	0.001	
Coefficient of Variation			0.02	0.10	0.11		0.03		0.03	0.08	

The reinforcing steel satisfied the minimum requirements outlined by CSA G30.18-M92<sup>1</sup> with respect to minimum yield strength and elongation of 400 MPa and 13% elongation at rupture respectively. Figure 3-14 illustrates average stress-strain relationships for each size of bar based on strain-gauge measurements.

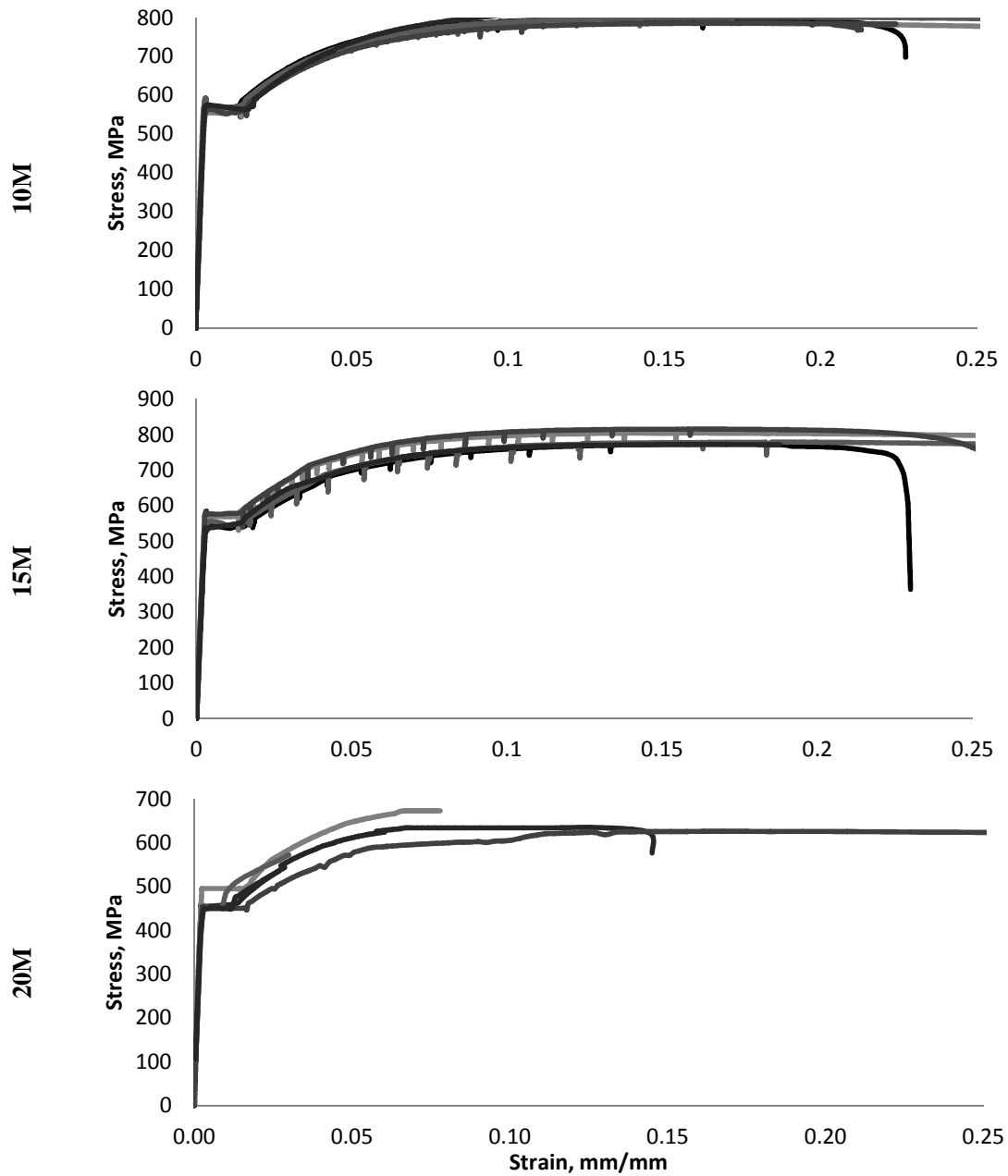


**Figure 3-14 Stress-strain relationship for reinforcing bars**

<sup>1</sup> CSA G30.18-M92 requires all reinforcement to have a minimum ultimate strength of 540MPa and minimum ultimate elongation of 13%

Note that some of the strain gauges cease to function before the reinforcing bar being tested had reached its ultimate capacity. The ultimate stress and strains were then recorded based on manual readings taken from an extensometer that was also attached to each bar.

Maximum average elongation at rupture for the test specimens varied between 27% and 34%. The results also indicate that the onset of strain hardening occurs at 1.5% (an average value). This is less than the maximum tensile strain which the RM column specimens are expected to be exposed to (2%).

### **3.3 Test Setup**

Since each specimen represented the end zone of a wall, the test setup had to consist of a test apparatus capable of applying axial tension forces sufficiently large to cause yielding of the reinforcement, and sufficiently high compression forces to cause either the out-of-plane buckling of the specimen or its crushing. Also, the specimens had to be instrumented in such a way to allow the measurement of axial and the out-of-plane displacements along the height. This section describes the details of the test apparatus and the specimen instrumentation.

#### **3.3.1 Test Apparatus**

Since the objective of this phase of the experimental study was to understand the phenomena of out-of-plane instability as a mode of failure and to investigate the factors influencing it, the compression end of the shear walls was represented by isolated slender reinforced masonry panel specimens. As such, each column-like specimen was subjected to axial tension and compression loads with semi-rigid top and bottom boundary conditions.

The test apparatus was designed in such a way to ensure that axial tension and compression are applied to the specimen in as uniform manner as possible. Also, efforts were made to minimize chances for lateral instability of the test setup as a whole due to eccentric loading. As such, the test apparatus consisted of two double-acting MTS actuators mounted vertically on either face of the specimen as shown in Figure 3-15. The actuators were anchored into the strong floor at the bottom and attached to a top steel loading beam via extension columns. These extension columns were steel wide flange sections that acted as spacers bridging the gap between the MTS actuators and the top loading beam. In this way, the full stroke of the actuators could be utilized.

Unfortunately, it was not possible to use two identical actuators with adequate capacity for the purpose of this experimental study - the actuators were notably different in terms of dimensions. However, the two MTS actuators used in the test apparatus were compatible with one another and with the data acquisition system, and could be controlled in a master and slave fashion to ensure their simultaneous displacement control.

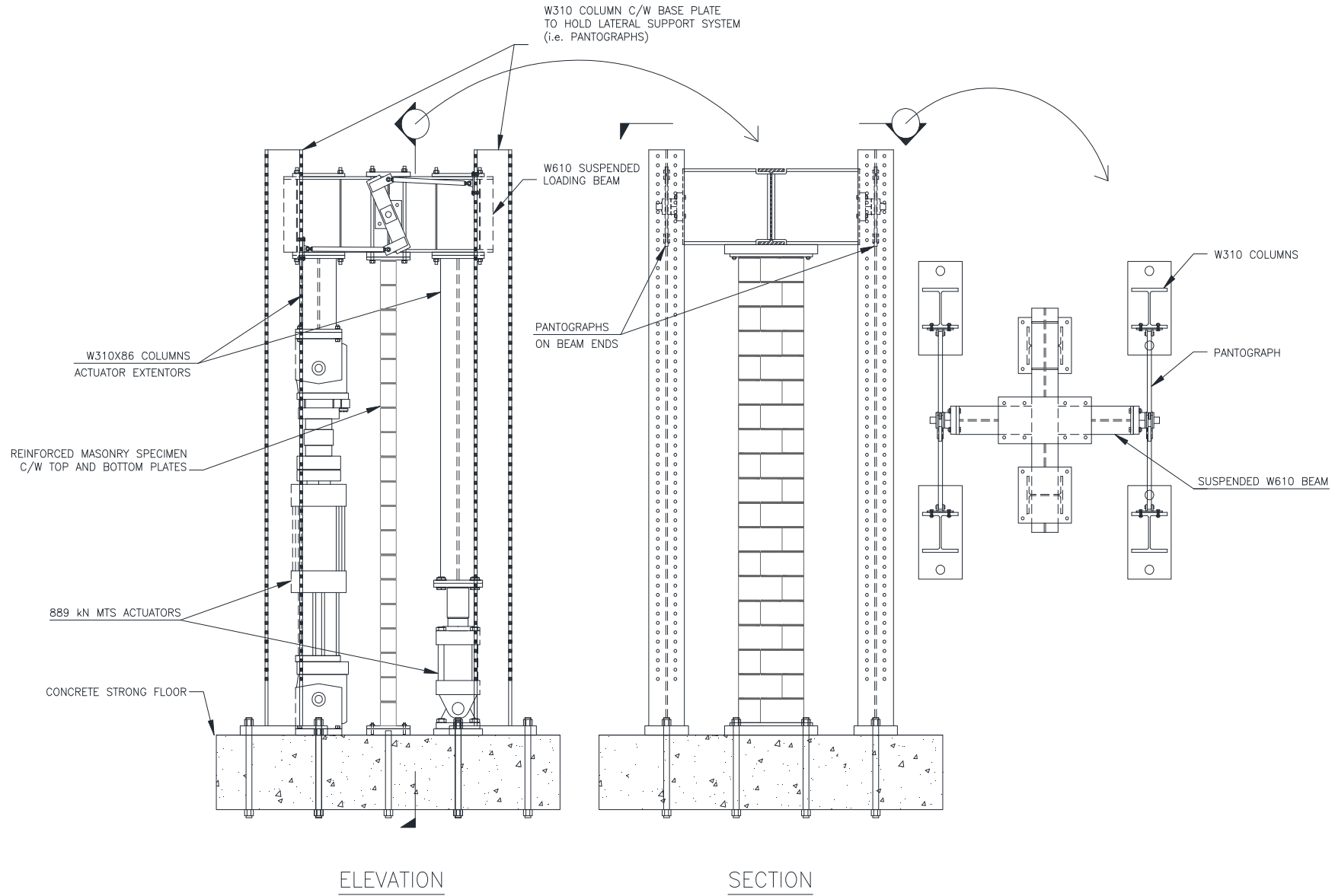


**Figure 3-15 Test apparatus**

Two steel pantographs were used to provide lateral stability to the test setup during the experiment. The pantographs used here were a type of mechanical linkage consisting of two pin-connected arms which act in tension to restrict the vertical translational movement, as shown in Figure 3-16.

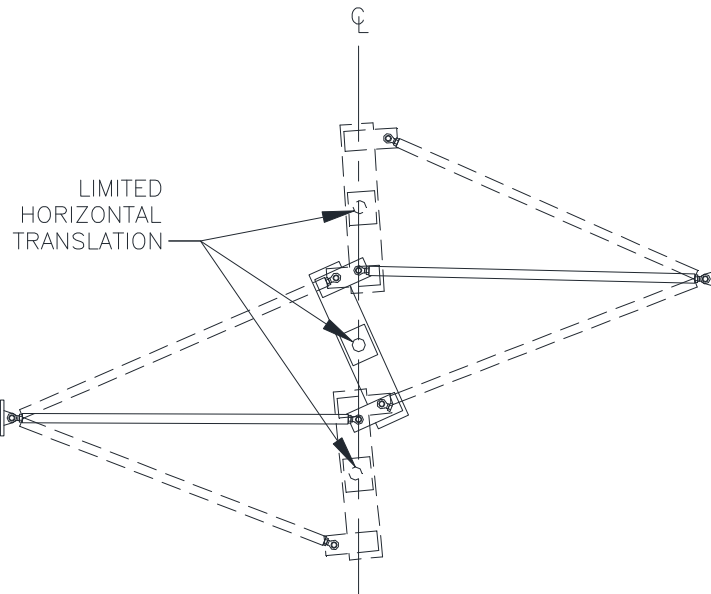


**Figure 3-16 Two-dimensional pantograph acting as a motion guide by restricting translation along one axis while allowing translation in the other**

The pantographs were mounted at the two ends of the top loading beam, parallel to one another, allowing its free movement up and down in the vertical direction, while restricting the system to move from side to side in one horizontal direction parallel to the weak axis of the specimen; this direction coincided with the direction in which the two MTS actuators were free to rotate at their hinges. Ideally, the test rig should be restricted against lateral translation in both horizontal directions. Although the system was quite stiff in the other horizontal direction, the horizontal displacements in that direction were also monitored in order to ensure they were minimal.

One steel column was placed in each of the four corners surrounding the test apparatus. Each arm of the pantograph was bolted to a column, as shown in Figure 3-15.

Note that the arms of the pantograph are only loaded in tension. For very small vertical movements, the pantograph acts as a very rigid guide, allowing negligible horizontal translation. However, as the range of vertical movement increases, the central pivot of the pantograph begins to undergo some horizontal translation. The amount of this horizontal translation increases non-linearly with increased vertical movement as shown in Figure 3-17.

## Pantograph Translation

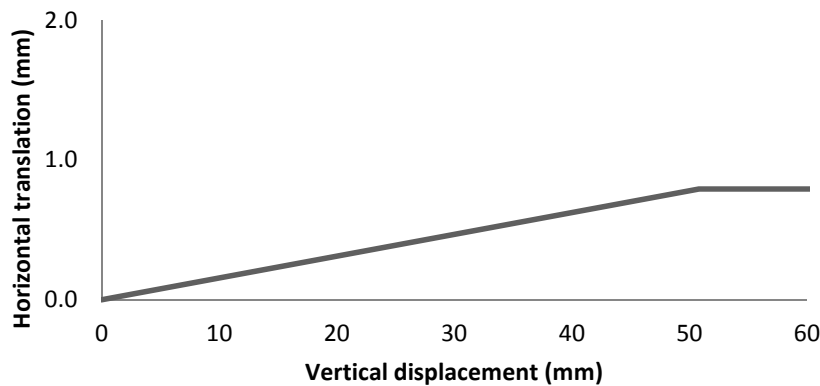


**Figure 3-17 Horizontal translation of the pantograph (showing a nonlinear increase at large deformations)**

Also shown in Figure 3-15 is a plan view of the top steel loading beam, in the form of an X-shaped floating steel beam made up of wide flange section. In one horizontal direction, the beam extended past each face of the specimen to the point of attachment of the actuators, while in the other horizontal direction it extended beyond the length of the specimen to reach the columns which provided lateral support.

All steel components of the test rig were built and assembled with the help of the trained lab technicians at UBC. Prior to testing, it was confirmed that actuators were mounted in perfectly vertical position. All components of the test rig were connected as specified in design drawings with bolts with nuts and plate washers, and each bolt was hand-torqued.

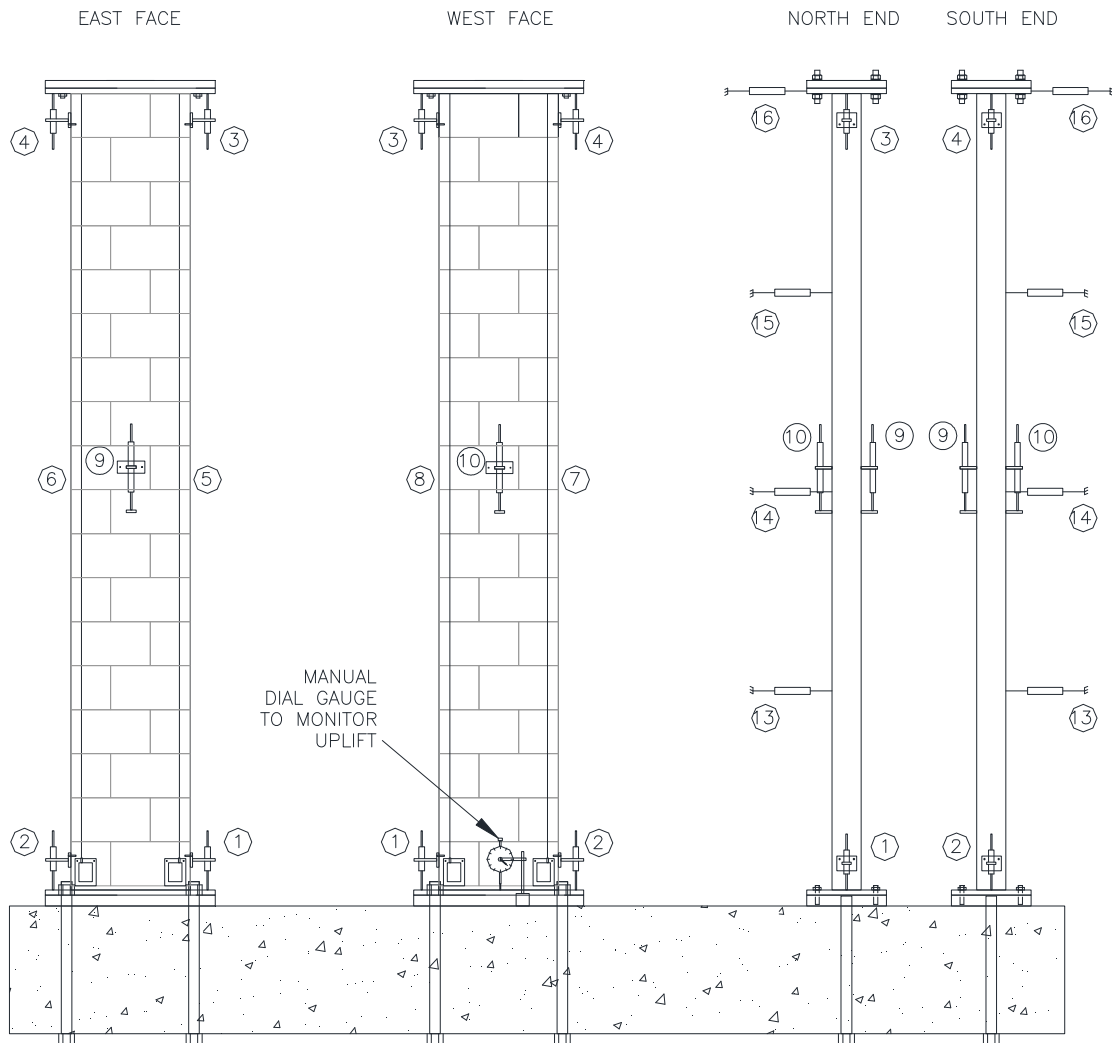
Detailed design and drawings of the test rig are included in Appendix D .

### 3.3.2 Instrumentation

Since all specimens were essentially loaded in the same manner, a single instrumentation scheme was developed for all experiments. The instrumentation layout was developed such that all necessary information was obtained using minimal data with some redundancy to safeguard against potential failure of displacement transducers. The main objective of the instrumentation was to monitor overall vertical tension and compression loads, displacements, uplift, and rotation.

Prior to the development of the instrumentation scheme, conservative estimates of the deformations of interest were made based on established concepts of mechanics of materials.

With the above estimates, it was possible to select appropriate instrumentation for the experiments. A mix of linear potentiometers and string potentiometers was chosen and installed in such a way to allow bi-directional measurement of the wall deformations. The instrumentation scheme is shown in Figure 3-18.



Channel	Description	Full stroke & Resolution
1-4	Separation between the masonry and specimen plates	25mm +/-0.1
5-8	Overall deformation and rotation	250mm +/-0.5
9-10	Localized vertical deformation at bedjoint	100mm +/-0.1
13-15	Out-of-plane displacement	600mm +/-0.2
16	Lateral movement of top loading beam	75mm +/-0.1
17	Load applied by short MTS actuator	970 kN
18	Load applied by long MTS actuator	970 kN

**Figure 3-18 Instrumentation scheme**

As shown in Figure 3-18, linear potentiometers **1** through **4** monitored the separation between the masonry wall element and the specimen steel plates welded to its reinforcing bars at top and bottom. This was intended to ensure that the failure of steel was not localized at the specimen end connections to the steel plate.

String potentiometers **5** to **8** measured the overall deformation of the panel, and also indicated whether the specimen had undergone rotation during the test as they were placed along the four corners of the specimen. Cracks at every bed joint were measured manually and documented after each tensile loading cycle. Linear potentiometers **9** and **10** were installed on the two sides of the bedjoint at midheight for specimens C3 through C5 to measure the crack rotation at that bedjoint as the specimen experienced out-of-plane displacements. Instruments **1** through **10** were mounted on the specimen using aluminum angles that were glued onto the specimen with LePage, Epoxy Steel Syringe Glue, a high strength, epoxy paste adhesive with equal amounts of resin and hardener to bond steel and concrete.

String potentiometers **13** to **15** were used to monitor out-of-plane displacements in either lateral direction at quarter-points along the specimen height. Although the top loading beam was restrained against lateral translation with the use of pantographs, this motion was monitored for accidental eccentric loading. These devices were mounted on a free-standing timber frame and were attached to the specimen with hooks secured to the surface of the specimen using mounting pins threaded with 3/16-inch diameter screws drilled 25 mm deep into the block face.

The uplift of the test rig during the tension cycle of loading was deemed very unlikely. Therefore, the uplift of the bottom of the test rig relative to the strong floor of the laboratory was monitored with a manual dial gauge.

### **3.3.3 Data Acquisition System**

The primary components of the data acquisition system used in this experimental program were a Digital Equipment Station, real-time data acquisition program named DASyLab, and an analog-to-digital converter. All transducers, including the linear and string potentiometers as well as the load cells attached to the MTS actuators, were connected to a signal conditioning unit, and then to an individual channel.

Prior to testing, the load cells were calibrated and all channels were balanced. During testing, the control system offered a real-time digital display of instrumentation readouts. For each test, both plots of applied vertical load versus vertical deformation as well as applied vertical load versus out-of-plane displacement were displayed simultaneously on the control monitor.

Also, the signals from all channels were periodically scanned and saved. After the experiment was completed, the data file was converted into individual channel files and downloaded to a personal computer for analysis.

### **3.4 Testing Procedure**

All specimens were tested to failure. Two out of five specimens had identical design and construction (C1 and C2). One of these specimens (C1) served as the control specimen which was tested first under compression, with manual control of displacement i.e. loading steps were determined by observation of the response of the specimen as the test progressed. The

remaining specimens were subjected to alternating cycles of tension and compression to simulate the behaviour of the wall end zone under lateral seismic loads.

### **3.4.1 Loading Protocols**

Specimen C1 was tested first under monotonic compression while the remaining specimens were subjected to cyclic axial tension and compression with increasing amplitudes of tensile displacement. The tensile displacements were applied such that at each cycle a target multiple of the yield deformation was achieved. Both cycles of tension and compression were displacement controlled in order to ensure that the actuator arms are displaced at the same rate and simultaneously. However, while the peak amplitudes in tension half cycles was reached with a displacement target, the peak amplitude in compression was achieved with a load target. In other words, in the compression half cycles, actuator arms were retracted simultaneously until a total load approximately equal to one-half of the specimen compression capacity (determined based on the results of the first experiment) was reached. The cyclic loading was displacement-controlled at the rate 0.01 mm/second.

The test data obtained from testing specimen C1 was used to obtain a realistic estimate for the masonry modulus of elasticity. This was used to modify the loading protocol for compression load cycles for the remaining specimens. Moreover, during testing of specimen C1, potential issues with regards to the lateral stability of the test setup and consistent loading of the specimen were observed and resolved. During the testing of all specimens, lateral displacement in the top beam and the supporting columns in both horizontal axes were closely monitored. Two total stations were used for this purpose.

Efforts were made to keep the loading protocol similar for specimens C2 through C5. However, there were slight differences in loading due to the differences in response of each specimen. Loading protocols for each specimen is discussed in the following sections.

#### **3.4.1.1 Specimen C1**

Two short-range tests within the elastic limit of the specimen were performed before the full-range test was carried out. These short-range tests served to ensure that the test apparatus performed as intended and that test equipment was not at risk of being damaged.

At the beginning of the full-range test, axial compression was applied by retracting the actuator arms downwards in increments of 1 mm at a time under displacement control. The actual displacement of the jacks was confirmed with manual dial gauges. Both actuators acted as slaves of a third actuator and as such their displacement was simultaneous. The actuator arms were retracted to apply compression at a rate of 0.02 mm/second for the first 5 mm and then rate of downward displacement was slowed down to 0.01 mm/second. After each increment of downward movement, the test was paused and the actual deformation in the specimen examined.

Each increment of downward displacement in the jacks produced an equal amount of force in each jack. This indicated that there was no additional bending moment in the system which

could contribute to the out-of-plane displacement in the specimen. For this specimen only, compressive displacements were applied until the specimen failed.

### 3.4.1.2 Specimen C2

Since the main objective of this experimental study was to characterize the strain levels at which the specimen end zone becomes susceptible to out-of-plane displacements causing lateral instability, it was deemed appropriate to apply each level of tensile deformation only in one cycle, as opposed to two or three repetitive cycles (a conventional approach followed in reversed cyclic testing). Moreover, based on the results of the tests, it was confirmed that each cycle did not lead to further degradation in the specimen. Reversed-cyclic loading was applied in a displacement-controlled manner for specimens C2 through C5.

In the tension cycles, the specimen was subjected to displacements equal to increasing multipliers of the yield displacement. The yield strain for steel reinforcement of 0.0026 used in the test was obtained from the tensile testing of bar samples. For example, the tensile displacement corresponding to yield,  $\Delta_y$ , was approximately equal to 10 mm for specimen C2. Compressive displacements were incrementally increased until a load approximately close to one-half of the crushing load for the specimen C1, ( $P_{cr}/2=700$  kN) was reached. Figure 3-19 shows the loading protocol for specimen C2.

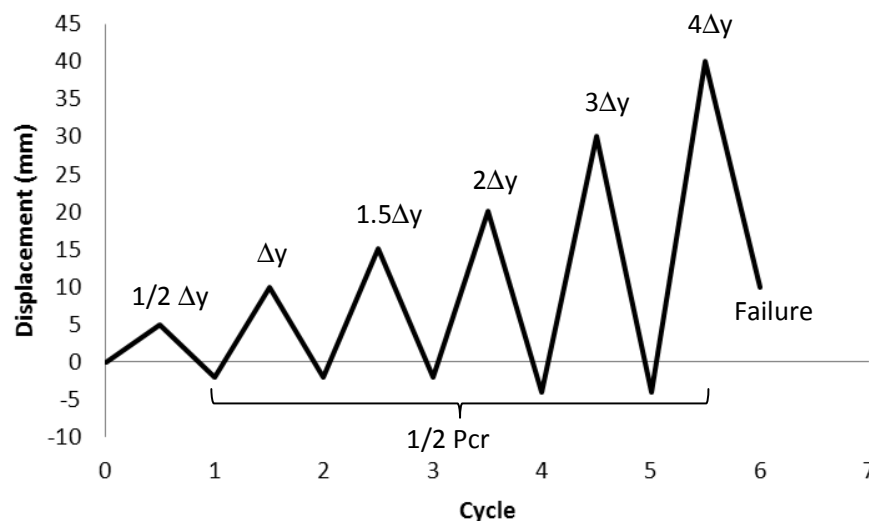


**Figure 3-19 Loading protocol for specimen C2**

The loading was stopped after the specimen became unstable.

### 3.4.1.3 Specimen C3

Efforts were made to use a similar loading protocol to that used for testing of specimen C2, shown in Figure 3-19. During the first two cycles, the specimen was subjected to just enough compression load to cause full crack closure (less than  $P_{cr}/4$ ). In subsequent cycles, the compression load was first increased to approximately a quarter and later to half of the

crushing strength. Out-of-plane displacements were closely monitored after the tensile displacements reached  $2\Delta_y$ . This was done in an effort to close in on the actual tensile strain level past which the specimen becomes susceptible to out-of-plane instability. Figure 3-20 shows the loading protocol for specimen C3.

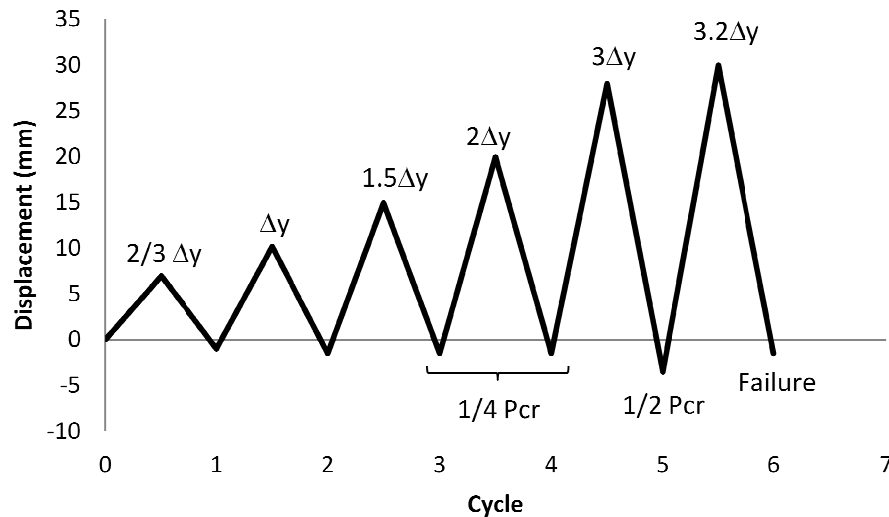


**Figure 3-20 Loading protocol for Specimen C3 after the retrofit**

#### 3.4.1.4 Specimen C4

The specimen was subjected to a similar loading protocol as specimens C2 and C3, however the amplitude of tension cycles was increased in smaller increments after the specimen had experienced close to critical out-of-plane displacements equal to half the block thickness. Therefore, out-of-plane displacements of the specimen were closely monitored after unloading from tension half-cycle with maximum displacements of  $3\Delta_y$ . In this case,  $\Delta_y$  was 7 mm. Figure 3-21 shows the loading protocol for specimen C4.

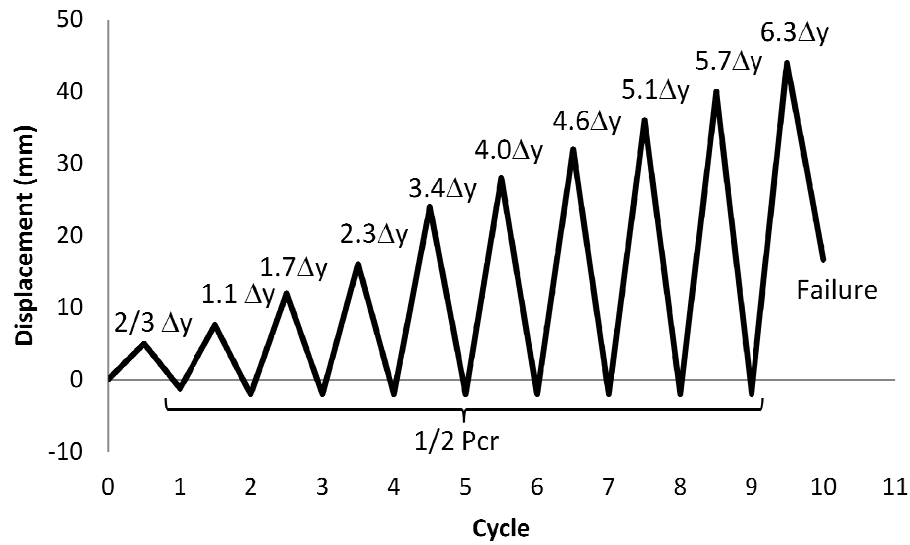


**Figure 3-21 Loading protocol for specimen C4**

### 3.4.1.5 Specimen C5

The specimen was subjected to a similar loading protocol to that used for the testing of specimens C2, C3 and C4. The estimated yield displacement ( $\Delta_y$ ) was 5.7 mm. In compression, maximum displacements corresponded to half the crushing strength of the specimen ( $P_{cr}/2$ ). However, near the end of the experiment, the specimen was only subjected to compression until the cracks closed, since there were concerns that it would fail prematurely in local crushing. Figure 3-22 shows the loading protocol for specimen C5.

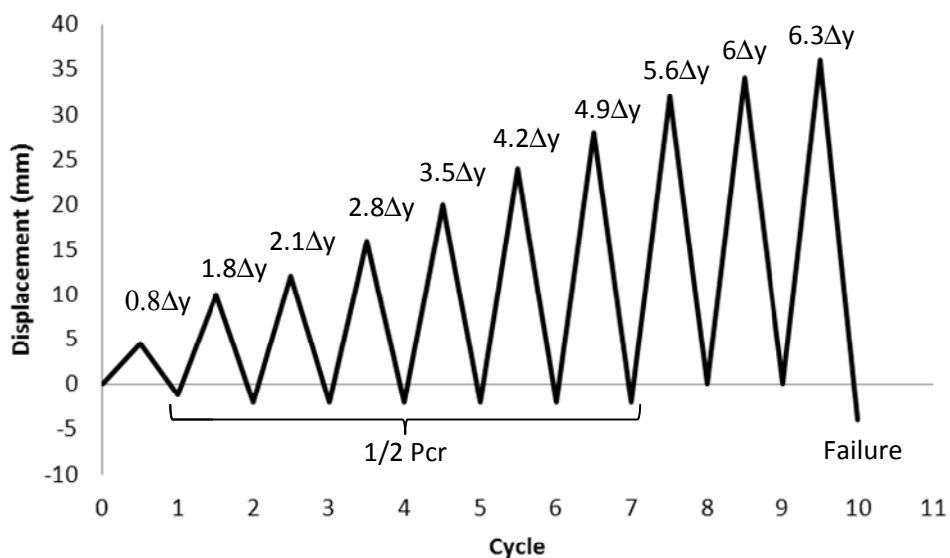


**Figure 3-22 Loading protocol for specimen C5**

### **3.5 Conclusions**

To achieve the objectives of this research, five RM column specimens were constructed, using the same 140 mm thick blocks, to the same original height. The amount of longitudinal reinforcement was one of the major design parameters that initially varied across the test matrix. However, in order to investigate the effects of varying the plastic hinge height, three of the specimens were later retrofitted with GFRP material over their top halves, effectively reducing the height over which tensile cracking was possible (ie. their plastic hinge height). The mechanical properties of the material used in the construction of the specimens and potential design issues were evaluated through the tensile capacity testing of welded connections, mortar and grout compression tests, masonry prism compression tests, and steel rebar tension tests.

The analysis of compressive and tensile resistance of RM columns was performed to provide the estimates needed for the full-scale RM column testing and the test setup design. It was determined that the maximum tensile and compressive capacity for the test specimens are approximately 520 kN and 1660 kN respectively. The aforementioned tensile resistance corresponds to that of the largest reinforcing bars (20M bars) and the compressive strength corresponds to the compressive strength of the masonry prisms. It is also expected that the column compressive resistance will be reduced due to reversed cyclic loading.

## Chapter 4: Experimental Results

In this experimental study, reinforced masonry uniaxial specimens were constructed and tested under uniaxial tension and compression in order to simulate the behaviour of the end zone of RM shear walls subjected to gravity and in-plane lateral loads. This chapter summarizes observations associated with the response of the specimens during the testing, including test data, a description of the events preceding the failure, as well as a discussion on the failure mechanisms.

### 4.1 Failure Mechanisms

Table 4-1 summarizes the response and failure mode for all five reinforced masonry specimens tested.

**Table 4-1 Summary of specimen behaviour and failure modes**

Specimen	h/t	$\rho$	Yield Tensile Displacement, $\Delta_y$	Maximum Applied Tensile Strain, $\epsilon_{sm}$ (%)	Maximum Compressive Strain, $\epsilon_c$ (%)	Compressive Load at Failure, $P_c$ (kN)	Failure Mode*
C1	27	0.71% (3-15M)	-	-	0.13	1400	1
C2	27	1.07% (3-20M)	10	1.05	0.10	250	2
C3	22	0.71% (3-15M)	9	0.87	0.21*	280	2
C4	19	0.48% (2-15M)	6.2	1.85	0.05	118	2
C5	16	0.24% (2-10M)	5.7	1.65	0.13	445	3

**Failure Mode:**

1. Crushing

2. Out-of-plane Instability

3. Reinforcement buckling

**Note:**

\* this compressive strain does not taken into account the open cracks over which GFRP was applied and therefore is not a pure compression strain

As can be seen from Table 4-1, three main failure mechanisms were observed during the testing of the reinforced masonry uniaxial specimens as follows:

1. **Crushing:** This failure mechanism is associated with the specimen reaching its axial compression load capacity without experiencing buckling. This failure occurred in specimen C1, which was subjected to monotonic axial compression, without evidence of notable out-of-plane displacements.
2. **Global out-of-plane instability of the plastic hinge zone:** This mechanism was observed in specimens C2 through C4. The instability was observed when the specimens were

subjected to low compressive loads (relative to the pure compressive capacity of specimen C1, see Table 4-1), following a load cycle where large axial tensile strains were applied. As can be seen from Table 4-1, the required level of applied axial tensile strain to cause out-of-plane instability was reduced with increasing  $h/t$ .

3. **Reinforcement buckling:** this failure mechanism was observed in specimen C5 which contained the lowest reinforcement ratio of 0.24% and was reinforced with the bars of smallest size compared to other specimens (10M bars with a nominal diameter of 11 mm). Although out-of-plane displacements were recorded in the region where horizontal cracks developed, the failure took place when a reinforcing bar buckled and the masonry faceshell in that zone spalled (disintegrated). The specimen therefore did not experience global instability, like specimens C2, C3 and C4. The cause for this failure mechanism is attributed to the small bar size with a small surface area (10M bars), since the bar buckling was preceded by significant vertical splitting cracks and loss of bond with the grouted portion when the specimen was subjected to high tensile strains.

Detailed observations related to the experiments performed in this study are discussed in the following sections.

## 4.2 Experimental Observations

### 4.2.1 Specimen C1

Specimen C1 was reinforced with three 15M bars (3-15M) placed in every core resulting in reinforcement ratio of 0.71%. This specimen served as a control specimen and it was subjected to monotonic uniaxial compression to determine its load capacity.

It should be noted that during the initial two short-range tests of the specimen, some crushing had been observed at the interface of the first and last courses of masonry and the top and bottom specimen plates. Figure 4-1a illustrates the crack pattern for specimen C1 before the full-range test. After the second short-range test, two vertical cracks were detected. One of the vertical cracks was along the interface of two masonry blocks and another one was directly above it, down the middle of the masonry face shell. All these vertical cracks were less than 0.2 mm in size. Before the start of the full-range test, a few hairline cracks were also noticed along the bed joint in the top two masonry courses as shown in Figure 4-1a. It was also noted that the pre-existing crack at the interface of the top masonry course and the steel plate was slightly widened. These horizontal cracks were formed as the specimen was slightly tensioned while it was being bolted to the top loading beam. The horizontal cracks were 0.4 mm in size.

During the full-range test, it was not possible to approach the specimen too closely due to safety concerns. However, no major cracks were observed at lower displacement levels. The first and final major event was the formation of a vertical crack which started on the south face of the top masonry course and rapidly propagated downwards along four masonry courses (see Figure 4-1b). This was accompanied by a loud popping sound. A similar event but with less intensity occurred simultaneously on the north side of the specimen. Almost immediately afterwards, the specimen failure took place in the form of explosive crushing in

the top six courses and the propagation of the vertical crack. Face shell spalling occurred on the east face; this is typical of a crushing failure as shown in Figure 4-1b. Also shown in Figure 4-1b is the full-height continuous vertical splitting crack which was observed on the south face. The location of this large splitting crack coincided with the head joint between half-block and full-size (stretcher) block.

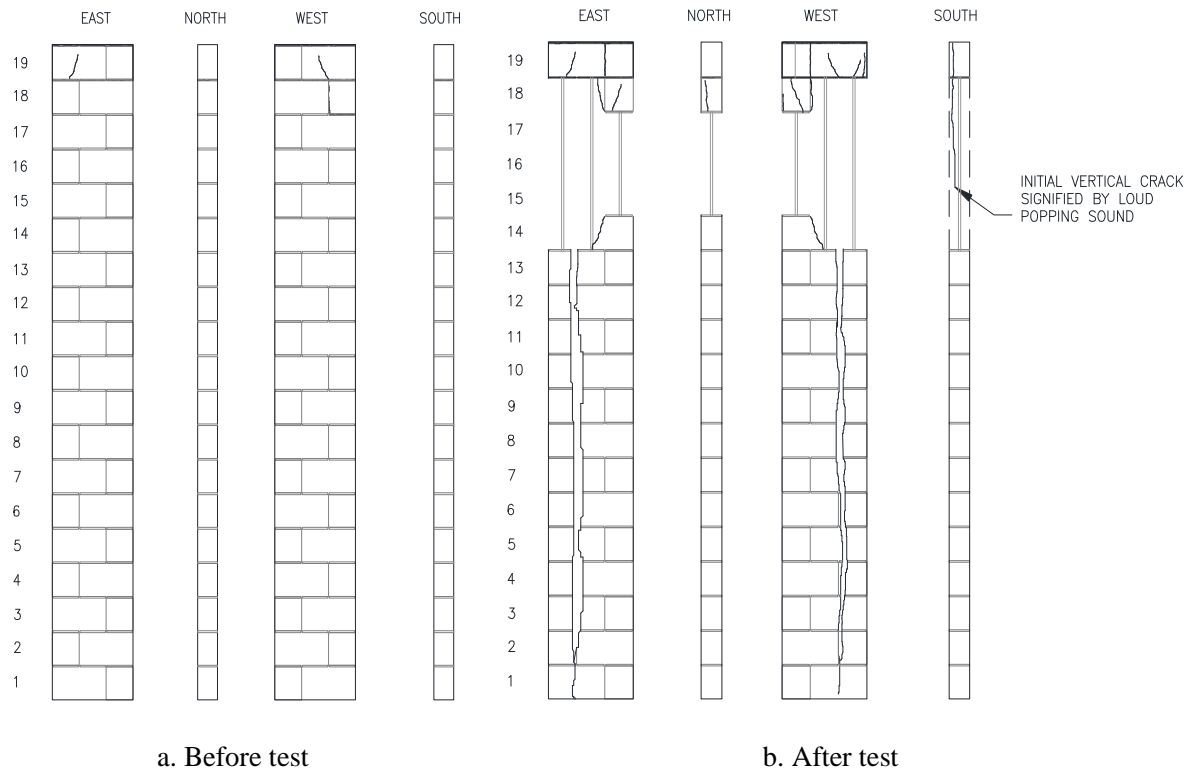


**Figure 4-1 Crack pattern for Specimen C1**

From the crack pattern in specimen C1 after the test, as illustrated in Figure 4-1b, it can be seen that most of the damage was concentrated in the top six courses, with the top course remaining intact. The courses below the top course (15, 16, 17 and 18 from the bottom) were completely crushed. Reinforcing bar in the end core was exposed in the final stage of testing. The bar had bent and buckled under the explosive crushing failure.

It is noteworthy that two reinforcing bars were bent westwards (in the direction of the lateral deformation of the specimen) as shown in Figure 4-5 (right). After the grout hardened, it was noticed that these reinforcing bars were slightly offset with regards to the centerline towards west, as shown in Figure 4-2. The third reinforcing bar (located closer to the centerline of the specimen) was bent in the plane of the specimen.

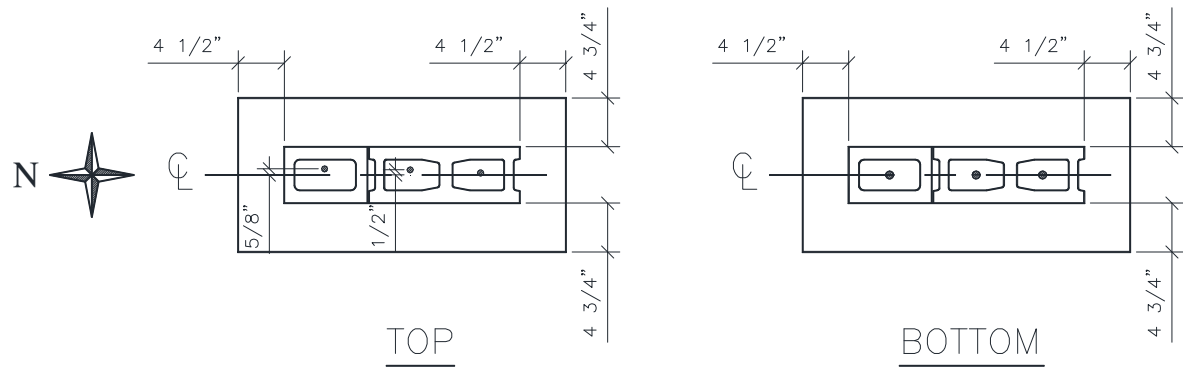


**Figure 4-2 Rebar location within the specimen core (specimen C1)**

Visual inspection of the specimen after the failure, especially the damaged portion, confirmed the presence of grout in all cores, and good bond between the grout and the reinforcing bars. Therefore, it was concluded that the buckling of reinforcement occurred as a side effect of the crushing failure (as opposed to being due to the out-of-plane displacement of the specimen). This is because for 3-20M bars, over the effective length of the specimen ( $0.8 \times 3800\text{mm} = 3040\text{mm}$ ) the buckling load is very low ( $\sim 5\text{kN}$ ) and for the three bars to buckle at compressive loads above 1000 kN, their unsupported height must be less than the height of one masonry course. The low strain levels at which the final crushing failure occurred also confirm this.

Figure 4-3 and Figure 4-4 illustrate the axial load vs. total axial deformation and axial load vs. lateral deformation at midheight for specimen C1 respectively. As indicated on Figure 4-3, specimen C1 failed at a compressive load of about 1400 kN (corresponding to compressive stress of 17 MPa). This stress is significantly less than the masonry compressive strength ( $f'_m$ ) value of 23.2 MPa obtained through material testing (see Section 3.2.3.4). The maximum capacity of the specimen was achieved at a compressive strain level of 0.13%. Based on the compressive response of the specimen, elastic modulus for masonry ( $E$ ) of 13.6 GPa was calculated.

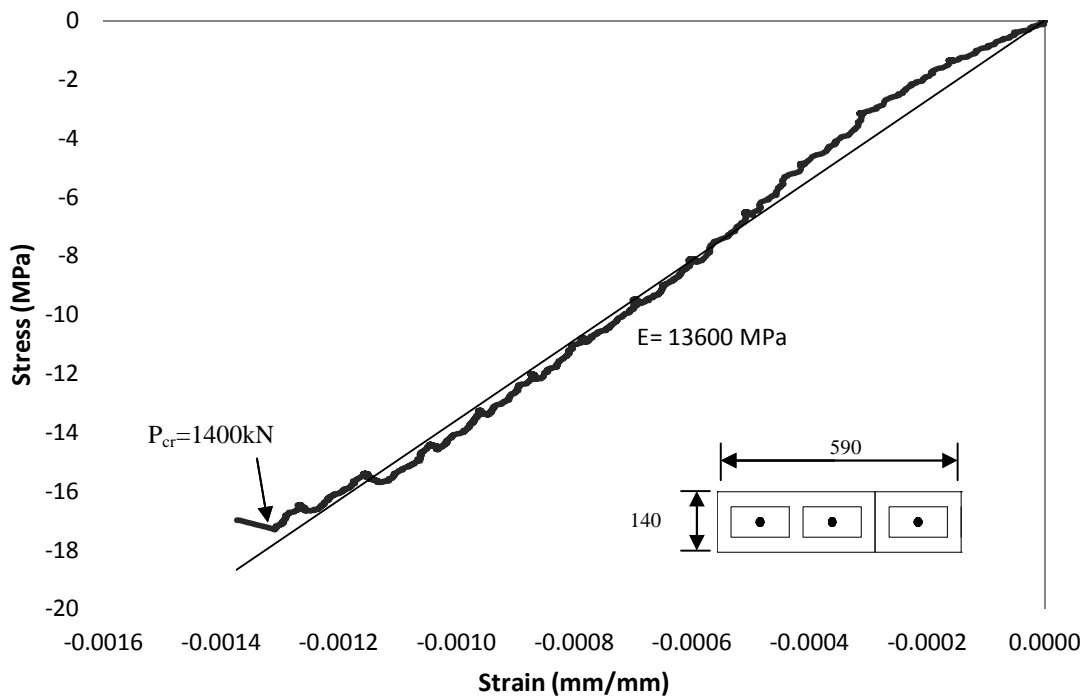


**Figure 4-3** Axial stress vs. axial compressive strain response for specimen C1

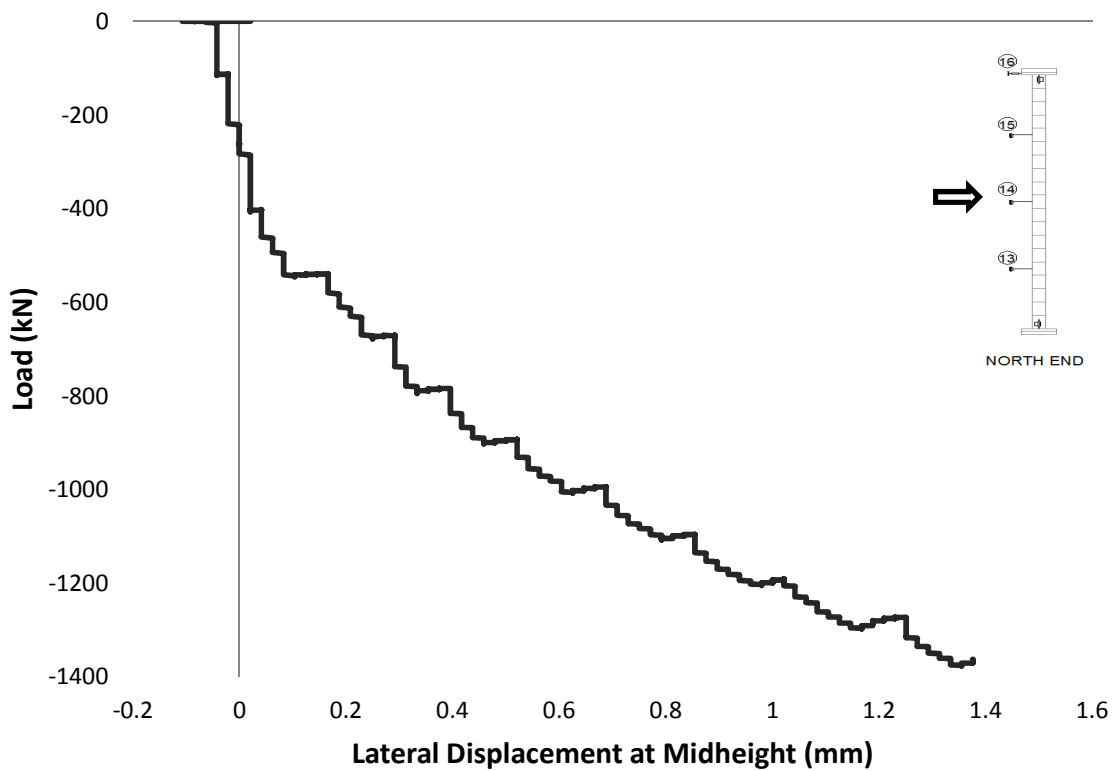


**Figure 4-4** Axial load versus lateral displacement at midheight for specimen C1



**Figure 4-5** Specimen C1 at failure: note a continuous vertical splitting crack along the end block core (left) and disintegration of masonry in the crushed portion of the specimen (right)

#### 4.2.2 Specimen C2

Specimen C2 was reinforced with 3-20M bars (one in each core), resulting in a reinforcement ratio of 1.07%, as shown in Figure 4-6. This specimen had the highest ratio of reinforcement of all specimens. According to the literature review discussed in Chapter 2, this specimen was most likely to experience out-of-plane instability under reversed cyclic loading.

As mentioned previously, reinforcing bars in all specimens were welded to top and bottom steel plates, which were subsequently attached to the strong floor at the bottom and to the floating loading beam at the top through bolted connections. During the construction of specimen C2, the reinforcing bars were welded to the bottom specimen plate exactly along the centerline of the bottom specimen plate. However, it was noted that masonry blocks were not perfectly centered on the specimen plate. Figure 4-6 shows the plan view of the specimen in relation to the top and bottom specimen plates.

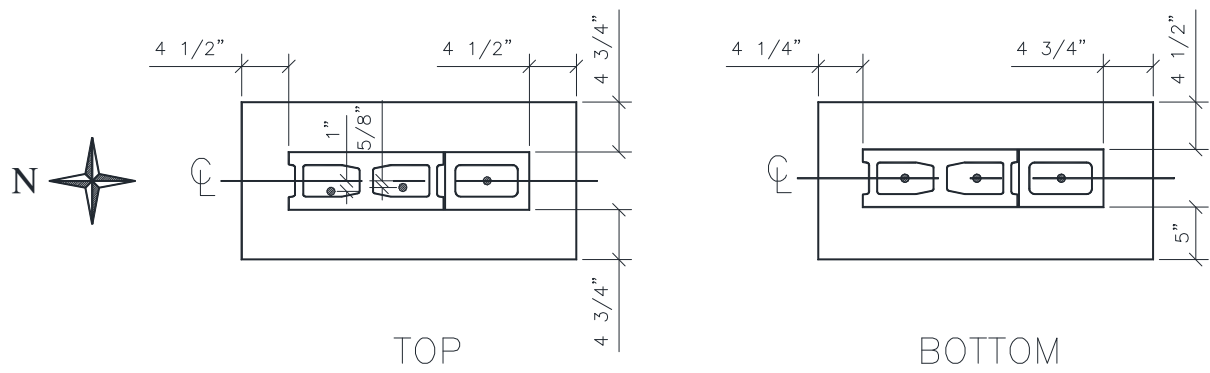
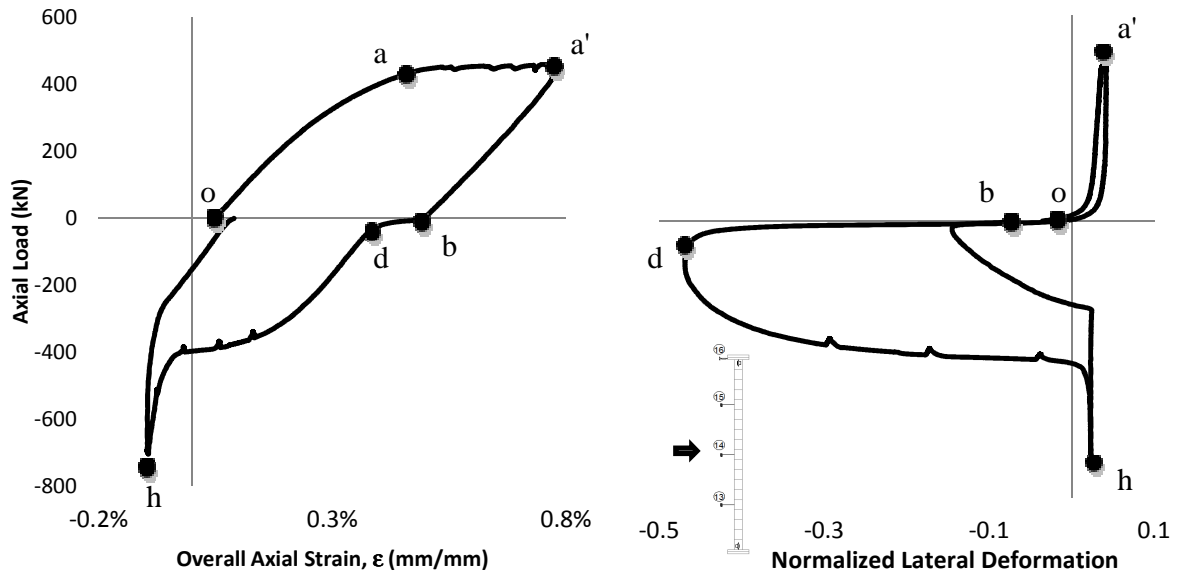


**Figure 4-6 Specimen C2 cross-section and reinforcement layout relative to top and bottom specimen plates**

As can be seen in Figure 4-6, two reinforcing bars at the top were closer to the western edge of the specimen, while the whole specimen was shifted by  $\frac{1}{2}$ " towards north and by the same amount towards east at the bottom. Note that such misalignment is not unusual for field applications. For the purposes of our experiments, it was concluded that this offset in the North-South direction should not affect the out-of-plane stability of the specimen along its weak axis. However, there was a concern that an offset in the East-West direction might cause a P- $\Delta$  effect, thereby increasing chances for out-of-plane instability. However, the bolt holes in the connecting plate attached to the top beam were modified such that after the specimen was placed within the test apparatus and all bolts were tightened, the specimen remained out-of-plumb by only 0.05 degrees. Therefore, it was deemed appropriate to assume that P- $\Delta$  effects due to this offset were negligible. This was confirmed by the observation that during the experiment, equal displacements in the actuators created equal loads in the load cells.

Figure 4-7 shows the plots of applied axial load vs. axial strain of the plastic hinge zone as well as the axial load vs. the maximum lateral displacements of the plastic hinge zone

normalized by specimen thickness. The points **o** through **h** identified on these two plots indicate the important events that were observed during a typical loading cycle.



**a.** Applied axial load vs. axial strain over the plastic hinge region

**b.** Applied axial load vs. maximum lateral deformation at midheight normalized with respect to thickness

- o:** Beginning of cycle in tension
- a:** Yielding of reinforcement
- a':** Peak of tension half cycle (uniformly distributed horizontal cracks along the height)
- b:** Beginning of compression half cycle (most horizontal cracks remain open but are reduced in size)
- d:** Most out-of-plane instability has already occurred
- h:** Peak of compression half cycle (the specimen has restored its original vertical alignment and all horizontal cracks are closed)

**Figure 4-7** Plot of **a.** applied axial load vs. axial strain over the plastic hinge height and **b.** applied axial load vs. maximum normalized lateral deformation at midheight at  $\epsilon_t=0.80\%$

In general, horizontal cracks developed along bed joints during the tension portion of each loading cycle, shown in Figure 4-7 as the path along points **o** through **b**. Examples of such horizontal cracks are shown in Figure 4-8. Point **a** on the plot of axial load vs. axial strain corresponds to the yielding of reinforcement. Although there were no strain gauges attached to the reinforcement, the yielding of reinforcement was easily identifiable by the onset of a plateau in the loading. At the peak of the tension half cycle, identified by point **a'**, the horizontal cracks reached their maximum size. The crack pattern at the peak of each loading cycle is shown in Figure 4-9.



**Figure 4-8 Uniformly distributed horizontal cracks developed in specimen C2 along mortar bed joints during a tension loading cycle**

The subsequent compression portion of the loading cycle is shown in Figure 4-7 as the path from point **b** back to point **o** through point **h**. At the beginning of the compression half cycle, point **b**, the horizontal cracks remained open. As can be seen from the comparison of the two plots in Figure 4-7, the plateau from point **b** to **d** is where most of the out-of-plane displacements occurred. It must also be noted that throughout this phase the load levels were quite low and almost close to zero. The out-of-plane displacements during this phase led to rotation of the open cracks. With increasing compression, masonry compression forces developed at the edge of the rotated cracks. As long as out-of-plane displacements were smaller than one-half of the wall thickness (70 mm), the development of masonry

compression forces caused the closure of horizontal cracks. Therefore, the specimen eventually restored its original vertical alignment and was subjected to pure axial compression at the peak of the compression half-cycle, indicated by point **h**.

Application of larger tensile strains led to larger horizontal cracks at bedjoints and caused the formation of horizontal cracks through some blocks as well.

Eventually, the out-of-plane displacements experienced by the specimen during the plateau between points **b** and **d** in the compression half cycle were too large to allow the specimen to restore its original vertical alignment. At this point, increasing compression forces led to increasing out-of-plane displacements, despite the fact that masonry compression forces had developed at the edge of rotated cracks. Therefore, the specimen became laterally unstable. This was followed by local crushing of some masonry blocks where compression forces exceeded masonry compressive strength. Figure 4-10 illustrates the major cracks and the buckled shape of specimen C2 after instability had occurred while Figure 4-11 shows a photo of the buckled shape. Figure 4-12 illustrates the location of the masonry crushing near the top of the specimen (18th masonry course from the bottom) after the specimen had already become laterally unstable.

Table 4-2 summarizes the important observations made during the testing of specimen C2.

**Table 4-2 Experimental observations for specimen C2**

Loading Cycle			Range of crack widths (mm)	Maximum out-of-plane displacement (mm)	Key Observations
1	T	$\Delta=0.5\Delta_y$ =5mm P=222 kN	0.2-0.3	0	Uniformly distributed horizontal cracks formed at most bed joints along the specimen height. A few horizontal cracks were discontinuous; for example, a crack developed above the mortar bed joint and then shifted below the bed joint
	C	P=-645 kN	0	0	All cracks fully closed and the specimen restored to its original vertical alignment
2	T	$\Delta=\Delta_y$ =9.5mm P=427kN	0.3-0.5	0	A larger crack developed at the bed joint between the bottom first and second course (0.75 mm width), and a 2 mm gap developed at the interface of the top masonry course and the specimen plate on the north face.
	C	P=-40 kN	0-0.5	1.5 (east) at midheight	Most cracks closed, except for a large crack which with a width that decreased from 0.75 mm to 0.5 mm
		P=-716 kN	0	0	All cracks fully closed and specimen restored to its original vertical alignment
3	T	$\Delta=1.5\Delta_y$ =15mm P=437 kN	0.5-0.75	0.7	Horizontal cracks formed at each bed joint
	C	P=-91kN	0-0.4	7 (east) at $\frac{3}{4}$ from the base of the wall	Lateral displacement was observed shortly after the compression load was applied, but the cracks closed at one end, and the specimen began to resist compression..
		P=-800 kN	0	0	One crack between the first and second course at the bottom of the specimen remained open, but its width decreased.
4	T	$\Delta=2.0\Delta_y=20$ mm P=445kN	0.75-1.0	5 (west) at midheight	Very small cracks appeared along head joints near the top of the specimen.
	C	P=-79 kN	0-0.5	29.3 (east) at midheight	The specimen began to show out-of-plane displacements towards east at low compressive loads; this trend continued at a slower rate after the cracks began to close.
		P=-693 kN	0	0	After the compression load was reduced to zero, horizontal cracks opened again and the specimen experienced 11 mm of eastward out-of-plane displacements.
5	T	$\Delta=3.0\Delta_y$ P=450kN	1-1.5	5.5 at midheight	A few new cracks developed along vertical head joints in the tension cycle and the width of the existing cracks increased to about 0.2 mm.
	C	P=-60kN	0.5-0.75	65.5 (east) at midheight	The specimen started to experienced out-of-plane displacements towards east at low compressive loads, and these lateral displacements were maintained (although the magnitude decreased) after the cracks began to close at one face.
		P=-700 kN	0	3.2 at midheight	At the end of the compression cycle, the specimen almost restored its original vertical alignment, however upon unloading it experienced westward out-of-plane displacements on the order of 20 mm before it re-aligned again during the tension load cycle.
6	T	$\Delta=4.0\Delta_y$ P=454 kN	2	6.5 at midheight	During the tension cycle, the specimen was not able to fully restore its vertical alignment. However, the maximum out-of-plane displacement was relatively small at the end of the tension cycle.
	C	P=-44 kN	1.5-2	100 (east) at midheight	The specimen started to move out-of-plane towards east at low compressive loads.
		P=-250 kN		120 (east) at midheight	The specimen became unstable in compression as the horizontal cracks failed to close completely, and out-of-plane displacements continued to increase in compression until the specimen crushed at the edge of the rotated crack at the east bed joint of the second masonry course from the top.

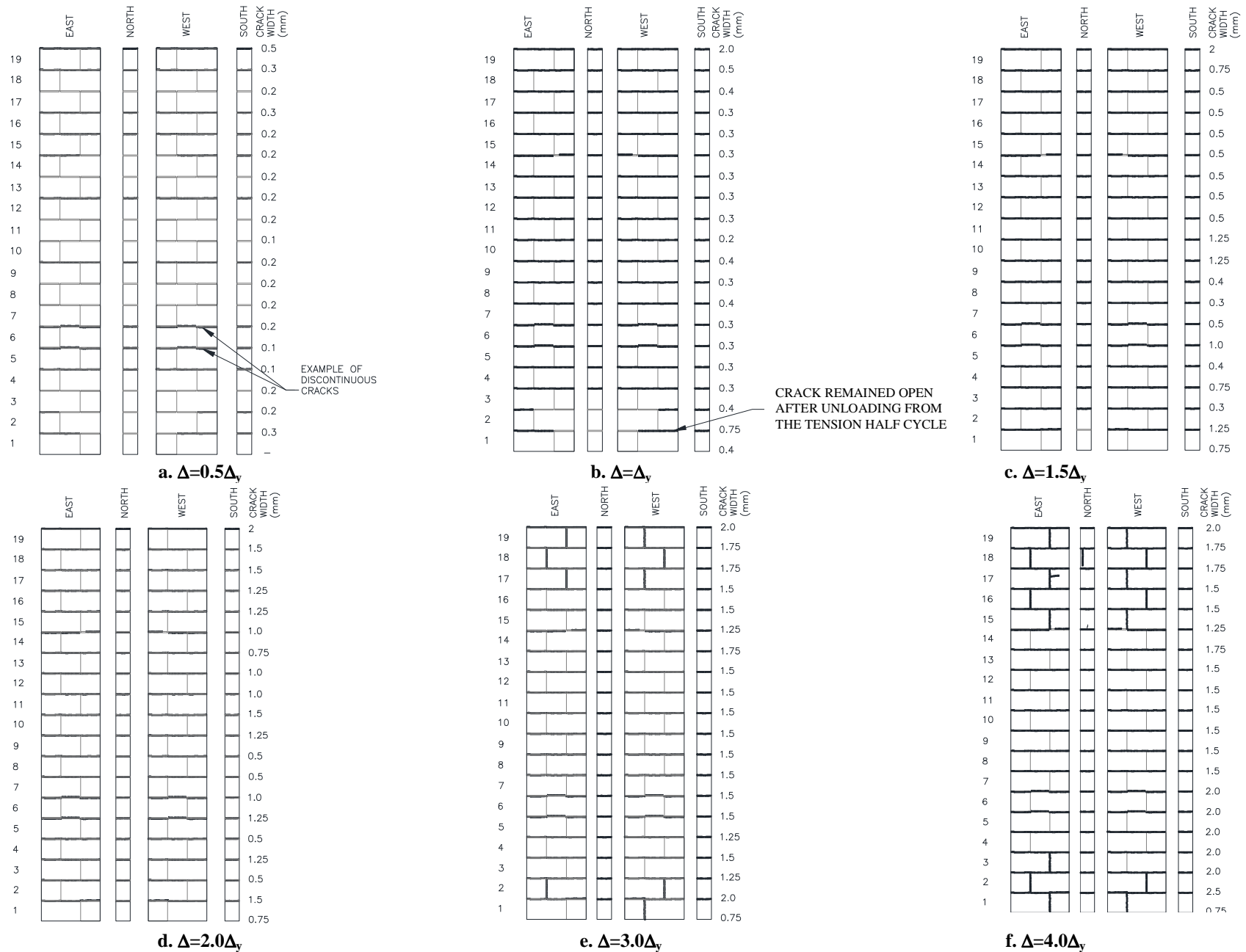


**Figure 4-9 Crack patterns for specimen C2 at increasing levels of tension displacements**

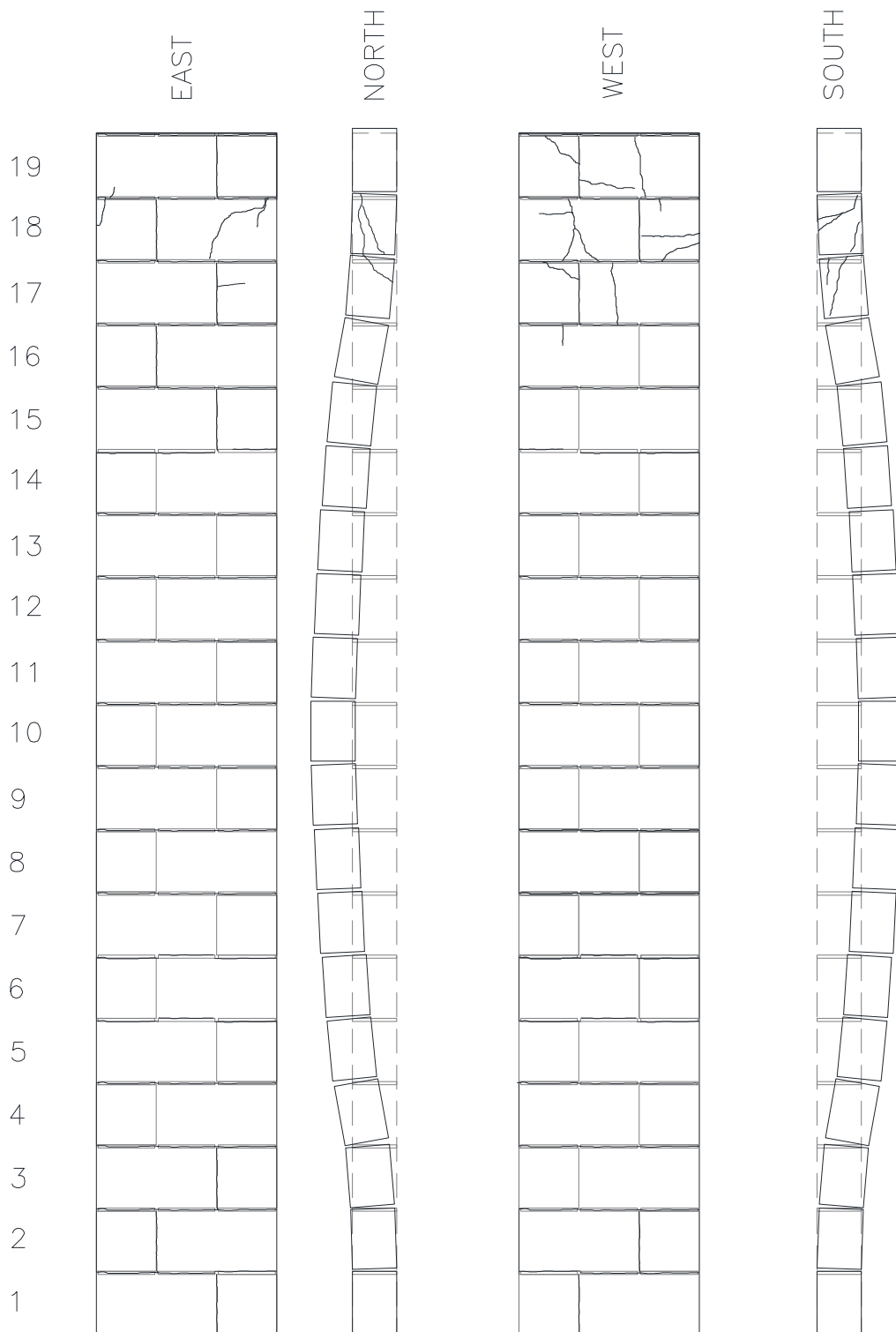


**Figure 4-10 Specimen C2 at failure**



**Figure 4-11 Specimen C2 at the end of the test, after experiencing out-of-plane instability**

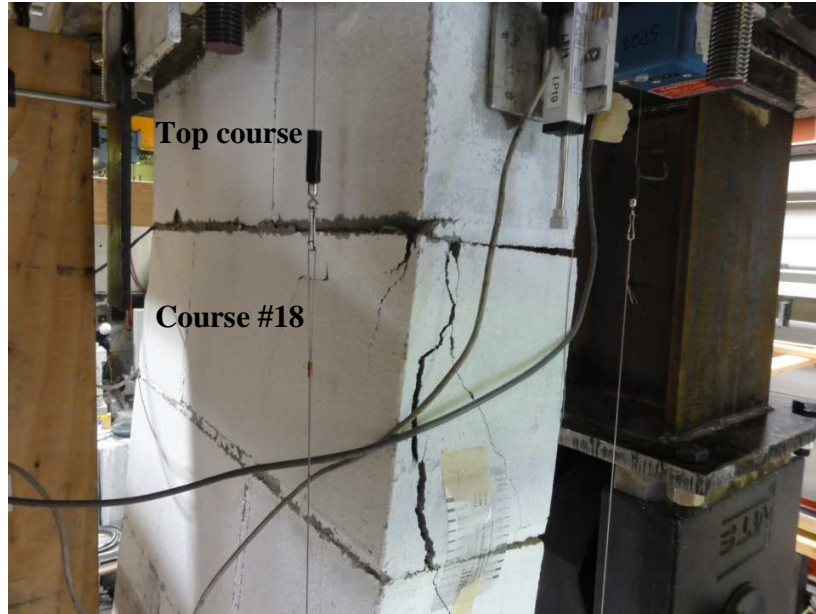


Figure 4-12 Local crushing of the masonry face shell at the top of specimen C2 after experiencing out-of-plane instability

Figure 4-14 shows the hysteretic plot of axial load vs. total axial deformation for specimen C2. As can be seen from Figure 4-14, the plateau **b-d** shown in Figure 4-7, which corresponds to the period during which the specimen is experiencing out-of-plane displacements, gets larger with increasing tensile strain levels. The increasing lateral displacements are indicated on the plot of axial load vs. lateral deformation in Figure 4-15. Figure 4-13 also shows the buckled shape of the specimen during the cycle corresponding to a tensile strain of 0.8%.

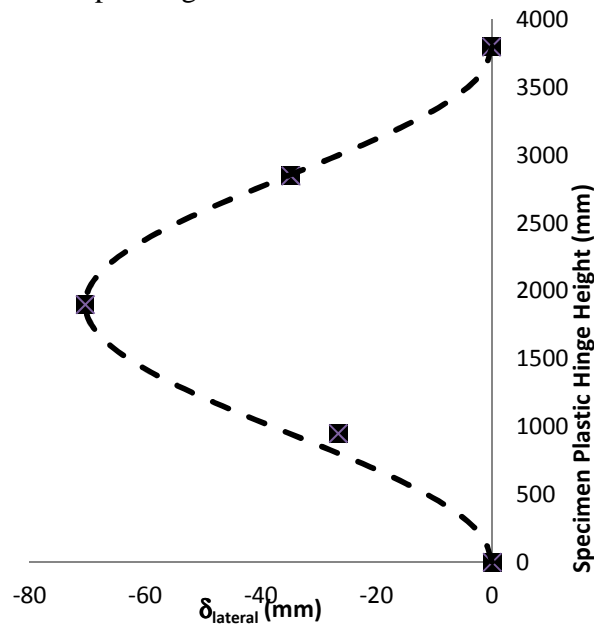


Figure 4-13 Buckled shape of specimen C2 during the cycle of  $\epsilon_t=0.8\%$

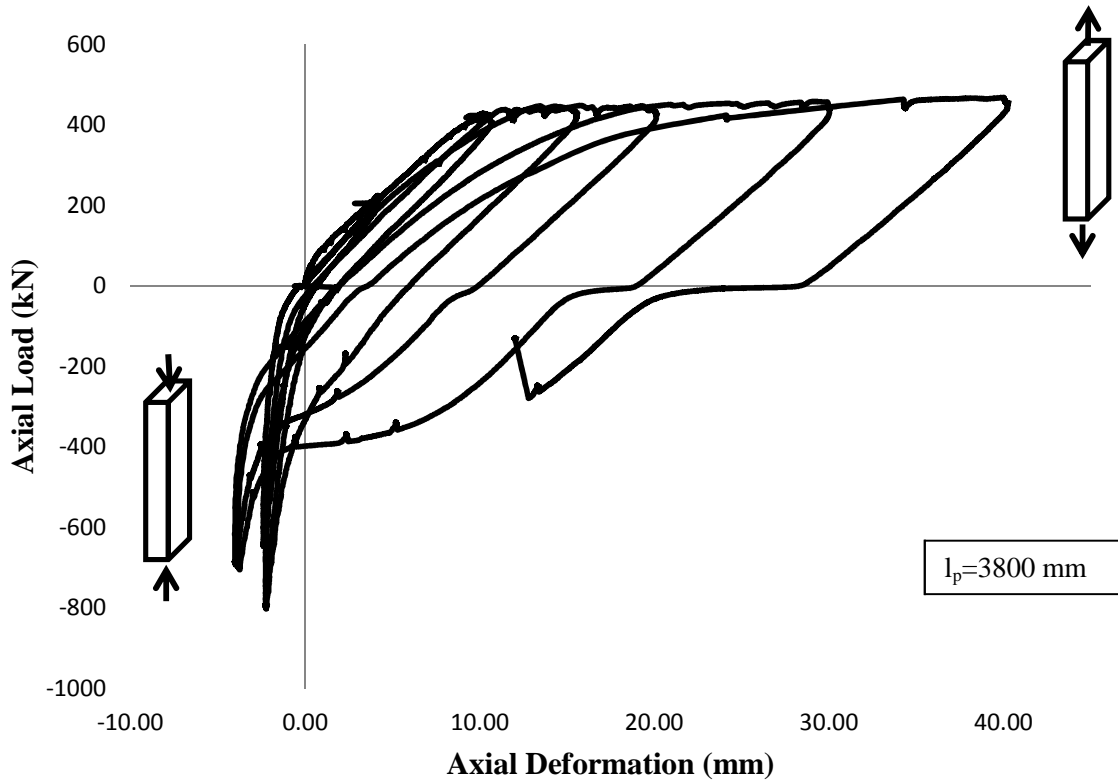


Figure 4-14 Axial load versus axial deformation response for specimen C2.

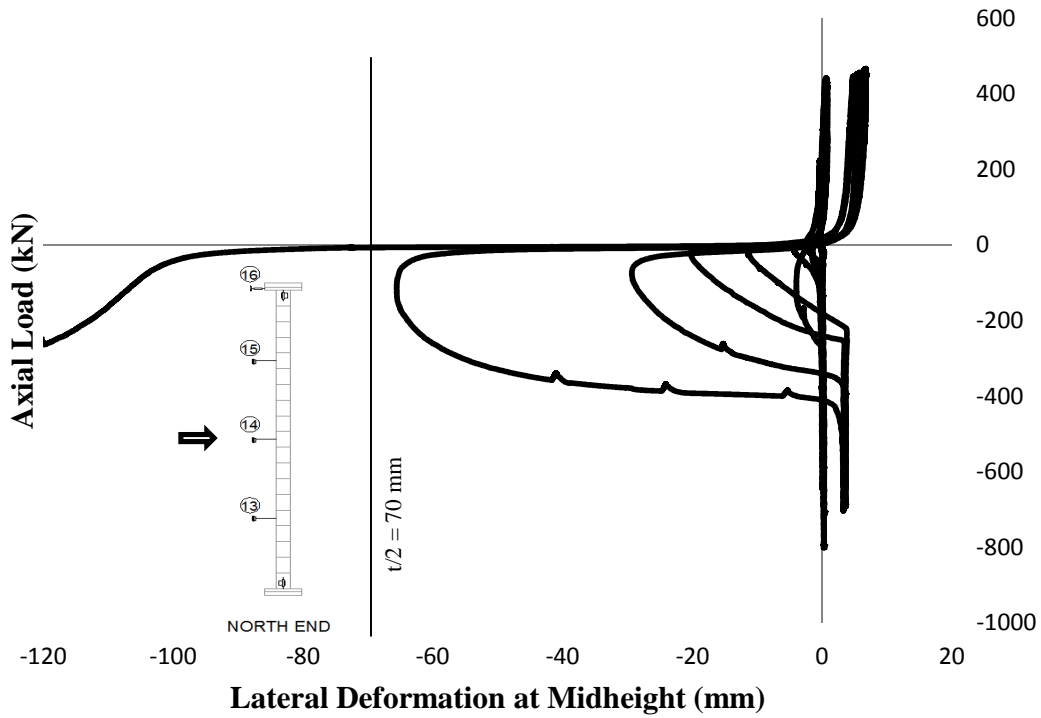
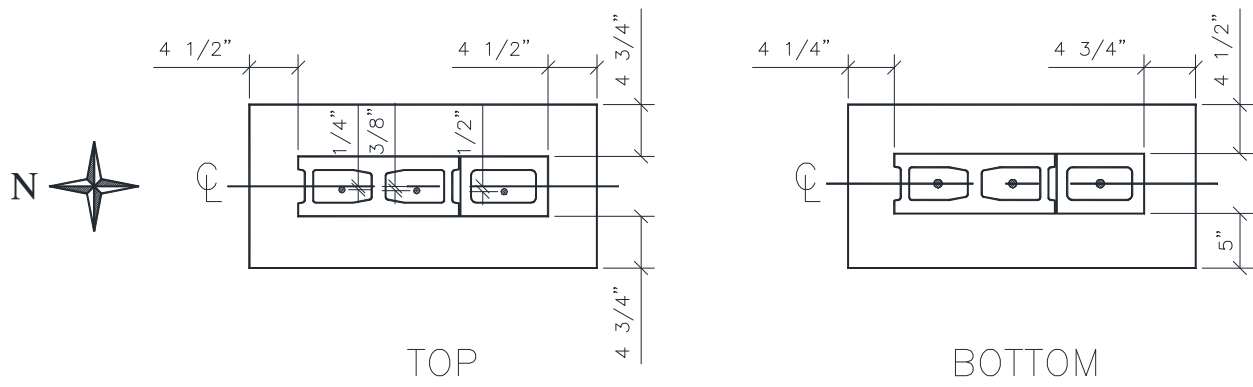


Figure 4-15 Axial load versus lateral deformation at mid-height of specimen C2

### 4.2.3 Specimen C3

Specimen C3 was reinforced with 3-15M bars (one in each core); this corresponds to a reinforcement ratio of 0.73%. As with specimen C2, it was noted after the construction that the masonry blocks were not laid perfectly centered on the specimen plate at the bottom, and also the reinforcing bars had moved off-centre at the top after the grout was poured. Figure 4-16 shows the plan view of the specimen and reinforcement layout in relation to the top and bottom specimen plates.



**Figure 4-16 Specimen C3 cross-section and reinforcement layout relative to top and bottom specimen plates**

However, the modifications made previously to the attachment at the top floating beam allowed the specimen connection which ensured that loads were evenly applied from actuators. As a result, the specimen was aligned in vertical position after it was put in place, and the chances for developing P- $\Delta$  effects were minimized.

Originally, it was intended that the only difference between specimens C2 and C3 and be their reinforcement ratios. However, this was not possible due to problems with the welding connection of reinforcement at the top of the specimen. During the first test run, the reinforcing bars disconnected from the top specimen plate at relatively low tensile strain levels. This transpired through the development of significant vertical splitting cracks in the top three masonry courses, as shown in Figure 4-17. This occurred before the specimen even reached the expected yield tensile capacity of reinforcement. These vertical cracks indicated that the reinforcement had detached from the top specimen plate at different times and had caused rotation about the specimen's weak axis at the top. The testing had to be discontinued at early tension cycles.

Subsequently, the top half of the specimen was stiffened using Glass Fiber-Reinforced Polymer (GFRP) overlay. The reinforcing bars at the top were grinded smooth and re-welded to ensure an effective connection to the top plate according to the original design. The retrofit design and construction were discussed in Sections 3.2.1 and 3.2.2 respectively.



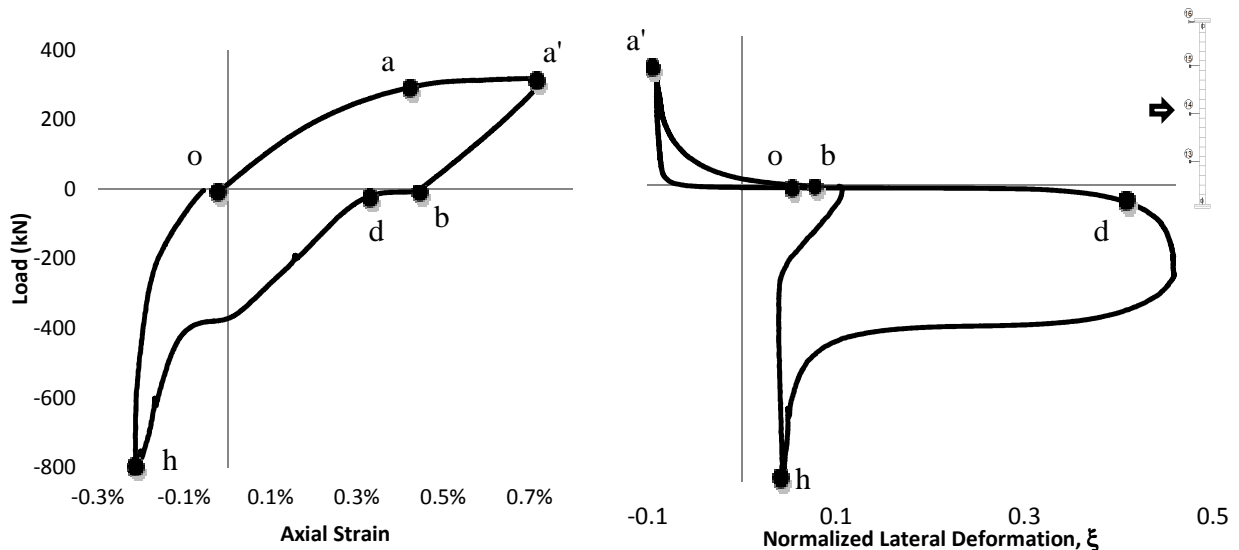
a. West face



b. East face

**Figure 4-17 The splitting cracks at the top three courses of specimen C3 before retrofitting**

As can be seen from the plots of applied axial load vs. axial strain and axial load vs. maximum lateral deformation (normalized by specimen thickness) shown in Figure 4-18, the response of specimen C3 during a typical loading cycle was very similar to that of specimen C2.



**a.** Applied axial load vs. axial strain over the plastic hinge region

**b.** Applied axial load vs. maximum lateral deformation at midheight normalized with respect to thickness

- o: Beginning of cycle in tension
- a: Yielding of reinforcement
- a': Peak of tension half cycle (uniformly distributed horizontal cracks along the height)
- b: Beginning of compression half cycle (most horizontal cracks remain open but are reduced in size)
- c: Most out-of-plane instability has already occurred
- h: Peak of compression half cycle (the specimen has restored its original vertical alignment and all horizontal cracks are closed)

**Figure 4-18 Plot of a. applied axial load vs. axial strain over the plastic hinge region and b. applied axial load vs. maximum normalized lateral deformation at midheight at  $\epsilon_t=0.8\%$**

In a similar fashion to specimen C2, specimen C3 formed horizontal cracks along the bed joints during tension portion of each cycle as shown in Figure 4-19. The crack pattern at the peak of each tension half cycle is shown in Figure 4-28.



**Figure 4-19** Horizontal cracks developed along all bed joints in the last tension cycle in specimen C3

In the subsequent compression portion of each loading cycle (except for the last cycle), these horizontal cracks eventually closed and the specimen was subjected to pure axial compression.

It must be noted that the GFRP was applied to the specimen in its damaged state and horizontal cracks were not completely closed at the time of the retrofit. As a result, vertical GFRP strips crossing these cracks would crush during the compression load cycles when the cracks in the retrofitted portion would begin to close as shown in Figure 4-20. Although the GFRP application increased the stiffness of the retrofitted portion, the retrofit was not fully effective in restricting the tensile cracking to the bottom half of the wall, which was the objective. Also, although the top half of the wall acted essentially as a rigid link, it experienced slight bending due to the presence of open cracks. These observations are unique to specimen C3, that is, they do not apply to specimens C4 and C5 which were stiffened in the same manner.



**Figure 4-20** Open cracks underneath the GFRP overlay led to crushing of the overlay under compression loads (specimen C3)

As in the case of specimen C2, out-of-plane displacements in the specimen lead to rotation of open cracks along bedjoints as shown in Figure 4-21. At higher tensile strain levels, the specimen experienced an increase in out-of-plane displacements prior to full crack closure. Figure 4-25 shows the hysteretic plot of axial load vs. total axial deformation for specimen C3. As can be seen from Figure 4-25, the plateau **b-d** shown in Figure 4-18, which corresponds to the period during which the specimen is experiencing out-of-plane displacements, gets larger with increasing tensile strain levels. This is better indicated on the plot of axial load vs. lateral deformation in Figure 4-26.

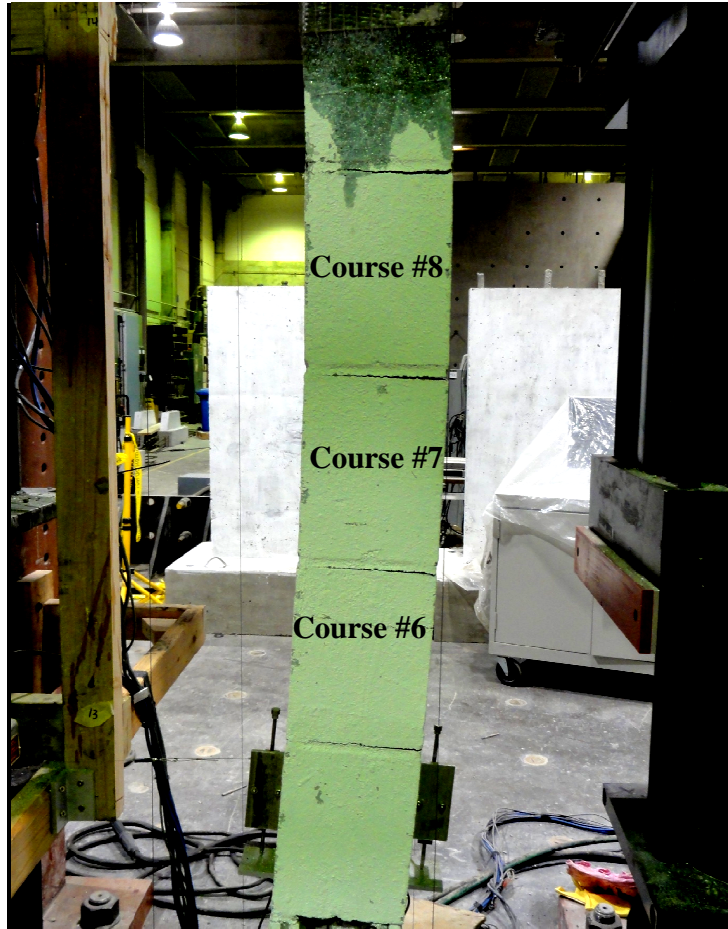


**Figure 4-21** Rotation of the open cracks at bed joints at low compression loads during the compression half-cycle (specimen C3)

As mentioned previously, the application of GFRP was not fully effective in restricting tensile cracking to the lower half of the specimen. Therefore, out-of-plane displacements were observed along the entire height of the specimen during testing. However, the deformed shape along the top half was different from that of the bottom half; the top half exhibited a deformed shape corresponding to a combination of rotation of a rigid link and slight out-of-plane buckling while the lower half exhibited pure out-of-plane buckling. This is illustrated in Figure 4-22. In this way, the maximum out-of-plane displacements were visibly occurring at the bedjoint between the 7th and 8th masonry course from the bottom. However, the instrumentation did not measure the lateral displacement at this location. Therefore, the maximum measured out-of-displacements were generally at midheight.

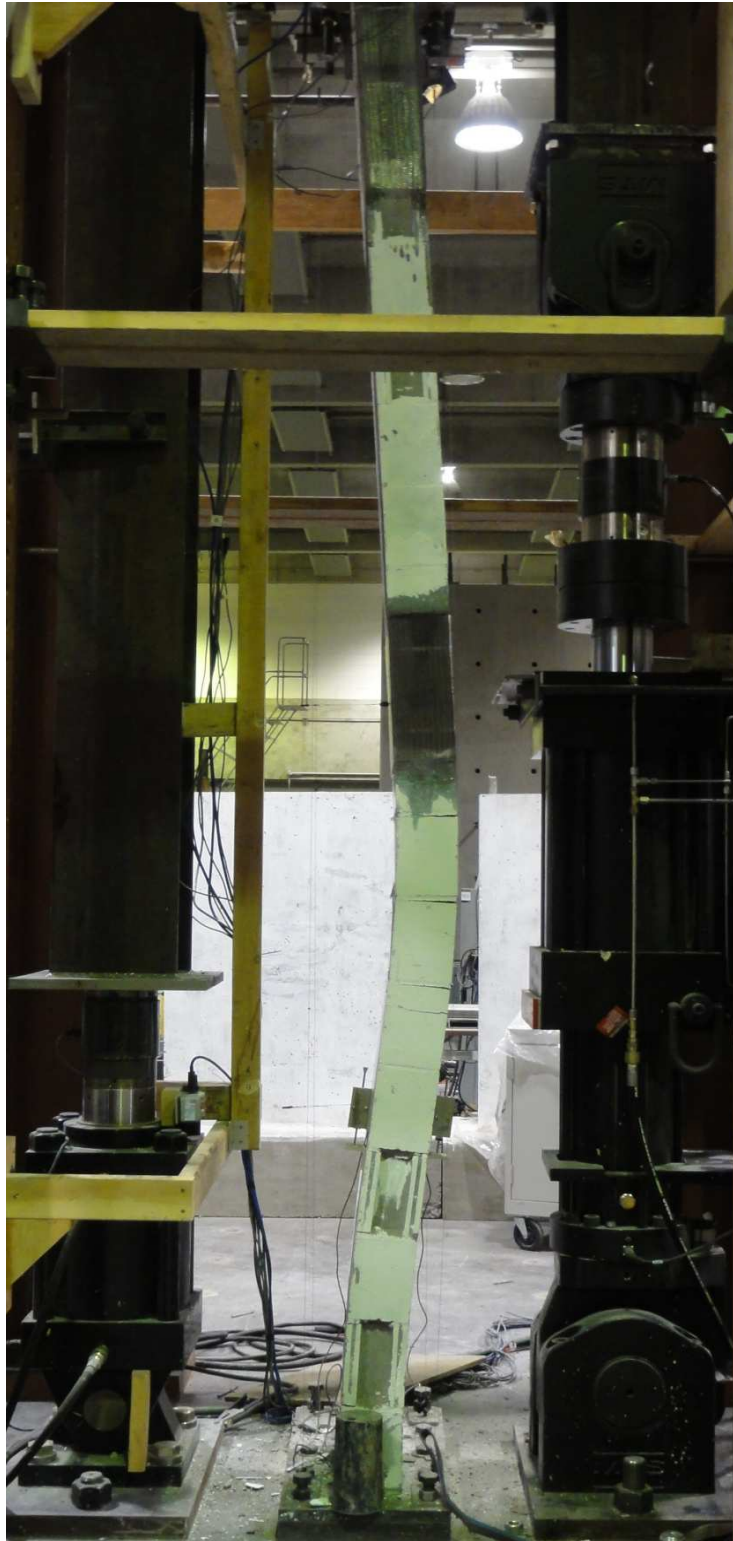


**Figure 4-22 Specimen C3 at the end of the test, after experiencing out-of-plane instability**

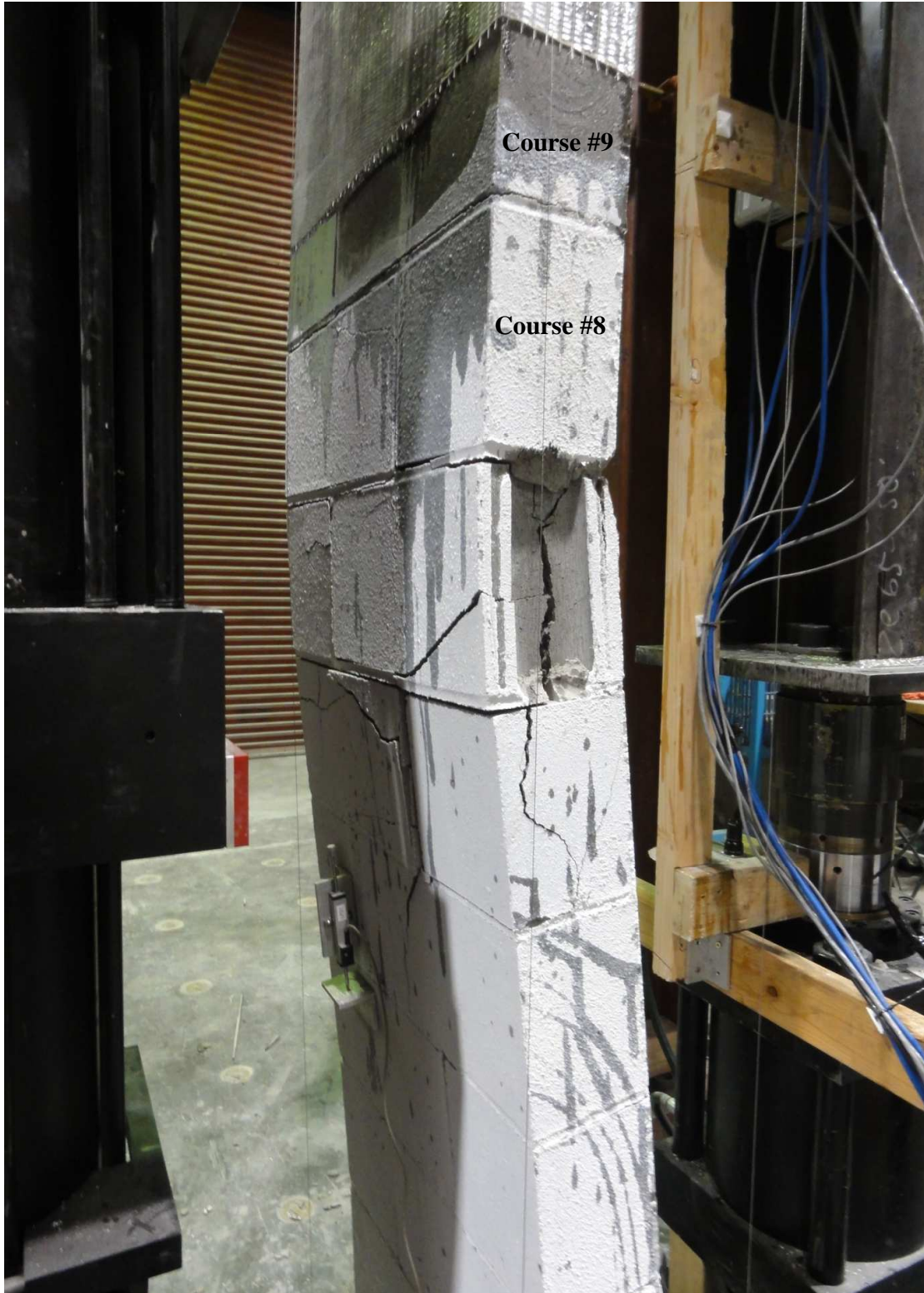


**Figure 4-23** Local crushing of specimen C3 at the compression face where crack closed after the specimen had become laterally unstable

Overall, as long as out-of-plane displacements were less than half of the wall thickness, horizontal cracks along the bed joints closed under compression loading. The specimen was able to restore its original vertical alignment, and resist compression loads without experiencing lateral instability. However, during the last compression cycle, the specimen experienced out-of-plane displacements greater than half its thickness and eventually became unstable. The failure occurred by lateral instability over the full specimen height as shown in Figure 4-22. This lateral instability eventually led to local crushing below the location of the maximum out-of-plane displacement (at the seventh masonry course from the bottom) as shown in Figure 4-23. Figure 4-24 illustrates the buckled shape of specimen during the load cycle corresponding to tensile strain of 0.8%.

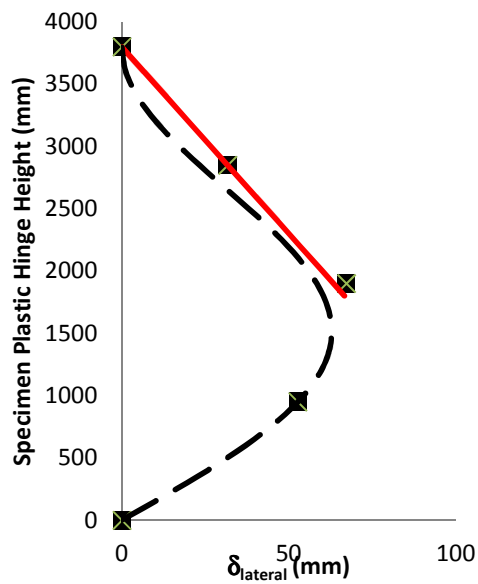


**Figure 4-24** Buckled shape of specimen C3, during load cycle  $\epsilon_t=0.8\%$

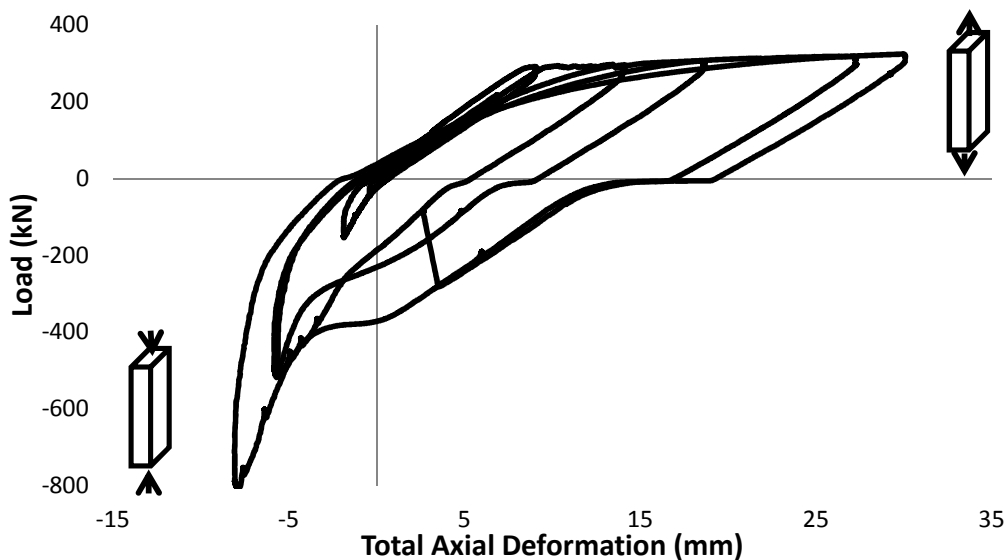


**Figure 4-25** Axial load versus axial deformation for specimen C3

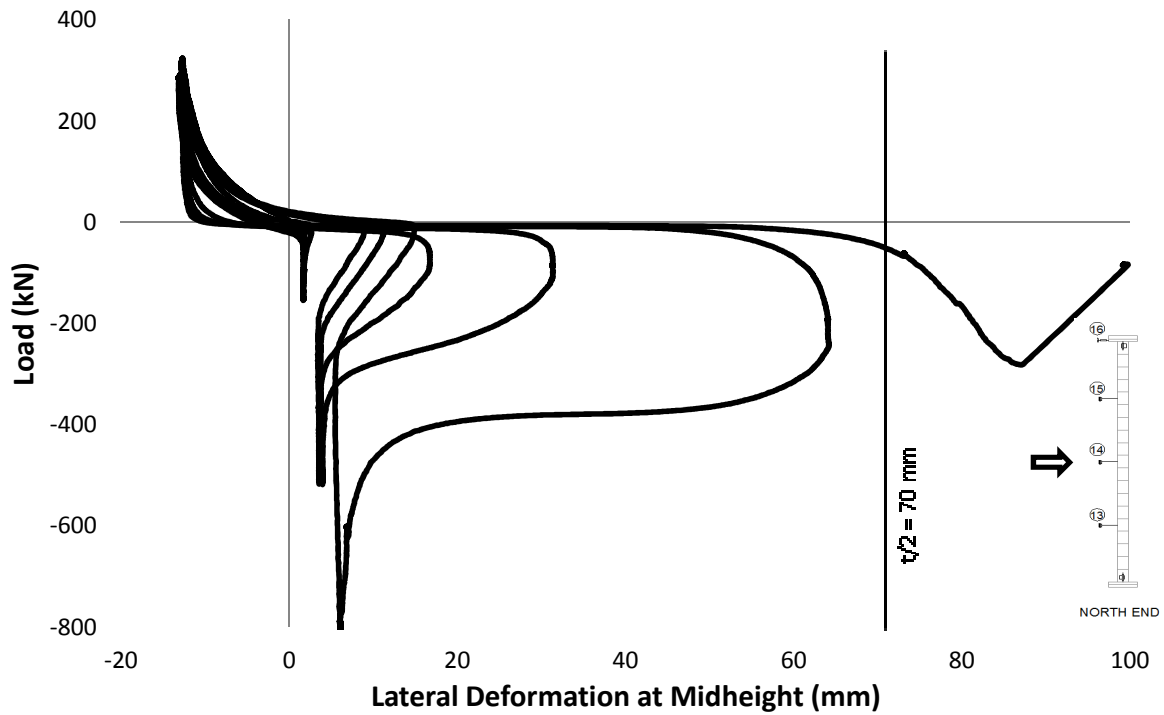


Figure 4-26 Axial load versus lateral deformation at mid-height for specimen C3

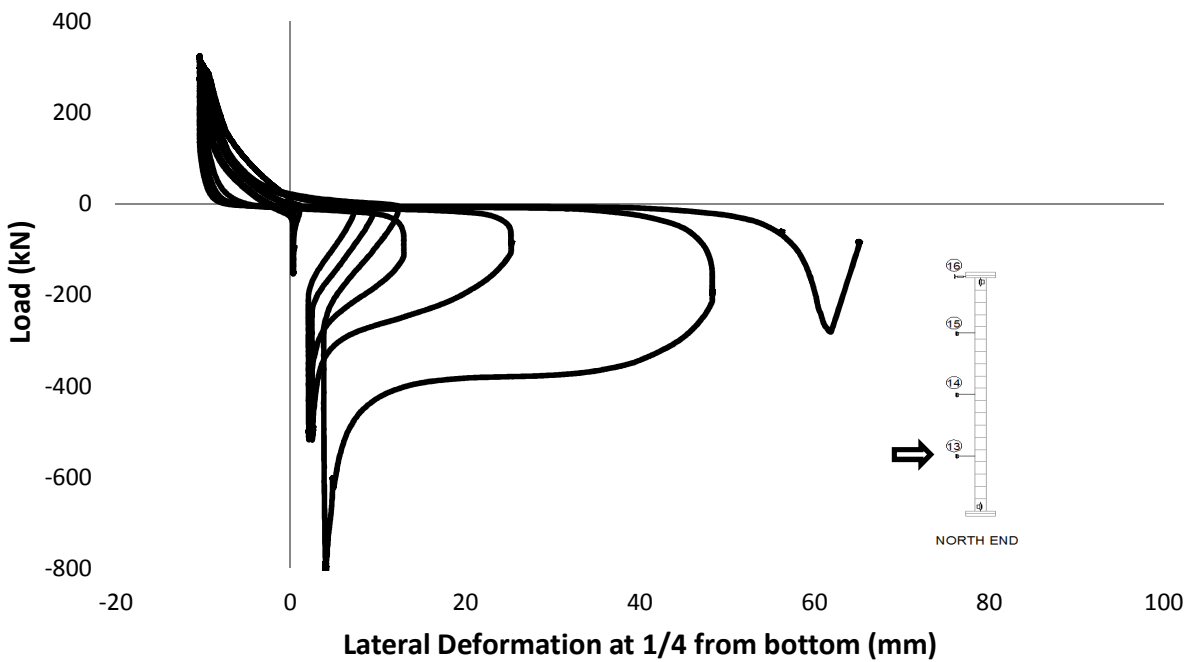


Figure 4-27 Axial load versus lateral deformation at  $\frac{1}{4}$  from the bottom for specimen C3

Table 4-3 summarizes major observations during the testing of specimen C3.

**Table 4-3 Experimental observations for specimen C3**

Loading Cycle		Range of crack widths (mm)	Maximum out-of-plane displacement (mm)	Key Observations	
1	T	$\Delta=0.68\Delta_y$ =6.8mm P=218 kN	0.3-0.5	17.2 (east) at midheight	Cracks seemed to be more concentrated in the lower portion of the specimen, although a few cracks were observed in the retrofitted portion as well. Some cracks were discontinuous along the bed joint. A 1 mm gap between the top of the specimen and the steel plate was observed. The out-of-plane displacement in the tension cycle was related to the reinforcement inside the specimen straightening out.
	C	P=-151 kN	0	0	All cracks fully closed and the specimen restored original vertical alignment.
2	T	$\Delta=\Delta_y$ =9.1mm P=291kN	0.4-0.75	17.5 (east) at midheight	Most cracks in the lower half increased in size, while the open cracks in the upper retrofitted portion remained unchanged. Larger cracks at the two successive bed joints immediately below the retrofitted portion had a width of 1.0 mm and 0.75 mm respectively. The gap between the top of the specimen and the steel plate increased to 1.5 mm.
		P=-50 kN	0	0	All cracks fully closed and specimen restored its original vertical alignment.
3	T	$\Delta=1.5\Delta_y$ =14.8mm P=293 kN	0.5-0.75	17.9 (east)	All crack widths increased in the lower portion of the specimen. An average crack width in the bottom portion was 1.0 mm while the crack size in the retrofitted the top portion was much smaller (0.4 mm width). The two larger cracks immediately below the retrofitted half increased to 1.25 mm in width
		P=-41kN	0-0.4	16.4 (west) at midheight	The specimen began to move out-of-plane at a compressive load of -7 kN. As the compressive load increased to approximately -19kN, the cracks on the east face began to close, but the specimen continued to move out-of-plane. At a load close to -88 kN, the specimen began to restore its vertical alignment. At the end of the compression half-cycle, all cracks fully closed and specimen restored its original alignment. When the specimen was unloaded after the compression half-cycle, the cracks re-opened and the specimen momentarily experienced out-of-plane displacement in the westward direction of 4 mm at approximately the same load at which maximum out-of-plane displacements had previously occurred.
	C	P=-518 kN	0	0	
4	T	$\Delta=2.0\Delta_y$ =19.2mm P=307kN	0.75-1.25	18 (east) at midheight	Very small cracks developed along head joints near the top of the specimen. The gap at the top increased to 2.0 mm at the north end and 3.0 mm at the south end. A few minor vertical cracks were noticed along the specimen thickness and along some head joints.
		P=-54 kN	0-0.5	31 (west) at midheight	The specimen began to move out-of-plane at a compressive load of -8.75 kN. At a compressive load close to -19kN, the cracks began to close on the east face, but the specimen continued to move out-of-plane. At a load close to -246 kN, the specimen began to restore its straightness. At the end of the compression cycle, when the specimen was unloaded, the horizontal cracks re-opened and the specimen momentarily experienced 6.3 mm of westward out-of-plane displacement at around the same load at which maximum out-of-plane displacements had occurred previously
	C	P=-512 kN	0	0	

Loading Cycle		Range of crack widths (mm)	Maximum out-of-plane displacement (mm)	Key Observations	
5	T	$\Delta=3.0\Delta_y$ =27.5mm P=318kN	1.0-4.0	18 (east) at midheight	More cracks in head joints developed during the tension cycle, and the size of existing cracks increased to about 0.2 mm width. Horizontal cracks developed at mid-course away from the bed joints. Gap at the top increased to 3 mm both at the south and north faces.
	C	P=-110kN  P=-819 kN	0.5-0.75  0	64 (west) at midheight  1.5 (west) at ¾ from the base of the wall	The specimen began to move out-of-plane at a compressive load of 7.15 kN. The cracks began to close on the east face t at a compressive load close to 21 kN, . At a load close to -246 kN, the specimen began to restore its vertical alignment. Compression yielding of reinforcement was observed at a compressive load of -370 kN. All cracks fully closed at a load of -400 kN, and the specimen almost restored its original vertical alignment. During the unloading from the compression half-cycle, the specimen experienced out-of-plane displacements in the westward direction; the displacement at the midheight was on the order of 9.55 mm corresponding to the compressive load of -35kN.
6	T	$\Delta=3.2\Delta_y$ =30.8mm P=324 kN	2.0-5.0	18 (east) at midheight	New vertical cracks developed along head joints and split some blocks in half along the specimen thickness, while the width of the existing cracks increased to about 1.0 mm. More horizontal cracks developed away from the bed joints in the bottom half of the wall. Gap at the top increased to 4 mm at the south face and 2 mm at the north face.
	C	P=-280 kN	1.5-2	80.9 (west) at midheight	The specimen began to move out-of-plane at a compressive load of -6 kN. When the compression load increased to -15 kN, the cracks began to close at one end, however the specimen continued to move outwards. The specimen became unstable in compression when the horizontal cracks failed to fully close, and out-of-plane displacements continued to increase in compression until the specimen crushed locally near midheight.

Figure 4-28 shows crack patterns along the height of the specimen at the peak of the tension half-cycle. It can be seen from the figure that the crack width in the lower half of the specimen increased with increasing tensile deformations, while the crack width in the top half remained more-or-less unchanged. It was also observed that the cracks became more uniform in size at increasing tensile deformations. During the later cycles, horizontal cracks started to develop away from the bed joints while vertical cracks appeared at head joints.

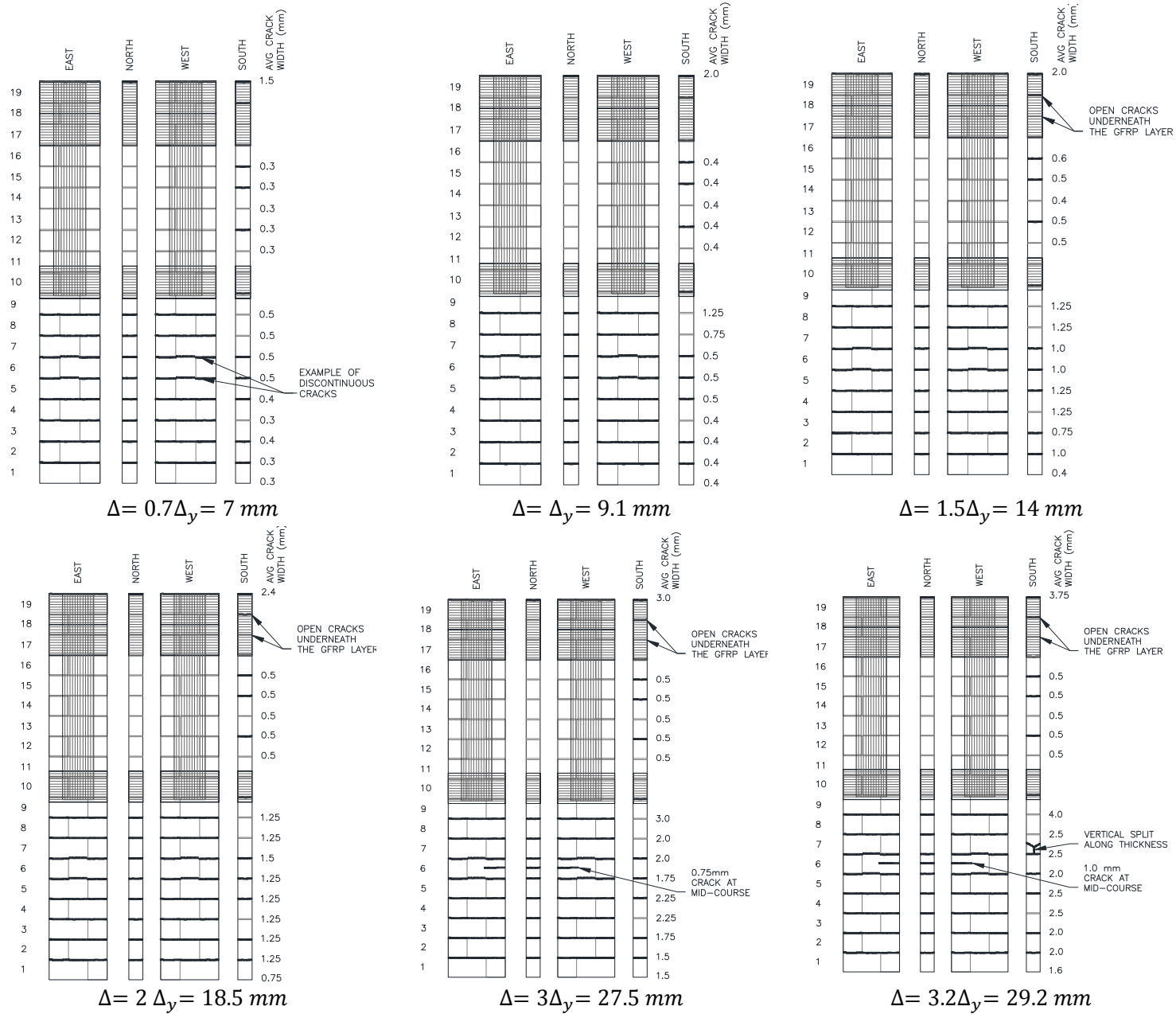
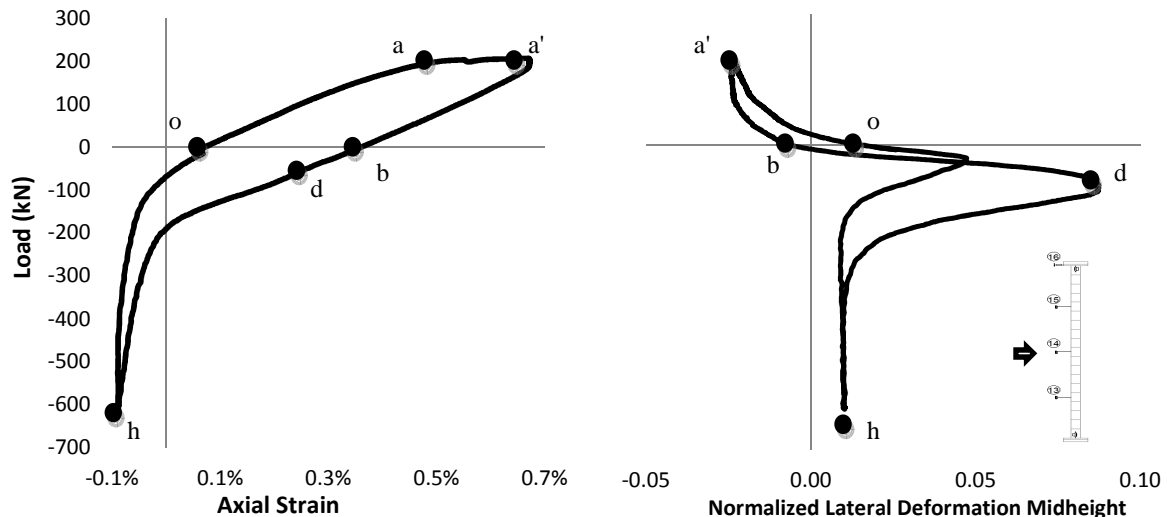


Figure 4-28 Crack patterns at increasing tension displacements for specimen C3

#### 4.2.4 Specimen C4

Specimen C4 was reinforced with 2-15M bars placed in the end cores, corresponding to a reinforcement ratio of 0.5%. The top half of this specimen was also stiffened with GFRP overlay in the same manner as specimen C3. This was done to force plastic deformations to the bottom half of the specimen, thereby effectively reducing the height of the plastic hinge. This would provide insight into the effect of plastic hinge height on out-of-plane deformations. The reinforcing bars in this specimen were aligned in vertical position, and there was no offset with regards to the centerline (unlike specimens C2 and C3).

Figure 4-29 shows plots of applied axial load vs. axial strain and axial load vs. maximum lateral deformation (normalized by specimen thickness). In general, the response of specimen C4 during a typical loading cycle was very similar to that of specimens C2 and C3. The plots shown in Figure 4-29 correspond to a strain level of about 0.7% in order to allow comparison between the behaviour of specimen C4 with those of specimens C2 and C3.



**a.** Applied axial load vs. axial strain over the plastic hinge region

**b.** Applied axial load vs. maximum lateral deformation at midheight normalized with respect to thickness

- o: Beginning of cycle in tension
- a: Yielding of reinforcement
- a': Peak of tension half cycle (uniformly distributed horizontal cracks along the height)
- b: Beginning of compression half cycle (most horizontal cracks remain open but are reduced in size)
- d: Most out-of-plane instability has already occurred
- h: Peak of compression half cycle (the specimen has restored its original vertical alignment and all horizontal cracks are closed)

**Figure 4-29** Plot of **a.** applied axial load vs. axial strain over the plastic hinge region and **b.** applied axial load vs. maximum normalized lateral deformation at midheight at  $\epsilon_t=0.7\%$

In a similar fashion to that of specimens C2 and C3, horizontal cracks developed along bedjoints during the tension portion of each loading cycle, shown in Figure 4-29 as the path

along points **o** through **b**. The first difference between the specimens C3 and C4 was that almost all tensile cracking in specimen C4 was limited to the bottom half; this was not the case with the specimen C3. Figure 4-30 shows examples of such horizontal cracks. The upper stiffened half of the specimen acted as a rigid link and there were no visible signs of bending. Moreover, since the bottom portion of the specimen experienced tensile cracking, the largest out-of-plane displacements were closer to the first quarter-point (relative to the base of the specimen), as opposed to the midheight point (where the largest lateral displacements were observed in specimens C2 and C3).

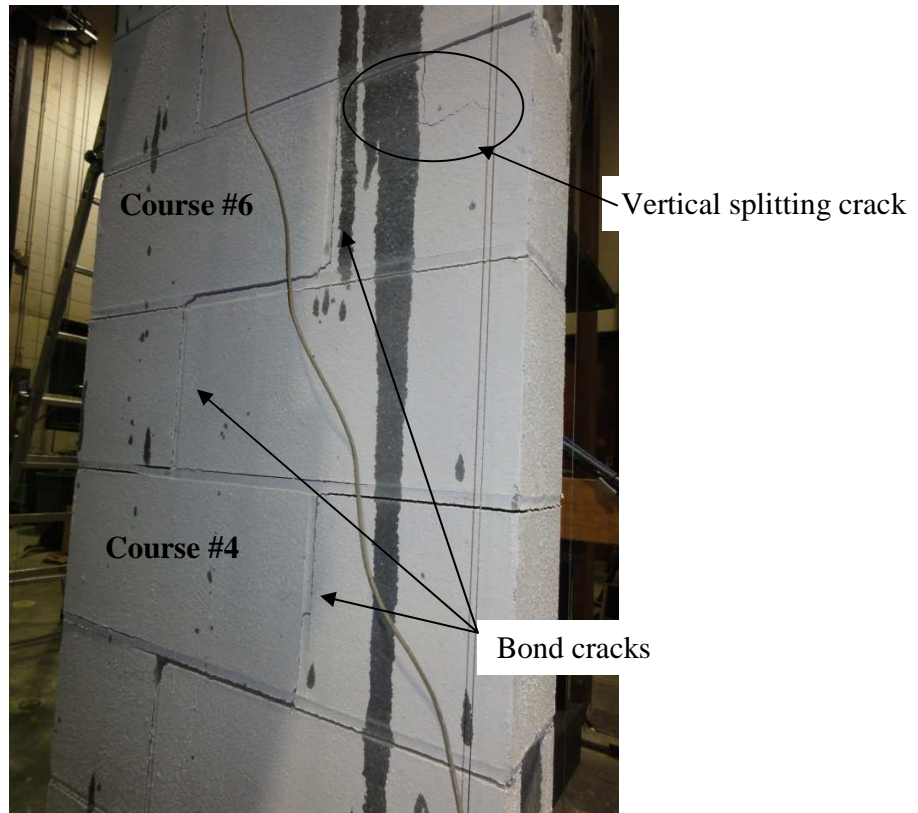


**Figure 4-30 Uniformly distributed horizontal cracks over as well as vertical splitting cracks at tensile strain level equal to 1.3% (specimen C4)**

At the peak of the tension half cycle, identified by point **a'**, the horizontal cracks reached their maximum size. The crack pattern at the peak of each loading cycle is shown in Figure 4-40. Note that the size of the cracks at the bedjoints immediately below the stiffened portion were larger than the rest.

In a similar way to specimens C2 and C3, at the beginning of the compression half cycle, point **b**, most of the horizontal cracks remained open. However, note that at the time of application of a similar level of tensile strain (~0.8%) there was not much of a plateau between points **b** and **d** in specimen C4. Subsequently, the corresponding lateral displacements at this loading cycle were also much less than that experienced by specimens C2 and C3. This leads to the conclusion that lowering the height of plastic hinge, while

keeping the specimen thickness unchanged, will entail larger tensile strains are required to cause lateral instability.

In later loading cycles, as applied tensile strains were increased, the path from point **b** to **d** became more horizontal similar to that shown in Figure 4-7 and Figure 4-18 for specimens C2 and C3 respectively. The out-of-plane displacements during this phase led to rotation of the open cracks as shown in Figure 4-31.

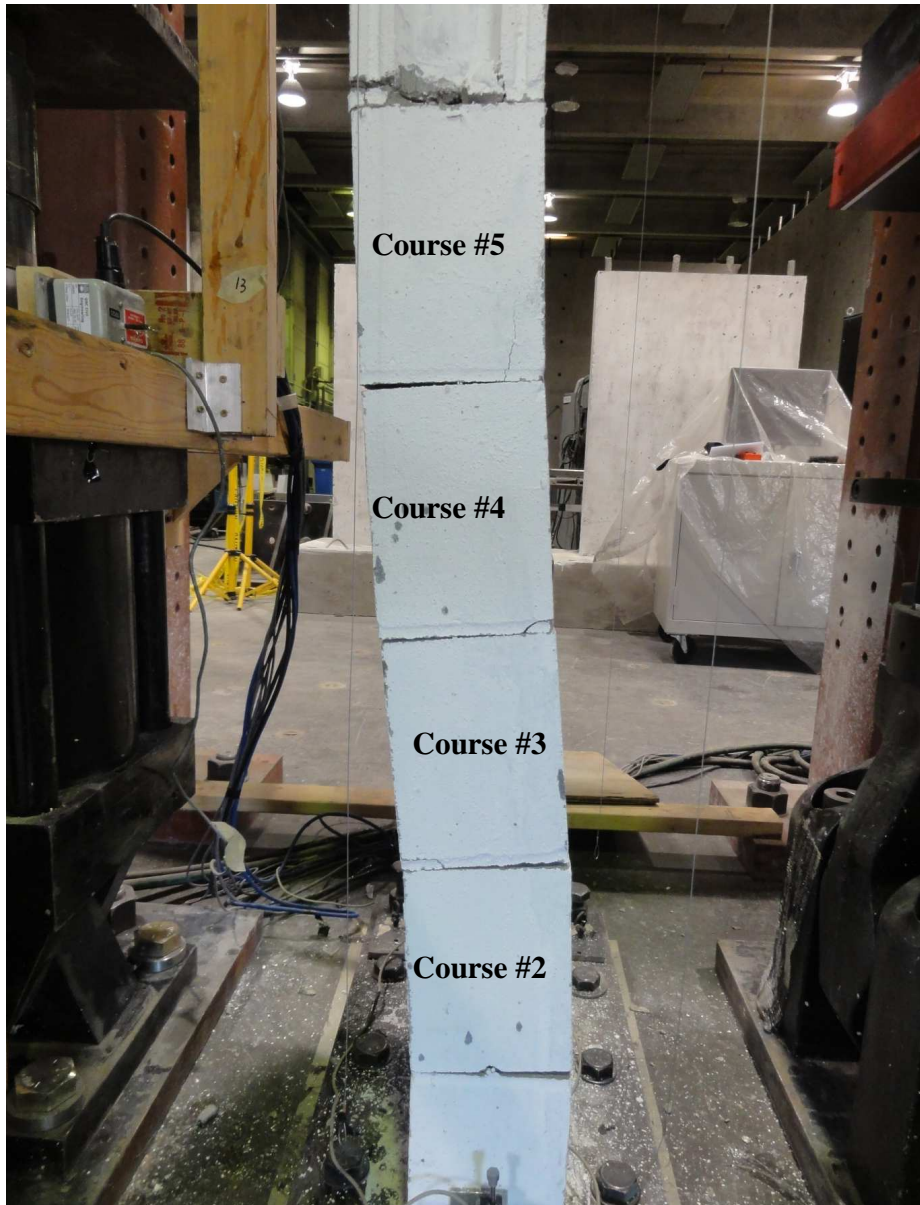


**Figure 4-31** Rotation at the location of open horizontal cracks when specimen C4 experienced lateral displacements (Loading cycle #5)

Another difference in behaviour between specimen C4 and specimens C2 and C3 was in the direction of out-of-plane displacement. Initially, the specimen seemed to bow laterally westward at low compressive loads after unloading from previous tension half-cycle characterized by low axial tensile displacements. As tensile displacement amplitudes increased in subsequent cycles, (ie. after the application of tensile strains larger than 0.75%) the specimen would initially start to move laterally in westward direction after it was subjected to compression, but then its direction of lateral displacement would suddenly shift and it would start to bow in the east direction. This is attributed to two different buckling modes in this specimen. From the crack patterns shown in Figure 4-40, it can be seen that the horizontal crack above the 8th masonry course (approximately at midheight) was much larger than the remainder of the cracks. Therefore, it is speculated that there was a plastic hinge formed at this point which led to the second buckling mode as shown in Figure 4-32c with increased compressive forces.

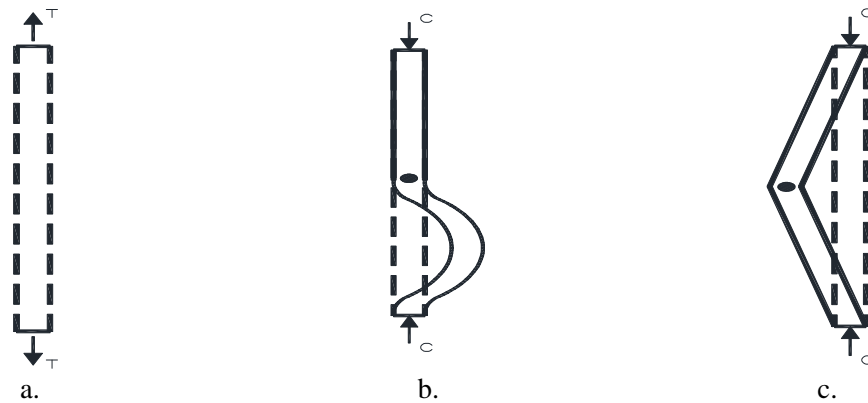


**Figure 4-32 a. Specimen in tension, b. first mode of buckling, c. second mode of buckling**

Figure 4-33 illustrates the actual buckled shape of specimen C4 during loading cycle corresponding to tensile strain of 1.7%.

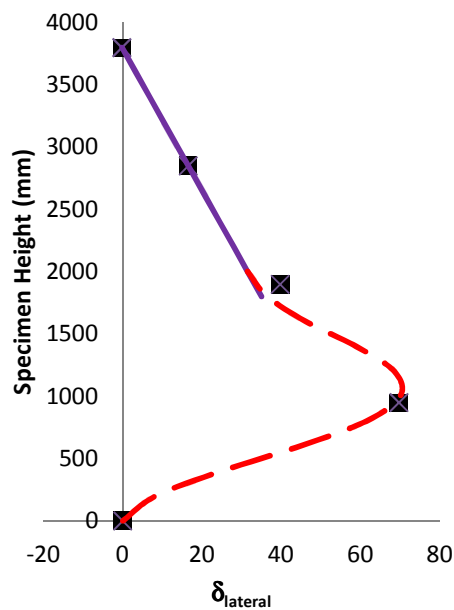


**Figure 4-33 Buckled shape of specimen C4 during the load cycle  $\epsilon_t=1.7\%$**

As a result of the changing directions in the buckled shape of specimen C4, relatively large tensile displacements (compared to specimens C2 and C3) were required to cause critical lateral displacements and instability in this specimen. This is shown in the plots of axial load vs. out-of-plane displacement for specimen midheight and lower quarter point in Figure 4-35 and Figure 4-36 respectively.

Also, note that for the first four cycles of loading, the maximum out-of-plane displacement was measured at the specimen midheight rather than at the lower quarter point. This is because during the first few cycles, the rotation of the rigid link over the top half of the specimen exceeded the out-of-plane displacements experienced over the plastic hinge. As in the case of specimen C2 and C3, the onset of out-of-plane displacement occurred at low compression loads.

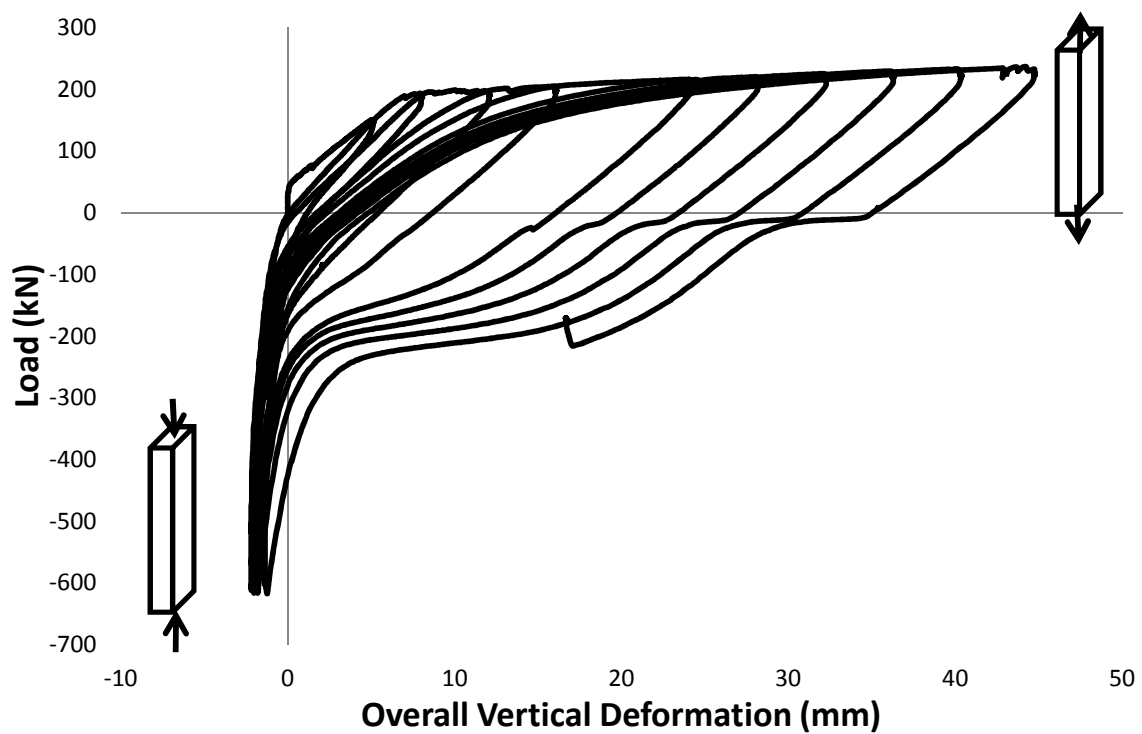


**Figure 4-34** Axial load versus overall axial deformation for specimen C4

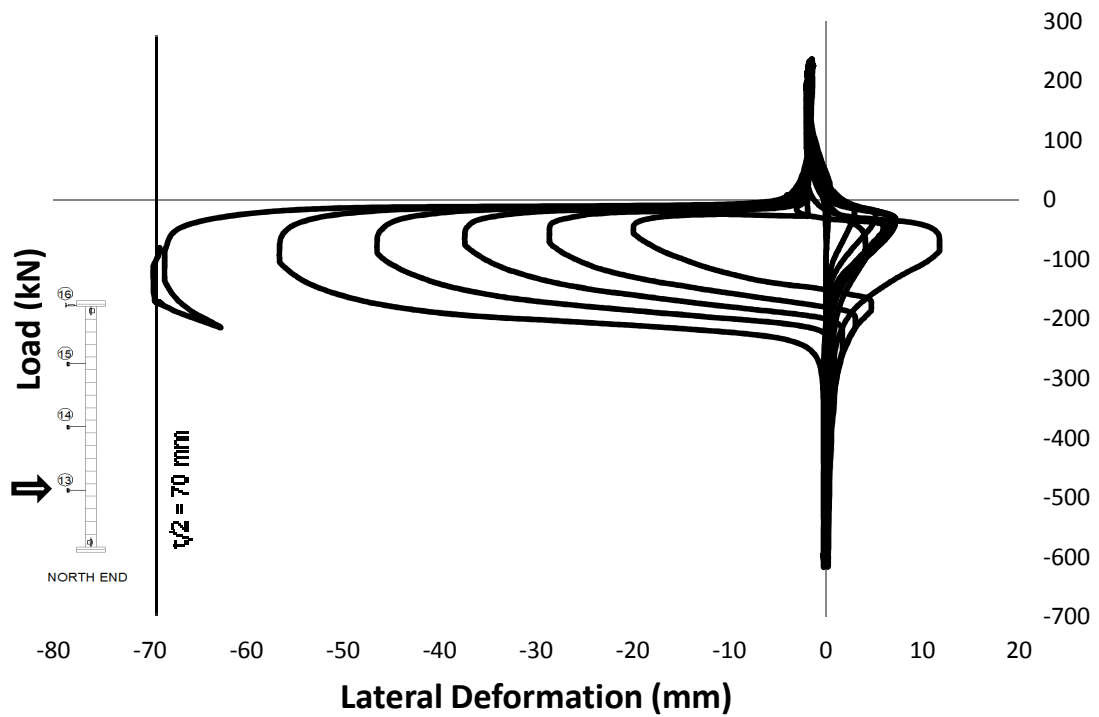


**Figure 4-35** Axial load versus lateral deformation at the lower quarter point for specimen C4

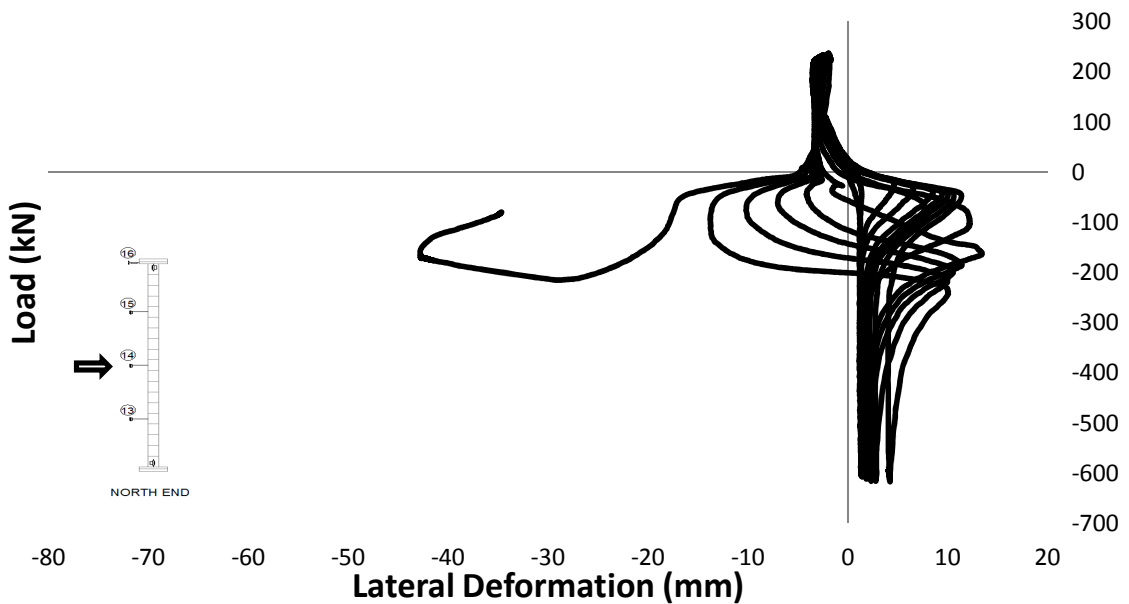


**Figure 4-36** Axial load versus lateral deformation at midheight for specimen C4

In much the same way as specimens C2 and C3, with increasing compression, masonry compression forces developed at the edge of the rotated cracks and as long as out-of-plane

displacements were smaller than one-half of the wall thickness (70 mm), these masonry compression forces caused the closure of horizontal cracks. Therefore, the specimen eventually restored its original vertical alignment and was subjected to pure axial compression at the peak of the compression half-cycle, indicated by point **h**.

Eventually, the out-of-plane displacements experienced by the specimen between points **b** and **d** in the compression half cycle were too large to allow the specimen to restore its original vertical alignment. At this point, increasing compression forces led to increasing out-of-plane displacements and the specimen became laterally unstable. Also, it was noticed that there was some horizontal translation at the bedjoint immediately below the stiffened portion during this final cycle of loading as shown in Figure 4-37.



**Figure 4-37 Sliding at the bed joint on the north face of specimen C4 at the ultimate stage**

Figure 4-38 illustrates the overall buckled shape of specimen C4 and the location of the horizontal sliding after instability had occurred while Figure 4-39 shows a photo of the buckled shape over the lower half of the specimen only.



**Figure 4-38 Specimen C4 at the end of the test after experiencing lateral instability**

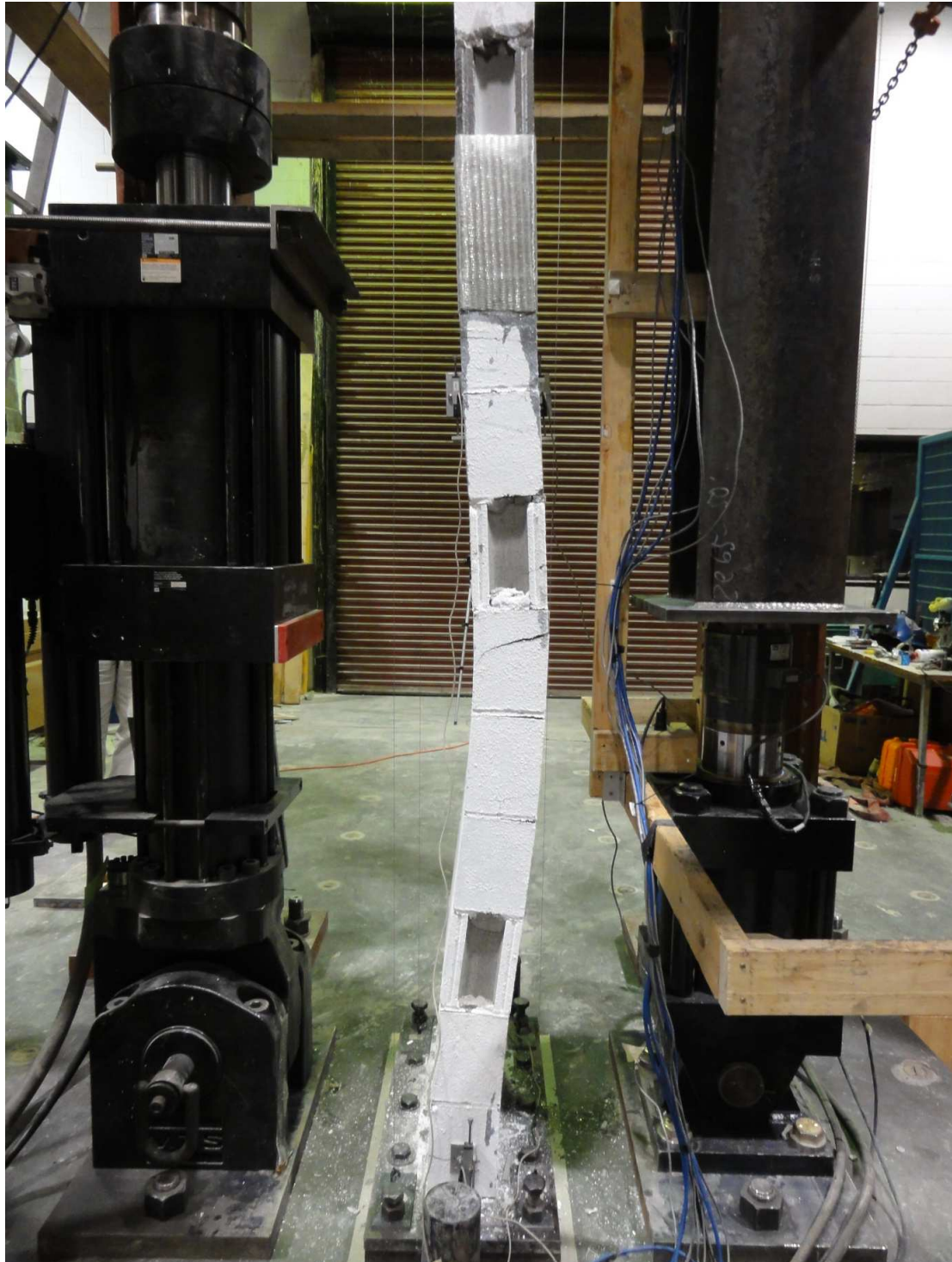


**Figure 4-39 Deformed shape of the bottom portion of specimen C4 after experiencing lateral instability**

Table 4-4 summarizes all major observations made during testing of specimen C4.

**Table 4-4 Experimental observations for specimen C4**

Loading Cycle		Range of crack widths (mm)	Maximum out-of-plane displacement (mm)	Key Observations	
1	T	$\Delta=0.7\Delta_y$ =5mm P=149 kN	0.2-0.4	2.9 (east) at midheight	Cracks were concentrated in the bottom portion of the specimen. There was a 0.7 mm gap between the top of the specimen and the top specimen plate. Relatively small out-of-plane displacements in the tension half-cycle were associated with the straightening of reinforcing bars in tension. The north face of the specimen seemed to be subjected to higher tension compared to the south face. However, a gap observed at the south face of the specimen at the interface of the top masonry course and the steel plate was larger than that at the north face. The overall axial deformation was by about 20% larger along the north face compared to the south face.
	C	P=-296 kN	0	0	All cracks fully closed and the specimen restored its original vertical alignment.
2	T	$\Delta=\Delta_y$ =8.0mm P=194 kN	0.4-0.75	3.3 (east) at midheight	Most cracks in the lower half increased in size, while there were no visible cracks in the top half. A larger crack developed on the north face the two bed joints immediately below the retrofitted portion of the wall (above the 7th and 8th masonry course from the bottom) and the width was approximately 1.2 mm. A gap between the specimen and the top steel plate increased to 1.0 mm width. The overall axial deformation was by about 20% larger at the northern end than the southern end.
	C	P=-600 kN	0	0	All cracks fully closed and the specimen restored its original vertical alignment.
3	T	$\Delta=1.5\Delta_y$ =12.0 mm P=198 kN	0.4-1.25	3.3 (east)	All cracks in the lower portion of the specimen increased in size. Hairline cracks developed in the bed joints in the top half of the specimen. A large horizontal crack along the bed joint immediately below the retrofitted half (above the 7th and 8th masonry course from the bottom) increased to 2.25 mm in width. Stepped cracks developed along the head joints in the bottom four courses of masonry. The difference in the overall axial displacement measured along the north and the south face decreased to 15%.
	C	P=-75.8 kN	0-0.4	7.7 (west) at midheight	A crack above the first course remained open, but its width was reduced.
		P=-607 kN	0	0	All cracks fully closed and the specimen restored its original vertical alignment. When the specimen was unloaded at the end of the compression half-cycle, the horizontal cracks re-opened and the specimen suddenly experienced 4.7 mm westward out-of-plane displacement at the compression load of -22 kN
4	T	$\Delta=2.0\Delta_y$ =16.0 mm P=205 kN	0.75-2.25	3.4 (east) at midheight	A few new small vertical cracks were noticed along the head joints in the bottom half of the wall. The gap at the top increased to approximately 2.0 mm at the north face and 3.0 mm at the south face. A few very small vertical cracks developed along the specimen thickness and at some head joints. The difference in the overall axial displacement measured along the north and the south face dropped down to 8%.
	C	P=-86 kN	0-0.75	12.1 (west) at midheight	When the specimen was unloaded at the end of the compression half-cycle, the horizontal cracks re-opened and the specimen suddenly experienced 6.6 mm westward out-of-plane displacement at the compression load of -38 kN.
		P=-607 kN	0	0	

Loading Cycle		Range of crack widths (mm)	Maximum out-of-plane displacement (mm)	Key Observations	
5	T	$\Delta=3.0\Delta_y$ =24mm P=216 kN	1.5-5.0	3.3 (east) at $\frac{3}{4}$ from the base of the wall	A few very small vertical cracks developed during the tension half-cycle along the specimen width in the lower half of the wall. The gap at the top of the specimen increased to 2 mm at the south face and 1 mm at the north face. The difference in the overall axial displacement measured along the north and south face remained unchanged at 8%.
	C	P=-50.3 kN	0-3.0	19.9 (east) at $\frac{1}{4}$ from the base of the wall	The maximum out-of-plane displacements were recorded at the lower quarter point in the westward direction, as opposed to previous cycles where the maximum occurred at midheight. Upon unloading from tension, the maximum out-of-plane movement changed direction, and it was recorded at the lower quarter point in the eastward direction. Interestingly, the direction of lateral displacement changed again with an increase in the compression load. Deflection at the lower quarter point dropped down to zero, but the midheight point started bowing out-of-plane westward. At the end of the compression cycle, the specimen almost restored its original vertical alignment. However, the specimen experienced westward out-of-plane displacements at its midheight towards the end of the unloading. The maximum displacement of 8.55 mm developed at the compressive load of -43kN.
		P=-162.6 kN	0-1.25	13.5 (west) at midheight	
		P=-612 kN	0	1.4 (west) at $\frac{3}{4}$ from the base of the wall	
6	T	$\Delta=3.5\Delta_y$ =28.0 mm P=220 kN	2.0-6.0	3.2 (east) at midheight	A few new vertical cracks developed along head joints and split some blocks in half along the specimen thickness. The width of the existing cracks increased in size to about 0.4 mm. Also, a few vertical cracks developed along the wall thickness, as well as in the middle of the masonry courses. A few new horizontal cracks appeared away from the bed joints in the bottom half of the wall. The overall axial displacement was almost the same along the north and south faces of the specimen.
	C	P=-64 kN	0-1.75	28.7 (east) at $\frac{1}{4}$ from the base of the wall	The specimen experienced out-of-plane displacements after unloading from the tension half-cycle, and the maximum displacement was recorded at the lower quarter point in eastward direction. With a further increase in the applied compression, lower portion of the bottom half of the specimen restored some of its vertical alignment while the middle portion of the wall started to slightly bow out westwards. All cracks closed at the point of maximum compression, all and the specimen restored its original vertical alignment.
		P=-185.5 kN	0-0.4	11.4 (west) at midheight	
		P=-611 kN	0	2.1 (west) at midheight	
7	T	$\Delta=4.0\Delta_y$ =32.0 mm P=225 kN	2-6.5	3.2 (east) at midheight	The overall axial deformation was almost the same along the north and south face of the specimen. A few tension cracks appeared in the top portion of the specimen (which was retrofitted by applying GFRP overlays), however the average crack width was rather small (0.2 mm). A few more vertical cracks developed along head joints, and some horizontal cracks developed through the masonry courses in the lower half of the specimen.
	C	P=-64.6 kN	0-2.25	37.4 (east) at $\frac{1}{4}$ from the base of the wall	Like in the previous load cycle, the maximum out-of-plane displacement was observed at the lower quarter point towards east after the tension load was removed. With an increase in the compression loading, the lower bottom of the specimen restored some of its vertical alignment, while the middle portion started to slightly bow out westward. At the point of maximum compression, all cracks closed and the specimen was again aligned in its original vertical position.
		P=-199 kN	0-0.4	10.6 (west) at midheight	
		P=-615 kN	0	2.1 (west) at midheight	

Loading Cycle		Range of crack widths (mm)	Maximum out-of-plane displacement (mm)	Key Observations	
8	T	$\Delta=4.5\Delta_y$ =36.0 mm P=229 kN	1.5-8.0	2.9 (east)	The overall axial deformation was almost the same along the north and south face of the specimen. The number of horizontal cracks away from the bed joints increased and cracks developed along almost all head joints.
	C	P=-79.3 kN	0-2.5	46.5 (east) at ¼ from the base of the wall	Similar to the previous cycle, the maximum out-of-plane displacements were observed at the lower quarter point in eastward direction after the tension load was removed. With an increase in the compression loading, the lower bottom of the specimen restored some of its vertical alignment while the middle portion started to slightly bow out in westward direction. At the point of maximum compression, all cracks closed and the specimen restored its vertical alignment.
		P=-213 kN	0-0.5	10 (west) at midheight	
		P=-615 kN	0	2.8 (west) at midheight	
9	T	$\Delta=5.0\Delta_y$ =40.0 mm P=233 kN	2.0-9.0	2.5 (east)	The number of horizontal cracks at through the blocks (away from bedjoints) increased, and the existing cracks increased in terms of the width. A few new vertical cracks developed along the specimen width.
	C	P=-93.7 kN	0-3.0	56.6 (east) at ¼ from the base of the wall	The same trend was followed like in the previous load cycle. The maximum out-of-plane displacement was observed at the lower quarter point in eastward direction after the tension load was removed. The lower bottom portion of the specimen restored its vertical alignment, while the middle portion started to slightly bow out westward. In compression, vertical cracks along specimen width increased in terms of the width. At the point of maximum compression, all cracks closed and the specimen was effectively aligned in vertical position.
		P=-234 kN	0-0.6	10 (west)	
		P=-616 kN	0	4.25 (west) at midheight	
10	T	$\Delta=5.5\Delta_y$ =44.0 mm P=236 kN	1.0-11.0	1.8 (east) at ¾ from the base of the wall	A few new horizontal cracks appeared through the blocks (away from the bed joints), and the existing cracks considerably increased in terms of width. A large vertical crack developed underneath the retrofitted portion of the specimen (above the 8th course of masonry from the base), which was 3 mm wide, and another crack at a lower elevation (after 6th masonry course) was 4 mm wide. The crack at the bed joint above the 8th masonry course increased to 11.0 mm in width. The gap between the top masonry course and the top specimen plate was 3.0 mm wide at the north face and 0.7 mm wide at the south face.
	C	P=-117.5 kN	0-2.0	69.7 (east) at ¼ from the base of the wall	For the first time during the test, it was noticed that the specimen was almost visibly bowing in the direction of its strong axis towards North. The specimen became unstable during the compression half-cycle as the horizontal cracks failed to fully close before the out-of-plane displacement in the lower quarter of the wall exceeded half the wall thickness. The reinforcing bar exposed at the bed joint directly below the retrofitted portion of the specimen (above 8th course of masonry from the base) seemed to have experienced local buckling, as the open crack had slid sideways instead of undergoing uniform rotation like the remainder of open cracks. This can be seen in Figures 4-33 and 4-35.

Figure 4-40 shows crack patterns during each loading cycle for specimen C4. Figure 4-28 shows the recorded axial load versus axial deformation over the total specimen height. Figures 4-29 and 4-30 show the axial load versus out-of-plane displacement at the lower quarter point and at midheight respectively.

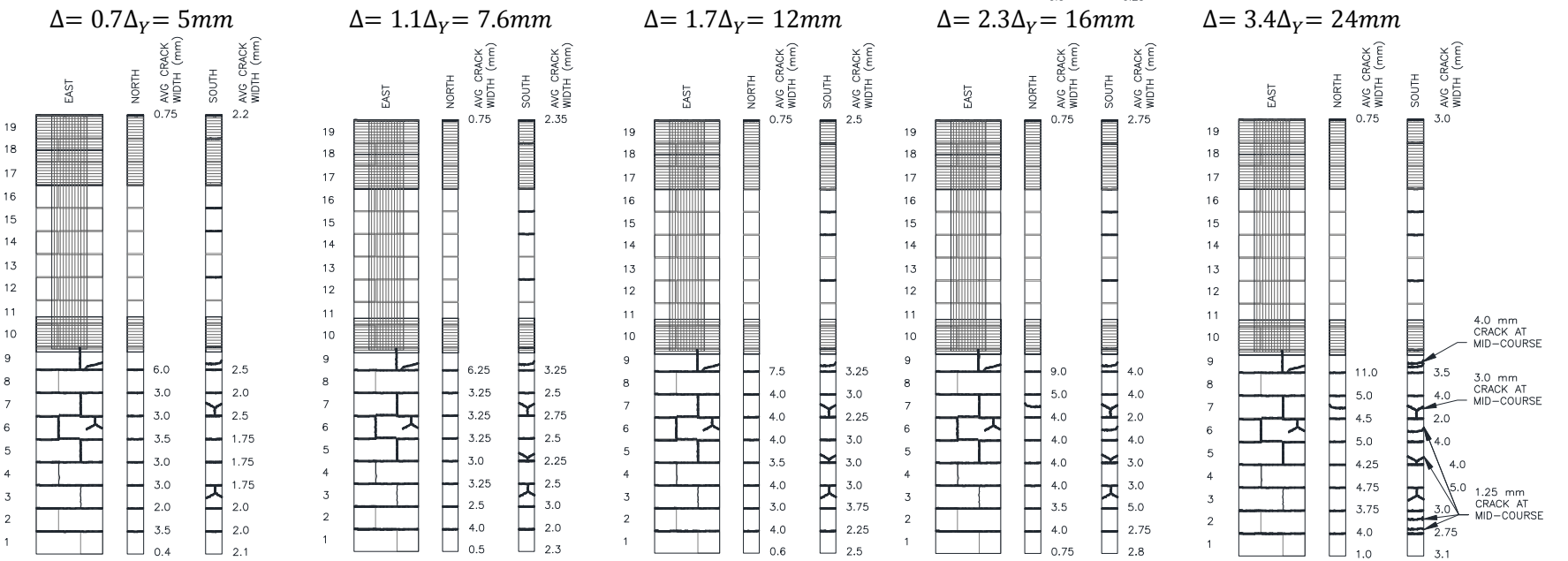
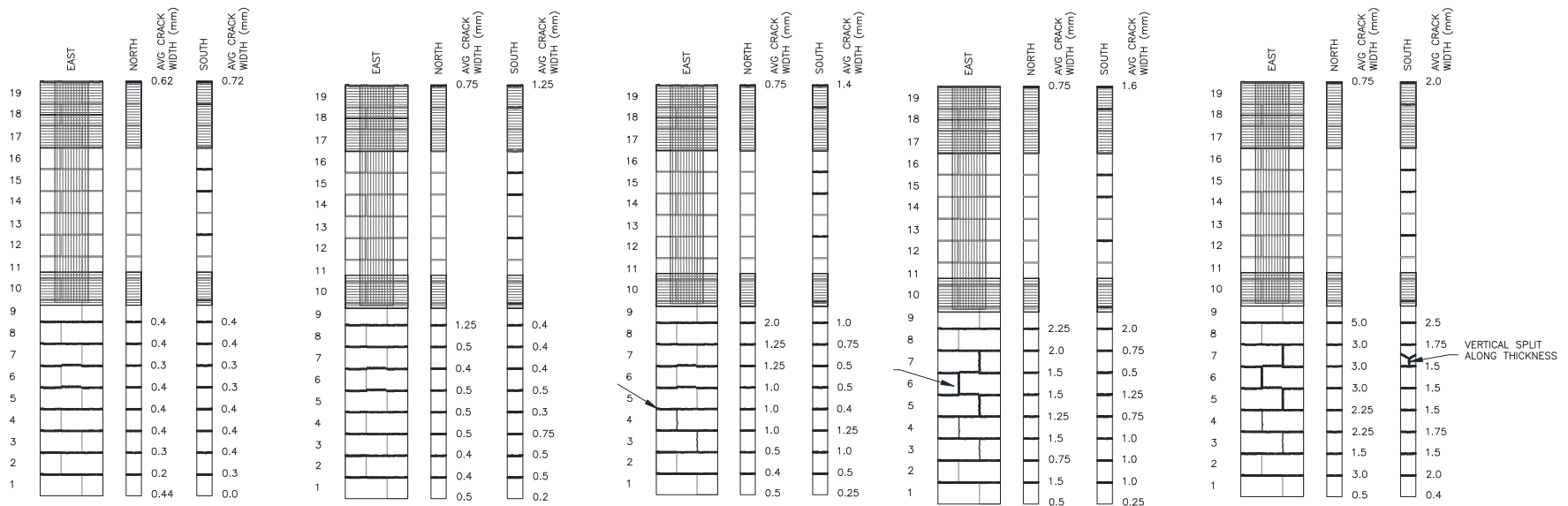


**Figure 4-40 Crack patterns at increasing tensile displacement levels for specimen C4**

#### 4.2.5 Specimen C5

Specimen C5 was reinforced with 2-10M bars (one in each end core), corresponding to reinforcement ratio of 0.24%.

The specimen was retrofitted with GFRP overlay applied in the top half portion of the specimen (same as specimens C3 and C4).

Although the masonry blocks were laid centered on the specimen plate at the bottom, one of the reinforcing bars had moved off-centre at the top after the grout was poured. Figure 4-41 shows the plan view of the specimen in relation to the top and bottom specimen plates.

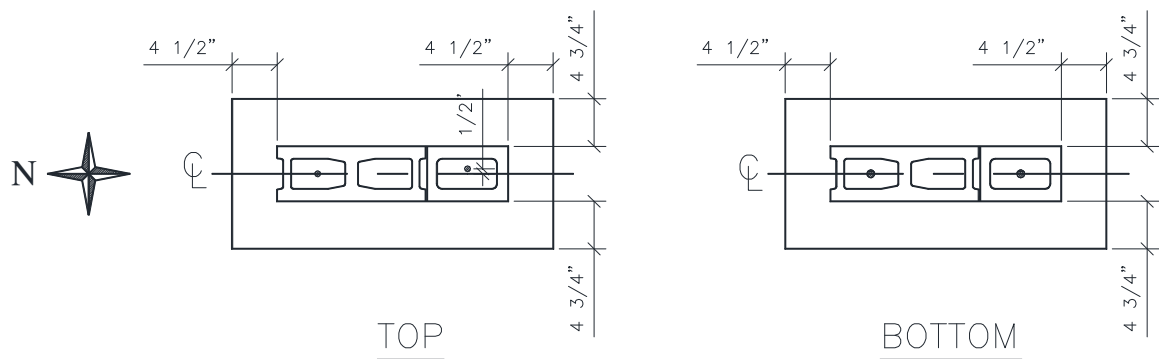
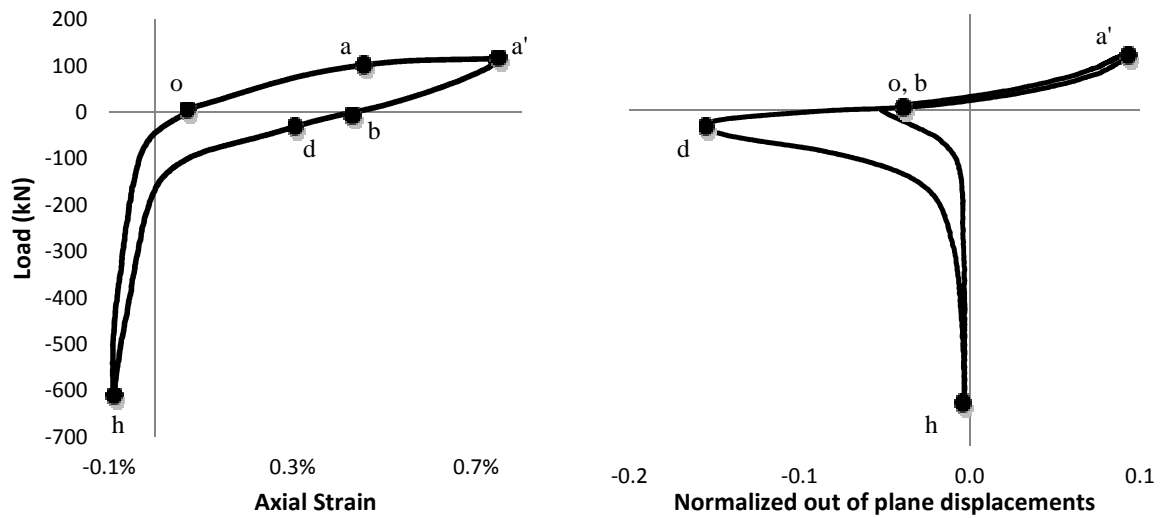


**Figure 4-41 Specimen C5: cross-section and reinforcement layout relative to top and bottom specimen plates**

Figure 4-42 shows plots of applied axial load vs. axial strain and axial load vs. maximum lateral deformation (normalized by specimen thickness). Response of specimen C5 was very similar to that of specimen C4. As can be seen, for the same strain level of about 0.7%, the link between points **b** and **c** did not result in as much out-of-plane displacement in specimen C5 as it did in specimens C2 and C3. Hence, there is not much of a plateau between these two points on Figure 4-42a, while this segment on Figure 4-42b indicates that most of the lateral displacement is still taking place between these points. Also note that the peak of the tension half cycle, point **a'**, corresponds to relatively larger lateral displacements in tension than those seen with specimens C2 through C4. This is caused by the off-centre location of the reinforcement within the masonry core and may have contributed to more of a debonding between the rebar and the grout in this specimen relative to the remainder of the specimens.



**a.** Applied axial load vs. axial strain over the plastic hinge region      **b.** Applied axial load vs. maximum lateral deformation at midheight normalized with respect to thickness

- o: Beginning of cycle in tension
- a: Yielding of reinforcement
- a': Peak of tension half cycle (uniformly distributed horizontal cracks along the height)
- b: Beginning of compression half cycle (most horizontal cracks remain open but are reduced in size)
- d: Most out-of-plane instability has already occurred
- h: Peak of compression half cycle (the specimen has restored its original vertical alignment and all horizontal cracks are closed)

**Figure 4-42 Plot of a. Applied axial load vs. axial strain over the plastic hinge region and b. Applied axial load vs. maximum lateral deformation at midheight normalized with respect to thickness for specimen C5,  $\epsilon_t=0.73\%$**

The general response of specimen C5 was similar to the rest of the specimens as can be seen from Figure 4-42.

Similar to specimens C2, C3 and C4, horizontal cracks developed in the specimen along the bed joints during tension half-cycles as shown in Figure 4-43. The horizontal cracking was mainly concentrated in the lower (unstiffened) portion of the specimen. Since the tensile deformation of the specimen was accompanied by considerable out-of-plane displacements at the midheight, it became obvious early on during the experiment that the rebar was not completely straight within the core of the specimen. Note that this misalignment of the reinforcement within the concrete core is not thought to have a significant impact on the out-of-plane instability of the specimen. However, it is speculated that such misalignment combined with the small surface area of the rebar may cause severe de-bonding between the specimen and the grout core which might contribute to failure in local buckling of reinforcement. This is discussed again in more detail shortly.

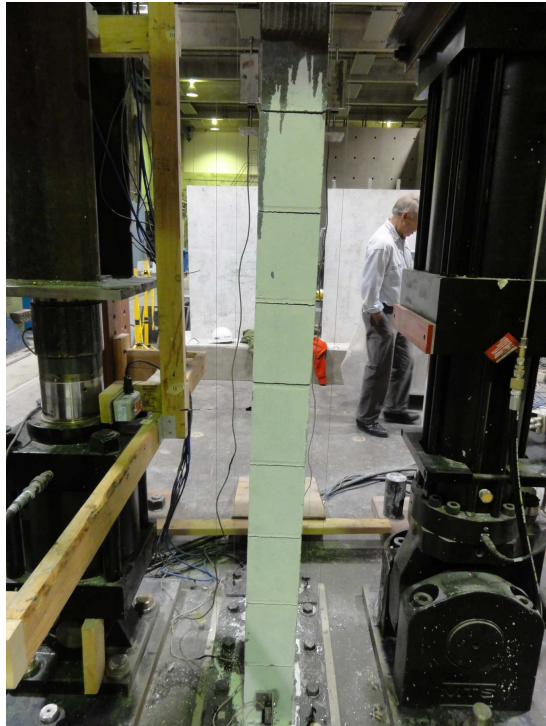


**Figure 4-43 Horizontal cracks at bed joints uniformly distributed over the bottom half of specimen C5**

As in the case of specimens C2, C3 and C4, larger horizontal cracks at the bed joints and additional horizontal cracks through the blocks developed at higher tensile displacement levels. Also, cracks at head joints appeared as soon as the specimen was subjected to tension. A few new vertical cracks developed along the specimen thickness in the later loading cycles (corresponding to higher tensile strains).

After the tension half cycle, the reinforcing bars began to move out-of-plane after they had undergone some tensile plastic strains at low compressive load levels. Figure 4-44 shows the sequence of events from the beginning of the compression half cycle, point **b**, to the point of maximum out-of-plane displacement, point **d** for a typical loading cycle during the testing of specimen C5.

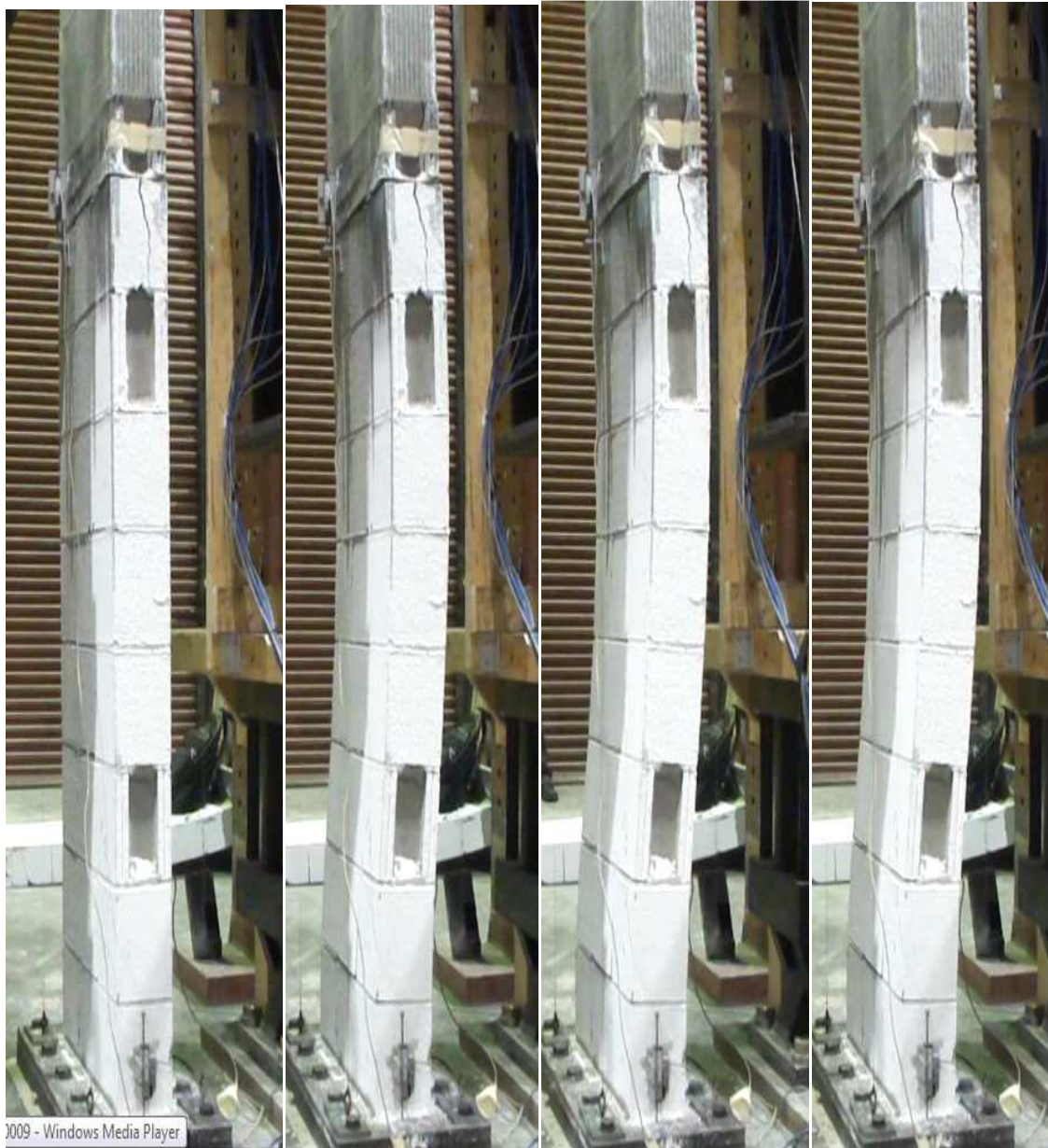


**Figure 4-44 Specimen C5 experienced eastward out-of-plane displacements after tensile half-cycle with the maximum axial displacement of  $4.9\Delta_y$**

The lateral displacements continued to exist until the open cracks rotated sufficiently such that they began to close on the west face of the specimen. Subsequently, the compression force, resulting from the engagement of masonry blocks at one corner, caused a bending moment which restored the original vertical alignment of the specimen.

However, before the out-of-plane displacements became critical (reaching close to half the specimen thickness), a large vertical crack appeared at the masonry course immediately above the 8th course of masonry from the wall base as shown in Figure 4-45.



**Figure 4-45 Large horizontal and vertical crack developed at the masonry course below the stiffened portion (above the 8th masonry course from base of the wall) of specimen C5 during load cycle #6 ( $\Delta = 4.3\Delta_y$ )**

A subsequent increase in the tensile strains did not result in further increase in out-of-plane displacements. In fact, the subsequent load cycles with axial tensile displacements of  $6\Delta_y$  and  $6.3\Delta_y$  produced smaller out-of-plane displacements than the displacements which occurred after a tensile displacement of  $5.6\Delta_y$ . During the larger tensile excursions, the rebar at the location of the abovementioned large vertical crack began to buckle and push outward on the face shell, resulting in spalling of the face shell and crumbling of the grout at this location. This is shown in Figure 4-46.



**Figure 4-46 Reinforcing bar protruding through the block face shell during the compression half-cycle after the tensile axial displacement of  $5.9\Delta_y$**

It should be noted that (unlike previous specimens) specimen C5 continued to restore its original vertical alignment even at large tensile strains. It was concluded that the local buckling of the reinforcement was the mode of failure as shown in Figure 4-47.



**Figure 4-47 Localized buckling of the reinforcing bar, caused spalling of block face-shells and crumbling of the grout.**

The buckling of reinforcement led to disintegration of the grout core and severe spalling of the masonry faceshell. This lateral buckling of reinforcement was followed by the formation of a large continuous vertical crack at the northern end of the specimen which indicates crushing of masonry in this part of the specimen. See Figure 4-48 and Figure 4-49.

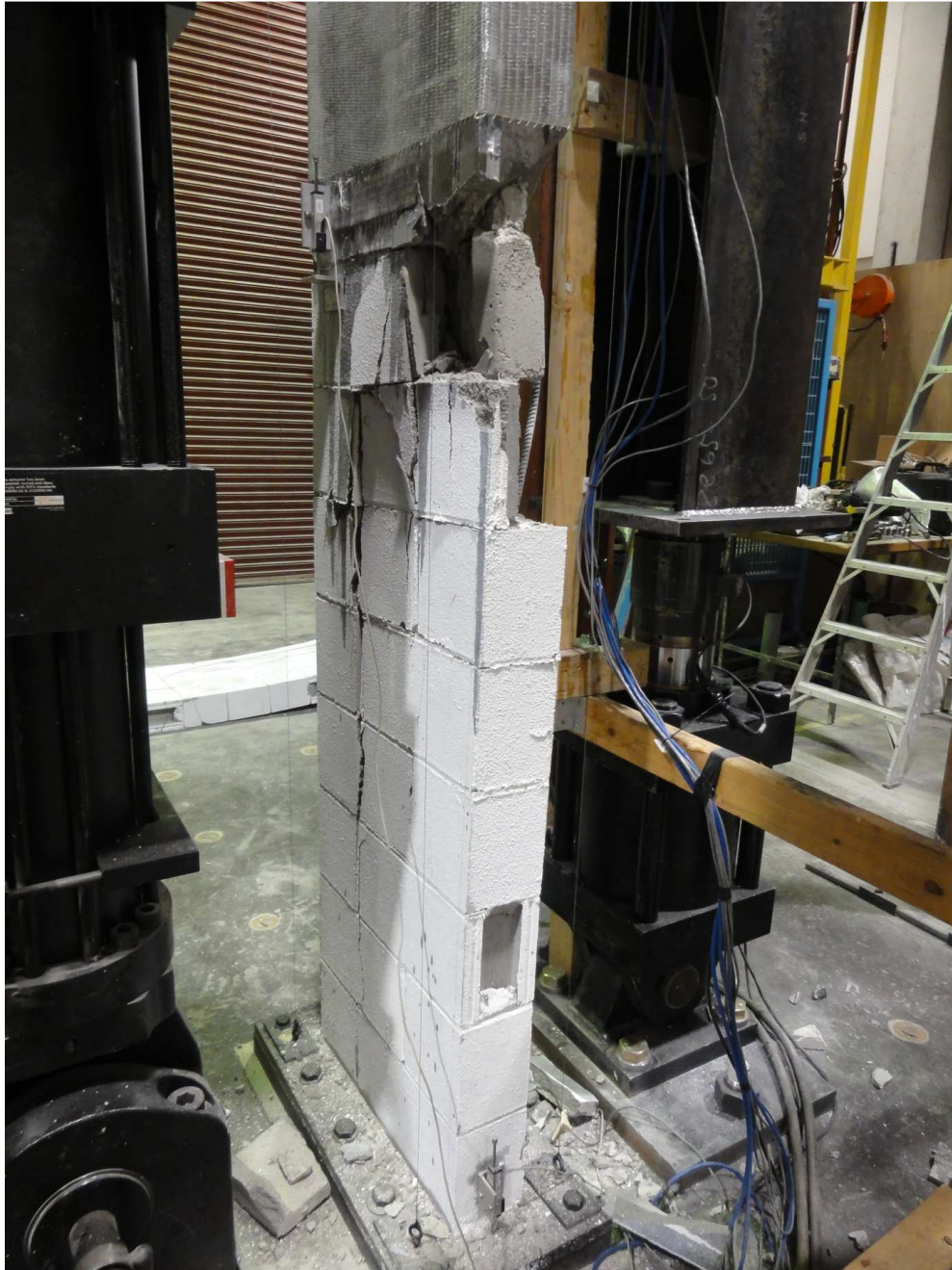


**Figure 4-48 Specimen C5 after experienced the failure characterized by localized buckling of the reinforcement and crushing of the masonry**

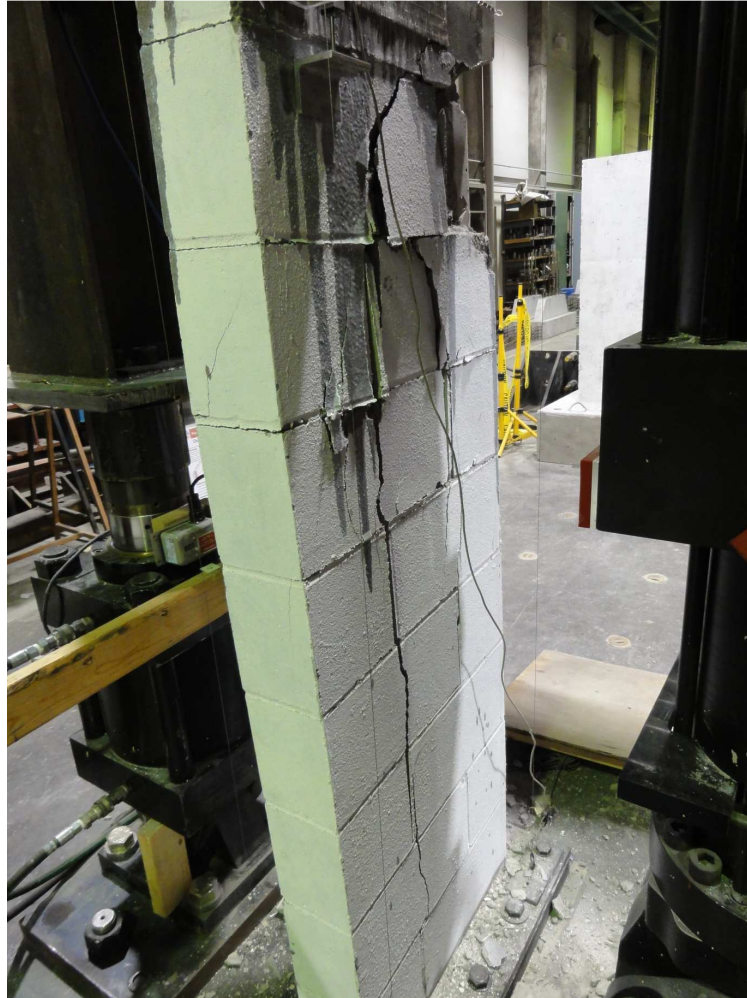


**Figure 4-49** Continuous vertical splitting crack in specimen C5 at the end of the test

It is speculated that the smaller amount of reinforcement (reinforcement ratio) played an important role in determining the mode of failure of this specimen. A possible explanation is that, due to a smaller amount of reinforcement, a smaller compressive load on the edge of the closing crack is required to restore balance across the specimen thickness (compared to other specimens). In this case, significant tensile strains are required to allow the specimen to move laterally outward beyond the point of return before the onset of crack closure. In addition, larger tensile strains combined with reinforcing bars with smaller area and moment of inertia resulted in bond degradation between the grout and the rebar which resulted in local buckling of the reinforcement. This is confirmed by comparing the buckling load of 2-10 bars with the load at which the specimen began to experience out-of-plane displacement. If the laterally unsupported length of the 2-10 bars had been reduced to 400 mm (equivalent to two courses of masonry), their combined buckling load would be equal to 9.1 kN which is comparable to the 8 kN load at which the out-of-plane displacements during the last loading cycle were observed. From Figure 4-47, it can be seen that the local buckling of the bar over two masonry courses caused disintegration of grout and masonry faceshell close to specimen's midheight.

Figure 4-50 illustrates the buckled shape of specimen C5 during the load cycle corresponding to a tensile strain of 1.6%. Figure 4-51 shows the hysteretic plot of total axial load vs. total axial deformation while Figure 4-52 and Figure 4-53 show plots of applied axial load vs. lateral displacement at specimen's lower quarter point and midheight respectively.

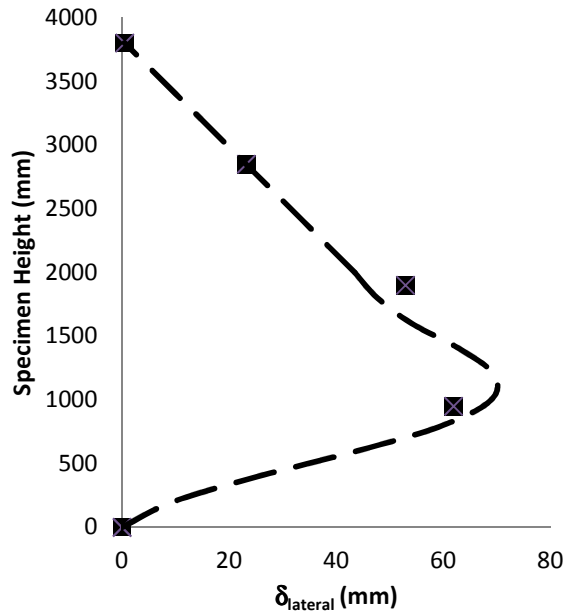


**Figure 4-50** Buckled shape of specimen C5 during load cycle  $\epsilon_t=1.6\%$

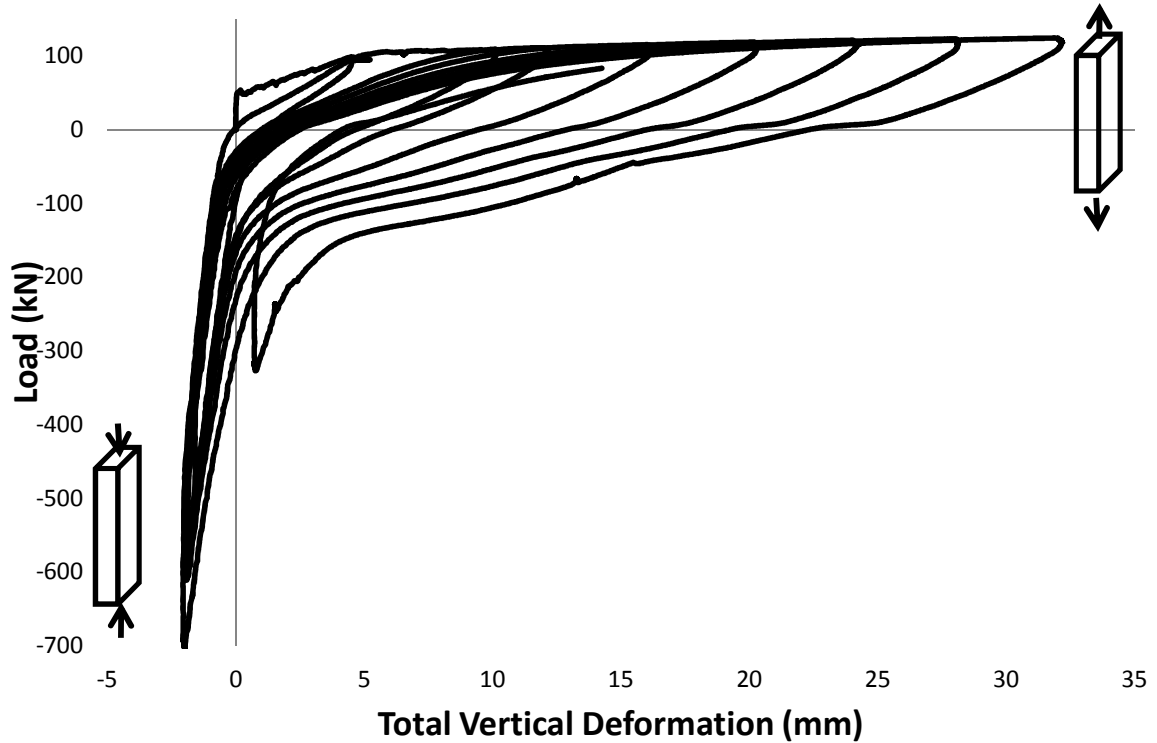


**Figure 4-51** Axial load vs. overall axial deformation for specimen C5

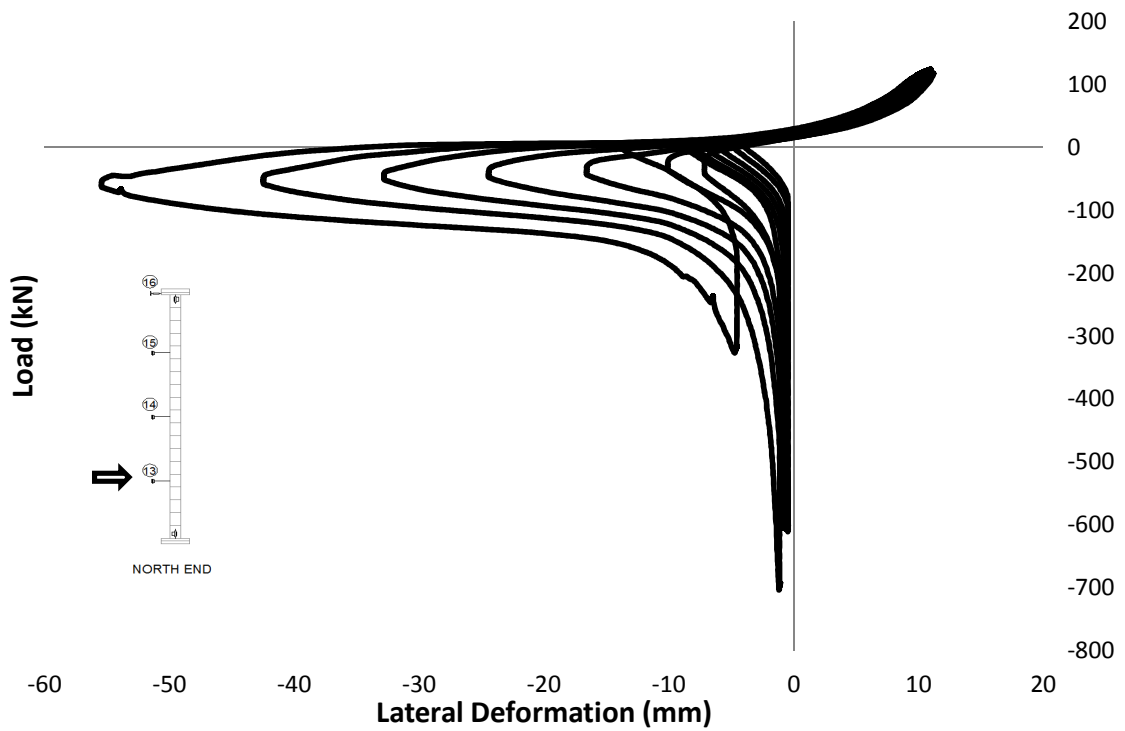


**Figure 4-52 Axial load vs. lateral deformation at lower quarter point for specimen C5**

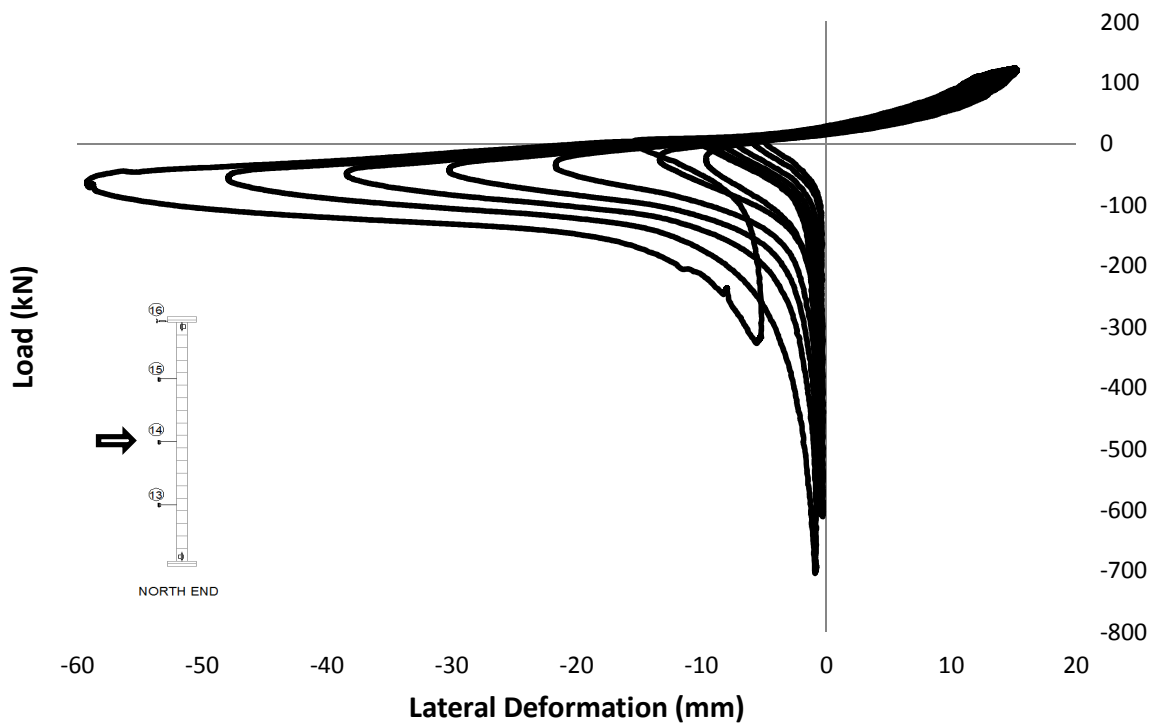


**Figure 4-53 Axial load vs. lateral deformation at midheight for specimen C5**

Table 4-5 summarizes major experimental observations related to the testing of specimen C5.

**Table 4-5 Experimental observations for specimen C5**

Loading Cycle		Range of crack widths (mm)	Maximum out-of-plane displacement (mm)	Key Observations	
1	T	$\Delta=0.8 \Delta_y$ =5 mm P=98.5 kN	0.0-1.0	10 (west) at midheight	The GFRP caused the specimen to experience almost no vertical deformation until it failed in tension (brittle failure) at a load of 54 kN Cracks were concentrated over the lower portion of the specimen, and there was no evidence of tensile cracking over the top half of the wall which had been fiber-reinforced One headjoint crack had formed on the east face of the 5th masonry course from the bottom There was noticeable out-of-plane displacement over the lower half (10 mm) in the tension cycle indicating that the reinforcement was significantly off-centre The size of horizontal cracks over the lower portion were uniform except for one considerably larger crack immediately below the point at which the GFRP wrap stopped
	C	P=-497 kN	0	0	When the specimen was unloaded, it did not experience any lateral movement At the end of the compression half-cycle, all cracks fully closed and specimen restored original straightness
2	T	$\Delta=1.8\Delta_y$ =10 mm P=108.9 kN	0.5-1.0	-11.7 (west) at midheight	Most cracks over the lower half had increased in size while there were still no visible cracks in the top half On the northern end, the larger crack at the bedjoint immediately below the retrofitted portion of the wall had widened to about 3 mm in width on the northern end and 1 mm on the southern end.
	C	P=-17.15 kN	0-0.5	9.44 (east) at midheight 7.15 (east) at ¼ from bottom	Almost immediately after being put in compression, the specimen began to move laterally outward towards east to a maximum of 9.44 mm at midheight
		P=-611 kN	0	0	All cracks fully closed and specimen restored original straightness
3	T	$\Delta=2.1 \Delta_y$ =12.0 mm P=110.9 kN	1.0-1.75	12.22 (west)	All cracks in the lower portion had increased in size. There were hairline cracks starting to appear in the bedjoints over the top half of the wall. The large crack at the bedjoint immediately below the retrofitted half had grown to 4 mm in width on the northern end and 2 mm on the southern end. The specimen had already started forming stepped cracks along the headjoints in the lower four courses of masonry.
	C	P=-19.4 kN	0-0.4	13 (east) at midheight 10 (east) at ¼ from bottom	Upon being put in compression, the specimen began to move laterally eastward as before, this time to a maximum of 13 mm at midheight at a compressive load of -19 kN All cracks fully closed and specimen restored original straightness
		P=-608 kN	0	0	At the end of the compression cycle, when the specimen was unloaded, the horizontal cracks re-opened and the specimen momentarily experienced 6.0 mm of eastward out-of-plane displacement at almost zero load
4	T	$\Delta=2.8 \Delta_y$ =16.0 mm P=115 kN	0.75-2.25	13 (west) at midheight	The specimen experienced larger lateral displacements at midheight in tension (maximum of 13mm) More small cracks had appeared along the remainder of the head joints in the lower half of the wall. Some very thin vertical cracks along the specimen thickness and at some headjoints were noticed
	C	P=-35 kN	0-0.75	21.7 (east) at midheight 16.6 (east) at ¼ from bottom	Upon being put in compression, the specimen began to move laterally eastward as before, this time to a maximum of 21.7 mm at midheight at a load of -35 kN At the peak of the compression half-cycle, all cracks had closed and the specimen restored its straightness
		P=-607 kN	0	0	At the end of the compression half cycle, when the specimen was being unloaded, the horizontal cracks re-opened and the specimen momentarily experienced 7.4 mm of eastward out-of-plane displacement at almost zero load

Loading Cycle		Range of crack widths (mm)	Maximum out-of-plane displacement (mm)	Key Observations	
5	T	$\Delta=3.5 \Delta_y$ =20 mm P=117.7 kN	1.5-3.0	13.7 (west) at midheight	Consistent with previous cycles, the wall experienced increasing lateral displacements in tension as a result of reinforcing bars straightening themselves out The large crack at the bedjoint immediately below the retrofitted half had grown to 5.4 mm in width on the northern end and 2.5 mm on the southern end. Some very thin vertical cracks started appearing along the specimen thickness in the tension cycle in the lower half of the wall.
	C	P=-41kN	0-0.75	30.2 (east) at midheight 24.4 (east) at ¼ from bottom	The maximum out-of-plane displacement was still at midheight and grew to 30.2 mm towards east Although at the peak of the compression cycle, the specimen had almost restored its original straightness, when it was unloaded, it experienced westward out-of-plane displacements at its midheight as large as 8.57 mm at almost zero load
		P=-603 kN	0	0	
6	T	$\Delta=4.2 \Delta_y$ =24.0 mm P=121 kN	2.0-5.5	14.34 (west) at midheight	The specimen experienced yet larger lateral displacements in tension as a result of reinforcing bars straightening themselves out. More vertical cracks along headjoints and down the middle of some blocks along the specimen thickness started appearing while the width of the existing ones grew in size to about 1 mm. Some horizontal cracks away from the bedjoints in the bottom half of the wall appeared. Also, some vertical cracks along the thickness of the wall as well as in the middle of the masonry courses started appearing. Before being completely unloaded from the tension half cycle, the specimen began to move laterally outward (with the maximum at midheight) at near zero loads. During this short time, it did not seem to pick up any compressive load, creating a small plateau on plot of load versus vertical deformation diagram (this plateau, as discussed in the next chapter, corresponds to the reloading strain)
	C	P=-50 kN	0-1.75	38.4 (east) at midheight 32.8 (east) at ¼ from bottom	Similar to the last cycle, the maximum out-of-plane displacement was observed at midheight. The lateral movement continued to increase even after the specimen began picking up compressive load. However, as before, the specimen eventually began to restore its straightness with increased compression. At the point of maximum compression, all cracks had closed and the specimen was effectively plumb again. However, when the specimen was unloaded from compression, it experienced westward out-of-plane displacements at its midheight as large as 9.6 mm at almost zero load
		P=-605 kN	0	0	
7	T	$\Delta=4.9 \Delta_y$ =28.0 mm P=225 kN	2-6.5	14.9 (west) at midheight	Some tension cracks had started appearing in the upper portion but their width was generally much smaller than those in the lower half More headjoint cracks and some horizontal cracks in the middle of masonry courses in the lower half of wall had started appearing. Before being completely unloaded from the tension half cycle, the specimen began to move laterally outward (with the maximum at midheight) at near zero loads. During this time, it did not seem to pick up any compressive load. This time, this portion of the vertical strain was slightly larger than that in the last loading cycle
	C	P=-54 kN	0-2.25	47.9 (east) at midheight 42.5 (east) at ¼ from bottom	The specimen eventually began to pick up compressive load while still moving laterally outward towards east (with the maximum at midheight) However, as before, the specimen eventually began to restore its straightness with increased compression. Some relatively large vertical cracks started forming on the southern end of the specimen along the thickness and on the east face. This was at the masonry course immediately below the FRP (course 9) At the point of maximum compression, all cracks had closed and the specimen was effectively plumb again. However, when the specimen was unloaded from compression, it experienced westward out-of-plane displacements at its midheight as large as 10.2 mm at almost zero load
		P=-703.8 kN	0	0	

Loading Cycle		Range of crack widths (mm)	Maximum out-of-plane displacement (mm)	Key Observations	
8	T	$\Delta=5.6 \Delta_y$ =32.0 mm P=124.1 kN	1.5-7.0	15.22 (west) at midheight	The number of horizontal cracks away from the bedjoints had increased More vertical splitting cracks were forming along the thickness on the northern and southern end. The horizontal crack at the bedjoint immediately below the retrofitted portion was now 7 mm in size on both northern and southern ends More horizontal and vertical cracks above this bedjoint seemed to be leading to spalling of the faceshell Similar to last cycle, some reloading strain took place near zero load as the specimen was being unloaded from tension. This was the beginning of out-of-plane movement.
	C	P=-60.7 kN	0-2.5	59.23 (east) at midheight 55.5 (east) at ¼ from bottom	The specimen continued to move laterally outward as it picked up compression and cracks began closing at one end.
		P=-326.5 kN	0	0	As before, the maximum out-of-plane displacement was observed at midheight. Though, again, with increased compression, the specimen restored its straightness. At the point of maximum compression, all cracks had closed and the specimen was effectively plumb again. The reinforcement on the southern end seemed to have undergone local buckling as it slightly pushed out through the broken face-shell. This happened at midheight on the eastern face.
9	T	$\Delta=6.0\Delta_y$ =34.0 mm P=123 kN	3.0-9.0	14.9 (west) at midheight	The crack widths became more uniform with the exception of the largest crack still being at the bedjoint immediately below the retrofitted portion. This is also where the face-shell on the eastern face was beginning to spall. More vertical cracks were developing along the specimen thickness and on both faces. Horizontal cracks were also appearing away from the bedjoints. While the specimen was being unloaded from tension, the rebar on the southern end buckled out towards east, causing severe face-shell spalling at the masonry course immediately below the retrofitted portion It was evident that the grout pour had pushed the rebar off-centre such that it was resting against the face-shell
	C	P=-69.3 kN	0-3.0	54.7 (east) at midheight 59.5 (east) at ¼ from bottom	As before, the maximum out-of-plane displacement was observed at midheight. Though, again, with increased compression, the specimen restored its straightness. At the point of maximum compression, all cracks had closed and the specimen was effectively plumb again.
		P=-215.9 kN	0	0	In compression, the width of the vertical cracks along specimen thickness increased. At the point of maximum compression, which was reduced significantly to ensure the specimen does not experience crushing, all cracks had closed and the specimen was effectively plumb again.
10	T	$\Delta=6.3\Delta_y$ =36.0 mm P=121.7 kN	4.0-9.0	15 (west) at midheight	The specimen was put in tension one last time to ensure that its failure mechanism was in fact local buckling of reinforcement and not out-of-plane instability. As before the crack widths had become more uniform and increased with increased tension. The buckled rebar which was now clearly visible straightened itself out in tension. However, as the specimen was being unloaded from tension, it buckled out again while the specimen was also moving out-of-plane. This happened at near zero load.
	C	P=-59.8 kN	0-2.0	53.5 (east) at midheight -61.87 (east) at ¼ from bottom	Although the specimen moved significantly outward towards east at midheight with increased compression, it never became laterally unstable. As with previous cycles, it restored its straightness and started to resist loads in pure compression. However this time, at a load much lower than its crushing capacity, a large vertical crack split the specimen over its lower half. This happened closer to the northern end and was a result of the reduced cross-sectional area after the face-shell spalling and crumbling of grout in the previous cycles.
		P=-445 kN	0	2.5 (east) at midheight	

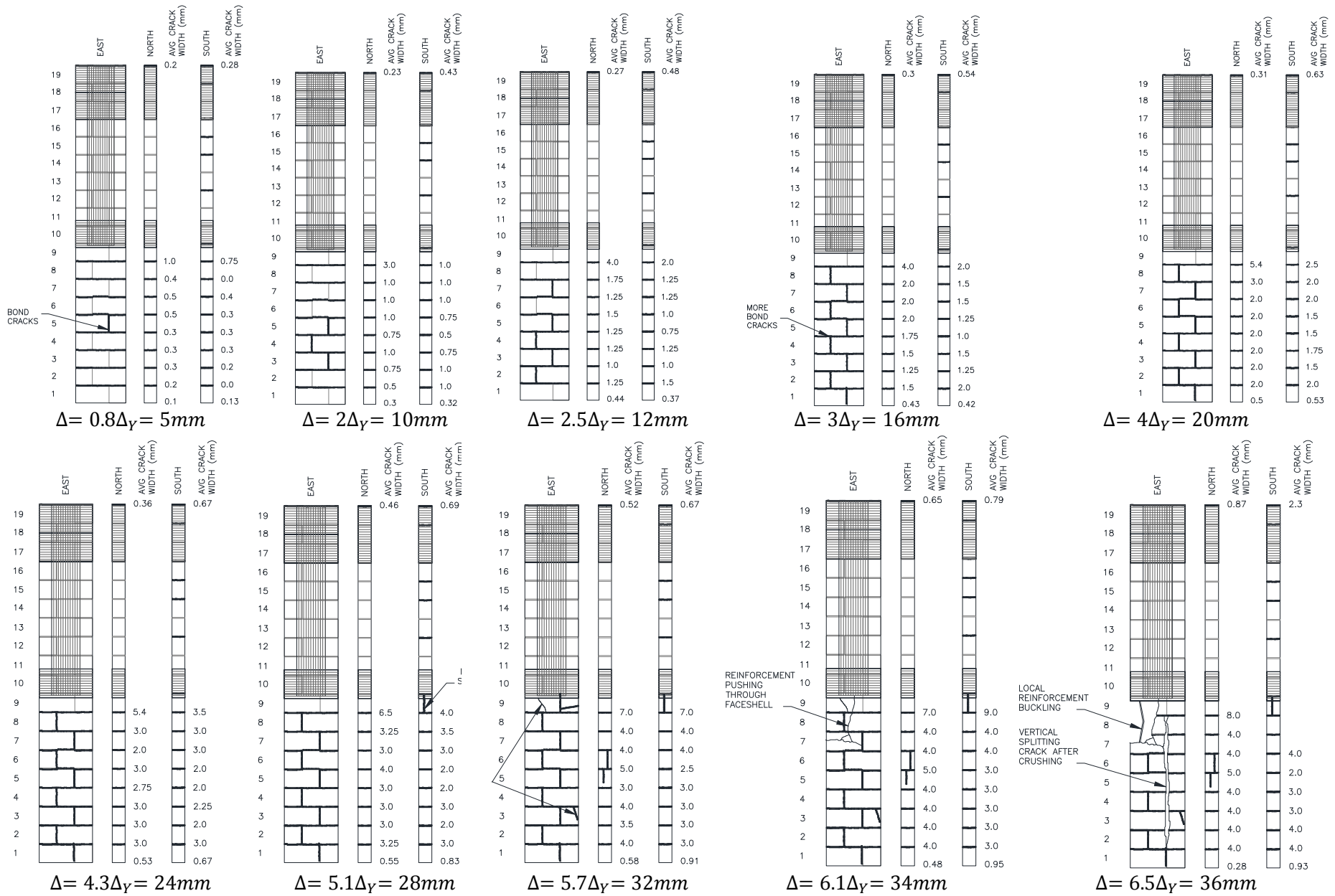


Figure 4-54 Crack patterns at increasing tensile displacement levels for specimen C5

### 4.3 Summary of Experimental Results

From the results of the experimental study, it appears that the level of applied tensile strain as a function of the height and thickness is a useful tool in characterizing out-of-plane instability as a mode of failure. Even though specimen C1 was quite slender with a  $h/t$  ratio of 27, it failed in pure crushing in the absence of preceding application of tensile strains. In specimen C2, horizontal cracks formed at every bedjoint when subjected to tensile strains. The size of the cracks increased and their distribution became more uniform with increasing tensile strains. Beyond the steel yield point, the specimen began experiencing out-of-plane displacements even at low compressive loads. However, further application of compressive loads caused the rotated cracks to close at one end and masonry blocks were engaged in resisting compression. For as long as this crack closure occurred before the specimen had moved out-of-plane an amount close to half its thickness, the engagement of masonry blocks in resisting compression caused the specimen to return to its original straight shape. Beyond an out-of-plane displacement equal to half the specimen thickness, crack closure at one face resulted in out-of-plane instability of the specimen and local crushing of masonry.

A similar behaviour was observed in specimens C3, C4 and C5 with the difference that tensile cracking was limited to the lower half of the specimen through the application of GFRP over the top half of these specimen. Therefore, it was expected that the location of the maximum out-of-plane displacement would also be shifted to the bottom quarter of these specimen. However, this was only the case for specimen C4 and C5. In specimen C3, due to existing cracks in the upper half of the specimen underneath the applied layers of GFRP, the plastic hinge was much larger than half the specimen height. Though, it must be noted that in specimen C5, the out-of-plane displacements measured at midheight were quite similar to those measured at the lower quarter point. It was also observed that the lower height of the plastic hinge required the application of larger tensile strains to cause out-of-plane instability in these specimen.

It also appears that reinforcement ratio plays a role in determining whether the wall will fail in out-of-plane instability. This is because the specimen with the least amount of reinforcing ratio (specimen C5 with  $\rho_f=0.24\%$ ) and the smallest bar size failed in local buckling of reinforcement as opposed to general lateral instability.

These observations will be taken into account in characterizing out-of-plane instability as a failure mode in the next chapter.

## **Chapter 5: Characterization of Lateral Instability**

The axially loaded uniaxial specimens tested in the experimental portion of this study represent the idealized end-zone of a reinforced masonry shear wall subjected to in-plane reversed cyclic lateral loads during an earthquake. The experimental results indicate that the out-of-plane instability of such shear walls is a predictable mechanism. Therefore, as a starting point, an effort has been made to characterize the instability of axially loaded reinforced masonry columns discussed in the previous chapter, bearing in mind that the strain gradient expected across the section of a real wall has not been taken into account. For ease of description, the specimens will simply be referred to as columns in this chapter.

### **5.1 The General Behaviour of Reinforced Masonry Columns Subjected to Cyclic Axial Tension and Compression Loading**

As is evident from the results of the experimental study, all specimens subjected to reversed cyclic axial tension and compression loading, followed a general pattern of behaviour. A similar behaviour pattern was previously observed by Chai and Elayer (1999), and before that by Paulay and Priestley (1993), in reinforced concrete columns and walls respectively, subjected to cycles of axial tension and compression. In a similar approach to that used by Chai and Elayer (1999), the plot of the axial force versus nominal axial strain, as shown in Figure 5-1 is used to describe the basic behaviour of the columns tested for this study. For purposes of comparison, efforts were made to use the same notation and the same labeling system for pertinent points, as that used by the abovementioned authors.

The nominal axial strain is the average strain along the height of the column over which tensile cracking is possible. This height for specimen C2 corresponds to the whole height of the column (3800 mm). Although it was intended that in specimens C3 through C5 this height would correspond to the un-stiffened half of the column, from the results of the experimental study, it is evident that some cracking also took place in that portion of the column that was retrofitted with GFRP. Therefore, with the knowledge that the reinforcing steel yielded at 0.26% of tensile strain, (see Figure 3-14) an effective plastic hinge length is determined from the column deformation that resulted in tensile yielding. Note that even though strain gauges were not used to measure the exact point at which yielding occurred, this point was easily identifiable from the plateau formed on the real-time plot of axial load versus axial deformation displayed on the data acquisition system during testing. For simplicity, this height is referred to as the plastic hinge height hereafter.

The normalized out-of-plane displacement is the maximum measured lateral displacement of the column divided by its thickness. It must be noted that tension is taken as positive force throughout this document. It must also be noted that as is the case for most masonry structures, the figures shown here and the subsequent discussion are based on the assumption that there is one layer of reinforcement in the column. This is a distinct and important difference between this study and that described by Chai and Elayer (1999).

As seen in the previous chapter, the loading protocol for specimens C2 to C5 consisted of incrementally increasing cycles of tension followed by cycles of compression that loaded the

specimen up to a fraction of its compressive strength at which point all cracks closed and the specimen restored its straightness. As such, the general behaviour of the column can be described as a series of events, identified on Figure 5-1, as points *o* through *h*.

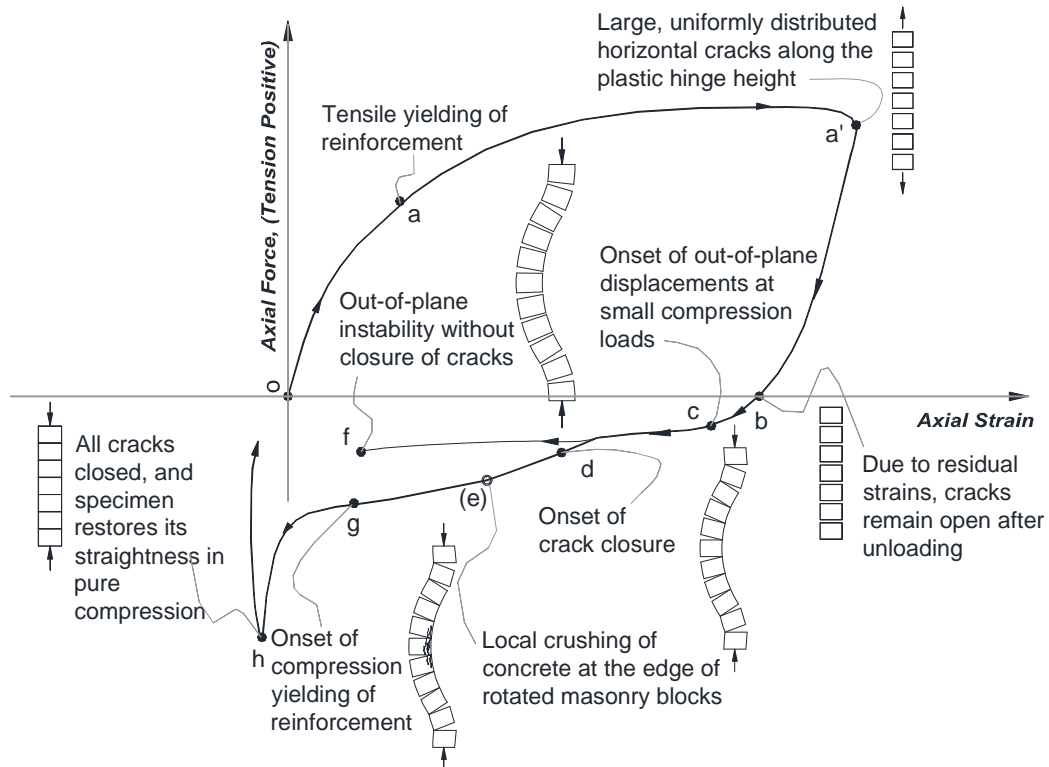


**Figure 5-1** Axial reversed cyclic response of a reinforced masonry column with point (e) only occurring during the loading cycle corresponding to lateral instability

The column is loaded in tension through the path *o-a'*, and after passing through point *a*, which corresponds to the tensile yielding of its reinforcement, begins to experience plastic tensile strains and a degree of strain hardening until the end of the tension half cycle indicated by point *a'*. At this point, large, uniformly distributed horizontal cracks have appeared over the plastic hinge height. Also, since the hypothetical column discussed here is assumed to be ideal, the out-of-plane displacements due to straightening of the misaligned reinforcing bars inside the column are considered negligible. However, in reality, as was discussed in Section 3.4.1.5, severe misalignment of reinforcement may lead to de-bonding of rebar from grout in tension cycles and increase the possibility of failure by local buckling of reinforcement.

Upon unloading from the large tensile peak (point *a'*), the reinforcing bars will recover some of their elastic strain, as expected, resulting in reduced size of the open cracks at the bedjoints (point *b*). It is assumed that contraction of masonry and grout during this phase is negligible.

Upon reloading in compression, the size of cracks are further reduced as the column is loaded through the path *b-c*. During this phase, the reinforcing bars will have to carry all

compression across the cracks. Since there is only a single layer of reinforcement and grouted units will only provide additional bending stiffness between cracks, at very low compressive loads reinforcing bars, and hence the entire wall, will begin to move out of plane (i.e. buckle) over the full length of the plastic hinge. This out-of-plane displacement essentially causes the rotation of the horizontal cracks during a downward movement as shown in Figure 5-2.

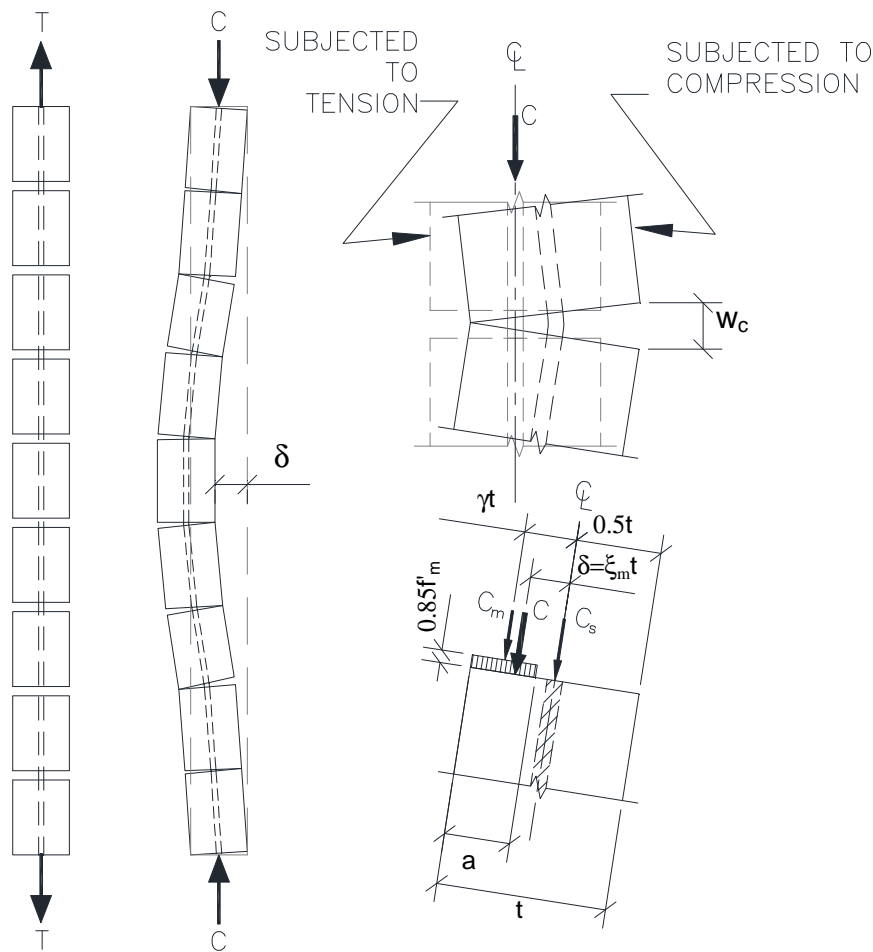


**Figure 5-2 Vertical forces across the wall thickness**

With added compression, along the path *c-d*, the entire column will follow the out-of-plane deformed shape of the reinforcing bars until open cracks begin to close at one end as shown in Figure 5-2. This is because the transverse rotation across the open cracks increases. If the size of the open cracks are sufficiently small, contact will be achieved at one end of the rotated crack (as shown in Figure 5-2). Compression forces will develop at the point of contact, as shown in Figure 5-2, creating a restoring moment which leads to further closure of cracks as indicated by path *d-h*.

As can be seen, both concrete and steel are engaged in resisting the applied compression force or:

$$C = C_m + C_s \quad 5-1$$

Taking moments about the centre-point along the column thickness gives:

$$C_m(\gamma t) = C\delta \quad \text{where} \quad \delta = \xi t \quad 5-2$$

With increasing out-of-plane displacements,  $\delta$ , the location of the total compression force gets closer and closer to the location of the resultant masonry compression force developed along the edge. At the extreme case where,  $C_m = C$ , the lever arm for the masonry stress block approaches half the column thickness or  $\gamma = \xi = 0.5$ . Therefore, from Figure 5-2, it is evident that the column will become unstable if the out-of-plane displacement,  $\delta$ , exceeds half the thickness of the column (i.e. if  $\xi = 0.5$ ). This out-of-plane displacement causing instability will be referred to as critical displacement hereafter.

Note that this critical displacement is related to the location of the reinforcement along the thickness of the wall. For example, if the reinforcing bars are placed exactly centered over the column width, then this critical out-of-plane displacement will be half the thickness of the column.

If the masonry compression forces develop at one edge of the crack prior to the point at which out-of-plane displacements exceed critical, the specimen will continue to restore its straightness with increased compression, leading to compression yielding of the reinforcement (point *g*). At the end of the compression half cycle, all cracks are closed and the masonry cross-section is fully engaged in resisting compression forces. This is indicated by point *h*.

If out-of-plane displacements are larger than or equal to critical prior to closure of cracks, the column will continue to move laterally, even after cracks start to close at one corner, until the compressive stress on that corner exceeds the compressive strength of masonry and the column crushes locally. This is represented by point *e*, in Figure 5-1, and corresponds to the ultimate limit state where crushing of the concrete occurs under the combined axial force and the P- $\Delta$  moment.

However, if the cracks are too large at point *c* such that under increased compressive loads no contact at one edge of the crack is achieved with out-of-plane movement of the wall, the wall will become unstable as indicated by point *f*.

It must be noted that although there are substantial similarities between the hysteretic of response of reinforced masonry specimens tested here and the reinforced concrete specimens tested by Chai and Elayer (1999), there is one important difference and that is the level of load at which the plateau between points *c* and *d* occurs. Chai and Elayer argue that for reinforced concrete with two layers of reinforcement, such a plateau is linked to the compression yielding of steel reinforcement. However, as mentioned previously, in the case

of the reinforced masonry specimens tested here, this plateau occurs at very low compressive loads (near-zero) which clearly rules out reinforcement compression yielding. Instead, this is attributed to the global out-of-plane displacement of the column which occurs because the reinforcement bars, being the only components engaged in resisting compression forces at point *b*, begin elastic buckling over the entire length of the plastic hinge at low compression loads. Refer to Figure 5-3 for a chart of critical buckling load vs. Unsupported height for the different reinforcement schemes present in the specimens tested.

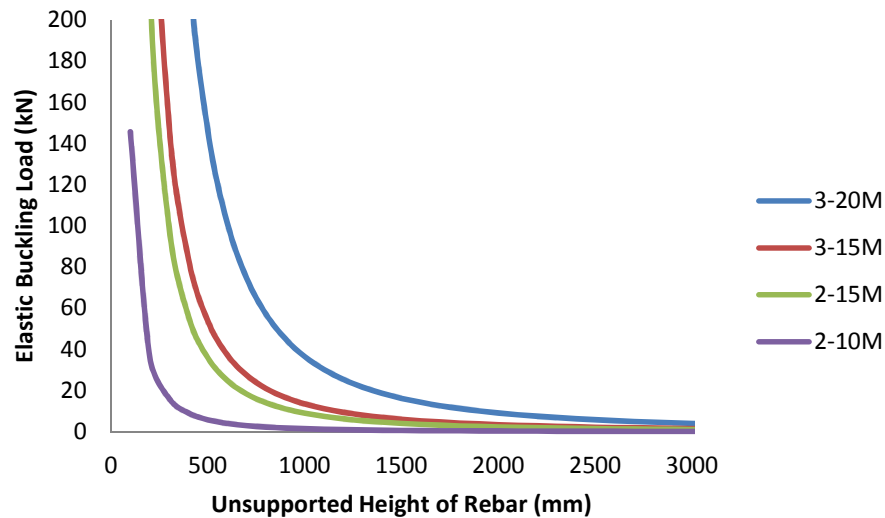


**Figure 5-3 Elastic buckling load of rebar for the different reinforcement schemes**

From the above Figure, it is confirmed that for unsupported heights larger than 1500 mm, which was the case for all specimens, the reinforcement will start to buckle at very low loads (close to zero). This is consistent with the experimental results presented in the previous chapter.

For purposes of characterizing the out-of-plane instability of reinforced masonry columns/walls, the maximum tensile strain, after which the column will be vulnerable to lateral instability can be determined in terms of column physical parameters such as its thickness, height, its boundary conditions and the location of reinforcement along its width. In other words, the goal is to determine the maximum tensile strain corresponding to point *a'* which will lead to the column moving to point *f* in compression. This tensile strain leading to wall instability, which we will call  $\epsilon_{sm}$ , can then be compared to the tensile strain demands on a wall based on ductility demands anticipated from NBCC (2010) seismic design forces.

## 5.2 Strain-Based Design Criteria

The inelastic tensile strain demand in the end zone of a reinforced masonry wall,  $\epsilon_{id}$ , implied by 2010 NBCC can be determined based on the required ductility level, expressed as the product of the ductility and overstrength factors,  $R_d$  and  $R_o$  in NBCC. Comparing this strain demand with the maximum tensile strain,  $\epsilon_{sm}$ , which will lead to out-of-plane instability can lead to the development of a design criteria as follows

$$\epsilon_{id} \leq \epsilon_{sm}$$

This would be similar to the ductility check for reinforced concrete shear walls as per CSA A23.3 Cl. 21.6, except that the concrete code prescribes a rotation check.

The inelastic strain demand,  $\epsilon_{id}$ , can be determined based on the lateral displacements corresponding to the design loads and an assumed plastic hinge length. In general terms,  $\epsilon_{id}$  can be estimated based on the given wall properties and the expected/desired ductility levels.

In the remainder of this Chapter, Section 5.3.1 explores an approach to estimating  $\epsilon_{sm}$ , according to the mechanism described in section 5.1, while Section 5.4 discusses the approach to determining  $\epsilon_{id}$  based on reinforced masonry wall properties and the required ductility level.

### 5.3 Characterizing Out-of-plane Instability of Reinforced Masonry Columns

As discussed previously, after a cycle of large axial tension, the axial force-strain response of an idealized reinforced masonry column will either follow path *c-d-e* or *c-f*, in compression, as shown in Figure 5-1a. What happens in the compression half cycle largely depends on the magnitude of the preceding tensile strains imposed on the section. Therefore, tensile strains endured by the end-zone of a reinforced masonry shear wall in an earthquake event are believed to govern the wall lateral stability. In this section, an effort has been made to estimate the magnitude of the maximum tensile strain that would lead to lateral instability of reinforced masonry columns representing the shear wall end zone.

To avoid lateral instability of reinforced masonry walls, the magnitude of the maximum tensile strain must be such that, in the subsequent compressive cycle, the horizontal cracks formed along the height of the plastic hinge in the wall end zone can close before the maximum out-of-plane displacements, caused by out-of-plane movement of the reinforcement, have become critical. This will allow the section to restore its original straightness and develop its full crushing capacity. As discussed in Section 5.1, it can be assumed that the critical out-of-plane displacement is equal to half the wall thickness, unless the reinforcing bars are placed off-center.

Beyond this tensile strain limit, the end zone of the wall will experience excessive out-of-plane displacements caused by bar buckling over the full height of the plastic hinge and will either

- a) become unstable as a result of continued lateral displacement without crack closure (path *c-f* in Figure 5-1a) or
- b) crush at the corner of closed cracks due to the combined effects of the applied axial compressive load and its associated P- $\Delta$  effect, prior to reaching the full compressive strength of its cross section (path *c-d-e* in Figure 5-1a).

In order to estimate,  $\epsilon_{sm}$ , we will focus our attention on scenario (a).

### 5.3.1 Determining Maximum Tensile Strain which Leads to Lateral Instability, $\epsilon_{sm}$

In an approach similar to that employed by Chai and Elayer (1999), the maximum tensile strain was written in terms of its constituents according to Figure 5-4.

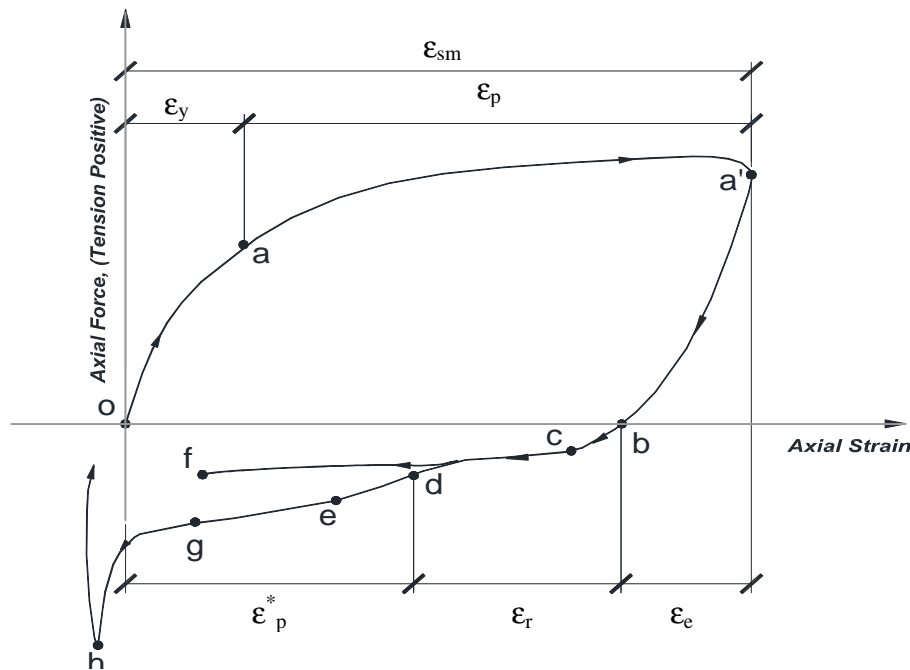


**Figure 5-4** The maximum tensile strain in terms of its constituents

The maximum tensile strain,  $\epsilon_{sm}$ , can be expressed as a sum of

- 1) elastic recovery strain,  $\epsilon_e$ , indicated in Figure 5-4 as the distance between points **a'** and **b**.
- 2) reloading strain,  $\epsilon_r$ , which corresponds to the downward vertical displacement of the column associated with out-of-plane displacement of longitudinal bars under small axial compressive loads up to the onset of crack closure, indicated in Figure 5-4 as the horizontal distance between points **b** and **d**.
- 3) residual axial strain at the onset of crack closure that remains throughout the plastic hinge height in the form of open but rotated cracks,  $\epsilon_p^*$ , represented in Figure 5-4 as the horizontal distance between point **d** and the vertical axis

or

$$\epsilon_{sm} = \epsilon_e + \epsilon_r + \epsilon_p^*$$

**5-3**

The first term corresponds to the elastic recovery process. For an elastic-perfectly plastic tensile response,  $\varepsilon_e$  would be equal to the yield strain. However, given that there may exist some strain hardening, the value of  $\varepsilon_e$  may be larger than yield strain. Assuming that the contraction in masonry is negligible during unloading,  $\varepsilon_e$  can be expressed as proportional to the yield strain of reinforcing steel as follows:

$$\varepsilon_e = \eta_1 \varepsilon_y \quad 5-4$$

where  $\eta_1 > 1.0$ .

The reloading strain,  $\varepsilon_r$ , is the strain needed, in addition to the elastic recovery strain, to cause critical out-of-plane displacements. Note that this strain is essentially a portion of the total tensile strain. However, in compression it is associated with the downward displacement of the column as its reinforcing bars buckle out-of-plane, leading to the rotation of the open horizontal cracks until the point of first crack closure. As discussed previously, when the column is unloaded from its tensile excursion, there still remain large cracks at bed joints along the specimen height. Therefore, any applied axial compression must be entirely resisted by the reinforcing bars. Since these bars extend the whole height of the plastic hinge of the column and have relatively small cross sectional area and moment of inertia, they almost immediately begin to move laterally outward (i.e. buckling over the full length occurs). It is assumed that this continues until the onset of crack closure due to rotation of the section. Based on this mechanism, the reloading strain can be approximated based on an idealized buckled shape.

Assuming fixed-fixed boundary conditions and ignoring the fact that the reinforcing bars more or less remain straight through the height of the blocks in which they are encased<sup>1</sup>, the deformed shape can be determined by solving the second order differential equation corresponding to the curvature of the column along its height,  $\varphi$ , as follows

$$\varphi = \frac{d^2y}{dx^2} = \frac{M}{EI} + \frac{Cy}{EI} \quad 5-5$$

Where,  $M$  is the applied moment,  $E$  is the material modulus of elasticity,  $I$  is the moment of inertia of the cross section along the weak axis,  $C$  is the applied compressive load and  $y$  is the varying out-of-plane displacement. The term  $Cy$  corresponds to  $P-\Delta$  effects. For simplicity, equation 5-5 will be solved for two separate boundary conditions present during the experimental study as follow:

---

<sup>1</sup> This assumption is justifiable since at large strains, strain penetration into grout will lead to bond failures within the grouted blocks and horizontal cracks may form along the height of individual masonry courses as well as at bedjoints.

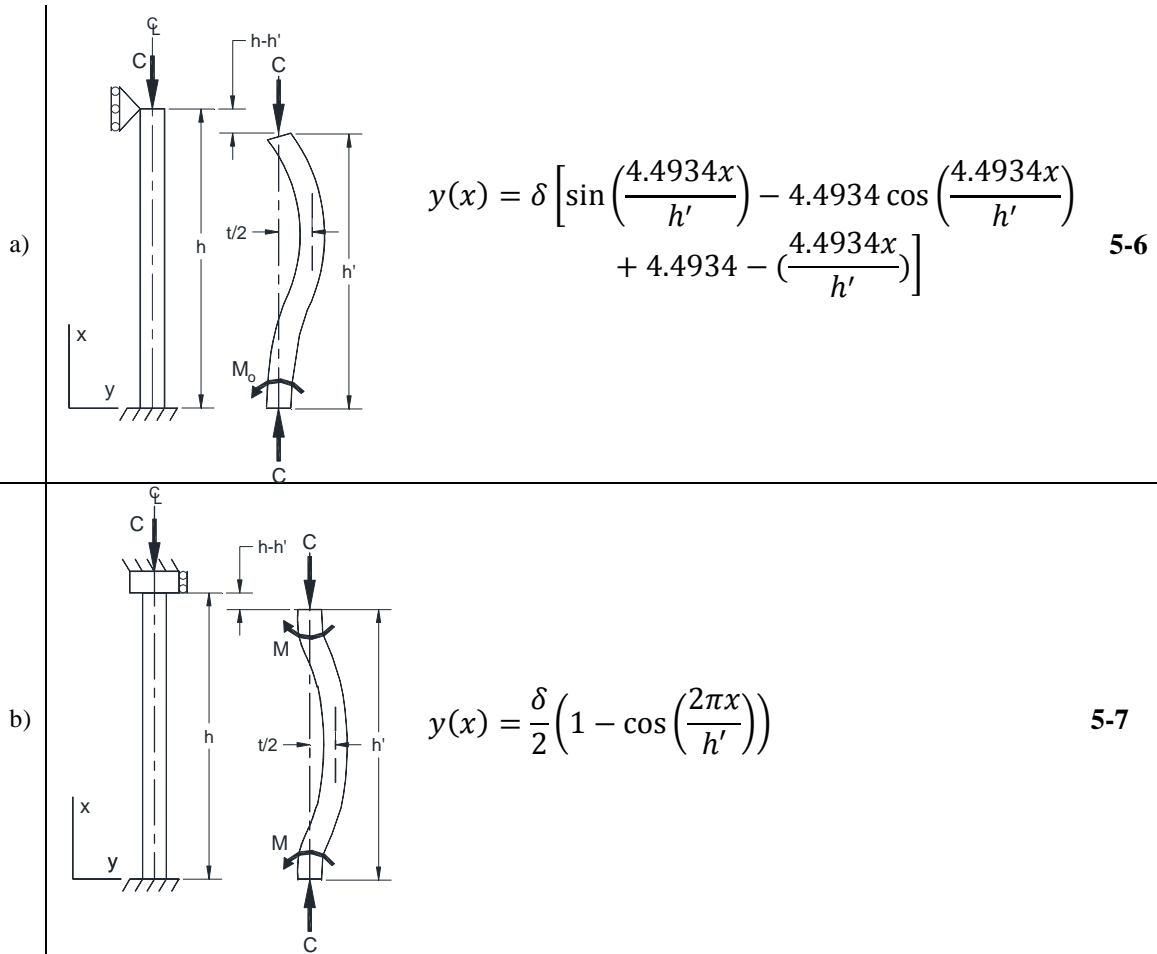


**Figure 5-5 The assumed deformed shape of the wall end zone under pinned-fixed and fixed-fixed boundary conditions**

Based on the assumption that the buckled shape, with its maximum amplitude equal to half the column thickness (corresponding to the onset of crack closure), the reloading strain can be determined by calculating the vertical displacement ( $h-h'$ ) due to the assumed buckled shape. This is done by determining the change in height of the column from the point the elastic recovery is complete (point **b** in Figure 5-1) and the point where cracks begin to close (point **d** in Figure 5-1). Assuming that the deformed shape is determined by equation 5-7, this height change can be written as follows:

$$\Delta h = h - h' = \int_0^{h'} \sqrt{1 + \left(\frac{dy}{dx}\right)^2} dx - h' = \int_0^{h'} \sqrt{1 + \left(\frac{\delta\pi}{h'} \cdot \sin\left(\frac{2\pi x}{h'}\right)\right)^2} dx - h' \quad 5-8$$

Note that, since the total height of the deformed shape was assumed to be equal to  $h'$  at the time when the equation of the deformed shape was being developed, the arclength calculated based on the deformed shape is naturally larger than  $h'$  and is assumed to correspond to  $h(1 + \epsilon_{sm} - \epsilon_e)$ . Furthermore, the term in the integral in equation 5-8 can be written more simply as the first two terms of its Taylor series as:

$$f(x) = \sqrt{1 + \left[ \frac{\delta\pi}{h'} \cdot \sin\left(\frac{2\pi x}{h'}\right) \right]^2} = 1 + \frac{1}{2} \left[ \frac{\delta\pi}{h'} \cdot \sin\left(\frac{2\pi x}{h'}\right) \right]^2 \quad 5-9$$

Substituting equation 5-9 into equation 5-8 gives

$$\Delta h = \int_0^{h'} 1 + \frac{1}{2} \left[ \frac{\delta\pi}{h'} \cdot \sin\left(\frac{2\pi x}{h'}\right) \right]^2 dx - h' = \frac{2.5 \delta^2}{h'} \quad 5-10$$

Therefore, the reloading strain which is the vertical strain required to cause the unloaded column to move out-of-plane an amount equal to the critical out-of-plane displacement (leading to the closure of cracks at one edge) can be written as

$$\varepsilon_r = \frac{\Delta h}{h'} = \frac{2.5 \delta^2}{h'^2} \quad 5-11$$

Assuming that the difference between  $h$  and  $h'$  is small, the reloading strain can be rewritten in terms of the critical lateral displacement as

$$\varepsilon_r = \frac{\Delta h}{h} = 1.25 \xi_m \left(\frac{t}{h}\right)^2 \quad 5-12$$

where, as discussed in Section 5.1,  $\xi_m$ , is the normalized out-of-plane displacement leading to lateral instability, and is related to the location of the reinforcement along the wall thickness. For example, if the reinforcement is exactly centered along the of the wall width, then  $\xi_m = 0.5$ .

It must be emphasized that the reloading strain approximated as above is based on the idealization that the reinforcing bars, which are considered to be homogeneous material, will have a smooth deformed shape whose curvature follows a sinusoidal distribution with the maximum at midheight. As mentioned previously, in reality this is not the case, since the bars will be more straight along the height of each masonry course. Also, it is assumed that at the time when the out-of-plane displacements have reached half the thickness of the wall, the cracks have just begun to close.

With the above assumption, the remainder of the plastic strain may be approximated from what residual strain still remains at the rotated bedjoints. Two different approaches were employed to do this as follows:

1. Estimating residual strains based on an assumed bedjoint rotation distribution
2. Estimating residual strains based on an assumed curvature distribution with maximum at midheight

These two approaches are discussed in Sections 5.3.1.1 and 5.3.1.2 respectively.

### 5.3.1.1 Estimating residual strains based on an assumed bedjoint rotation distribution

In a reinforced masonry wall, the residual strains at the onset of crack closure are concentrated mostly at the bedjoints. This is the case since even though horizontal cracks do form away from bedjoints at high tensile strains, they are relatively few in number and thin compared to those that form at bedjoints.

Under low compressive loads, the reinforcing bars begin to experience out-of-plane displacements which cause the rotation of open cracks as shown in Figure 5-6a. This process eventually results in the overall buckled shape of the column which is dependent on the boundary conditions (see Figure 5-5). A downward vertical displacement takes place during this phase to allow for the rotation of the cracks and formation of the buckled shape. This downward vertical displacement was presented in the previous section as being associated with the reloading strain,  $\epsilon_r$ . At the end of this downward displacement, the open cracks at bedjoints have experienced a vertical rotation as shown in Figure 5-6a. Therefore, if the distribution of these bedjoint cracks can be estimated, the total residual strain corresponding to the critical out-of-plane displacement can be determined based on geometry of the rotated bedjoint cracks.

From Figure 5-6b it can be seen that the relative lateral displacement of each masonry course,  $\delta_i$ , can be written as

$$\delta_i = [\theta_i + \theta_{i-1} + \theta_{i-2} + \cdots + \theta_o]H_b \quad 5-13$$

where  $H_b$  is the height of one masonry block and  $\theta_i$  is the angle of rotation of the bedjoint that precedes the point at which lateral displacement is being considered.

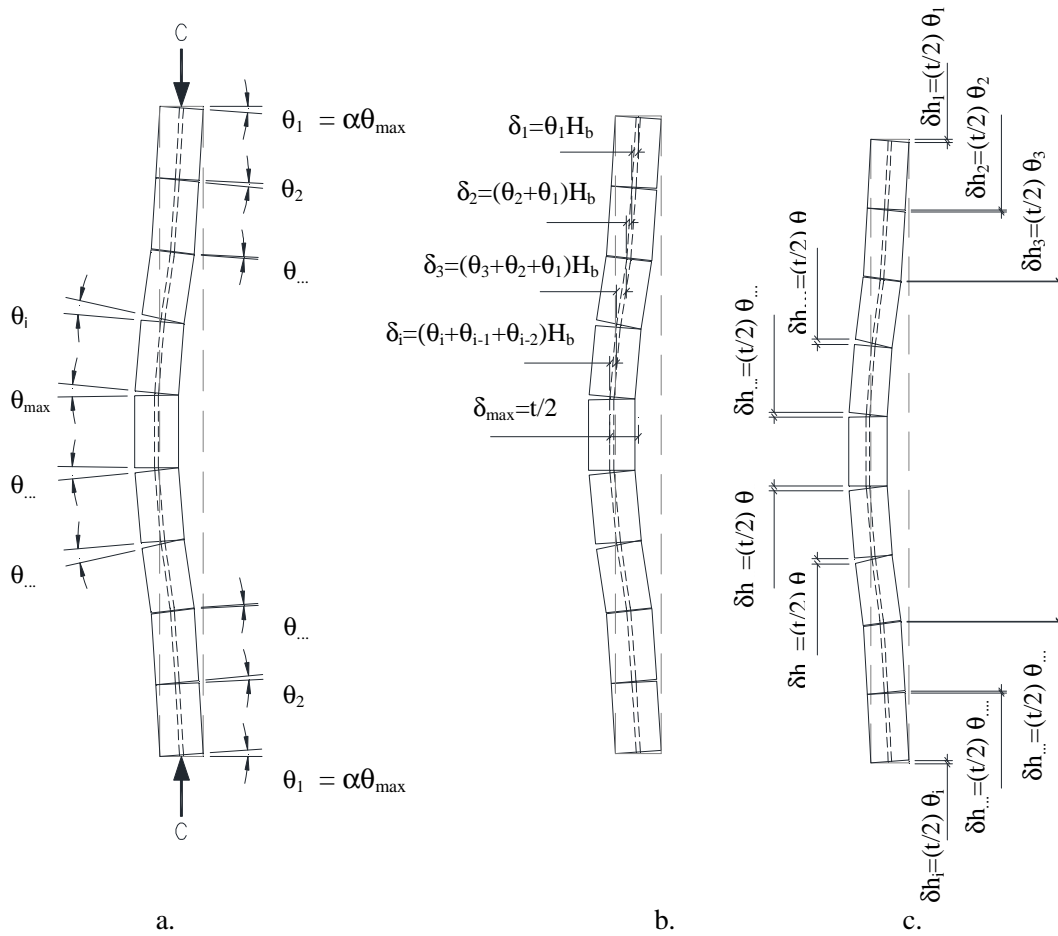


**Figure 5-6 Rotation of bedjoints related to residual plastic strains**

The sum of these relative lateral displacements over half the panel's plastic hinge height will give the maximum lateral displacement as follows:

$$\delta_{max} = \sum_{i=1}^{(h/2)/H_b} \delta_i = \sum_{i=1}^{(h/2)/H_b} \theta_i H_b = (\theta_1 + \theta_2 + \theta_3 + \dots + \theta_i) H_b \quad 5-14$$

where the term  $(h/2)/H_b$  corresponds to the number of bedjoints from the bottom of the plastic hinge zone to the mid-height, where maximum out-of-plane deflection occurs.

Assuming that the bedjoint rotations vary linearly along the height of the plastic hinge, and that the rotations at the boundaries are proportionate to the maximum rotation at midheight by a constant  $\alpha$  (i.e.  $\theta_1 = \theta_{i_9} = \alpha \theta_{max}$ ), gives the following relationship for bedjoint rotation distribution:

$$\theta_i = \alpha \theta_{max} + \frac{2\theta_{max}}{h} (1 - \alpha) H_b (i - 1) \quad \text{for} \quad 1 \leq i \leq \left(\frac{h}{2}\right)/H_b \quad 5-15$$

where  $i$  corresponds to the number of bedjoints from the bottom of the plastic hinge length. Recognizing that the rotations in equation 5-14 are related to each other through equation 5-15, the expression for maximum lateral displacement at midheight can be rewritten as follows:

$$\delta_{max} = \sum_{i=1}^{(h/2)/H_b} \theta_i H_b = \left(\frac{h}{2H_b}\right) H_b \alpha \theta_{max} + \frac{2\theta_{max}}{h} (1-\alpha) H_b^2 \frac{1}{2} \left(\frac{h}{2H_b}\right) \left(\left(\frac{h}{2H_b}\right) - 1\right) \quad 5-16$$

From the above it can be seen that

$$\sum_{i=1}^{(h/2)/H_b} \theta_i = \left(\frac{h}{2H_b}\right) \alpha \theta_{max} + \frac{2\theta_{max}}{h} (1-\alpha) H_b \frac{1}{2} \left(\frac{h}{2H_b}\right) \left(\left(\frac{h}{2H_b}\right) - 1\right) \quad 5-17$$

On the other hand, the height of the rotated cracks at the location of reinforcing bar along the wall thickness is related to the residual strain that remains in that bedjoint. This discrete vertical deformation, shown in Figure 5-6c, can be written in terms of the crack rotations as follows:

$$\Delta h = \sum_{i=1}^{(h/2)/H_b} \delta h = \sum_{i=1}^{(h)/H_b} \theta_i \xi_m t = 2 \sum_{i=1}^{(h/2)/H_b} \theta_i \xi_m t \quad 5-18$$

Substituting equation 5-17 into 5-18 gives

$$\Delta h = 2 \xi_m t \left[ \left(\frac{h}{2H_b}\right) \alpha \theta_{max} + \frac{2\theta_{max}}{h} (1-\alpha) H_b \left(\frac{h}{4H_b}\right) \left(\left(\frac{h}{2H_b}\right) - 1\right) \right] \quad 5-19$$

Finally, assuming that  $\delta_{max} = \frac{t}{2}$  is the critical out-of-plane displacement at which the plastic hinge zone becomes laterally unstable, and also dividing  $\Delta h$  by the height of the plastic hinge to get strains,  $\varepsilon_p^*$  can be written as

$$\varepsilon_p^* = 2 \xi_m t \left[ \left(\frac{1}{2H_b}\right) \alpha \theta_{max} + \frac{2\theta_{max}}{h} (1-\alpha) H_b \left(\frac{1}{4H_b}\right) \left(\left(\frac{h}{2H_b}\right) - 1\right) \right] \quad 5-20$$

where  $\xi_m = 0.5$ . Note that with this approach, it is necessary to determine the discrete sum of all the bedjoint rotations up to the point of maximum deflection. To do this, the distribution of bedjoint rotations along the height must be known.

Unfortunately, during the experimental portion of this study, crack rotations and in particular the maximum crack rotations were not measured. For specimens C3, C4, and C5, linear potentiometers were installed on either side of a single bedjoint, from which insight is provided into the nature of crack rotations. In specimen C3, this instrumentation was

installed at the lower quarter point, while the maximum rotation seemed to occur closer to midheight of specimen. In specimens C4 and C5, this instrumentation was installed at midheight while the maximum rotation occurred closer to the lower quarter point of the specimen.

Figure 5-8, Figure 5-9, Figure 5-10, and Figure 5-11 at the end of the next section illustrate the assumed distribution of crack rotation and the corresponding deformed shape for specimens C2, C3, C4 and C5 respectively.

In the abovementioned figures, the plot to the left is the plot of crack rotation distribution over the plastic hinge height of the specimen. As can be seen, for specimen C2, this height corresponds to the full height of the specimen while for the remainder of the specimens, the plastic hinge is assumed to be concentrated over the lower half. To obtain the plots of crack rotation distribution, the magnitude of the maximum rotation and the factor  $\alpha$  had to be assumed. It was also assumed that the maximum crack rotation occurred at the midheight of the specimen plastic hinge.

The black squares on the plots on the right side of each figure represents the actual measured lateral displacements. As can be seen from the outline of the measured lateral displacements represented by the black squares, in specimens C3, C4 and C5, there was a considerable amount of rigid body rotation over the top half of these specimens. Therefore, the magnitude of the maximum crack rotation and the factor  $\alpha$  were assumed such that they produced the maximum lateral displacements measured during the experiment minus the lateral displacements caused by the rigid body rotation over the top half of specimen.

The plot on the right side of each figure also shows the buckled shape of each specimen according to various possible models. Namely, the curve represented by the solid blue line corresponds to the buckled shape as determined according to the linearly varying crack rotations shown on the plot to the left. The various models represented on this figure will be discussed in more detail at the end of the next section.

Given the linearly varying crack rotations shown on the plots of Figure 5-8 through Figure 5-11, residual plastic strains,  $\epsilon_p^*$ , were calculated according to Equation 5-20 for the normalized lateral displacements listed in Table 5-1. For the same lateral displacements, the elastic recovery strain and the reloading strain were also calculated according to 5-4 and 5-12 respectively. The calculated magnitude of each of these strain components as well as their calculated sum are listed in Table 5-1 under the heading *Calculated*. The lateral displacements listed correspond to the last cycle during testing of each of the specimens. From the test data during that cycle, the same strain components were approximated from the average measured axial deformations and are also listed in Table 5-1.

The elastic recovery strain,  $\epsilon_r$ , was determined as the total displacement between the point of maximum tensile deformation and the point of zero load after unloading from the tension half cycle divided by the height of the plastic hinge. The reloading strain was determined as the total deformation between the point where the compression half cycle began and the point at which compressive loads started to develop more rapidly than the lateral displacements

divided by the height of the plastic hinge. Though this approach is taken since theoretically it corresponds to the distance between points *b* and *d* on the plot of axial load vs. Axial deformation in Figure 5-1, it still is an approximation. Note also that the model proposed to in Section 5.3.1 is highly idealistic and assumes that at point *d*, all cracks simultaneously begin to close at one end and that this point corresponds to the point where the critical lateral displacement has already occurred. In reality this is not exactly what happens and not all cracks close at once and therefore the critical lateral displacement occurs slightly beyond the plateau between points *b* and *d*. The residual plastic strain was then taken as the remainder of the applied tensile strain during the same loading cycle.

**Table 5-1 Comparison between experimental total tensile strain leading to lateral instability and calculated maximum tensile strain based on crack rotations**

Specimen	h (mm)	$\xi_m = \frac{\delta_{max}}{t}$	Experimental				Calculated			
			$\epsilon_e$	$\epsilon_r$	$\epsilon^*_p$	$\epsilon_t$	$\epsilon_e = \eta_1 \epsilon_y$	$\epsilon_r$	$\epsilon^*_p$	$\epsilon_{sm}$
C2	3800	0.44	0.30%	0.10%	0.39%	<b>0.79%</b>	0.31%	0.08%	0.41%	<b>0.80%</b>
C3	3462	0.46	0.31%	0.08%	0.40%	<b>0.80%</b>	0.31%	0.10%	0.93%	<b>1.34%</b>
C4	2385	0.40	0.39%	0.18%	1.13%	<b>1.69%</b>	0.31%	0.17%	0.99%	<b>1.47%</b>
C5	2192	0.42	0.32%	0.09%	1.05%	<b>1.46%</b>	0.31%	0.22%	0.99%	<b>1.52%</b>

Table 5-1 indicates that the elastic recovery strains,  $\epsilon_e$ , calculated according to Equation 5-4 are a relatively good match for the elastic recovery strains measured during the experiment. The biggest discrepancy between the experimental elastic recovery strains and that calculated is the 21% difference for specimen C4. The calculated reloading strain also matches the experimental reloading strains for specimens C2 through C4 but reveals a 144% discrepancy for specimen C5. The biggest difference between the calculated and experimental residual plastic strains exists for specimen C3. These discrepancies for specimens C3 through C5 are in part attributed to the extra complexity introduced in the behaviour of these specimens through the application of GFRP over their top half. This is specially the case for specimen C3 which was retrofitted with GFRP applied over existing open cracks.

However, in the case of specimen C2 whose behaviour was least influenced by external factors, all three calculated strain components seem to produce a close match to the strains measured during the experiment. This suggests that the model proposed in Section 5.3.1, though idealistic, is applicable to the prediction of maximum tensile strains leading to out-of-plane instability in the end zone of RM shear walls. However, the disadvantage of estimating the residual plastic strains through the application of a discrete sum as presented here is that information about the size and number of blocks as well as specific information about the distribution of crack rotations (i.e. maximum crack rotation, etc.) must be available to the designer. Since this information is not usually available, another approach which relies on an assumed curvature distribution to estimate residual plastic strains is proposed in the next section.

### 5.3.1.2 Estimating residual strains based on an assumed curvature distribution

With this approach, it is assumed that the total residual plastic strain that remain in the buckled shape of the specimen in the form of open cracks can be estimated based on the maximum transverse curvature,  $\varepsilon_p^*$ , in the reinforcing steel, occurring at midheight of the plastic hinge as follows:

$$\varepsilon_p^* = 0.5t \varphi_{max} \quad 5-21$$

Note that the above equation is valid based on the assumption that horizontal cracks through the specimen plastic hinge height are equal. Given equal height of blocks, the total strain over the plastic hinge height is therefore equal to the strain at the location of maximum curvature at midheight. There are several different approaches in estimating the maximum curvature based on the assumption of the buckled shape. For example, if the deformed shape is assumed to be circular, then curvature is distributed uniformly. With the assumption of the deformed shape as  $y(x) = \frac{\delta_{max}}{2} \left[ 1 - \cos\left(\frac{2\pi x}{h}\right) \right]$ , radius of curvature at midheight can be determined as

$$R_{x=\frac{h}{2}} = \frac{\left[ 1 + \left( \frac{dy}{dx} \right)^2 \right]^{3/2}}{\frac{d^2x}{dy^2}} \bigg|_{x=\frac{h}{2}} = \frac{h^2 \left[ 1 + \frac{\delta_{max}^2 \sin^2\left(\frac{2\pi x}{h}\right) \pi^2}{h^2} \right]^{3/2}}{2 \delta_{max} \cos\left(\frac{2\pi x}{h}\right) \pi^2} \bigg|_{x=\frac{h}{2}} = \frac{1}{2\pi^2} \left( \frac{h^2}{\delta_{max}} \right) \quad 5-22$$

Rearranging the above equation gives

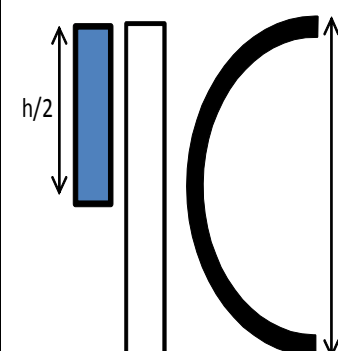
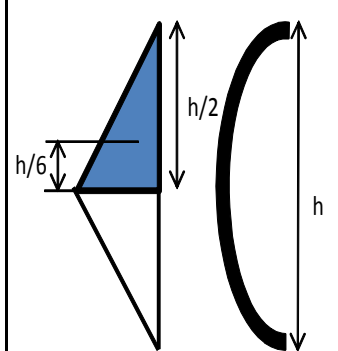
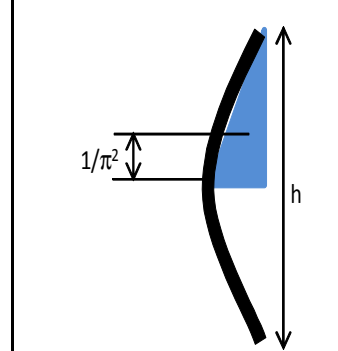
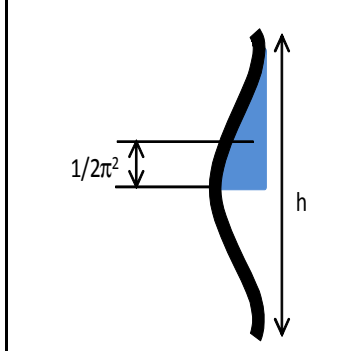
$$\varphi_{max} = 2\pi^2 \left( \frac{\delta_{max}}{h^2} \right) \quad 5-23$$

where maximum out-of-plane displacement leading to instability,  $\delta_{max}$ , can be written as a proportion of the wall thickness, depending on the location of reinforcing bars along wall width, or  $\delta_{max} = \xi_m t$ . Substituting equation 5-23 into equation 5-21 gives

$$\varepsilon_p^* = \xi_m \left( \frac{\pi t}{h} \right)^2 \quad 5-24$$

The residual plastic strain using the above approach has been calculated for different curvature distribution models as listed in Table 5-2, where coefficient  $1/c$  refers to the constant multiplied by the term  $\left( \frac{\delta_{max}}{h^2} \right)$  to give  $\varphi_{max}$ .

**Table 5-2 Residual plastic strain based on different curvature models**

	Curvature Distribution															
	Uniform				Linear w $\phi_{max}$ at $h/2$				Sinusoidal				Based on deformed shape			
Boundary condition																
	pin-pin				pin-pin				pin-pin				fixed-fixed			
$c=$	0.13				0.08				0.10				0.05			
Specimen	C2	C3	C4	C5	C2	C3	C4	C5	C2	C3	C4	C5	C2	C3	C4	C5
$\xi_m=$	0.435	0.459	0.404	0.422	0.435	0.459	0.404	0.422	0.435	0.459	0.404	0.422	0.435	0.459	0.404	0.422
$\delta_{max}=$	60.9	64.26	56.56	59.08	60.9	64.26	56.56	59.08	60.9	64.26	56.56	59.08	60.9	64.26	56.56	59.08
$h=$	3800	3462	2385	2192	3800	3462	2385	2192	3800	3462	2385	2192	3800	3462	2385	2192
$0.8 \cdot h=$	3040	2769	1908	1754	3040	2769	1908	1754	3040	2769	1908	1754				
$\epsilon_p^*=$	0.37%	0.47%	0.87%	1.08%	0.55%	0.70%	1.31%	1.61%	0.46%	0.58%	1.07%	1.33%	0.58%	0.74%	1.37%	1.70%
$\epsilon_{p\text{ experimental}}^*=$	0.39%	0.40%	1.13%	1.05%	0.39%	0.40%	1.13%	1.05%	0.39%	0.40%	1.13%	1.05%	0.39%	0.40%	1.13%	1.05%

Note that in Table 5-2, the effective height over which the curvature was integrated was taken as 80% of the plastic hinge length to account for boundary conditions. From Table 5-2, it appears that using a circular curvature distribution, integrated over half of the effective height gives more consistent results for  $\varepsilon_p^*$  with experimental values. However, it must be noted that the circular curvature distribution is not consistent with the assumption of a sinusoidal buckled shape. Though, it must also be noted that a circular curvature distribution was used by Paulay and Priestley (1993) in their efforts to characterize the instability phenomena in reinforced concrete and reinforced masonry shear walls.

Equation 5-25 relates residual plastic strain based on the circular distribution of curvature along the plastic hinge height.

$$\varepsilon_p^* = 4 \xi_m \left( \frac{t}{h} \right)^2 \quad 5-25$$

Therefore, as a preliminary approach, the above equation will be used to predict residual plastic strains. Substituting equations 5-4, 5-12, and 5-25 into back into equation 5-3 gives an estimate of the maximum tensile strain,  $\varepsilon_{sm}$ , as follows:

$$\varepsilon_{sm} = 5.25 \xi_m \left( \frac{t}{h} \right)^2 + \eta_1 \varepsilon_y \quad 5-26$$

where,  $\eta_1$  is related to the amount of strain hardening. Based on the results of the experimental study,  $\eta_1$  is assumed to be equal to 1.2.

**Table 5-3 Comparison between experimental total tensile strain leading to lateral instability and calculated maximum tensile strain based on linear curvature distribution**

Specimen	h (mm)	$\xi_m$ = $\delta_{max} t$	Experimental				Calculated			
			$\varepsilon_e$	$\varepsilon_r$	$\varepsilon_p^*$	$\varepsilon_t$	$\varepsilon_e$ = $\eta_1 \varepsilon_y$	$\varepsilon_r$	$\varepsilon_p^*$	$\varepsilon_{sm}$
C2	3800	0.44	0.30%	0.10%	0.39%	<b>0.79%</b>	0.31%	0.08%	0.37%	0.76%
C3	3462	0.46	0.31%	0.08%	0.40%	<b>0.80%</b>	0.31%	0.10%	0.47%	0.88%
C4	2385	0.40	0.39%	0.18%	1.13%	<b>1.69%</b>	0.31%	0.17%	0.87%	1.35%
C5	2192	0.42	0.32%	0.09%	1.05%	<b>1.46%</b>	0.31%	0.22%	1.08%	1.61%

Note that the only difference between Table 5-1 and Table 5-2 is in the calculated residual plastic strains and consequently the calculated sum of the strain components giving the maximum tensile strain leading to instability. Refer to Section 5.3.1.1 for details on how the experimental strain components were determined. However, note that there is some error associated with the experimental strain components listed above as they were interpreted from experimental data. It must also be kept in mind that the approaches employed here in estimation of  $\varepsilon_r$  and  $\varepsilon_p^*$  are highly idealistic since not all cracks begin closing simultaneously. Moreover,  $\varepsilon_p^*$  is determined based on the assumption that there is a continuous distribution of curvature over the effective height of the plastic hinge despite the

fact that due to the nature of masonry construction, there are discrete rotations at bedjoints as opposed to a continuous curvature.

However, for the purposes of estimating tensile strain levels leading to lateral instability, and in the absence of more test data, this is deemed an appropriate preliminary step. Further experimental studies on reinforced masonry columns and particularly on reinforced masonry walls are required to improve the accuracy of predicting the limiting tensile strain levels

So far in Sections 5.3.1.1 and 5.3.1.2, two different approaches to estimating the residual plastic strains were introduced. Together with the elastic recovery strain and the reloading strain, the estimate of the residual plastic strain will help predict a maximum tensile strain beyond which the column specimen becomes susceptible to failure in out-of-plane instability.

The plots of Figure 5-8 through Figure 5-11 illustrate the buckled shape of specimens C2 through C5 obtained based on the discrete sum of bedjoint rotations compared with experimental data as well as the buckled shape determined based on the sinusoidal mode shapes introduced in Section 5.3.1. As was mentioned in the previous section, the plot on the left side of each Figure represents the assumed distribution of crack rotations. The square black markers on the plot to the right indicate the lateral displacements measured during the experiment.

Also, note that as mentioned previously the height of the plastic hinge for each specimen was determined according to the point at which the reinforcement yielding was observed. Figure 5-7 illustrates the impact that the assumed length of the plastic hinge (as a proportion of the specimen height) has on the predicted value of  $\epsilon^*_p$ .

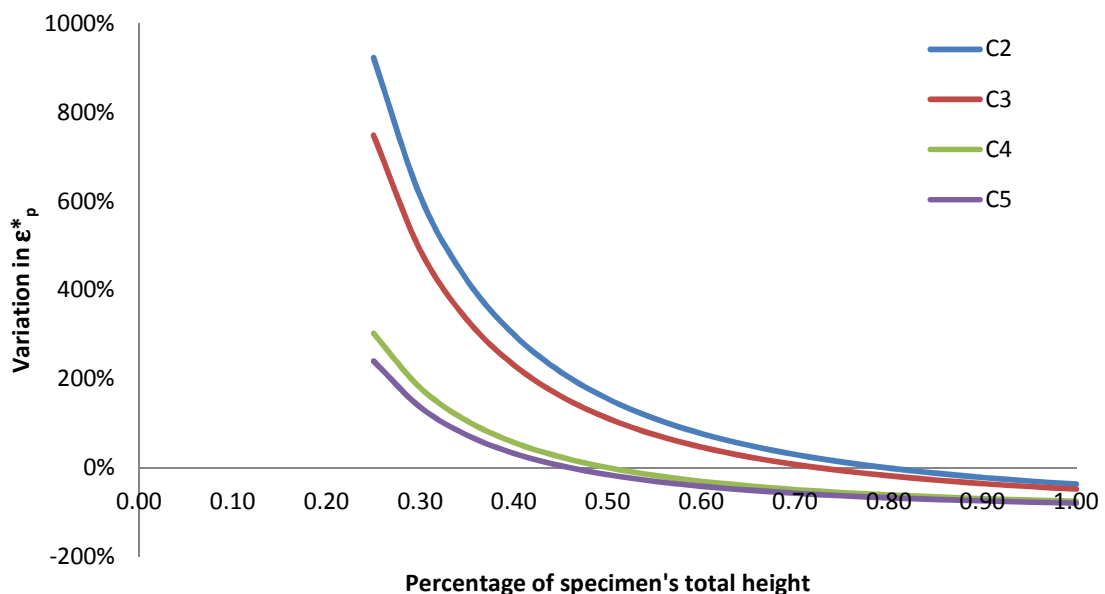


**Figure 5-7** Variation of the residual plastic strain vs. assumed length of plastic hinge

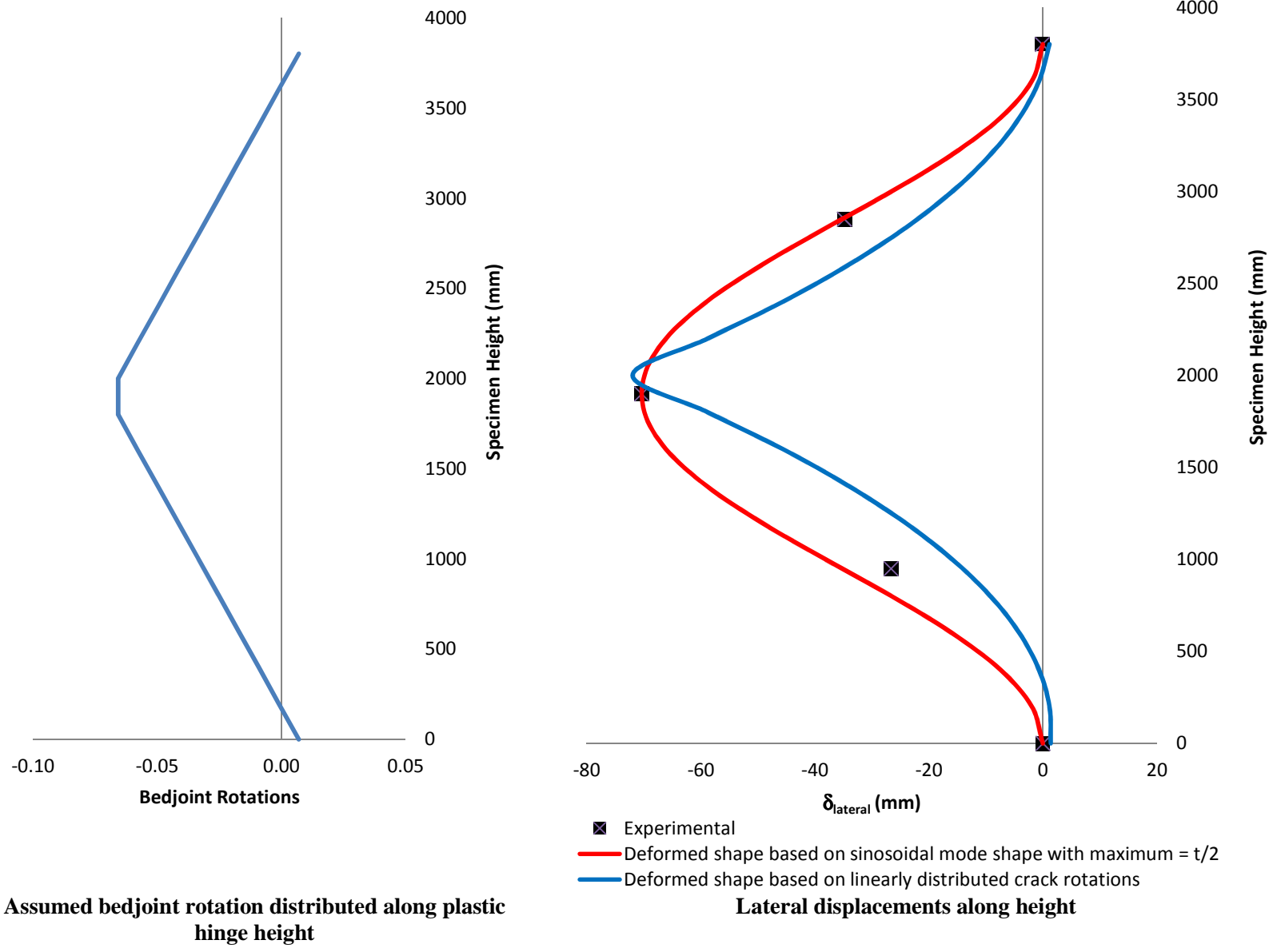
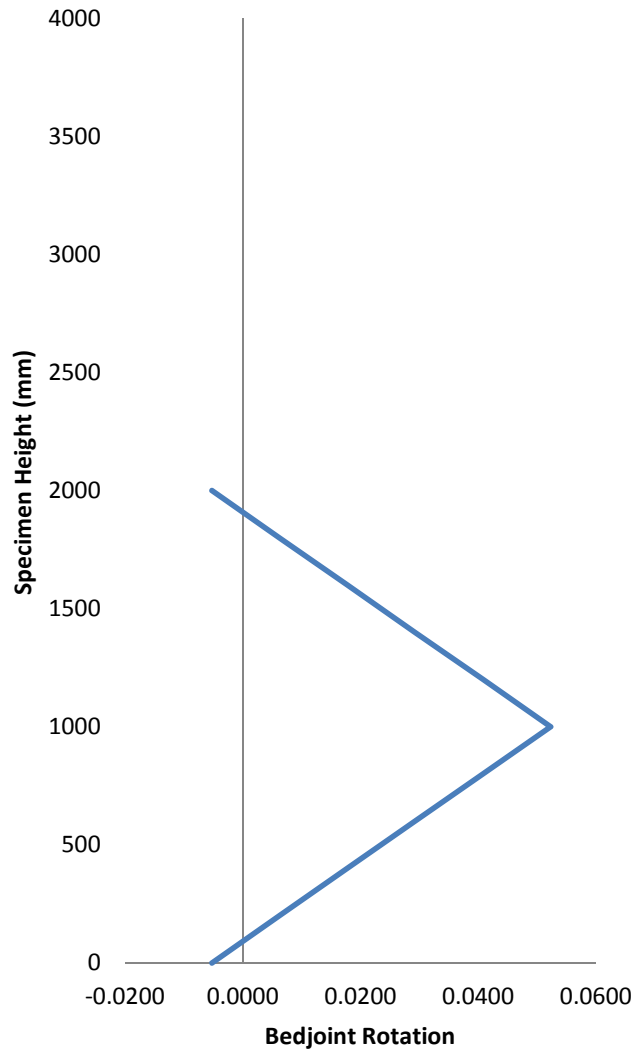
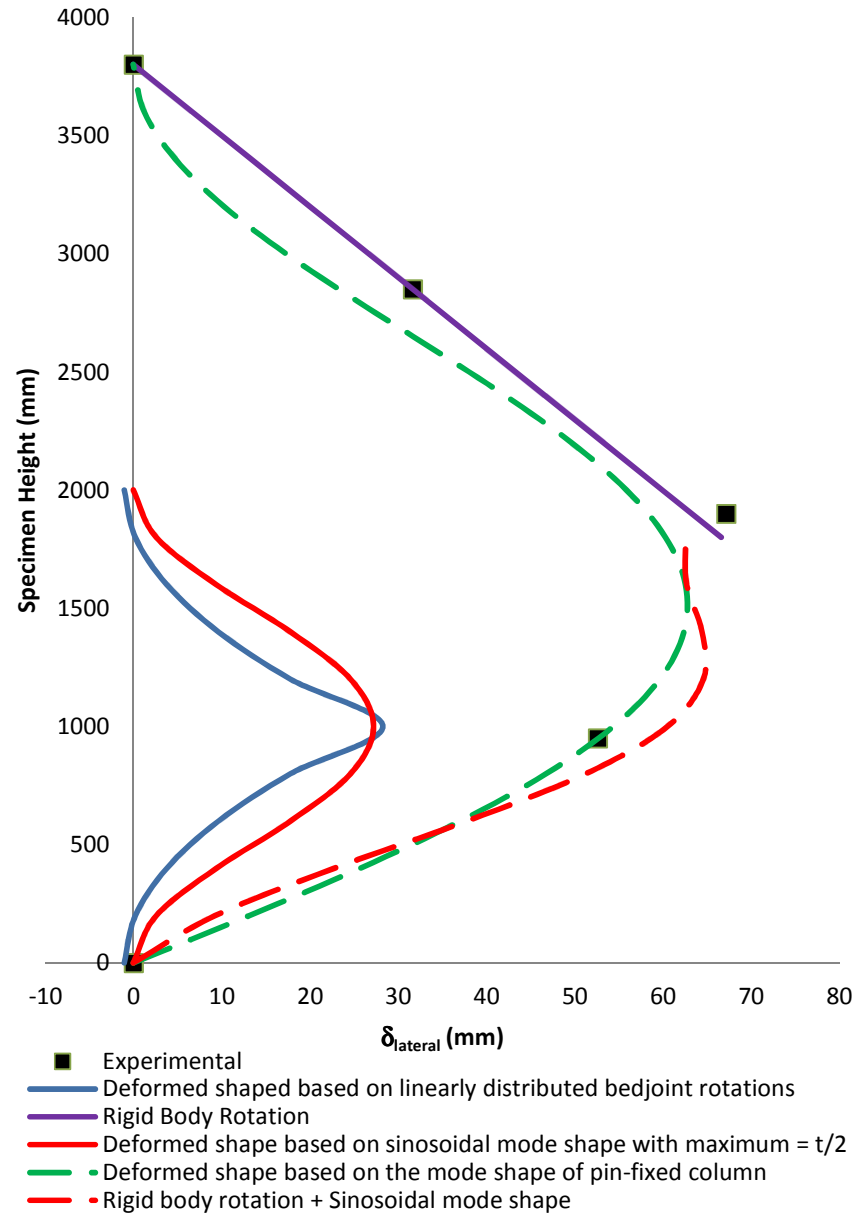


**Figure 5-8 Deformed shape experimental and predicted for specimen C2**

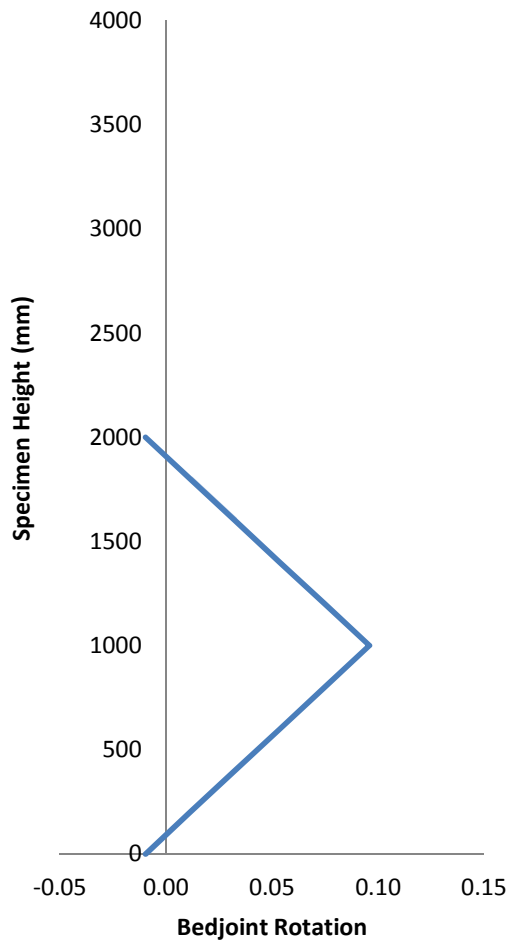


Assumed bedjoint rotation distributed along plastic hinge height

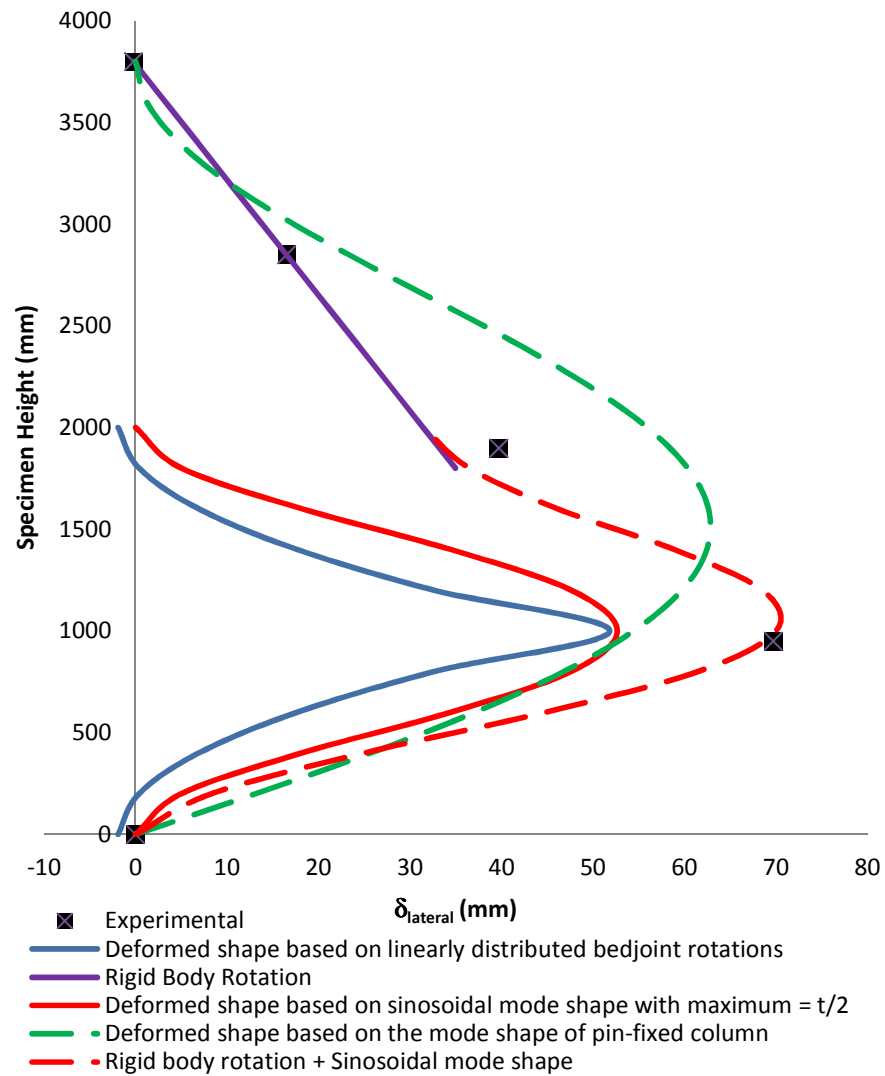


Lateral displacements along height

Figure 5-9 Deformed shape experimental and predicted for specimen C3

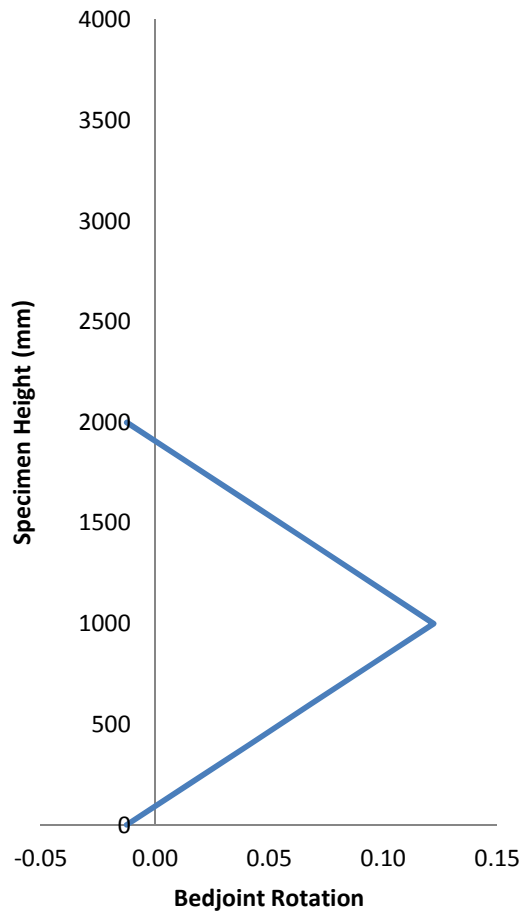


Assumed bedjoint rotation distributed along plastic hinge height

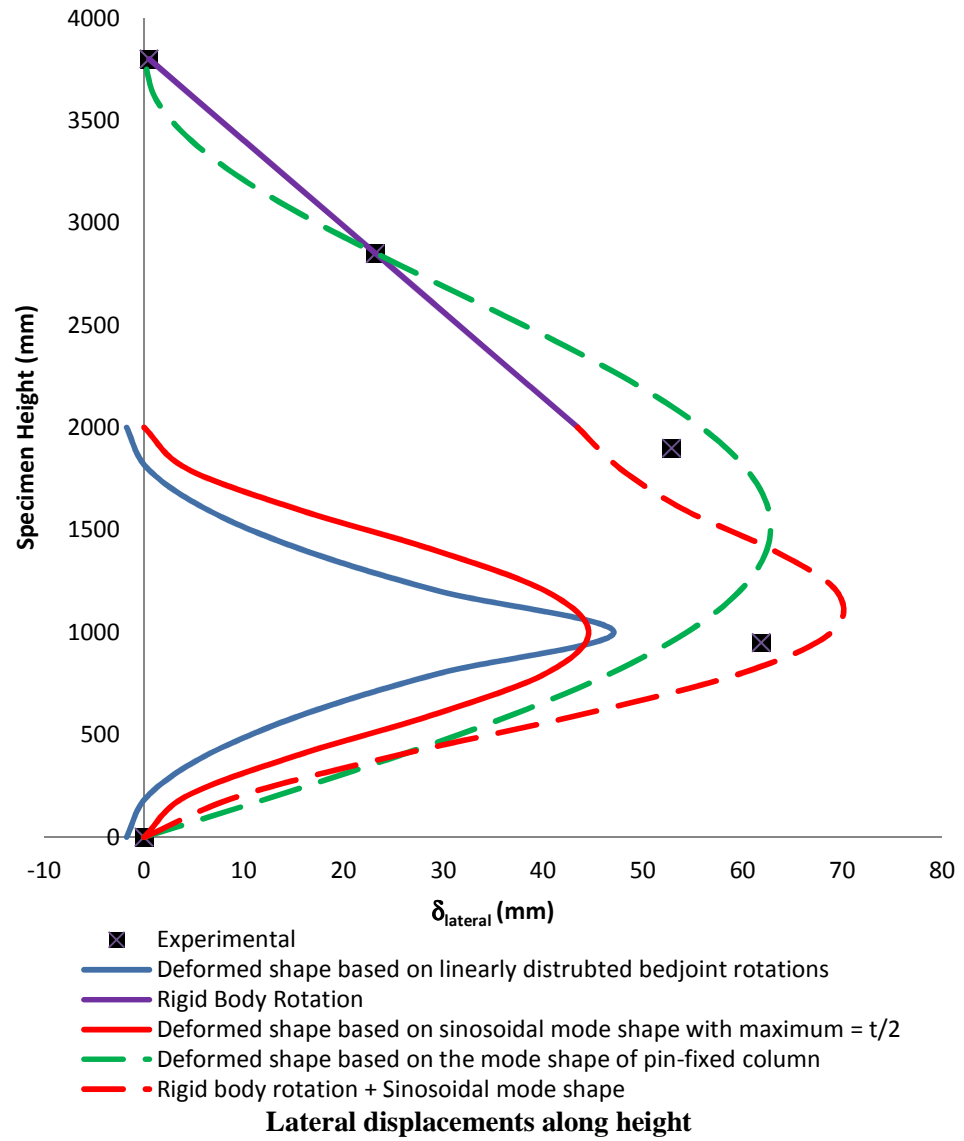


Lateral displacements along height

Figure 5-10 Deformed shape experimental and predicted for specimen C4



Assumed bedjoint rotation distributed along plastic hinge height



Lateral displacements along height

Figure 5-11 Deformed shape experimental and predicted for specimen C5

From these plots, it can be seen that the deformed shape predicted by the sinusoidal mode shape  $y(x) = \frac{\delta_{max}}{2} \left[ 1 - \cos\left(\frac{2\pi x}{h}\right) \right]$  with  $\delta_{max}$  equal to the actual maximum lateral displacement recorded at the midheight of the plastic hinge zone, gives reasonable results when compared with experimentally measured lateral displacements. For specimens C3 through C5, this is the case if the rigid body rotation of the retrofitted portion of the panel is taken into account.

For specimen C3, the mode shape of a pinned-fixed column under axial loads also produces reasonable results. This is because the upper, retrofitted portion of this specimen was still somewhat flexible due to existing cracks underneath the GFRP. Moreover, since the reinforcement was re-welded to the top, the anchorage for the GFRP at the top had to be removed which further allowed rotation at the top.

However, the most obvious comparison between these different approaches to predict the deformed shape is for specimen C2. This reveals that although most of the horizontal cracking occurs at the bedjoints between masonry courses, the final deformed shape is better approximated with a sinusoidal smooth function.

#### 5.4 Determining the Inelastic Strain Demand, $\epsilon_{id}$

For design purposes, the inelastic tensile strain demand can be compared against the estimated maximum tensile strains leading to out-of-plane instability. Codes and standards typically indirectly specify displacement ductility demands for design of structures. However, to estimate inelastic tensile strain demands, curvature ductility factors corresponding to specified ductility demands must be calculated.

For a cantilever wall subjected to lateral loads, the total displacement demand can be written in terms of the sum of the elastic and inelastic lateral displacements as shown in Figure 5-12. Assuming a linearly increasing strain along the in-plane length of the wall, the elastic deformation can be expressed in terms of the yield curvature as shown in Figure 5-12a. Similarly, assuming a uniform strain distribution after formation of plastic hinge, the inelastic deformation can be expressed in terms of the plastic curvature.

Rearranging the expressions for lateral deformation in terms of curvature gives

$$\mu_{\phi} = \frac{\phi_u}{\phi_y} = \frac{\phi_y + \phi_p}{\phi_y} = \frac{2h^2}{3lp(2h - l_p)} \left( \frac{\Delta_p}{\Delta_y} \right) + 1 = \frac{2h^2}{3lp(2h - l_p)} (\mu_{\Delta} - 1) + 1 \quad 5-27$$

where  $l_p$  is the length of plastic hinge and can be written as a proportion of the total height of the wall<sup>1</sup>. (Anderson and Brzev, 2009) In the above expression,  $\mu_{\phi}$  is the curvature ductility,  $\phi_u$ , is the ultimate curvature while  $\phi_y$  and  $\phi_p$  are elastic and inelastic curvatures respectively.

---

<sup>1</sup> In another recent study on the in-plane behaviour of reinforced masonry walls, efforts were made to relate plastic hinge length to the wall length, however, this study concluded that plastic hinge length should not only be related to wall dimensions that further investigation be conducted (Shedid, et al., 2010)

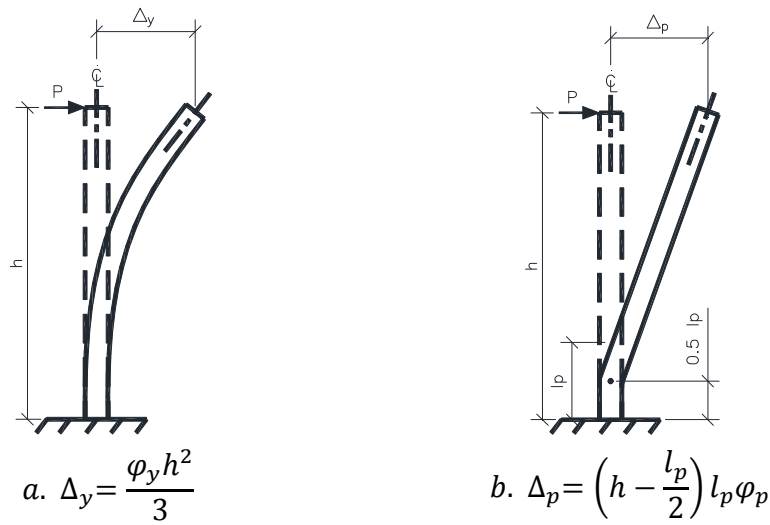


**Figure 5-12 Displacement demand in a cantilever wall subjected to lateral loads**

The yield curvature for a cantilever wall section can be written as

$$\phi_y = \frac{\epsilon_{sy} + \epsilon_{my}}{l_w} \quad 5-28$$

Where  $\epsilon_{sy}$  and  $\epsilon_{my}$  are elastic strain of steel and masonry respectively, while  $l_w$  is the in-plane length of wall, as shown in Figure 5-13. Note that in Figure 5-13, it is assumed that both masonry and steel yield at the same time for simplicity as is done for reinforced concrete according to CSA A23.3-04, Clause. 21.6.7.3.

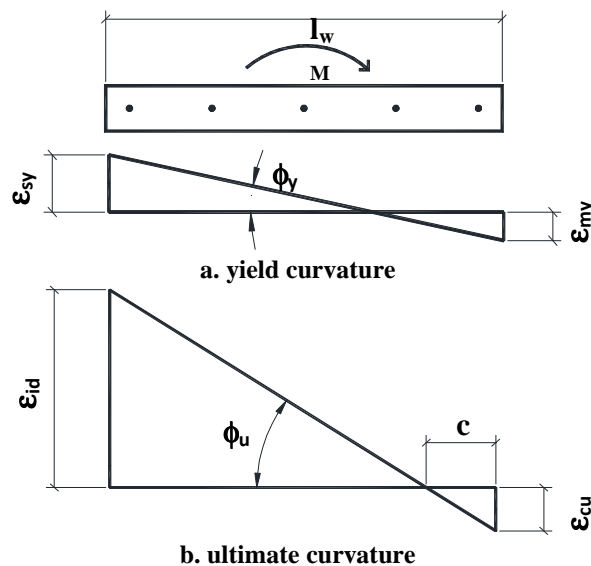


**Figure 5-13 Strain profile across the length of a shear wall subjected to overturning moment**

Therefore, the ultimate curvature becomes

$$\varphi_u = \mu_\varphi \varphi_y = \left[ \frac{2h^2}{3l_p(2h - l_p)} (\mu_\Delta - 1) + 1 \right] \left( \frac{\varepsilon_{sy} + \varepsilon_{my}}{l_w} \right) \quad 5-29$$

The maximum tensile strain imposed on a wall with the specified curvature ductility, based on Figure 5-13b, can then be determined as follows

$$\varphi_u = \frac{\varepsilon_{id}}{l_w - c} = \left[ \frac{2h^2}{3l_p(2h - l_p)} (\mu_\Delta - 1) + 1 \right] \left( \frac{\varepsilon_{sy} + \varepsilon_{my}}{l_w} \right) \quad 5-30$$

Solving equation 5-30 for the inelastic tensile demand gives

$$\varepsilon_{id} = \left[ \frac{2h^2}{3l_p(2h - l_p)} (\mu_\Delta - 1) + 1 \right] (\varepsilon_{sy} + \varepsilon_{my}) \frac{(l_w - c)}{l_w} \quad 5-31$$

where  $\varepsilon_{sy} = 0.0026$ ,  $\varepsilon_{my} = 0.001$ . Assuming that  $c = 0.15l_w$  (lower-bound prescribed by the CSA S304.1-04, as per code clause 10.16.5.2.3 for moderately ductile walls), gives

$$\varepsilon_{id} = 0.85 \left[ \frac{2h^2}{3l_p(2h - l_p)} (\mu_\Delta - 1) + 1 \right] (\varepsilon_{sy} + \varepsilon_{my}) \quad 5-32$$

## 5.5 Minimum Wall Thickness

For purposes of design, it can be said that the strain limit state must be satisfied as follows

$$\varepsilon_{id} \leq \varepsilon_{sm} \quad 5-33$$

Therefore, equations 5-26 and 5-32 can be combined to give

$$t \geq \sqrt{\left[ 0.85 \left[ \frac{2h^2}{3l_p(2h - l_p)} (R_d - 1) + 1 \right] (\varepsilon_{sy} + \varepsilon_{my}) - \eta_1 \varepsilon_y \right] \frac{h^2}{2.625}} \quad 5-34$$

where it is assumed that  $\xi_m = 0.5$  and  $\mu_\Delta = R_d$ . According to the above equation, a moderately ductile ( $R_d=2.0$ ) squat wall of height,  $h$ , equal to 3800 mm and a plastic hinge length,  $l_p$ , equal to 1/6 of its height, (Anderson and Brzev, 2009) ( $\therefore \varepsilon_{id} = 0.97\%$ ) must have a minimum thickness of about 190 mm.<sup>1</sup> This is equivalent to a  $h/t$  ratio of 20. Reducing the plastic hinge length would result in an increased tensile strain demand, and therefore, a larger height to thickness ratio. Figure 5-14 illustrates this relationship.

<sup>1</sup> Calculation is based on  $\varepsilon_{sy} = 0.0026$ ,  $\varepsilon_{my} = 0.001$  and  $\varepsilon_{cu} = 0.0025$

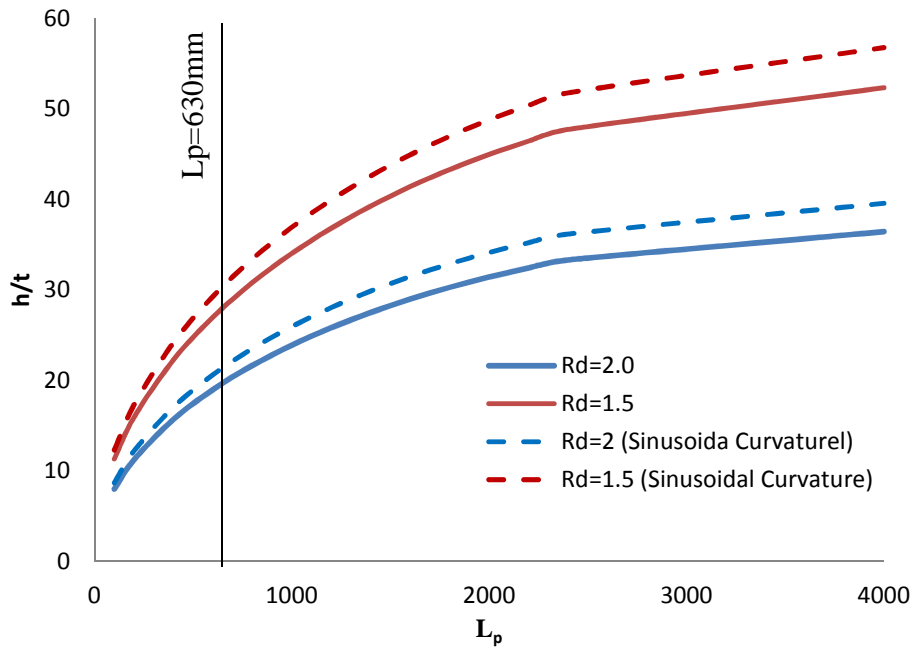


**Figure 5-14** Variation of h/t ratio with increased tensile strain demand.

## Chapter 6: Summary and Conclusions

The findings presented in this thesis are based on experimental studies conducted on five reinforced masonry (RM) uniaxial specimens subjected to reversed cyclic axial tension and compression. These uniaxial specimens are intended to represent the end zone of a reinforced masonry shear wall subjected to gravity loads and in-plane lateral loads. Based on the hysteretic response of these specimens, an analytical model has been proposed to estimate the magnitude of the maximum tensile strain that leads to out-of plane instability in the end zone of reinforced masonry shear walls. Note that the tests on the above specimens do not take into consideration the effects of strain gradient across the wall length due to in-plane bending and neither do they fully capture the boundary conditions that exist on the end zone of a RM shear wall. However, in the absence of previous experimental research and an analytical model that would help predict the behaviour of RM shear walls, the experimental study here is deemed an appropriate first step towards understanding the factors influencing the out-of-plane instability phenomena and its characterization.

The different failure modes encountered during the experimental study and the factors contributing to each are first summarized. Then the analytical investigation aimed at characterization of the most important parameters which govern out-of-plane stability in reinforced masonry columns is discussed. Finally, recommendations are made for future research.

### 6.1 Failure Mechanisms of Axially Loaded Reinforced Masonry Columns

The specimens tested in this study varied in their reinforcement ratio, the height-to-thickness ratio of their plastic hinge zone and the manner in which they were loaded. The different combinations of these parameters affected the failure mechanism as follows:

#### *Pure Crushing*

Although, only one of the specimens was subjected to monotonic compression loading, the results of this test combined with the observations made during the remainder of the tests, reveals that for height-to-thickness ratios of up to 27, unless relatively high levels of plastic tensile strain is experienced by the reinforced masonry uniaxial element, it will not experience out-of-plane displacements leading to lateral instability. Instead, even a very slender wall section, when subjected to monotonic compression loads will simply fail in pure crushing by forming vertical cracks and material failure. Having experienced tensile strains prior to experiencing compression in and of itself does not necessarily lead to lateral instability either. If the tensile strain levels applied to the wall section are not sufficiently large, the horizontal cracks formed during the tensile excursion will eventually close and the uniaxial specimen restores its straightness and is expected to fail in pure crushing at maximum compressive loads similar to those leading to failure of a monotonically loaded specimen.

### *Local Buckling of Reinforcement*

It is not possible to arrive at definitive conclusions about what factors will lead to this mode of failure since only one specimen failed with this mechanism and there was no evidence of it in any other specimen. The fact that the reinforcing bars in this specimen were not centred over the thickness of the specimen, also makes matters more complicated. However, there may exist a link between the size of reinforcing bars and the reinforcement ratio and this failure mode. Namely, reduced reinforcement surface area and smaller reinforcement ratio are thought to contribute to debonding between the reinforcement and the grout core during the tension half-cycle. The misalignment of the rebars within the grout core is also thought to exacerbate this problem. And larger tensile deformations produce larger horizontal gaps at the bedjoints and will result in more severe debonding between steel and concrete. Hence increasing the likelihood of local buckling in reinforcement.

### *Out-of-plane Displacements Leading to Lateral Instability*

The remaining three specimens failed by becoming laterally unstable. This occurred when the specimen had been subjected to large plastic tensile strains before being subjected to compression. From the results of the experiments, it can be said that with increased height-to-thickness ratio of the plastic hinge zone, smaller tensile strains are required to cause lateral instability in the specimen.

As explained in Section 5.1, under tensile strains, uniformly distributed horizontal cracks form along the height of the plastic hinge in the specimen. At the peak of the tension half cycle, once the specimen has experienced significant tensile strains beyond the point of yielding, these uniform horizontal cracks are at their largest. Upon unloading from the tension peak, their size is reduced but they remain open due to the presence of plastic strains. Therefore, at the beginning of the compression half-cycle, exposed reinforcing bars have to transfer all compressive loads across the cracks to the grout core. During this phase, reinforcing bars act essentially as though they were laterally unsupported for the entire height of the plastic hinge and begin to experience out-of-plane displacement due to their low lateral stiffness and small moment of inertia. Subsequently, the whole specimen experiences lateral displacements, causing the transverse rotation of the horizontal cracks at bedjoints. If the horizontal cracks that remained after the tension half cycle are large enough, these lateral displacements will exceed a critical limit (typically equal to half of the thickness of the specimen) and the specimen will become laterally unstable. However, if the cracks are small enough, the lateral displacement of the specimen and the subsequent rotation of the horizontal cracks will lead to the development of masonry compressive forces at one edge of the specimen before the critical lateral displacements are reached and a counteracting moment develops across the specimen thickness. This will lead to the restoration of the specimen's original vertical alignment and prevent out-of-plane instability.

## **6.2 Analytical Approaches in Characterization of the Lateral Instability Phenomena**

Based on the results of the experimental study, it was concluded that the magnitude of the tensile strain applied to the uniaxial specimen during the tension excursion of its cyclic

loading plays a key role in determining whether it will become laterally unstable in the subsequent compression cycle. Therefore, the focus of the analytical portion of this research was to find meaningful ways to predict the magnitude of the critical tensile strain beyond which the uniaxial specimen is expected to experience out-of-plane instability. This was done by defining the maximum longitudinal tensile strain in terms of its components as follows:

$$\varepsilon_{sm} = \varepsilon_e + \varepsilon_r + \varepsilon_p^* \quad \mathbf{5-3}$$

The equation above is based on the cyclic response of the uniaxial specimens as identified in Figure 5-1 and the break-down of the maximum tensile strain as shown in Figure 5-4. Where  $\varepsilon_e$  is the longitudinal strain associated with elastic recovery and given that there may exist some strain hardening, it is expressed as proportional to the yield strain of reinforcing steel as  $\varepsilon_e = \eta_1 \varepsilon_y$  where  $\eta_1 = 1.2$  is selected based on the experimental results. The term  $\varepsilon_r$ , corresponds to the reloading strain and is the longitudinal strain needed, in addition to the elastic recovery strain, to cause out-of-plane displacements that lead to lateral instability. Typically this out-of-plane displacement is equal to half the wall thickness as shown in Section 5.3 assuming that the reinforcing bars are centred over the wall thickness. Such out-of-plane displacement will be referred to as critical out-of-plane displacement hereafter.

Assuming a sinusoidal deformed shape with fixed-fixed boundary conditions, the reloading strain was predicted as

$$\varepsilon_r = 1.25 \xi_m \left(\frac{t}{h}\right)^2 \quad \mathbf{5-12}$$

Where  $\xi_m$  is the critical out-of-plane displacement normalized by the specimen thickness, or  $\xi_m = \frac{\delta}{t}$  and is typically equal to 0.5 if the reinforcement is centered within the grouted cells.

The term  $\varepsilon_p^*$  corresponds to the longitudinal residual plastic strain that remain in the open cracks after the specimen has experienced out-of-plane displacements equal to the critical limit. Two different approaches were employed in estimating  $\varepsilon_p^*$  as follows:

1. Estimating residual strains based on an assumed bedjoint rotation distribution
2. Estimating residual strains based on an assumed curvature distribution with maximum at the plastic hinge midheight

The first approach assumes a linear distribution of crack rotations across the height of the plastic hinge with the maximum  $\theta_{max}$ , occurring at midheight of the plastic hinge. It also assumes that the bedjoint rotations at either end of the plastic hinge can be written as a proportion of the maximum rotation by  $\theta_1 = \alpha \theta_{max}$ . Based on this assumption the residual plastic strain was determined to be

$$\varepsilon_p^* = 2 \xi_m t \left[ \left(\frac{1}{2H_b}\right) \alpha \theta_{max} + \frac{2\theta_{max}}{h} (1 - \alpha) H_b \left(\frac{1}{4H_b}\right) \left(\left(\frac{h}{2H_b}\right) - 1\right) \right] \quad \mathbf{5-20}$$

Where  $H_b$  is the height of one masonry block. The above equation is based on a discrete sum of bedjoint rotations over the plastic hinge height. It must also be noted that the magnitude of  $\theta_{max}$  and  $\alpha$  are highly uncertain.

The second approach used to predict the residual plastic strain,  $\varepsilon_p^*$ , was based on the assumption that the plastic strain at the location of maximum curvature is equal to the plastic strain over the full height of the plastic hinge. This is a reasonable assumption given that all cracks over the plastic hinge height are of equal size. The plastic strains based on several different curvature distributions with the maximum at midheight were calculated and compared with experimental results. It was revealed that a uniform curvature distribution produced the most accurate results. This would mean that all cracks not only would have to be equal in size but the onset of their closure would have to occur simultaneously leading to a circular buckled shape. However, from the boundary conditions, this is clearly not the case. Nevertheless, this approach is deemed an appropriate preliminary step given the good correlation with the test data.

Adopting the second approach,  $\varepsilon_p^*$  is estimated to be equal to  $4\xi_m \left(\frac{t}{h}\right)^2$ , where  $\xi_m$  is the out-of-plane displacement normalized with respect to thickness. With this approach, maximum tensile strain leading to out-of-plane instability in reinforced masonry columns is estimated as

$$\varepsilon_{sm} = 5.25 \xi_m \left(\frac{t}{h}\right)^2 + \eta_1 \varepsilon_y \quad 5-26$$

The above expression for maximum tensile strain can then be compared to the strain demands on the end zone of a shear wall. This is done by relating the maximum tensile strain imposed on a wall given the required displacement ductility as follows

$$\varepsilon_{id} = 0.85 \left[ \frac{2h^2}{3l_p(2h - l_p)} (\mu_\Delta - 1) + 1 \right] (\varepsilon_{sy} + \varepsilon_{my}) \quad 5-32$$

where  $\mu_\Delta$  is the displacement ductility demand which can be related to the code prescribed force-reduction factor  $R_d$ ,  $\varepsilon_{sy} = 0.0026$  is the yield strain in steel, and  $\varepsilon_{my} = 0.001$  is the yield strain in masonry. It can be seen that reducing the length of the plastic hinge,  $l_p$ , as a proportion of the wall height will result in increasing tensile strain demands.

By ensuring the tensile strain demands are less than or equal to the maximum tensile strains that lead to out-of-plane instability, (Equation 5-33) the minimum wall thickness can be written as

$$t \geq \sqrt{\left[ 0.85 \left[ \frac{2h^2}{3l_p(2h - l_p)} (R_d - 1) + 1 \right] (\varepsilon_{sy} + \varepsilon_{my}) - \eta_1 \varepsilon_y \right] \frac{h^2}{2.625}} \quad 5-34$$

In the above equation,  $l_p$  is the height of the plastic hinge and can be written as a proportion of the wall height. As such, the expressed relationship can be said to provide limits on height-to-thickness ratio of reinforced masonry shear walls for a given ductility demand,  $R_d$ . Based on this relationship, it can be said that increased tensile strain demands result in reduced height-to-thickness ratios. Though this assessment is conservative in nature, at this point it gives relatively consistent height-to-thickness ratios with those prescribed by the Canadian Standard Association, CSA S304.1 and NBCC 2010.

### 6.3 Recommendations for Future Research

#### Experimental

Experimental data from more specimens are required to confirm the observations made during this study. Also, the influence of other parameters contributing to out-of-plane instability of reinforced masonry columns/walls should be investigated as follows:

- The impact of different height-to-thickness ratios on the lateral instability should further be investigated. It is recommended that this be done through the use of shorter specimens or increasing the longitudinal reinforcement ratio over a portion of the wall which is a more realistic way to represent the plastic hinge region in an actual wall.
- The effect of varying reinforcement ratios should further be examined. Variation of this design parameter may be more useful when done in wall specimens rather than column specimens. It is recommended that rebar place holders be used to ensure that the rebar remains straight within the core of the column/wall after the grout has been poured. Ensuring that the rebar is placed vertically straight allows the investigator to ignore the out-of-straightness effects on the point at which the panel begins to experience lateral displacements. It will also lead to a more straightforward comparison between experimental and predicted strain levels.
- It is recommended that the instrumentation be modified such that more localized deformations can be recorded. For example, additional instrumentation placed along the specimen height would assist in more accurate prediction of the deformed shape. Similarly, placing instruments that measure the size of each horizontal crack along the specimen height will provide better insight into how these cracks rotate as the specimen undergoes lateral displacements and how their rotations are distributed along the height. Similarly, measuring vertical deformations over segments of the panel as well as over the entire height will reveal whether there are strain concentrations over the wall height.
- The effects of realistic boundary conditions on the out-of-plane phenomena should be investigated. Therefore, it is recommended that wall specimens with longer in-plane length be constructed on concrete footings and subjected to lateral loads to simulate earthquake motions. The embedment of the dowels extending from the footing into the wall will represent a more realistic boundary condition at the bottom while the in-

plane extension of the wall will result in more realistic strain gradient and boundary condition along the height of the wall end zone.

#### Analytical

- Better understanding of the distribution of the horizontal cracks formed along the plastic hinge height will help improve the analytical model especially with regards to predicting the reloading strain,  $\varepsilon_r$ , and the residual plastic strain,  $\varepsilon_p^*$ . Namely, developing a relationship between the buckled shape and the maximum rotation as well as assessing the sequence of crack closures, will greatly help in predicting these two strain components.
- The effects of reinforcement ratio on the required maximum tensile strain leading to out-of-plane instability should be incorporated into the relationship between the inelastic strain demand and the maximum strain capacity. One approach in doing this may include investigating the limits that the crushing capacity of the masonry in relation to the forces developed in the reinforcing bars has on how the wall end zone behaves beyond the point of critical out-of-plane displacement.

Note that as the title of this thesis implies, the experimental and analytical studies presented here are part of a larger experimental study. Based on the experimental and analytical results presented here, another set of experimental studies on full size reinforced masonry walls have been designed and are currently being conducted at the University of British Columbia. This set of experiments are aimed to further understand the factors influencing out-of-plane instability and further improve the analytical model presented here in predicting the onset of this failure mode. They also aim to eliminate any issues related to the representation of the boundary conditions that were present during the tests described here. An analytical model representing the hysteretic response of reinforced masonry walls using multiple vertical line elements was developed for the purposes of the next phase of studies which will also be calibrated according to both the test results of the first and second phase of experimental studies. The results of the next phase of investigation is expected in 2013.

## Bibliography

**Azimikor, N., Brzev, S., Elwood, K., and Anderson, D.** (2011). Out-of-Plane Stability of Reinforced Masonry Shear Walls, Proceedings of the 11th North American Masonry Conference, Minneapolis, MN, USA.

**Anderson and Brzev (2009).** Seismic Design Guide Anderson, D.L., and Brzev, S. (2009). "Seismic Design Guide for Masonry Buildings", Canadian Concrete Masonry Producers Association, Toronto, Ontario, 317 pp (www.ccmpa.ca).

**Brzev, S.** Review of Experimental Research Evidence on Out-Of-Plane Instability in Reinforced Concrete and Reinforced Masonry Shear Walls Under Seismic Loading, Department of Civil Engineering, British Columbia Institute of Technology, 2011 (pending publication).

**Chai Y. H. and Elayer D. T.** Lateral Stability of Reinforced Concrete Columns under Axial Reversed Cyclic Tension and Compression [Journal] // ACI Structural Journal. - 1999. - pp. 780-789.

**Corley W.G., Fiorato A.E. and Oesterle R.G.** Structural Walls // Publication SP-72. - Detroit : American Concrete Institute , 1981.

**EERI** The Mw 8.8 Chile Earthquake of February 27, 2010. EERI Special Earthquake Report Newsletter [Report]. - California : Earthquake Engineering Research Institute, 2010.

**Elshafie H., Hamid A. A. and Nasr E.** Post-Cracking Stiffness of Reinforced Masonry Shear Walls with Openings [Conference] // 8th North American Masonry Conference. - Austin, Texas : The Masonry Society, 1999.

**Foltz S. and Yancey C. WC.** The Influence of Horizontal Reinforcement on the Shear Performance of Concrete Masonry Walls [Book Section] // Masonry Design and Construction: Problems and Repairs / book auth. L. Melander J. and Lauersdorf. - Philadelphia : ASTM, 1993.

**Goodsir W.J.** Design of Coupled Wall-Frame Structures for Seismic Action // Research Report. - Christchurch : Department of Civil Engineering, University of Canterbury, August 1985.

**He L. and Priestley M. J. N.** Seismic Behavior of Flanged Masonry Shear Walls [Report]. - San Diego : Department of Applied Mechanics of Engineering Sciences, University of California, San Diego, 1992.

**Ibrahim K. and Suter G. T.** Ductility of Concrete Masonry Shear Walls Subjected to Cyclic Loading [Conference] // 8th North American Masonry Conference. - Austin, Texas : The Masonry Society, 1999.

**Innamorato D.** The Repair of Reinforced Structural Masonry Walls using a Carbon Fiber, Polymeric Matrix Composite Overlay [Report]. - San Diego : University of California, San Diego, 1994.

**Kikuchi K. [et al.]** Effect of Wall Aspect Ratio on Seismic Behavior of Reinforced Fully Grouted Concrete Masonry Walls [Conference] // Ninth North American Masonry Conference. - Clemson, South Carolina : The Masonry Society, 2003. - p. 214:225.

**Kikuchi K., Yoshimuar K. and Tanaka A.** Effect of the Presence of Masonry Units on the Seismic Behavior of Reinforced Fully Grouted Concrete Masonry Walls [Conference] // 8th North American Masonry Conference . - Austin, Texas : The Masonry Society, 1999.

**Manos G. C. [et al.]** The Performance of Partially Reinforced Masonry Subjected to Horizontal Cyclic and Compressive Loads [Conference] // Ninth North American Masonry Conference. - Clemson, South Carolina : The Masonry Society, 2003. - p. 238:249.

**Miller S. C., El-Dakhakhni W. and Drysdale R. G.** Experimental Evaluation of the Shear Capacity of Reinforced Masonry Shear Walls [Conference] // 10th Canadian Masonry Symposium. - Banff, Alberta : The Masonry Society, 2005.

**Minaie E. [et al.]** In-Plane Behavior of Partially Grouted Reinforced Concrete Masonry Walls [Journal] // Journal of Structural Engineering. - 2010. - p. 1089:1097.

**Nolph Shawn Mark** In-plane Shear Performance of Partially Grouted Masonry Shear Walls [Report]. - Pullman, Washington : Washington State University, 2010.

**Oesterle R.G. [et al.]** Earthquake Resistant Structural Walls-Tests of Isolated Walls // Report to National Science Foundation. - Skokie : Portland Cement Association, 1976.

**Oestrelle R.G. [et al.]** Earthquake Resistant Structural Walls-Tests of Isolated Walls-Phase II // Report to National Science Foundation. - Skokie : Portland Cement Association, 1979.

**Paulay T. and Priestley J. N.** Stability of Ductile Structural Walls [Journal] // ACI Structural Journal. - 1993. - pp. 385-392.

**Paulay T. and Priestley M.J.N** Seismic Design of Concrete and Masonry Buildings. - New York : John Wiley and Sons, Inc., 1992. - p. 744.

**Paulay T. and Priestley M.J.N** Stability of Ductile Structural Walls // ACI Structural Journal. - 1993. - Vol. 90. - pp. 385-392.

**Schultz A. E.** Seismic Performance of Partially-Grouted Masonry Shear Walls [Conference] // Eleventh World Conference on Earthquake Engineering. - Acapulco, Mexico : [s.n.], 1996.

**Shedid M. T., Dysdale R. G. and El-Dakhakhni W. W.** Behavior of Fully Grouted Reinforced Concrete Masonry Shear Walls Failing in Flexure: Experimental Results [Journal] // Journal of Structural Engineering. - 2008. - p. 1754:1767.

**Shedid M. T., El-Dakhakhni W. W. and Drysdale R. G.** Alternative Strategies to Enhance the Seismic Performance of Reinforced Concrete-Block Shear Wall Systems [Journal] // Journal of Structural Engineering. - 2009.

**Shedid M. T., Hamid A. A. and Drysdale R. G.** Ductility of Reinforced Masonry Shear Walls and Impact of Incomplete Grouting [Conference] // 10th Canadian Masonry Symposium. - Banff, Alberta : The Masonry Society, 2005.

**Shedid M., El-Dakhakhni W and Drysdale R.** Seismic Performance Parameters for Reinforced Concrete-Block Shear Wall Construction [Journal]. - [s.l.] : ASCE, 2010. - Vol. JOURNAL OF PERFORMANCE OF CONSTRUCTED FACILITIES.

**Thomsen IV J.H. and Wallace J.W.** Displacement-Based Design of Slender Reinforced Concrete Structural Walls-Experimental Verification // Journal of Structural Engineering. - [s.l.] : ASCE, 2004. - Vol. 130. - pp. 618-630.

**Vallenas J.M., Bertero V.V. and Popov E.P.** Hysteretic Behaviour of Reinforced Concrete Structural Walls // Report No. UBC/EERC-79/20. - Berkeley : University of California, Earthquake Engineering Research Centre, 1979. - p. 234.

**Wallace J.W.** Reinforced Concrete Walls: Recent Research and ACI 318-2001 [Conference] // Sixth U.S. National Conference on Earthquake Engineering. - Seattle, WA : [s.n.], 1998. - p. 12.

**Yancey C. and Fattal S.** Review of Research Literature on Masonry Walls [Report]. - 1991.

**Yoshida K., Kikuchi K. and Kuroki M.** Experimental Study on Sliding Strength of Reinforced Fully Grouted Concrete Masonry Walls [Conference] // Tenth North American Masonry Conference. - St. Louis, Missouri : The Masonry Society , 2007. - p. 1015:1026.

**Zhang Y. and Z Wang.** Seismic Behaviour of Reinforced Concrete Shear Walls Subjected to High Axial Loading // ACI Structural Journal. - 2000. - Vol. 97. - pp. 739-750.

## **Appendix A Design of Specimen Cap Plates**

Sizing the specimen plates:

Sizing the bolt:

Plate dimensions (see **Error! Reference source not found.**)

W =	15 inch	381 mm
L =	32 inch	812.8 mm
t =	1.5 inch	38.1 mm
bolt diameter = 1 inch		
hole size = $\phi_b + 1/16" = 17/16$ inch		
edge distance =		
	min = 44mm	or 2 inch
	max = 12 x t = 18 inch	
	< 150mm	6 inch
impact wrench clearance = 11/8 inch	use	1.5 inch

#### Checking for bending resistance

base plate properties: ASTM 44ksi

$$f_y = 303 \text{ MPa}$$

$$\text{cross section} = 14516 \text{ mm}^2$$

$$\text{Avg. force} = 2199 \text{ kN}$$

$$\text{moment arm} = 13 \text{ mm}$$

$$M_y = \text{Avg. force} \times \text{moment arm}$$

$$M_y = 28 \text{ kN.m}$$

$T_u$  on each rebar

$$T_u = 650 \text{ MPa} \times 300 \text{ mm}^2 = 195 \text{ kN}$$

#### Using only four bolts at the four corners

Along the short direction, W-Dimension

$$L = 11 \text{ inch}$$

$$P_1 = 3T_u = 585 \text{ kN}$$

$$M_{\max} = 40.86 \text{ kN.m}$$

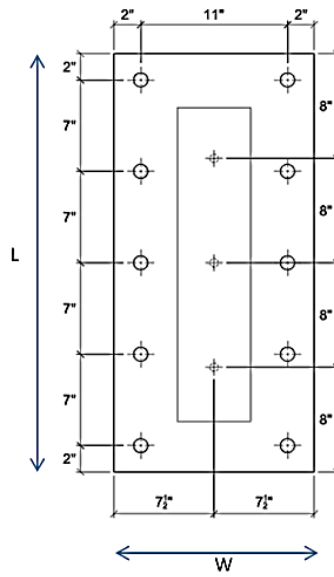


**Figure A- 1 Steel specimen plate**

Along the long direction, L-Dimension

$$L = 28 \text{ inch}$$

$$P_1 = P_2 = P_3 = T_u = 195 \text{ kN}$$

$$M_{\max} = 69.34 \text{ kN.m}$$

The bending across the width will govern due to larger bolt spacing.

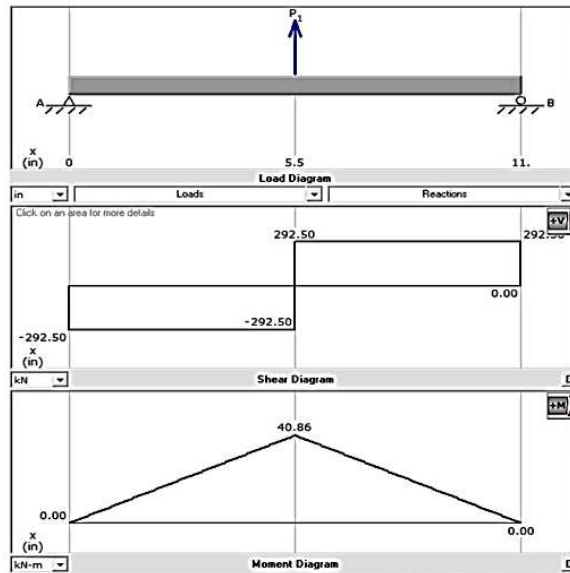


**Figure A- 2 Shear and moment diagrams along the width of specimen plate**

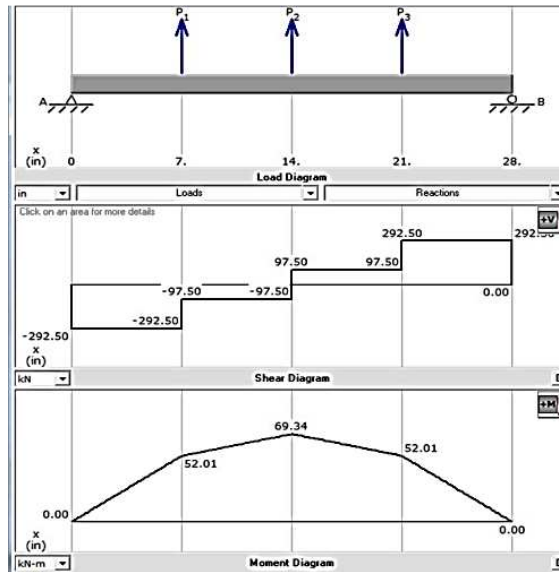


Figure A-3 Shear and moment diagram along the specimen plate length

Plate with 3-20M bars	Plate with 3-15M bars	Plate with 2-10M bars
Along the short direction	Along the short direction	Along the short direction
L = 11 inch	L = 11 inch	L = 11 inch
$P_1 = 3T_u = 585 \text{ kN}$	$P_1 = 3T_u = 372 \text{ kN}$	$P_1 = 3T_u = 210 \text{ kN}$
$M_{\max} = 40.86 \text{ kN.m}$	$M_{\max} = 34.65 \text{ kN.m}$	$M_{\max} = 23.33 \text{ kN.m}$
Solve for minimum thickness	Solve for minimum thickness	Solve for minimum thickness
$M_r = Z \cdot f_y$	$M_r = S \cdot f_y$	$M_r = S \cdot f_y$
and $Z = (bd^2)/4$	but $S = I/(d/2)$	but $S = I/(d/2)$
solver $d, d = [(4 \cdot M_r / (b \cdot f_y))]^{0.5}$	and $I = (bd^3)/12$	and $I = (bd^3)/12$
short direction:	solver $d, d = [(4 \cdot M_r / (b \cdot f_y))]^{0.5}$	solver $d, d = [(4 \cdot M_r / (b \cdot f_y))]^{0.5}$
b = 812.8 mm	short direction:	short direction:
$M_r = 40.86 \text{ kN.m}$	b = 812.8 mm	b = 812.8 mm
$d_{\min} = 26 \text{ mm}$	$M_r = 34.65 \text{ kN.m}$	$M_r = 23.33 \text{ kN.m}$
use 1.5 inch	$d_{\min} = 24 \text{ mm}$	$d_{\min} = 20 \text{ mm}$
	use 1 inch	use 1 inch

## **Appendix B Development of the Reinforcement Weld Connection Detail**

Checking for bending failure:

**I. Sizing the Welding:**

From "Handbook of Steel Constructions", page 3-39:

Base Metal,  $V_r = 0.67\phi_w A_m F_u$

Plate 300W

Weld Metal,  $V_r = 0.67\phi_w A_w X_u (1.00 + 0.50 \sin^{1.5} \theta)$

t = 0.5 inch = 12.7 mm

for  $\theta = 90^\circ$   $(1.00 + 0.50 \sin^{1.5} \theta) = 1.5$

$F_u = 450$  MPa

$\phi_w = 0.67$

Fillet Welding E49XX

Rebar yield stress

$X_u = 490$  MPa

$F_y = 500$  MPa

maximum weld size = 10.7 mm

$T_y = \phi_s A_b F_y$

$\phi_s = 1$

$T_w = 1.25 T_y$

**Table B- 1 Weld sizes considered for connecting rebar to steel plates**

size = 10 mm for 10M								Base	Weld	Governed
Rebar	$D_b$ (mm)	$A_b$ (mm <sup>2</sup> )	Cir. (mm)	$T_y$ (kN)	$T_w$ (kN)	$A_m$ (mm <sup>2</sup> )	$A_w$ (mm <sup>2</sup> )	$V_r$ (kN)	$V_r$ (kN)	$V_r$ (kN)
10M	11	100	35	50.0	62.5	346	244	69.8	80.6	69.8
15M	16	200	50	100.0	125.0	503	355	101.5	117.3	101.5
20M	19.5	300	61	150.0	187.5	613	433	123.8	142.9	123.8
size = 14 mm for 15M								Base	Weld	Governed
Rebar	$D_b$ (mm)	$A_b$ (mm <sup>2</sup> )	Cir. (mm)	$T_y$ (kN)	$T_w$ (kN)	$A_m$ (mm <sup>2</sup> )	$A_w$ (mm <sup>2</sup> )	$V_r$ (kN)	$V_r$ (kN)	$V_r$ (kN)
10M	11	100	35	50.0	62.5	484	342	97.7	112.9	97.7
15M	16	200	50	100.0	125.0	704	498	142.2	164.2	142.2
20M	19.5	300	61	150.0	187.5	858	606	173.3	200.1	173.3
size = 16 mm for 20M								Base	Weld	Governed
Rebar	$D_b$ (mm)	$A_b$ (mm <sup>2</sup> )	Cir. (mm)	$T_y$ (kN)	$T_w$ (kN)	$A_m$ (mm <sup>2</sup> )	$A_w$ (mm <sup>2</sup> )	$V_r$ (kN)	$V_r$ (kN)	$V_r$ (kN)
10M	11	100	35	50.0	62.5	553	391	111.7	129.0	111.7
15M	16	200	50	100.0	125.0	804	569	162.5	187.6	162.5
20M	19.5	300	61	150.0	187.5	980	693	198.0	228.7	198.0

After considering several different sizes, the weld size selected for each type of rebar was as listed in **Error! Reference source not found.**

**Table B- 2 Weld size results**

Reinforcement	Weld Size
10M	10 mm
15M	14mm
20M	16mm

All welds to be applied around the entire perimeter of the rebar.

## II. Check Pullout Failure while Lifting

### Masonry Block

height, $h =$	3.6 m	density, $\rho =$	2100 kg/m <sup>3</sup>
wide, $w =$	0.6 m	$g =$	9.81 m/s <sup>2</sup>
dept, $d =$	0.14 m		
weigh, $w_{con} =$	6.230 kN		

### Reinforcement

3-20M (worst case when using 20M bars)	density, $\rho =$	2.355 kg/m
total L 10.8 m		
weigh, $w_{bar} =$	0.025 kN	

**Total weight of the column,  $w$  6.255 kN**

The weight of the column is less than the smallest value of the weld strength. Therefore, the column will not cause pull-out of the weld connection during lifting.

## III. Bolt Selection

using the maximum weld strength,  $T_w = 187.5$  kN  
 the worst case when there are 3-20M bars,  
 therefore, the required yield strength is  $T_{req} = 562.50$  kN

4 bolts will be used, so the required yield strength on each bolt  $T_{req} = 140.63$  kN

Using Handbook of Steel Construction, Table 3-4,  
 $\phi 3/4$ " bolt can be used while the allow force is  $T_b = 141$  kN

## IV. Performing Weld Test and Checking for Bending of Steel Plate

The weld connections were testing in the Baldwin Machine as shown in **Error! Reference source not found.**

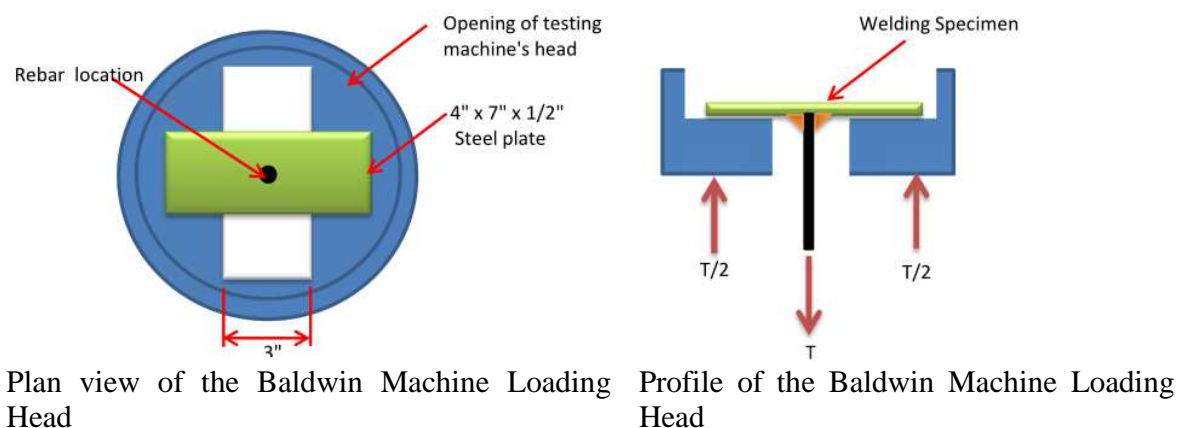


**Figure B- 1 Loading of the weld connection sample in the Baldwin Machine**

Consider 15M rebar:

$$T_y = 100.0 \text{ kN}$$

$$T_u = 1.25 * T_y = 125.00 \text{ kN}$$

$$L = 9" = 228.6 \text{ mm}$$

$$M = 7.1 \text{ kN.m}$$

Yield moment for the plate

$$F_y = 300 \text{ MPa}$$

$$M_y = 2.2 \text{ kN.m} < M$$

The plate will bend under the  $T_u$

There shorter length of L is required

$$\text{Try } L = 3 \text{ ''}$$

the new M value is

$$M = 2.4 \text{ kN.m}$$

### Welding Test Photos



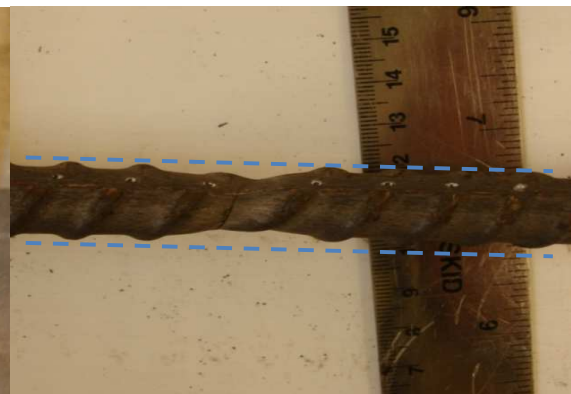
a



b



c



d

**Figure B-2 a. Specimens after the testing, b. Typical failure, c. Typical weld detail, d. Necking of the rebar**

**Weld Capacity Test Results:**

Weld Type 1, W1: Drilled plate then applied fillet weld on top and plug weld at bottom

Weld Type 2, W2: Applied fillet weld on top of the plate only without drilling hole

Weld Type 3, W3: Drilled a countersunk hole into the plate and filled it with weld

**Table B- 3 Results of welding capacity tests**

Spec.	Weld Type	Bar		Weld Size mm	P <sub>y</sub> kN	P <sub>u</sub> kN	P <sub>f</sub> kN	f <sub>y</sub> MPa	f <sub>u</sub> MPa	f <sub>f</sub> MPa	Fracture Strain %	Inspection Failure
		Type	A <sub>b</sub> , mm <sup>2</sup>									
W1-1	Type 1	15M	200	12	86	122.4	87	430	612	435	10.3	rebar / plate bent
W1-2		15M	200	10	86	120.7	90.1	430	604	451	18.5	rebar
W1-3		10M	100	11	N/A	N/A	57.5	N/A	N/A	575	N/A	rebar /above weld
W1-4		10M	100	11	N/A	N/A	57.1	N/A	N/A	571	N/A	rebar / above weld
W2-1	Type 2	15M	200	12	87	122.2	90	435	611	450	18.0	rebar
W2-2		20M	300	10	133	188.1	150	443	627	500	19.5	rebar / plate bent
W2-3		15M	200	9	86	123.2	90	430	616	450	19.0	rebar
W2-4		10M	100	9	47	63.3	60	470	633	600	9.4	weld
W2-5		10M	100	11	N/A	N/A	61.5	N/A	N/A	615	N/A	pull out
W3-1	Type 3	15M	200	10	86	120.7	88	430	604	440	9.4	rebar
W3-2		15M	200	10	96	121.64	89	480	608	445	17.5	rebar

Note: W1-1 strain was estimated based on the overall length, because failure was outside the marking range.

Observation:

All failures occurred within the rebar section, thus the tested weld types and sizes are suitable for use in the actual column specimens.

**Table B- 4 Results of welding capacity tests for connection of 10M bars with 2mm tip**

dia. = 10.3 mm

area = 83.3229 mm<sup>2</sup>

Spec.	Welding type	Weld Size	Yield	Yield Str.	Ultimate	Ultimate	Failure	Failure Stress	Fracture Strain	Failure Location
			Load, kN	MPa	Load, kN	Stress, MPa	Load, kN	MPa	mm/mm	From Weld, mm
W4-2	2mm root	18	40.2	482	56.7	680	49	586	18.5	250
W4-3	2mm root	15	42.6	511	57.6	691	52	619	out of range	150
W4-4	knife edge	10	42.6	511	57.9	695	52	624	out of range	120

Note: W4-4 weld with stainless steel weld material.

## **Appendix C Design of Specimen Retrofit with Glass Fiber Reinforced Polymer**

FRP Design: SIKAWrap Hex 100G, Cured Laminated with Sikadur Hex 306 Epoxy

**In Tension:**

$$A_{st} := 200\text{mm}^2$$

$$f_y := 558\text{MPa}$$

$$\phi_{frp} := 0.75$$

$$f_{frp} := 514\text{MPa}$$

$$E_{frp} := 25300\text{MPa}$$

$$\epsilon_{frpu} := 0.0214$$

$$N_{frp} := 1$$

$$t_{frp} := 1\text{mm}$$

$$b_{frp} := 2 \cdot (12 \cdot 25\text{mm}) = 0.6\text{m}$$

$$A_{frp} := N_{frp} \cdot t_{frp} \cdot b_{frp} = 6 \times 10^{-4}\text{m}^2$$

Area of one 15M bar

Yield strength of 15M bars

Yield strength

Elastic Modulus

Specified Tensile Elongation

Number of vertical layers

FRP ply thickness

In-plane length of FRP

Area of FRP in tension

Applied tensile strain based on maximum tensile displacement expected in the specimen

$$\epsilon_{frp} := \frac{(40\text{mm})}{2000\text{mm}} = 0.02$$

"OK" if  $\epsilon_{frpu} > \epsilon_{frp}$  = "OK"  
 "NOT OK" otherwise

$$T_{frp} := \phi_{frp} \cdot E_{frp} \cdot \epsilon_{frp} \cdot A_{frp} = 227.7\text{ kN}$$

"OK" if  $T_{frp} > A_{st} \cdot f_y$  = "OK"  
 "NOT OK" otherwise

Development length?

$$f_c := 23\text{MPa}$$

$$k := 0.184$$

$$b_w := b_{frp} = 0.6\text{m}$$

$$k_d := \left( \frac{b_{frp}}{b_w} \right) \cdot \left[ \frac{\epsilon_{frpu}}{k \cdot \sqrt{(f_c \cdot \text{MPa})}} \right] = 0.024 \frac{1}{\text{MPa}}$$

$$l_{frp} := k_d \cdot E_{frp} \cdot t_{frp} = 0.614\text{m}$$

## **Appendix D Design of the Test Apparatus**

Determine the required strength of the test rig based on the predicted strength of the specimens:

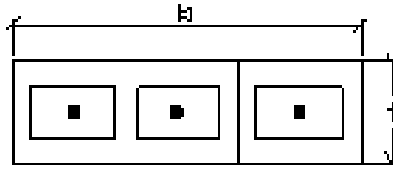


**Figure D- 1 Specimen cross section**

Cross-sectional and material properties:

$t := 140\text{mm}$	Thickness of the
$f_m := 29\text{MPa}$	Based on preliminary tests on the compressive strength of concrete masonry blocks
$L_w := 600\text{mm}$	
$f_y := 450\text{MPa}$	Maximum predicted yield strength of reinforcing steel
$h := 12.5 \cdot 12 \cdot 25.4\text{mm} = 3.81 \times 10^3\text{mm}$	Total height of specimen
$E_m := 850 \cdot f_m = 2.465 \times 10^4\text{MPa}$	Predicted elastic modulus for masonry
$E_s := 200000\text{MPa}$	Elastic Modulus of steel
$K := 0.8$	Effective height of specimen based on semi-rigid boundary conditions (Assume partial fixity for conservatism)
$A_b := 300\text{mm}^2$	Area of one 20M bar
$A_s := 3 \cdot A_b = 900\text{mm}^2$	Maximum area of rebar in cross section
$A_{\text{gross}} := L_w \cdot t = 8.4 \times 10^4\text{mm}^2$	
$I_{\text{gross}} := L_w \cdot \frac{t^3}{12} = 1.372 \times 10^8\text{mm}^4$	

Determine the crushing strength of column:

$$P_{\text{crushing}} = A_{\text{gross}} f_m = 2.436 \times 10^3\text{ kN}$$

$$\frac{P_{\text{crushing}}}{4.44\text{kN}} = 548.649\text{ kips}$$

Determine the Euler buckling capacity of column:

$$P_{\text{cr}} := \frac{(\pi^2 \cdot E_m \cdot I_{\text{gross}})}{(K \cdot h)^2} = 3.593 \times 10^3\text{ kN}$$

$$\frac{0.5 \cdot P_{cr}}{4.44 \text{ kN}} = 404.602 \text{ kips}$$

Design compressive force:

$$P_{\text{compressive}} := \begin{cases} (P_{cr}) & \text{if } P_{cr} < P_{\text{crushing}} \\ P_{\text{crushing}} & \end{cases} = 2.436 \times 10^3 \text{ kN}$$

Test apparatus and the actuators must be capable of exerting at least this amount of downward force if the specimen buckled according to Euler buckling. However, since the buckling capacity of a cracked section is much less than the Euler buckling capacity, (i.e.  $I_{cr} \sim 0.5 I_{\text{gross}}$ ) then the buckling capacity of the section is determined to be about 1776 kN (400 kips). This is the governing capacity for which the test rig will be designed.

Determine the tension capacity of the column:

Notes :

The tensile resistance of masonry is ignored.

It is assumed that the reinforcement undergoes strain hardening.

$F_s := 700 \text{ MPa}$   
predicted

Maximum ultimate strength or reinforcement

Assumed stress at large tensile strains

$$P_{\text{tensile}} := F_s \cdot A_s = 630 \text{ kN}$$

The test apparatus and the actuators must be capable of exerting at least this amount of upward force.

## D.1 Design Calculations

List all design values and strength factors for use in calculations:

### **BOLT DATA:**

BoltGrade := "A325"

Choose between A325 or A490 Grade

j := 1..5

BoltDiameter<sub>j</sub> :=

$\frac{5}{8} \cdot 25.4\text{mm}$
$\frac{3}{4} \cdot 25.4\text{mm}$
1 · 25.4mm
1.125 · 25.4mm
1.5 · 25.4mm

$$\text{BoltDiameter} = \begin{pmatrix} 15.875 \\ 19.05 \\ 25.4 \\ 28.575 \\ 38.1 \end{pmatrix} \text{ mm}$$

$$F_u_j := \begin{cases} \text{if BoltGrade} = \text{"A325"} & = \dots & \text{[S16-01 Table 3-3]} \\ \begin{cases} 825\text{MPa} & \text{if BoltDiameter}_j \leq 25.4\text{mm} \\ 725\text{MPa} & \text{otherwise} \end{cases} \\ 1035\text{MPa} & \text{otherwise} \end{cases}$$

ThreadsIntercepted := "Yes"

$\phi_{br} := 0.67$

$\phi_b := 0.8$

[S16-01 Cl.13.2.1]

$\phi := 0.9$

Steel resistance factor

*Unit shear resistance*

$$f_s := \begin{cases} 0.7 \cdot 0.6 \cdot \phi \cdot F_u & \text{if ThreadsIntercepted} = \text{"Yes"} \\ 0.6 \cdot \phi \cdot F_u & \text{otherwise} \end{cases} = \begin{pmatrix} 277.2 \\ 277.2 \\ 277.2 \\ 243.6 \\ 243.6 \end{pmatrix} \text{ MPa} \quad \text{[S16-01 Table 3-3]}$$

$k_s := 0.33$

Class A surface, clean mill scale, [S16-01 Table 3-10]

$$c1 := \begin{cases} 0.82 & \text{if BoltGrade} = \text{"A325"} \\ 0.78 & \text{otherwise} \end{cases} = 0.82 \quad [\text{S16-01 Table 3-10}]$$

Unit slip resistance for 5% probability of slip

$$f_{\text{slip}} := 0.53 \cdot c1 \cdot k_s \cdot F_u = \begin{pmatrix} 118.32 \\ 118.32 \\ 118.32 \\ 103.978 \\ 103.978 \end{pmatrix} \text{ MPa} \quad \text{on Class A surface, single shear [S16-01 Table 3-11]}$$

$$f_{\text{bolt}} := 0.75 \cdot \phi_b \cdot F_u = \begin{pmatrix} 495 \\ 495 \\ 495 \\ 435 \\ 435 \end{pmatrix} \text{ MPa}$$

Unit tensile resistance

$$A_{\text{bolt}_j} := \left( \text{BoltDiameter}_j \right)^2 \frac{\pi}{4} = \dots$$

$$V_{\text{rbolt}_j} := f_{s_j} \cdot A_{\text{bolt}_j} = \dots$$

$$V_{\text{sbolt}_j} := f_{\text{slip}_j} \cdot A_{\text{bolt}_j} = \dots$$

$$T_{\text{rbolt}_j} := f_{\text{bolt}_j} \cdot A_{\text{bolt}_j} = \dots$$

Shear resistance per bolt in single shear [S16-01 Table 3-4]

Slip resistance per bolt in single shear

Tensile resistance per bolt in single shear [S16-01 Table 3-4]

## **WELD DATA:**

Minimum and maximum size of weld

$$\text{WeldSizeMin}(t) := \begin{cases} \text{WeldSizeMin} \leftarrow 3\text{mm} & \text{if } t \leq 6\text{mm} \\ \text{WeldSizeMin} \leftarrow 5\text{mm} & \text{if } t > 6\text{mm} \wedge t \leq 12\text{mm} \\ \text{WeldSizeMin} \leftarrow 6\text{mm} & \text{if } t > 12\text{mm} \wedge t \leq 20\text{mm} \\ \text{WeldSizeMin} \leftarrow 8\text{mm} & \text{otherwise} \end{cases}$$

[Handbook of Steel Construction, 6-170]

$$\text{WeldSizeMax}(t) := \begin{cases} \text{WeldSizeMax} \leftarrow t & \text{if } t < 6\text{mm} \\ t - 2\text{mm} & \text{otherwise} \end{cases}$$

Shear resistance of weld [S16-01 Cl.13.13.2.2]:

$$\phi_w := 0.67$$

$$X_u := 490\text{MPa}$$

$$F_u := 450\text{MPa}$$

$$V_{\text{rWeld}}(A_m, A_w, \theta) := \min \left[ 0.67 \phi_w \cdot A_m \cdot F_u, 0.67 \phi_w \cdot A_w \cdot X_u \left[ 1 + 0.5 \cdot (\sin(\theta))^{1.5} \right] \right]$$

## **STEEL DATA:**

$$\phi := 0.9$$

$$f_y := 350\text{MPa}$$

$$f_{yp} := 300\text{MPa}$$

$$f_{up} := 450\text{MPa}$$

**Design the x-shaped top floating beam:**

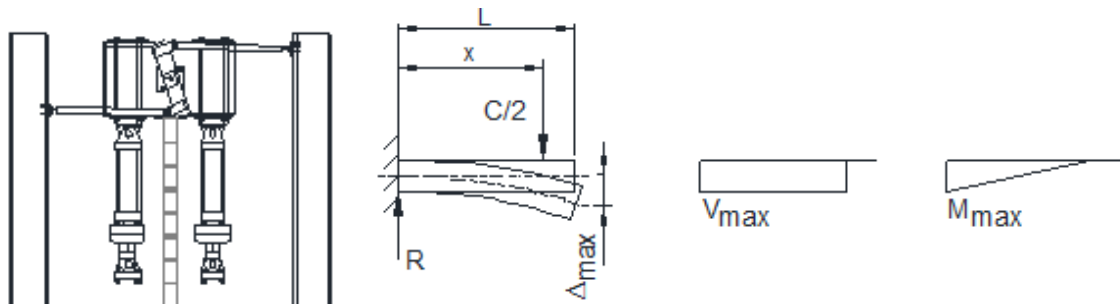


**Figure D- 2 Top floating beam shear and moment diagram**

$$C := 1776 \text{ kN}$$

$$R := \frac{C}{2} = 888 \text{ kN}$$

$$x := 2 \cdot 12 \cdot 25.4 \text{ mm} = 609.6 \text{ mm}$$

$$L1 := 0.5(5 \cdot 12) \cdot 25.4 \text{ mm} = 762 \text{ mm}$$

$$L2 := 2 \cdot L1 = 1.524 \times 10^3 \text{ mm}$$

Design compressive force

Reactions at each actuator location

Length of half of top beam

Total length of top beam

**Choose W610x140:**

$$I_x := 1120 \cdot 10^6 \text{ mm}^4$$

$$I_y := 45.1 \cdot 10^6 \text{ mm}^4$$

$$h_w := 617 \text{ mm}$$

$$A_{\text{section}} := 17900 \text{ mm}^2$$

$$t_w := 13.1 \text{ mm}$$

$$b_f := 230 \text{ mm}$$

$$t_f := 22.2 \text{ mm}$$

$$A_w := h_w \cdot t_w = 8.083 \times 10^3 \text{ mm}^2$$

$$A_f := b_f \cdot t_f = 5.106 \times 10^3 \text{ mm}^2$$

$$S_x := \frac{I_x}{\frac{h_w}{2}} = 3.63 \times 10^6 \text{ mm}^3$$

$$Z_x := 4150 \times 10^3 \text{ mm}^3$$

$$f_{y\text{grade}} := 350 \text{ MPa}$$

$$E_s = 2 \times 10^5 \text{ MPa}$$

$$G_s := 77000 \text{ MPa}$$

$$J_w := 2180 \cdot 10^3 \text{ mm}^4$$

$$C_w := 3990 \cdot 10^9 \text{ mm}^6$$

$$A_{\text{top}} := h_w \cdot t_w = 8.083 \times 10^3 \text{ mm}^2$$

Moment of inertia about X-X axis

Moment of inertia about Y-Y axis

Height of web

Area of cross section

Web thickness

Width of flange

Flange thickness

Area of web

Area of one flange

Section modulus

Plastic section modulus

Section yield strength

Section Young Modulus

Shear modulus of steel

Torsional constant

Warping torsional constant

**Check Moment Resistance of W610x140:**

$$M_y := S_x \cdot f_y = 1.271 \times 10^3 \text{ kN}\cdot\text{m}$$

$$M_p := Z_x \cdot f_y = 1.452 \times 10^3 \text{ kN}\cdot\text{m}$$

Elastic moment resistance of section

Plastic moment resistance of section

Check lateral torsional buckling

$$\omega_2 := 1.0$$

[S16-01 Cl.13.6]

When bending moments at ends of the unbraced length are zero [S16-01 Cl.13.8.5]

$$M_u := \left( \omega_2 \frac{\pi}{L_2} \right) \cdot \sqrt{E_s \cdot I_y \cdot G \cdot J + \left( \pi \frac{E_s}{L_2} \right)^2 \cdot I_y \cdot C_w} = 1.168 \times 10^4 \text{ kN}\cdot\text{m}$$

Critical elastic moment

Determine the class of section:

$$\text{Class} := \begin{cases} 1 & \text{if } \frac{h_w}{t_w} \leq \frac{1100}{\sqrt{\frac{f_y}{\text{MPa}}}} \\ 2 & \text{if } \frac{h_w}{t_w} > \frac{1100}{\sqrt{\frac{f_y}{\text{MPa}}}} \wedge \frac{h_w}{t_w} \leq \frac{1700}{\sqrt{\frac{f_y}{\text{MPa}}}} \\ 3 & \text{otherwise} \end{cases} = 1$$

$$M_r := \begin{cases} 1.15 \phi \cdot M_p \left[ 1 - \frac{(0.28 \cdot M_p)}{M_u} \right] & \text{if } M_u > 0.67 M_p \\ \phi \cdot M_u & \text{otherwise} \end{cases} = 1.451 \times 10^3 \text{ kN}\cdot\text{m}$$

$$M_y = 1.271 \times 10^3 \text{ kN}\cdot\text{m}$$

Check the effect of thin webs

[S16-01 Cl.14.3.4]

$$M_r := \begin{cases} M_r \cdot \left[ 1 - 0.0005 \frac{A_w}{A_f} \left( \frac{h_w}{t_w} - \frac{1900 \sqrt{\frac{\text{kN}\cdot\text{m}}{\text{mm}^3}}}{\sqrt{\frac{M_f}{S_x}}} \right) \right] & \text{if } \frac{h_w}{t_w} > \frac{1900}{\sqrt{\left( \frac{M_f}{S_x} \right) \frac{\text{mm}^3}{\text{kN}\cdot\text{m}}}} \\ M_r & \text{otherwise} \end{cases} = 1.451 \times 10^3 \text{ kN}\cdot\text{m}$$

$$\begin{cases} \text{"OK"} & \text{if } M_r > M_f \\ \text{"NOT OK"} & \text{otherwise} \end{cases} = \text{"OK"}$$

$$\text{FOS} := \frac{M_y}{M_f} = 1.878$$

Factor of Safety

Check deflection:

$$\Delta_{\text{specimen}} := \frac{C}{\frac{(E_m \cdot A_{\text{gross}})}{h}} = 3.268 \text{ mm}$$

$$\Delta_{\text{total}} := \Delta_{\text{max}} + \Delta_{\text{specimen}} = 3.567 \text{ mm}$$

Check Shear Capacity:

$$\text{StiffenerSpacing} := 0 \text{ mm}$$

No shear stiffeners provided

$$\text{AspectRatio} := \frac{\text{StiffenerSpacing}}{h_w} = 0$$

$$k_a := \frac{1}{\sqrt{1 + (\text{AspectRatio})^2}} = 1$$

$$k_v := \begin{cases} 5.34 & \text{if } (\text{AspectRatio} = 0) \\ 4 + \frac{5.34}{\text{AspectRatio}^2} & \text{if } \text{AspectRatio} > 0 \wedge \text{AspectRatio} < 1 \\ 5.34 + \frac{4}{\text{AspectRatio}^2} & \text{otherwise} \end{cases} = 5.34 \quad \text{Web Yielding Factor}$$

$$WY := \sqrt{\frac{k_v}{\frac{f_y}{\text{MPa}}}} = 0.124$$

$$F_{\text{shear}}(h, t) := \begin{cases} F_{\text{shear}} \leftarrow 0.66 \cdot f_y \cdot \frac{h}{t} & \text{if } \frac{h}{t} \leq 439 \cdot WY \\ F_{\text{shear}} \leftarrow 290 \cdot \frac{\sqrt{f_y \cdot k_v \cdot \text{MPa}}}{\left(\frac{h}{t}\right)} & \text{if } \frac{h}{t} > 439 \cdot WY \wedge \frac{h}{t} \leq 502 \cdot WY \\ F_{\text{shear}} \leftarrow 290 \cdot \frac{\sqrt{f_y \cdot k_v \cdot \text{MPa}}}{\left(\frac{h}{t}\right)} + k_a \left[ 0.5 \cdot f_y - 0.866 \left[ 290 \cdot \frac{\sqrt{f_y \cdot k_v \cdot \text{MPa}}}{\left(\frac{h}{t}\right)} \right] \right] & \text{if } \frac{h}{t} > 502 \cdot WY \wedge \frac{h}{t} \leq 621 \cdot WY \\ F_{\text{shear}} \leftarrow 180000 \cdot \frac{k_v \cdot \text{MPa}}{\left(\frac{h}{t}\right)^2} + k_a \left[ 0.5 \cdot f_y - 0.866 \left[ 180000 \cdot \frac{k_v \cdot \text{MPa}}{\left(\frac{h}{t}\right)^2} \right] \right] & \text{otherwise} \end{cases}$$

$$F_{\text{shear}}(h_w, t_w) = 231 \text{ MPa}$$

$$V_r := \phi \cdot F_{\text{shear}}(h_w, t_w) \cdot A_w = 1.68 \times 10^3 \text{ kN}$$

$$FOS := \frac{V_r}{V_f} = 1.892$$

Check to see if stiffeners are needed:

*Shear stiffeners:*

$$f_{\text{shear}} := \frac{V_f}{A_w} = 109.864 \text{ MPa}$$

Applied shear stress

$$\text{StiffenerNeeded} = \begin{cases} \text{"Stiffeners Required"} & \text{if } f_{\text{shear}} > F_s \\ \text{"Stiffeners NOT Required"} & \text{otherwise} \end{cases} = \text{"Stiffeners NOT Required"}$$

*Bearing stiffeners:*

Check web crippling:

[S16-01 Cl.14.3.2]

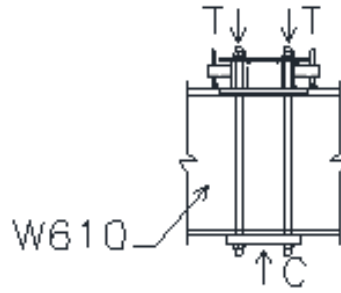


**Figure D-3 Free body diagram of top floating beam**

$N := 2 \cdot 25.4 \text{ mm} = 50.8 \text{ mm}$   
 $\phi_{bi} := 0.8$   
 $\phi_{be} := 0.75$

Length of bearing along the length of beam  
 Intermediate bearing  
 End bearing

$$Br := \begin{cases} \phi_{bi} \cdot t_w \cdot (N + 10 \cdot t_f) \cdot f_y & \text{if } \phi_{bi} \cdot t_w \cdot (N + 10 \cdot t_f) \cdot f_y < 1.45 \cdot \phi_{bi} \cdot t_w^2 \cdot \sqrt{f_y \cdot E_s} \\ 1.45 \cdot \phi_{bi} \cdot t_w^2 \cdot \sqrt{f_y \cdot E_s} & \text{otherwise} \end{cases} = 1.001 \times 10^3 \text{ kN}$$

[S16-01 Cl.14.3.2 & Cl.14.4.1]

$$BStiffenerNeeded := \begin{cases} \text{"B Stiff. Req'd"} & \text{if } \frac{hw}{t_w} > \frac{1100}{\sqrt{\frac{f_y}{\text{MPa}}}} \vee Br < P_{tensile} \\ \text{"B Stiff. NOT Req'd"} & \text{otherwise} \end{cases} = \text{"B Stiff. NOT Req'd"}$$

Add bearing stiffeners at the location of point loads anyway! Try 2 plates:

$t_s := 12.5 \text{ mm}$

Thickness of stiffener, 1" width of stiffener based on max width-to-thickness ratio [S16-01 Table 1]

$$b_{max} := \begin{cases} 200 \cdot \frac{t_s}{\sqrt{\frac{f_y}{\text{MPa}}}} & \text{if } 200 \cdot \frac{t_s}{\sqrt{\frac{f_y}{\text{MPa}}}} < \left(\frac{bf}{2}\right) - t_w \\ \left(\frac{bf}{2}\right) - t_w & \text{otherwise} \end{cases} = 101.9 \text{ mm}$$

$A_{eff} := 2 \cdot t_s \cdot b_{max} + 25 \cdot t_w \cdot (\text{mm}) = 2.875 \times 10^3 \text{ mm}^2$

[S16-01 Cl. 14.4.2]

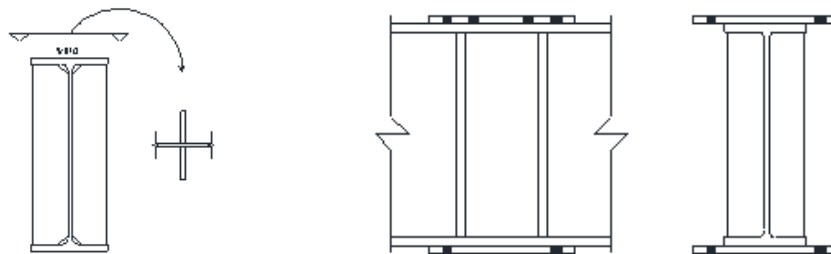


**Figure D-4 Cross section of top floating beam**

$$I_{\text{stiffener}} := 2 \left[ t_s \cdot b_{\text{max}} \cdot \left( \frac{b_{\text{max}}}{2} + \frac{t_w}{2} \right)^2 + t_s \frac{b_{\text{max}}^3}{12} \right] + 25 \frac{t_w^4}{12} = 1.069 \times 10^7 \text{ mm}^4$$

$$r := \sqrt{\frac{I_{\text{stiffener}}}{A_{\text{eff}}}} = 60.973 \text{ mm} \quad [\text{S16-01 Cl. 14.4.2}]$$

$$k := 0.75$$

$$\lambda_1 := \frac{(k \cdot h_w)}{r} \cdot \sqrt{\frac{f_y}{\pi^2 \cdot E_s}} = 0.101 \quad [\text{S16-01 Cl. 13.3.1}]$$

$$n := 1.34$$

For hot-rolled, fabricated structural sections  
[S16-01 Cl. 13.3.1]

Axial compressive resistance of doubly symmetric shapes, [S16-01 Cl. 13.3.1]:

$$C_r(\text{Area}, \lambda) := \phi \cdot \text{Area} \cdot f_y \cdot \left( 1 + \lambda^{2 \cdot n} \right)^{\frac{-1}{n}}$$

$$C_r(A_{\text{eff}}, \lambda_1) = 904.175 \text{ kN}$$

Check bearing at point load locations:

$$L_{\text{crop}} := 25 \text{ mm}$$

Assumed

$$A_{\text{bearing}} := 2 \cdot (b_{\text{max}} - L_{\text{crop}}) \cdot t_s = 1.923 \times 10^3 \text{ mm}^2$$

$$B_{r2} := \phi \cdot f_y \cdot A_{\text{bearing}} = 605.587 \text{ kN}$$

[S16-01 Cl.13.10]

Choose a suitable weld size for attaching stiffeners to beam web:

$$\text{WeldSizeMin}(t_s) = 6 \text{ mm}$$

$$\text{WeldSizeMax}(t_s) = 10.5 \text{ mm}$$

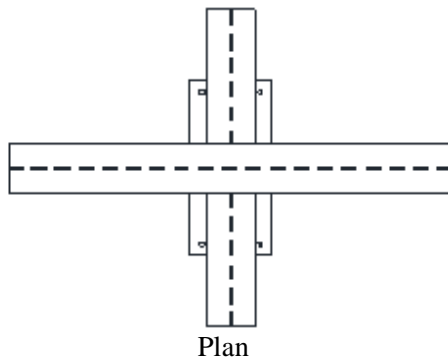
$$D := 6 \text{ mm}$$

Check the effect of combined shear and moment:

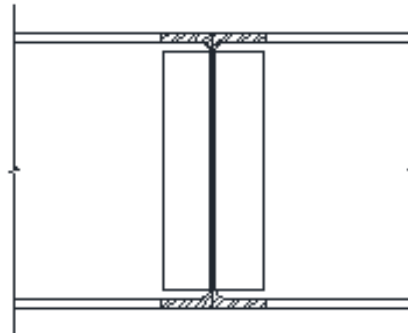
Note: interaction of shear and moment is critical when  $V_f > 0.6 V_r$

$$M_n V_{\text{interaction}} := \begin{cases} \text{if } V_f > 0.6 \cdot V_r & = \text{"OK"} \\ \begin{cases} \text{"NOT OK"} & \text{if } 0.727 \frac{M_f}{M_r} + 0.455 \frac{V_f}{V_r} > 1.0 \\ \text{"OK"} & \text{otherwise} \end{cases} \\ \text{"OK"} & \text{if } \frac{M_f}{M_r} \leq 1.0 \wedge \frac{V_f}{V_r} \leq 1.0 \text{ otherwise} \end{cases}$$

**Design the connection of the top w610 cropped beam to the continuous w610 beam:**



Plan



Cross-section of the connection at center

**Figure D- 5 Welded connections to the top floating beam**

Assume plate thickness (3/8"):

$$t_{plate1} := 10\text{mm}$$

$$t_w = 13.1\text{mm}$$

$$t1 := \max(t_{plate1}, t_w) = 13.1\text{mm}$$

$$\text{WeldSizeMin}(t1) = 6\text{mm}$$

$$\text{WeldSizeMax}(t1) = 11.1\text{mm}$$

$$D2 := 12.5\text{mm}$$

$$T := 529\text{mm}$$

$$A_{m1} := D2 \cdot (2T) = 1.323 \times 10^4 \text{mm}^2$$

$$A_{w1} := D2 \frac{2T}{\sqrt{2}} = 9.351 \times 10^3 \text{mm}^2$$

$$\theta_1 := 0$$

$$V_{rWeldTopBeam} := V_{rWeld}(A_{m1}, A_{w1}, \theta_1) = 2.057 \times 10^3 \text{kN}$$

**Check shear resistance of web after welding:**

$$V_{rweb1} := \phi \cdot (T - 2 \cdot D2) \cdot t_w \cdot F_{shear}(h_w, t_w) = 1.373 \times 10^3 \text{kN}$$

Thickness of web for W610

Weld Size

The height of the cropped portion of the beam

Area of weld parallel to the direction of loading

### Design plates attached to the ends of floating beam to support pantographs:

$$t_{\text{plate}} := 12.5 \text{ mm}$$

Assume the thickness of the plate

#### Check bearing capacity:

$$\text{BoltDiameter}_3 = 25.4 \text{ mm}$$

$$\text{PantographWeight} := 100 \text{ kN}$$

$$f_{\text{bearing}} := \frac{\left( \frac{\text{PantographWeight}}{2} \right)}{t_{\text{plate}} \cdot \text{BoltDiameter}_3} = 157.48 \text{ MPa}$$

#### Check bolt shear capacity:

$$V_{\text{rbolt}_3} = 140.459 \text{ kN}$$

#### Check End Plate Shear Block:

$$L_p := 9 \cdot 25.4 \text{ mm} = 228.6 \text{ mm}$$

$$\text{Edge} := 1.5 \cdot 25.4 \text{ mm} = 38.1 \text{ mm}$$

$$\text{Apgv2} := L_p \cdot t_{\text{plate}} = 2.858 \times 10^3 \text{ mm}^2$$

Plate gross area in shear

$$\text{Apsn2} := \text{Apgv2} - 2 \cdot (\text{BoltDiameter}_3 + 2 \text{ mm}) \cdot t_{\text{plate}} = 2.172 \times 10^3 \text{ mm}^2$$

Plate net area in shear

[S16-01 Cl.13.11]

$$V_{\text{rBlock2}} := 0.6 \cdot \phi \cdot \text{Apsn2} \cdot f_{\text{yp}} = 351.945 \text{ kN}$$

#### Check End Plate Tension and Shear Block:

Plate net area in shear under tension

$$\text{Apgv22} := (L_p - \text{Edge}) \cdot t_{\text{plate}} = 2.381 \times 10^3 \text{ mm}^2$$

$$\text{Apsn22} := \text{Apgv22} - (1 - 0.5) \cdot (\text{BoltDiameter}_3 + 2 \text{ mm}) \cdot t_{\text{plate}} = 2.21 \times 10^3 \text{ mm}^2$$

$$\text{Apnt2} := \left( \text{Edge} - \frac{\text{BoltDiameter}_3}{2} - 2 \text{ mm} \right) \cdot t_{\text{plate}} = 292.5 \text{ mm}^2$$

$$\text{TSBlock} := \begin{cases} (\phi \cdot \text{Apnt2} \cdot f_{\text{up}} + 0.6 \cdot \phi \cdot \text{Apgv22} \cdot f_{\text{yp}}) & \text{if } \text{Apgv22} \cdot f_{\text{yp}} < \text{Apsn22} \cdot f_{\text{up}} \\ \phi \cdot \text{Apnt2} \cdot f_{\text{up}} + 0.6 \cdot \phi \cdot \text{Apsn22} \cdot f_{\text{up}} & \text{otherwise} \end{cases} = 504.225 \text{ kN}$$

Evaluate Tension and Shear Block Failure at the Elastic level:

$$\text{TSBlock2} := \phi \cdot \text{Apnt2} \cdot f_{\text{yp}} + 0.6 \cdot \phi \cdot \text{Apsn22} \cdot f_{\text{yp}} = 436.995 \text{ kN}$$

#### Check the weld connection of the plate to the end of W610 floating beam:

$$\text{WeldSizeMin}(\max(t_{\text{plate}}, t_w)) = 6 \text{ mm}$$

$$\text{WeldSizeMax}(\max(t_{\text{plate}}, t_w)) = 11.1 \text{ mm}$$

$$D4 := 6 \text{ mm}$$

$$\text{WeldSize}$$

$$A_{m4} := 2D_4 \cdot L_p = 2.743 \times 10^3 \text{ mm}^2$$

$$A_{w4} := \frac{A_{m4}}{\sqrt{2}} = 1.94 \times 10^3 \text{ mm}^2$$

$$\theta_4 := 0$$

$$V_{rWeldTopPlate4} := V_{rWeld}(A_{m4}, A_{w4}, \theta_4) = 426.666 \text{ kN}$$

**Check shear resistance of web after welding:**

$$V_{rweb} := \phi \cdot (L_p - 2 \cdot D_4) \cdot t_w \cdot F_{shear}(h_w, t_w) = 589.908 \text{ kN}$$

**Design plates welded to the top and bottom of floating beam attached to specimen:**

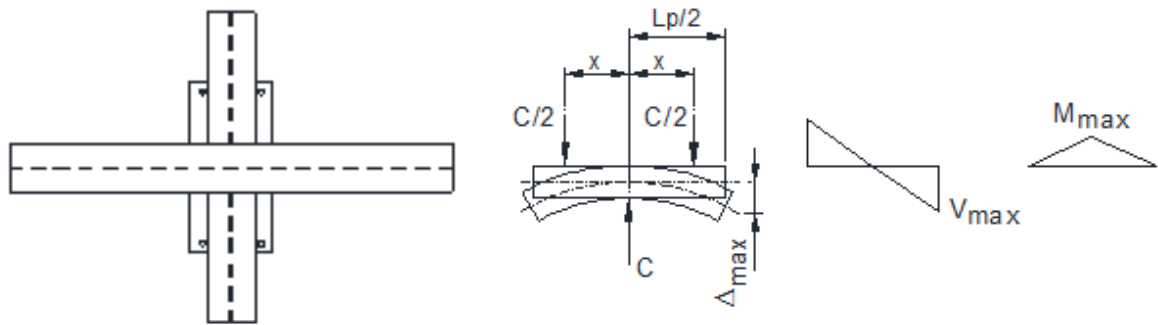


**Figure D- 6 Moment and shear diagram for plates**

$$xp3 := (2) \cdot 25.4\text{mm} = 50.8\text{mm}$$

Maximum moment arm off the edge of the beam

Length of plate perpendicular to the specimen length

$$bp3 := (9.75) \cdot 25.4\text{mm} = 247.65\text{mm}$$

$$V_{\max3} := \frac{C}{2} = 888\text{kN}$$

$$M_{\max3} := V_{\max3} \cdot xp3 = 45.11\text{ kN}\cdot\text{m}$$

**Determine the thickness of plate to provide required moment resistance:**

$$t_{\text{plate3min}} := \sqrt{6 \frac{M_{\max3}}{f_{yp} \cdot bp3}} = 60.358\text{mm}$$

Minimum plate thickness to meet moment requirements (based on elastic moment)

$$t_{\text{plate3}} := 38.1\text{mm}$$

$$I_{\text{plate3}} := bp3 \frac{(t_{\text{plate3}})^3}{12} = 1.141 \times 10^6 \text{ mm}^4$$

$$S_{\text{plate3}} := \frac{I_{\text{plate3}}}{\frac{t_{\text{plate3}}}{2}} = 5.992 \times 10^4 \text{ mm}^3$$

$$M_{r\text{plate3}} := f_{yp} \cdot (S_{\text{plate3}}) = 17.975\text{ kN}\cdot\text{m}$$

**Check for shear:**

$$V_{r\text{plate3}} := \frac{f_{yp}}{\sqrt{3}} \cdot 2 \cdot bf \cdot t_{\text{plate3}} = 3.036 \times 10^3 \text{ kN}$$

**Check for bearing:**

$$A_{\text{wall}} := t \cdot L_w = 8.4 \times 10^4 \text{ mm}^2$$

$$f_{\text{bearing3}} := \frac{C}{A_{\text{wall}}} = 21.143\text{MPa}$$

**Check the weld that connects the top plate to the floating beam:**

$$\text{WeldSizeMin}(\max(t_{\text{plate3}}, t_f)) = 8\text{mm}$$

$$\text{WeldSizeMax}(\max(t_{\text{plate3}}, t_f)) = 36.1\text{mm}$$

$$D_w := 8\text{mm}$$

Weld size

$$A_{m3} := D \cdot t = 11.25.4\text{mm} = 8.941 \times 10^3 \text{ mm}^2$$

$$A_{w3} := \frac{A_{m3}}{\sqrt{2}} = 6.322 \times 10^3 \text{ mm}^2$$

$$\theta_3 := \frac{\pi}{2}$$

$$V_{r\text{WeldTopPlate}} := V_{r\text{Weld}}(A_{m3}, A_{w3}, \theta_3) = 1.806 \times 10^3 \text{ kN}$$

### **Check capacity of lateral stability system:**

*Check tensile capacity of pantograph arms:*

$$P := 0.09 \cdot C = 159.84 \text{ kN}$$

Assume that maximum lateral force is equal to 10% of maximum compressive force

$$\text{ArmDiameter} := (1.5) \cdot 25.4 \text{ mm} = 38.1 \text{ mm}$$

$$A_{\text{arm}} := \pi \frac{\text{ArmDiameter}^2}{4}$$

Tensile Strength of Pantograph Arm:

$$T_r := \phi \cdot A_{\text{arm}} \cdot f_y = 359.129 \text{ kN}$$

Pantograph arms work in tension only. Therefore, there is no need to check for buckling of the pantograph arm in compression.

*Check moment capacity of W310x158 existing column and the base connection:*

$$h_{\text{column}} := 15 \cdot 12 \cdot 25.4 \text{ mm} = 4.572 \times 10^3 \text{ mm}$$

$$M_{\text{column}} := P \cdot h_{\text{column}} = 730.788 \text{ kN}\cdot\text{m}$$

$$S_{x\text{column}} := 2360 \cdot 10^3 \text{ mm}^3$$

$$M_{r\text{column}} := \phi \cdot S_{x\text{column}} \cdot f_y = 743.4 \text{ kN}\cdot\text{m}$$

$$d_1 := 327 \text{ mm}$$

$$b_{f1} := 310 \text{ mm}$$

$$t_{f2} := 25.1 \text{ mm}$$

Depth of the W310x158 section  
Flange width of the column section  
Flange thickness

*Check the moment resistance of the weld connection by the coupling action of the welds at flanges*

$$\text{Tension} := \frac{M_{\text{column}}}{(d_1 - t_{f2})} = 2.421 \times 10^3 \text{ kN}$$

Tension/compression force developed in the flanges of the column due to applied moment

$$\text{WeldSizeMin}(\max(75 \text{ mm}, t_{f2})) = 8 \text{ mm}$$

$$\text{WeldSizeMax}(\max(t_{\text{plate3}}, t_{f2})) = 36.1 \text{ mm}$$

$$D_5 := 16 \text{ mm}$$

$$A_{m5} := 2 \cdot D_5 \cdot b_f = 7.36 \times 10^3 \text{ mm}^2$$

$$A_{w5} := \frac{A_{m5}}{\sqrt{2}} = 5.204 \times 10^3 \text{ mm}^2$$

$$\theta_5 := \frac{\pi}{2}$$

$$V_r \text{WeldColumnflange} := V_r \text{Weld}(A_{m5}, A_{w5}, \theta_5) = 1.487 \times 10^3 \text{ kN}$$

$$\text{WeldSizeMin}(\max(75 \text{ mm}, 15.5 \text{ mm})) = 8 \text{ mm}$$

$$\text{WeldSizeMax}(\max(75 \text{ mm}, 15.5 \text{ mm})) = 73 \text{ mm}$$

$$D_5 = 16 \text{ mm}$$

Weld size

$$A_{m6} := 2 \cdot D_5 \cdot (d_1 - t_{f2}) = 8.858 \times 10^3 \text{ mm}^2$$

$$A_{w6} := \frac{A_{m6}}{\sqrt{2}} = 6.263 \times 10^3 \text{ mm}^2$$

$$\theta_6 := 0$$

$$V_{rWeldColumnWeb} := V_{rWeld}(A_{m6}, A_{w6}, \theta_6) = 1.378 \times 10^3 \text{ kN}$$

Although the welded connection in the perpendicular direction to the applied moment is calculated as insufficient, this is ignored since the applied lateral load was calculated in a very conservative manner.

**Design bottom plate attached to strong floor:**

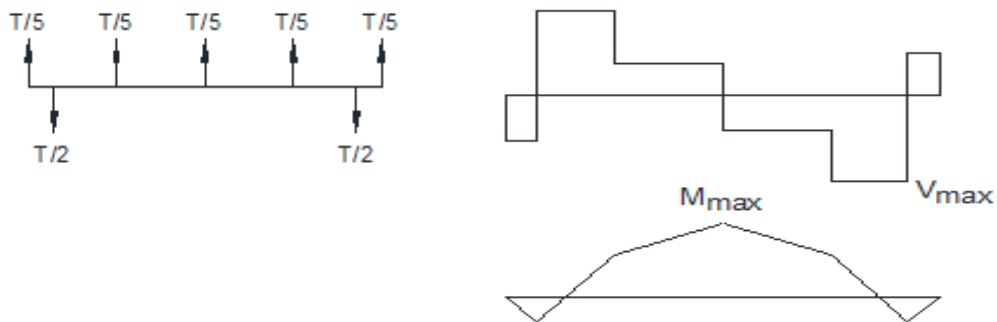


**Figure D-7 Shear and moment diagram for bottom plate**

Design values:

$$P_{\text{tensile}} = 630 \text{ kN}$$

$$V_{\text{max5}} := 180 \text{ kN}$$

$$M_{\text{max5}} := 30 \text{ kN}\cdot\text{m}$$

$$b_{p5} := 15 \cdot 25.4 \text{ mm} = 381 \text{ mm}$$

Width of the plate anchored into the strong floor

**Determine the thickness of plate to provide required moment resistance:**

Minimum plate thickness to meet moment requirements (based on elastic moment)

$$t_{\text{platemin5}} := \sqrt{6 \frac{M_{\text{max5}}}{f_{yp} \cdot b_{p5}}} = 39.684 \text{ mm}$$

Minimum plate thickness to meet moment requirements (based on plastic moment)

$$t_{\text{plate5}} := 50 \text{ mm}$$

Choose plate thickness

$$I_{\text{plate5}} := b_{p5} \frac{(t_{\text{plate5}})^3}{12} = 3.969 \times 10^6 \text{ mm}^4$$

$$S_{\text{plate5}} := \frac{I_{\text{plate5}}}{\frac{t_{\text{plate5}}}{2}} = 1.588 \times 10^5 \text{ mm}^3$$

$$M_{r\text{plate5}} := f_{yp} \cdot (S_{\text{plate5}}) = 47.625 \text{ kN}\cdot\text{m}$$

**Check for shear:**

$$V_{r\text{plate5}} := \frac{f_{yp}}{\sqrt{3}} \cdot b_{p5} \cdot t_{\text{plate5}} = 1.634 \times 10^3 \text{ kN}$$

**Check bolt requirements:**

Tensile capacity of bolts

$$\text{BoltDiameter}_5 = 38.1 \text{ mm}$$

$$V_{r\text{bolt}}_5 = 277.726 \text{ kN}$$

$$T_{r\text{bolt}}_5 = 495.94 \text{ kN}$$

*Check development length of threads for bolts:*

$$A_{\text{shear, nut}} = (\pi \cdot d \cdot m_{\text{eff}}) / P \cdot [P/2 + (d - D_2) / \sqrt{3}]$$

$$m_{\text{eff}} := 50 \text{ mm}$$

$$\text{ThreadPitch} := \frac{50}{24} = 2.083$$

**Fine threads at 12 threads per inch**

$$A_{\text{shear}} := \pi \cdot \text{BoltDiameter}_5 \cdot \frac{m_{\text{eff}}}{\text{ThreadPitch}} = 2.873 \times 10^3 \text{ mm}^2$$

$$V_r \text{Thread} := A_{\text{shear}} \cdot \frac{f_y}{\sqrt{3}} = 580.488 \text{ kN}$$

**Design the specimen plates:**

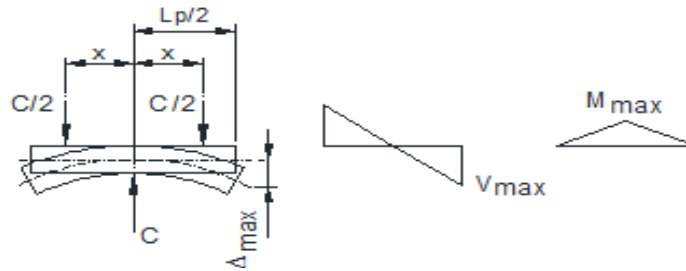


**Figure D- 8 Shear and moment diagram for specimen plates**

Design values:

$$xp6 := \left(\frac{11}{2}\right) \cdot 25.4 \text{ mm} = 139.7 \text{ mm}$$

Length of plate perpendicular to the specimen

$$bp6 := (2 \cdot 12 + 4.5) \cdot 25.4 \text{ mm} = 723.9 \text{ mm}$$

Length of plate parallel to the specimen length

$$f_{yp} := 300 \text{ MPa}$$

Yield strength of plate

$$V_{max6} := P_{tensile} = 630 \text{ kN}$$

$$M_{max6} := P_{tensile} \frac{(2 \cdot xp6)}{4} = 44.005 \text{ kN} \cdot \text{m}$$

**Determine the thickness of plate to provide required moment resistance:**

Minimum plate thickness to meet moment requirements (based on elastic moment)

$$t_{platemin6} := \sqrt{6 \frac{M_{max6}}{f_{yp} \cdot bp6}} = 34.868 \text{ mm}$$

Minimum plate thickness to meet moment requirements (based on plastic moment)

$$t_{plate6} := 1.5 \cdot 25.4 \text{ mm} = 38.1 \text{ mm}$$

$$I_{plate6} := bp6 \frac{(t_{plate6})^3}{12} = 3.336 \times 10^6 \text{ mm}^4$$

$$S_{plate6} := \frac{I_{plate6}}{t_{plate6}} = 1.751 \times 10^5 \text{ mm}^3$$

$$M_{rplate6} := f_{yp} \cdot (S_{plate6}) = 52.541 \text{ kN} \cdot \text{m}$$

**Check for shear:**

$$V_{rplate6} := \frac{f_{yp}}{\sqrt{3}} \cdot bp6 \cdot t_{plate6} = 4.777 \times 10^3 \text{ kN}$$

**Check for bearing:**

$$A_{wall} := t \cdot L_w = 8.4 \times 10^4 \text{ mm}^2$$

$$f_{bearing3} := \frac{P_{compressive}}{A_{wall}} = 29 \text{ MPa}$$

### Design the columns to support actuators:

$$H_{\text{column}} := (9 \cdot 12 + 8) \cdot 25.4 \text{ mm} = 2.946 \times 10^3 \text{ mm}$$

Height of columns

Choose W310x97:

$$d := 310 \text{ mm}$$

$$b := 254 \text{ mm}$$

$$\text{Area} := 11000 \text{ mm}^2$$

$$I_{x2} := 199 \cdot 10^6 \text{ mm}^4$$

$$I_{y2} := 44.5 \cdot 10^6 \text{ mm}^4$$

$$r_x := 134 \text{ mm}$$

$$r_y := 63.6 \text{ mm}$$

$$K_{xx} := 2$$

Check Tension/Compression Capacity of the Section:

$$Tr2 := \phi \cdot \text{Area} \cdot f_y = 3.465 \times 10^3 \text{ kN}$$

Tensile resistance of the gross cross-section at the elastic level

$$\lambda_{2x} := \frac{(K \cdot H_{\text{column}})}{r_x} \cdot \sqrt{\frac{f_y}{\pi^2 \cdot E_s}} = 0.586$$

$$K \cdot H_{\text{column}} = 5.893 \times 10^3 \text{ mm}$$

$$\lambda_{2y} := \frac{(K \cdot H_{\text{column}})}{r_y} \cdot \sqrt{\frac{f_y}{\pi^2 \cdot E_s}} = 1.234$$

$$Cr2 := \min(\text{Cr}(\text{Area}, \lambda_{2x}), \text{Cr}(\text{Area}, \lambda_{2y})) = 1.626 \times 10^3 \text{ kN}$$

$$FOS := \frac{\min(Cr2, Tr2)}{V_f} = 1.831$$

$$P_{cr2} := \frac{(\pi^2 \cdot E_s \cdot I_{y2})}{(H_{\text{column}})^2} = 1.012 \times 10^4 \text{ kN}$$

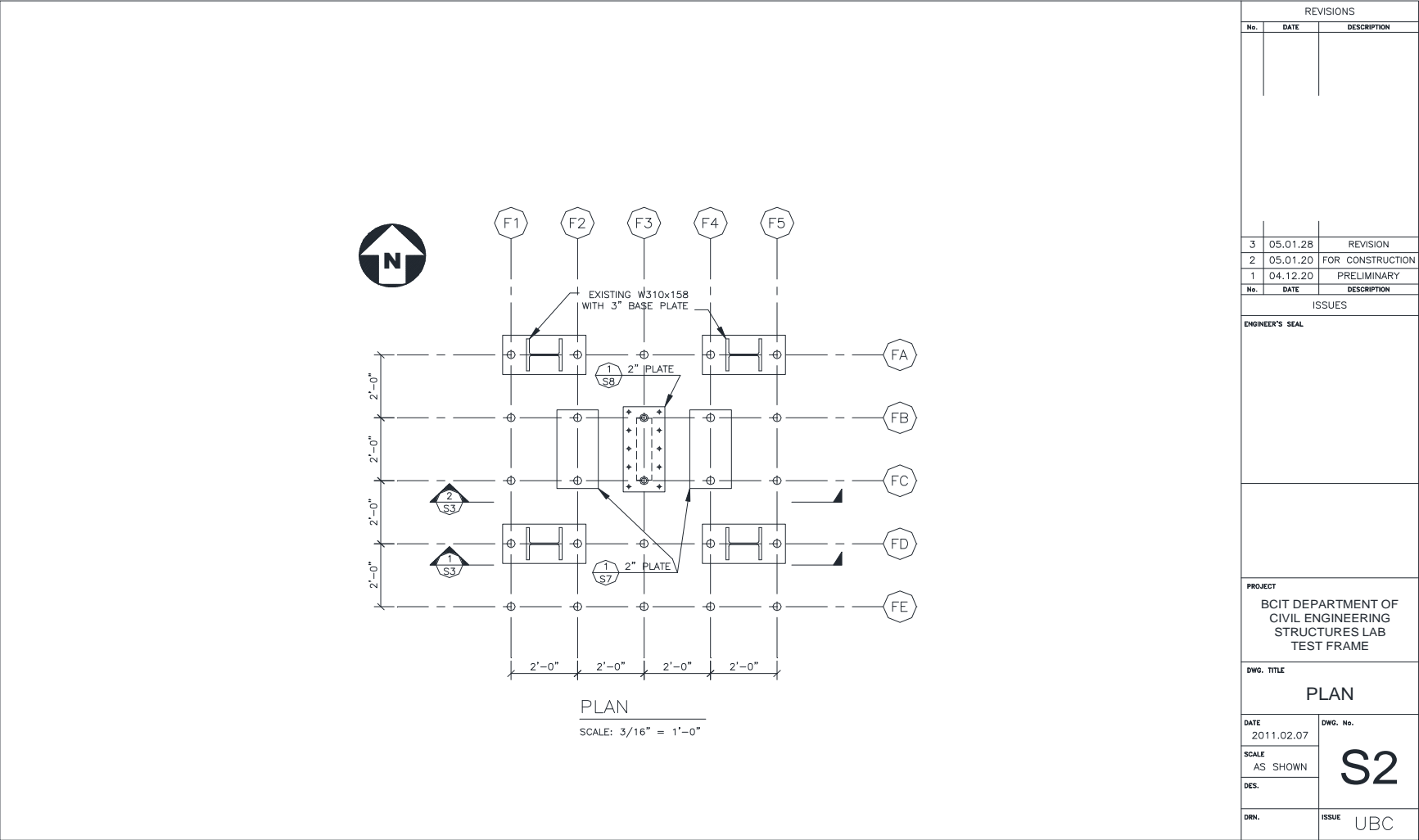
### DETERMINE BASE PLATE DIMENSIONS:

$$B_{\text{concrete}} := 15 \text{ MPa}$$

$$\text{Area}_{\text{Plate}} := \frac{V_f}{0.85 \cdot 0.6 \cdot B_{\text{concrete}}} = 1.161 \times 10^5 \text{ mm}^2$$

$$B := \sqrt{\text{Area}_{\text{Plate}}} = 340.703 \text{ mm}$$

**D.2 Design Drawings**



REVISIONS		
No.	DATE	DESCRIPTION
3	05.01.28	REVISION
2	05.01.20	FOR CONSTRUCTION
1	04.12.20	PRELIMINARY
No.	DATE	DESCRIPTION
ISSUES		
ENGINEER'S SEAL		
PROJECT		
BCIT DEPARTMENT OF CIVIL ENGINEERING STRUCTURES LAB TEST FRAME		
DWG. TITLE		
<b>PLAN</b>		
DATE	DWG. No.	<b>S2</b>
2011.02.07		
SCALE		
AS SHOWN		
DES.		
DRN.	ISSUE	UBC

**Figure D-9 Plan view of test apparatus**

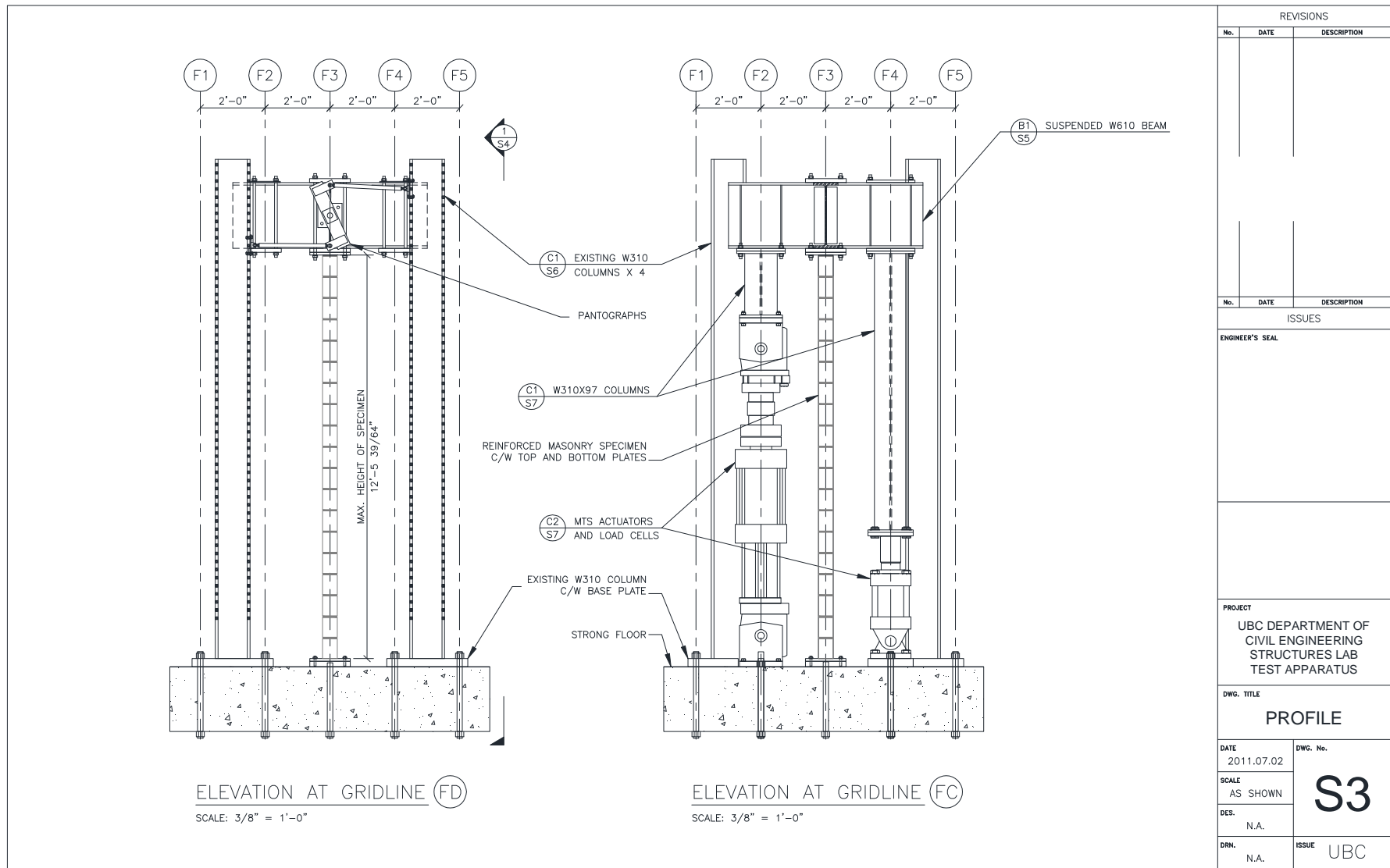
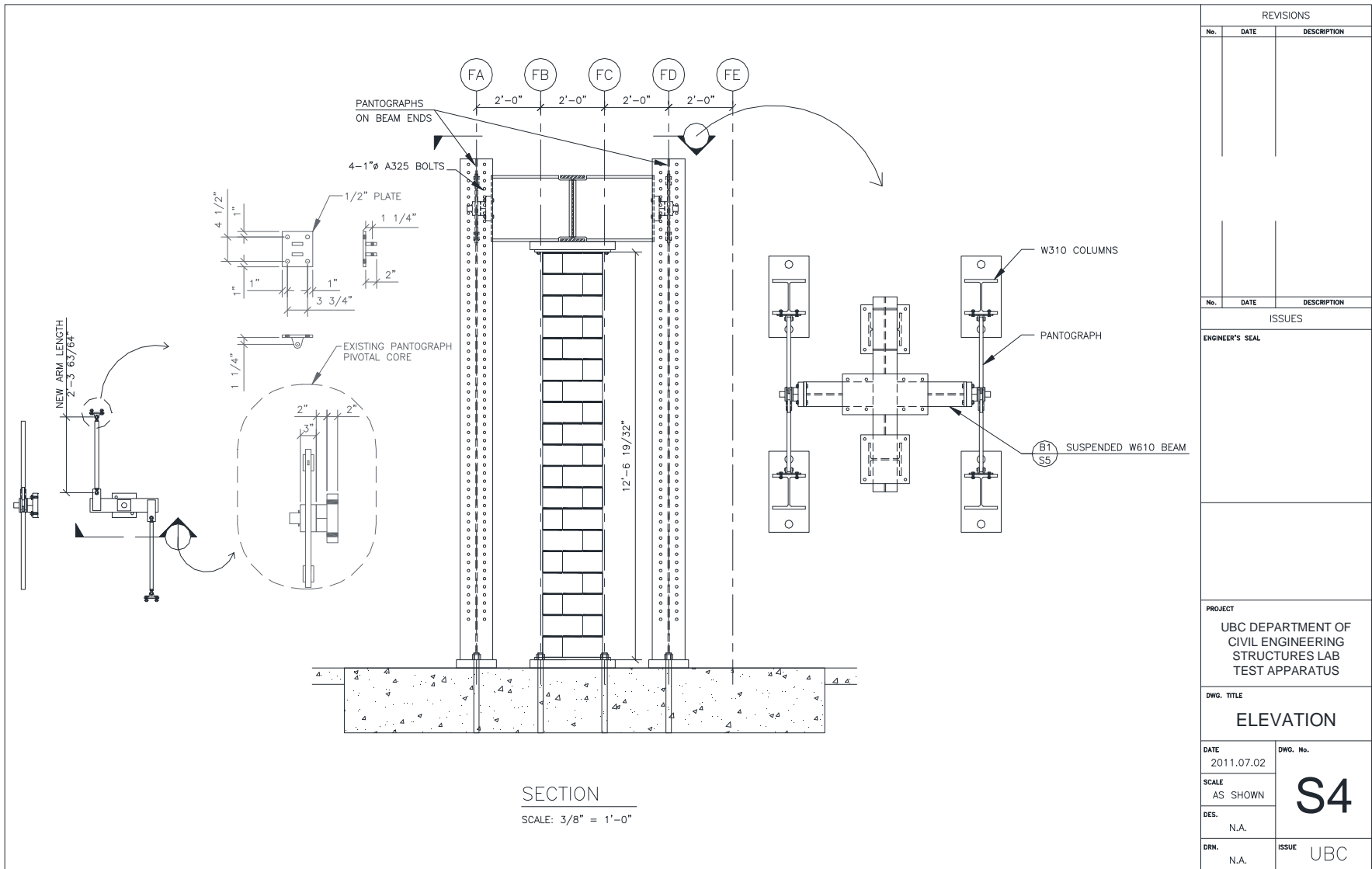


**Figure D-10 Profile view of test apparatus**



REVISIONS		
No.	DATE	DESCRIPTION
ISSUES		
ENGINEER'S SEAL		
PROJECT UBC DEPARTMENT OF CIVIL ENGINEERING STRUCTURES LAB TEST APPARATUS		
DWG. TITLE ELEVATION		
DATE 2011.07.02	DWG. No. <b>S4</b>	
SCALE AS SHOWN		
DES. N.A.		
DRN. N.A.	ISSUE	UBC

Figure D- 11 Elevation view of test apparatus and pantograph detail



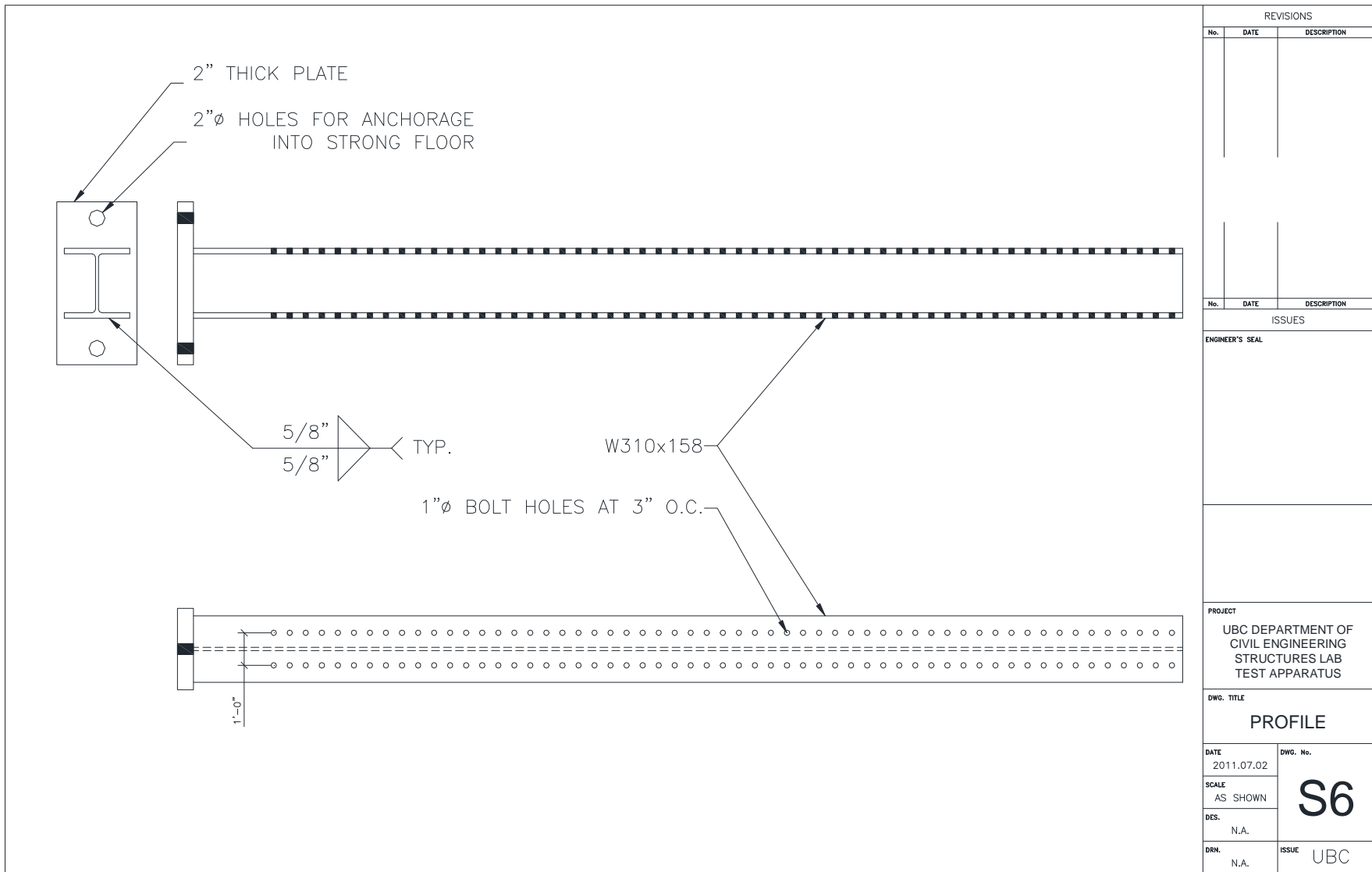


Figure D- 13 Column detail



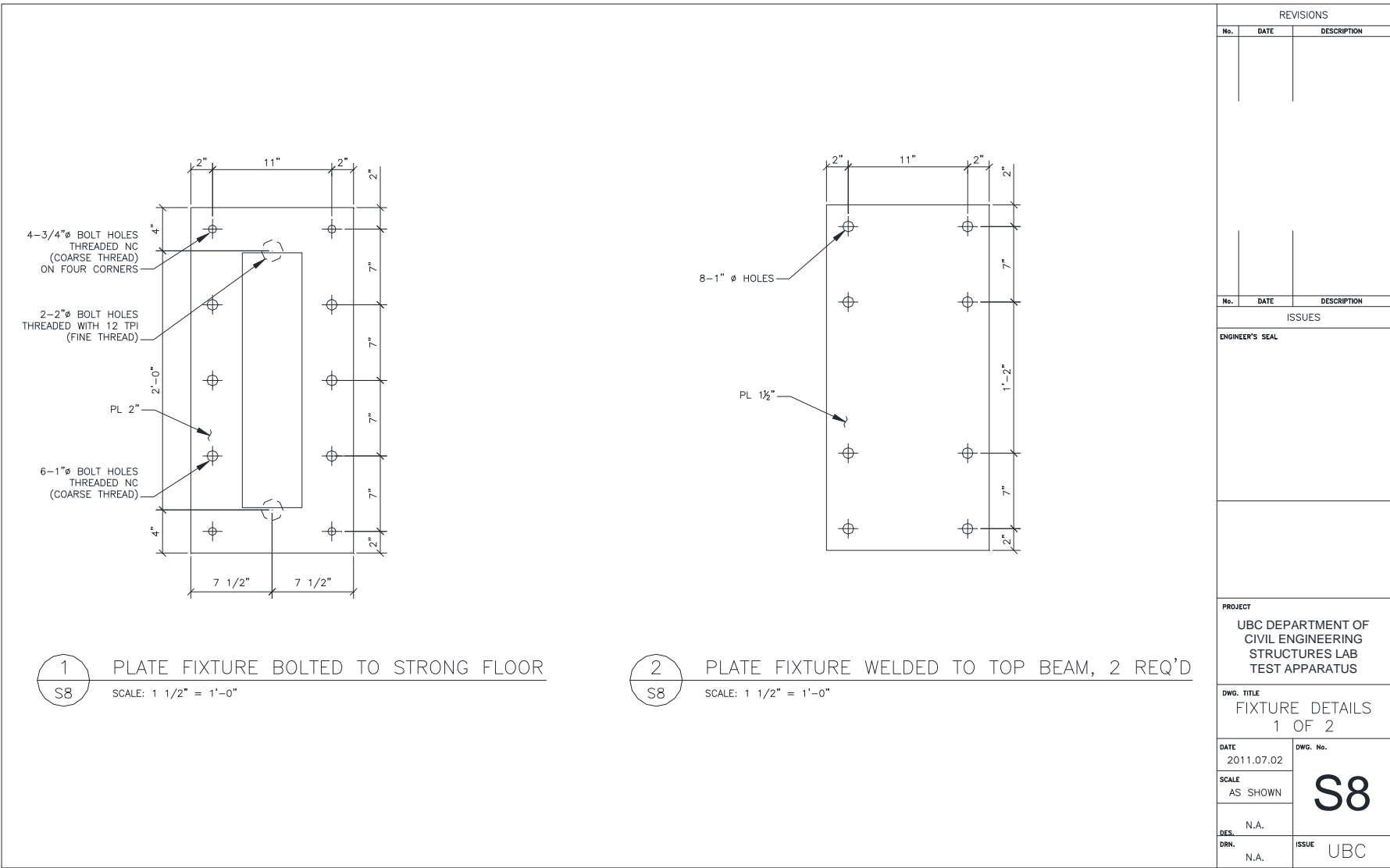


Figure D- 15 Plates detail

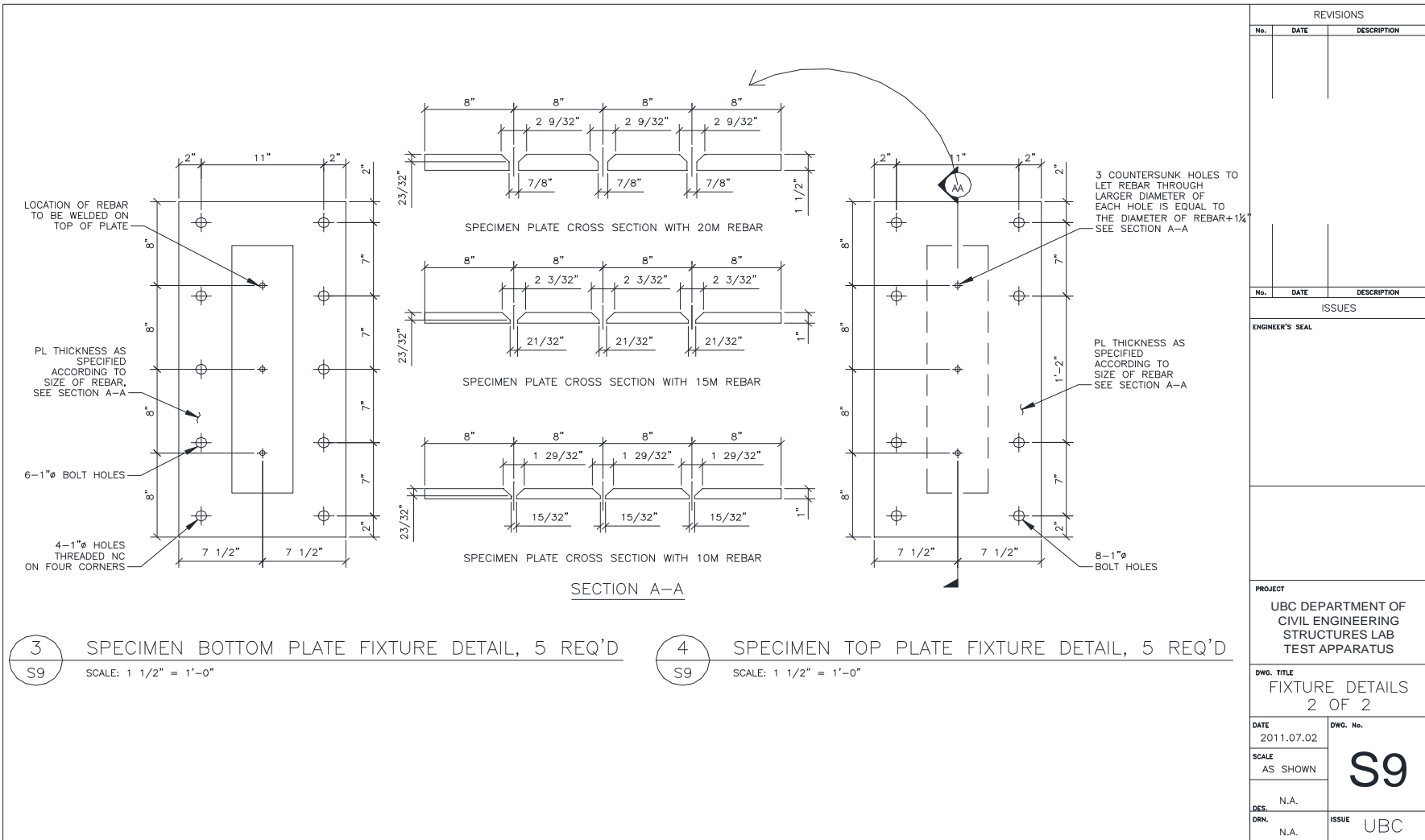


Figure D- 16 Specimen plates detail